Spring 11-22-2016

An Indirect and Dynamically Induced Energy Mechanism in a Plasma-Neutral Atmosphere

Vicki Wei Hsu
University of Colorado at Boulder, vicki.hsu@colorado.edu

Recommended Citation

Hsu, Vicki Wei, "An Indirect and Dynamically Induced Energy Mechanism in a Plasma-Neutral Atmosphere" (2016). *Aerospace Engineering Sciences Graduate Theses & Dissertations*. 188.
https://scholar.colorado.edu/asen_gradetds/188

An Indirect and Dynamically Induced Energy Mechanism in a Plasma-Neutral Atmosphere

by

Vicki W. Hsu

B.S., University of Colorado, 2011

M.S., University of Colorado, 2014

A thesis submitted to the

Faculty of the Graduate School of the

University of Colorado in partial fulfillment

of the requirements for the degree of

Doctor of Philosophy

Department of Aerospace Engineering Sciences

2016

This thesis entitled:
An Indirect and Dynamically Induced Energy Mechanism in a Plasma-Neutral Atmosphere
written by Vicki W. Hsu
has been approved for the Department of Aerospace Engineering Sciences

Prof. Jeffrey Thayer

Dr. Wenbin Wang

Date ____________________

The final copy of this thesis has been examined by the signatories, and we find that both the content and the form meet acceptable presentation standards of scholarly work in the above mentioned discipline.

Hsu, Vicki W. (Ph.D., Aerospace Engineering Sciences)

An Indirect and Dynamically Induced Energy Mechanism in a Plasma-Neutral Atmosphere

Thesis directed by Prof. Jeffrey Thayer

Plasma-neutral interactions play an integral role in governing the dynamics and energy of an upper atmosphere. In the Earth's ionosphere-thermosphere (I/T) region, these interactions can produce significant structure in neutral temperature, winds, mass density, and composition. External sources of momentum and energy that directly affect these properties of the upper atmosphere have been extensively investigated, but these investigations are not sufficient to fully describe thermosphere phenomenology. Considering the strong plasma-neutral coupling in the I/T region, an internal and indirect energy mechanism, or a feedback exchange between hydrodynamics and thermodynamics, can contribute to the resultant structure. The complex, indirect consequences of internal momentum changes on neutral gas properties have not been thoroughly assessed due to the multivariate nature of the problem and limited observations. Through the use of the National Center for Atmospheric Research Thermosphere-Ionosphere-Electrodynamics General Circulation Model, this thesis seeks to simulate, understand, and quantify how plasma-neutral interactions affect the energy distribution of the upper thermosphere via an indirect, dynamically induced mechanism, and to establish that this mechanism can explain the existence of thermospheric density features.

The main conclusions that stem from this dissertation are as follows: (1) Changes in the field-aligned ion drag force alter neutral temperature and mass density by means of a divergent neutral wind field, commanding the formation, local time, and solar cycle variations of the equatorial thermosphere anomaly trough; (2) Ion and viscous drag forces produce balanced motion with sustained, divergent winds that change thermal and mass density structure through adiabatic heating; (3) A boundary that delineates the lower and upper thermosphere is recognized and deemed the "thermopause", and helium is demonstrated to be an effective dynamic tracer for a circuitous

energy mechanism that is instigated by wind motion.

The results from this thesis provide an alternate and novel perspective on energy drivers in the geospace system. Space weather hinges greatly on the interactions between the charged and neutral particles of our partially-ionized atmosphere. Understanding the momentum and energy processes that occur between these species is imperative in forecasting space weather events on Earth, and it will assist further comprehension and exploration of other planetary atmospheres.

Dedication

To my parents, Kevin and Ava Hsu, for instilling in me that dreams are reality with hard work and perseverance, and for teaching me what selflessness truly means. To my mom, for supporting me no matter how wrong I am, and to my dad, for challenging me no matter how right I am. Thank you for being my safety net for when I fall, and my ladder to climb back up. To Dr. Victor Hsu, for your continuous encouragement and for inspiring me to be the best person that I can be. And finally, to Tim Duly, for your love, patience, compassion, and support. Thank you for making me laugh and smile every day.

Acknowledgements

I would not be where I am today without the help and mentorship of many people. First and foremost, I would like to thank my adviser, Professor Jeffrey Thayer, for his constant support, guidance, and empathy throughout my extended tenure at CU. Thank you for seeing potential in me as a sophomore undergraduate, welcoming me back from Illinois, believing in me when I stumbled, and fostering my transition from a fledgling student to an independent researcher. Few are as fortunate to have an adviser who always has your best interests in mind, and who is rooting for you in research and in life. I am forever grateful for the opportunities and doors you have opened for me, and you are the best graduate adviser in my world.

Thank you to committee member Dr. Wenbin Wang of the High Altitude Observatory (HAO) for his assistance in helping me conduct the numerical experiments for this thesis, and for his patience in answering my barrage of questions. I also wish to thank the other members of my committee, Professors Jeffrey Forbes, Delores Knipp, and Fran Bagenal for providing me with insight that greatly improves my work. Additionally, I am appreciative to Dr. Art Richmond (HAO) for his generosity in spending time to give me feedback on my results and to walk me through hairy derivations, and to Dr. Alan Burns (HAO) for his support and fruitful discussions and collaborations.

Thank you to the National Science Foundation Graduate Research Fellowship Program (NSF GRFP) for the financial assistance and the freedom to choose my own research path. I would also like to acknowledge the Research Experience for Undergraduates (REU) program at the MIT Haystack Observatory, with special thanks to Larisa Goncharenko and Phil Erickson for their kind words of encouragement, wise advice, and reassurance that I can be a great scientist and engineer. Finally, thank you to my fellow graduate students for their academic expertise, emotional support, and sincere friendship: Reham Elhawary, Vu Nguyen, Robert Stillwell, Ryan McGranaghan, Katie Greer, Greg Lucas, and McArthur Jones. Thank you for navigating this Ph.D. journey with me.

Contents

Chapter

Appendix

Tables

Table

Figures

Figure

Chapter 1

Introduction

1.1 Executive Summary

This thesis is aimed at understanding how the energy budget of the Earth's ionosphere-thermosphere (I/T) system ($\sim 200 - 500$ km) can be altered through plasma-neutral interactions during geomagnetically-quiet periods. Considerable attention has been dedicated to quantifying the direct effects of external energy sources, e.g., magnetospheric input, on the I/T region in order to decipher neutral gas behavior. However, the strong connection between neutral momentum and energy via dynamics enables processes internal to the system to greatly impact thermospheric variability. This component of geospace system science has not been comprehensively addressed and is not yet resolved. The hypothesis of this dissertation is: **Changes in drag forces on the neutral gas, initiated by changes in the plasma, induce an indirect energy mechanism driven by neutral winds that can significantly modify the energy distribution of the upper thermosphere.**

A sophisticated global circulation model of Earth's upper atmosphere is used to examine how changes in momentum (by neutral drag forces) can lead to changes in internal energy (indicated by variations in thermal structure) and subsequently total mass density through the altered neutral wind field, and to explore the implications of this indirect energy mechanism on the broader I/T system. By exploiting the model's ability to simulate tightly-controlled settings, the fundamental physics behind the intricate processes in the upper atmosphere can be extracted and elucidated. The methodology employed was to strip the model down to simpler situations in order to deeply understand how each added stratum of complexity affected the entangled system.

Notable outcomes of this dissertation work include:

- The trough of the equatorial thermosphere anomaly is produced by an indirect, wind-driven mechanism, where changes in the field-aligned ion drag force control its formation along with its local time and solar cycle variations
- The type of drag prevalent in the upper thermosphere, ion or viscous drag, is important in determining the resultant wind and temperature structure
- A “thermopause” is described that separates the lower thermosphere from the upper thermosphere, and demarcates the onset of an upper thermosphere layer where perturbations to the neutral gas can be sustainable
- Helium traces the vertical motion generated by momentum changes, delivering a promising outlook on using the inert gas as an effective diagnostic for an indirect energy mechanism

Space weather impacts on Earth range from satellite functionality to daily operations on the ground. The ability to predict how the conditions in the aerospace environment affect space technology and our space-reliant society has been a prime interest in the scientific community for many years. Localized plasma structures in the I/T region beget associated neutral structures through plasma-neutral interactions, and vice versa. Thus, understanding the dynamic and nonlinear coupling between the plasma and the neutrals in the Earth’s upper atmosphere will improve space weather forecasting. Furthermore, recognizing a comparative aeronomy parallel throughout this thesis will help advance our knowledge on the life cycle of an ionized atmosphere (formation, evolution, and disappearance), which is imperative to not only life on Earth now, but future exploration of life beyond Earth.

1.2 Plasma-Neutral Interactions in Atmospheres

Many bodies in our solar system, such as planets, stars, moons, and even comets, each possess an atmosphere that is comprised of an ionized gas containing neutrals and plasma (ions and electrons). Unraveling the physics of these ionized atmospheres requires a concrete understanding of the complex interplay between the plasma and the neutrals. Plasma-neutral interactions govern the momentum and energy exchanges between the neutrals, ions, and electrons, and are fundamental in studying the space weather of any plasma-neutral environment.

The focus of this dissertation will be on Earth's ionosphere-thermosphere (I/T) system, and primarily the F-region and upper thermosphere (approximately 200-500 km). However, the basic physical processes and concepts that will be addressed for the Earth's atmosphere can be extended to any celestial object harboring a plasma-neutral atmosphere. The main distinctions are in the species present, the rotation rate of the body, and the properties of its gravitational force and intrinsic magnetic field [Fuller-Rowell and Schrijver, 2009; Bougher et al., 2002]. For example, Mars rotates nearly at the same rate as Earth and exhibits an "Earth-like" seasonal cycle [Bougher et al., 2002], but due to its very weak intrinsic magnetic field, the interactions of the atmosphere of Mars with the solar wind will be very different from those on Earth, but the underlying physics will be the same.

1.3 The Terrestrial Atmosphere

The Earth's atmosphere is the primary source of plasma close to the planet, and it envelopes the Earth in a relatively thin sheath that extends from the surface to beyond 1000 km [Schunk and Nagy, 2009]. It can be sorted into layers based on the quantity of interest. Figure 1.1 presents the diverse classifications of the terrestrial atmosphere. In Fig. 1.1, temperature and composition refer to the temperature and number density of the neutral constituents, vertical transport describes the method with which the neutral gas behaves with height (diffusion or mixing), gravitational binding specifies if the neutrals are within the sphere of influence of the Earth's gravitational field, and thermal plasma relates to the ionization properties of the Earth's atmosphere.

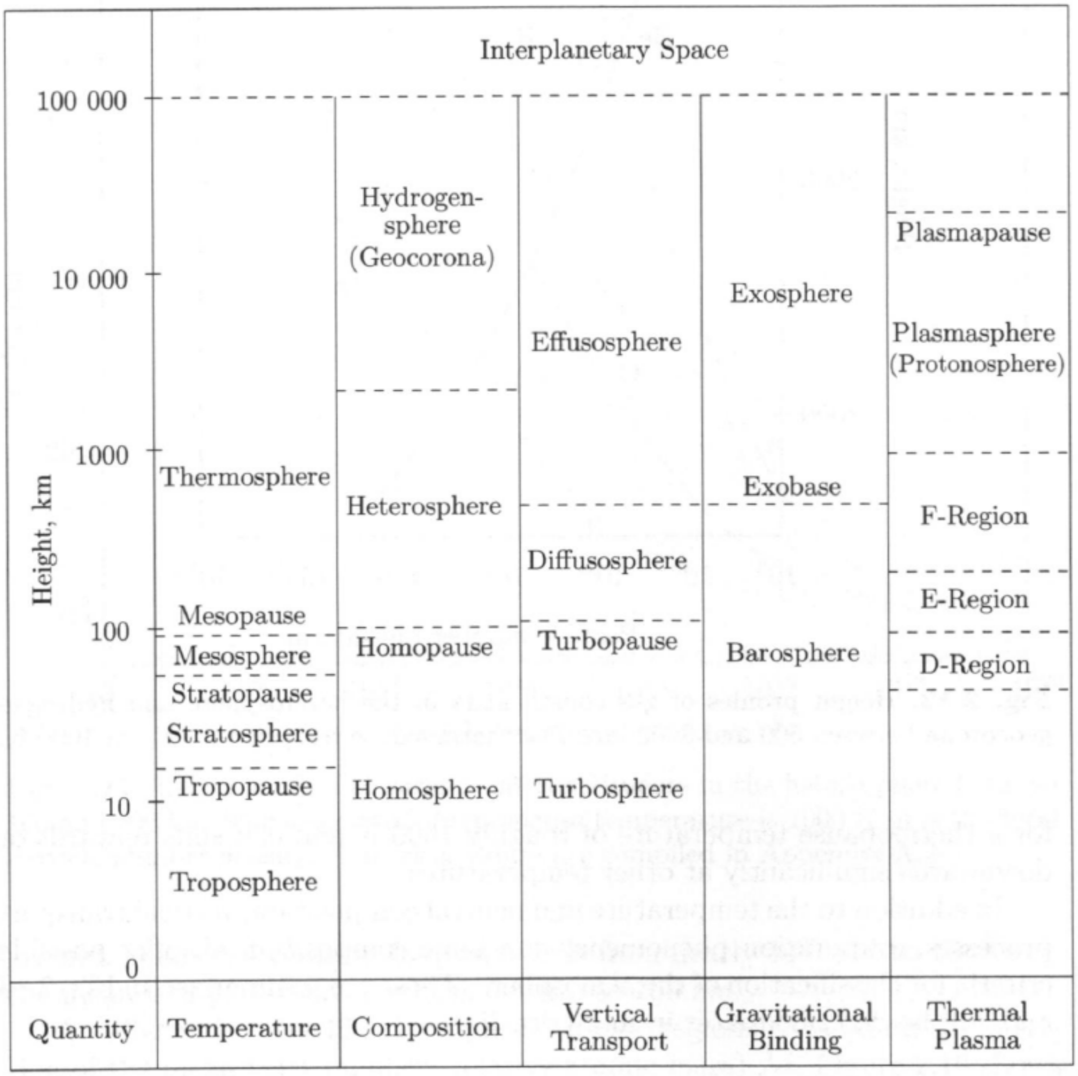

Figure 1.1: From Prölss [2004]: Categorizations of the terrestrial atmosphere.

If the atmosphere is separated by neutral temperature, then the layers are characterized by the temperature distributions illustrated in Fig. 1.2. Referring to Fig. 1.2, the lowest layer of the atmosphere, the troposphere, is where neutral temperature decreases with height until it reaches a boundary characterized by a minimum and called the tropopause. The troposphere is the region in which atmospheric weather, such as thunderstorms and hurricanes, develops and occurs. Above the tropopause is the stratosphere, where the temperature increases with height to a local maximum, denoting the location of the stratopause boundary. In the next layer, the mesosphere, neutral temperature decreases with height until it encounters its upper boundary, the mesopause, which is designated as the coldest region of the terrestrial atmosphere. Temperature begins to increase again above the mesopause and approaches an asymptotic limit. This region of the atmosphere is labelled the thermosphere, where the neutral gas temperature attains a maximum value and remains at this constant temperature up to the outer edge of the Earth's atmosphere.

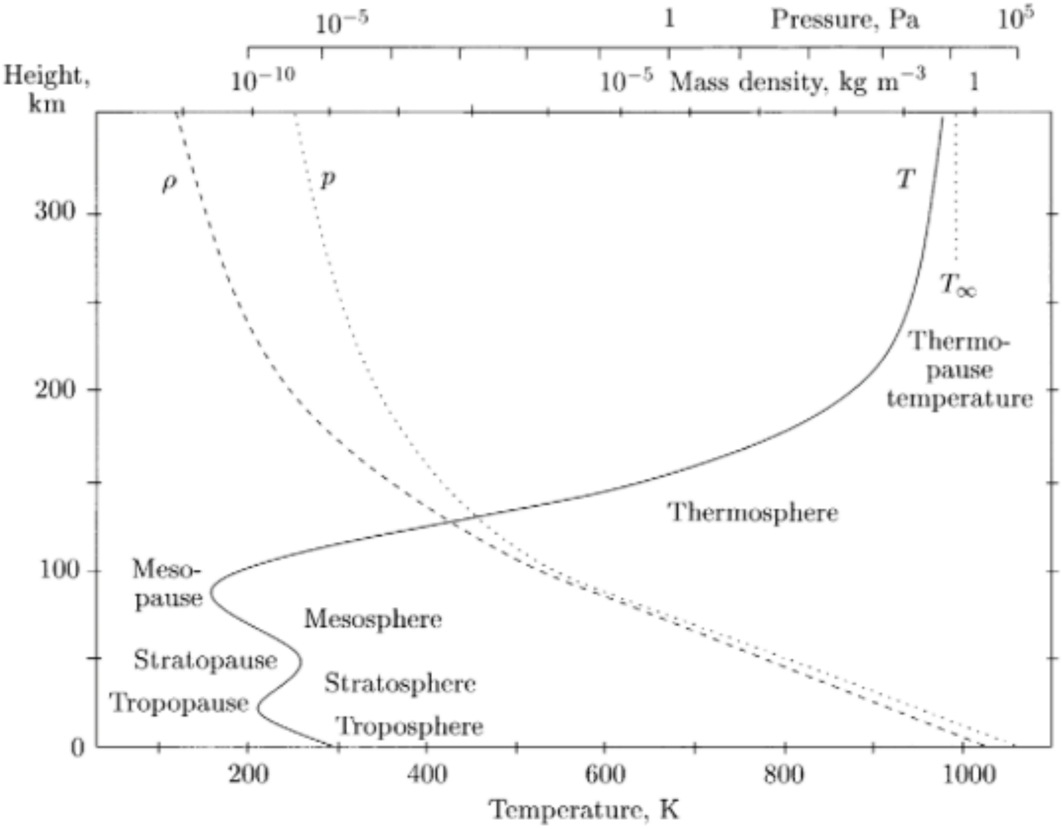

Figure 1.2: From Prölss [2004]: Nominal neutral temperature structure of the Earth's atmosphere as a function of height.

If the atmosphere is segregated by plasma number density, then the layers are distinguished by the electron density profiles depicted in Fig. 1.3, and this ionized portion is known as the ionosphere (~60 km to beyond 1000 km). The main source of ionization is photoionization of neutral molecules through solar EUV and soft X-ray radiation [Schunk and Nagy, 2009]. The lowest layer of the ionosphere is the *D*-region which disappears very rapidly after sundown due to the fast recombination of molecular ions with electrons. The following layer, the *E*-region, is the next altitudinal electron density maxima and is eliminated by recombination often before midnight. Above the *E*-region is the *F*-region, which encompasses the *F*1 and *F*2 layers. The *F*-region contains a persistent *F*2 electron density peak because of low collision rates between the ions and neutrals due to the exponential decrease of neutral constituents with altitude. The uppermost region of the ionosphere is regarded as the topside (approximately above 400 km), where the ions merge with the plasmasphere (defined as a torus-shaped volume filled with plasma that co-rotates with the Earth) and where charged hydrogen becomes important.

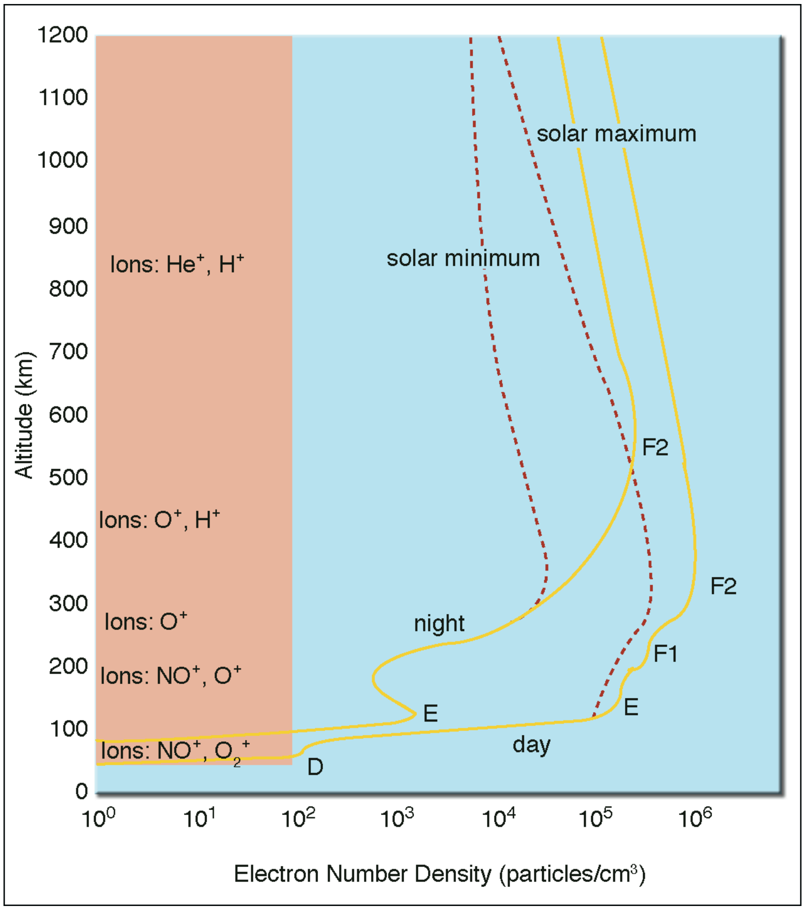

Figure 1.3: From Knipp [2011]: Nominal electron density structure of the Earth's atmosphere as a function of height.

The ionosphere and the neutral thermosphere occupy the same domain in the terrestrial atmosphere, allowing the plasma and the neutrals to interact, and cultivating a setting for the existence of space weather.

1.4 Research Application: Satellite Drag

Although the focus of this dissertation work is basic science research, the outcomes can be of great value to applied research activities. One particularly germane application is satellite drag assessment. Atmospheric drag is a consequence of an object, e.g., a satellite, that moves through a fluid, e.g., the neutral gas. It is the largest source of error in the prediction of trajectories of most objects in low-Earth orbit (LEO) [Emmert et al., 2014]. Accurately forecasting the orbital path a satellite follows is critical for successful operations and its overall mission, such as, estimating its lifetime and preventing it from colliding with the other thousands of orbiting objects in space.

Satellite drag estimates are acutely dependent on the neutral mass density of the aerospace environment. Figure 1.4 simulates a satellite in a 400 km circular orbit and illustrates the sensitivity of its in-track position error to neutral mass density errors. As Fig. 1.4 demonstrates, atmospheric density errors of less than 5% can erupt into severe positioning errors for a satellite residing in the upper thermosphere. Thus, it is essential to characterize the neutral mass density structure of this region in order to minimize the deviation of a satellite from its projected course.

Neutral mass density is proportional to the temperature of the neutral gas at a fixed altitude. Figure 1.5 shows the sensitivity of atmospheric density error to errors in upper atmospheric temperature (or exospheric temperature). Figure 1.5 reveals the incredible susceptibility of thermospheric mass density errors to exospheric temperature errors. Therefore, forecasting satellite drag correctly is a chain reaction: temperatures in the upper thermosphere must be properly described in order to accurately specify neutral mass densities, resulting in improved satellite drag predictions.

This dissertation work strives to understand the physics behind temperature and mass density structure in the LEO regime, thereby contributing to foundational research that will help protect the nation's space technology from natural weather hazards in the backdrop of space.

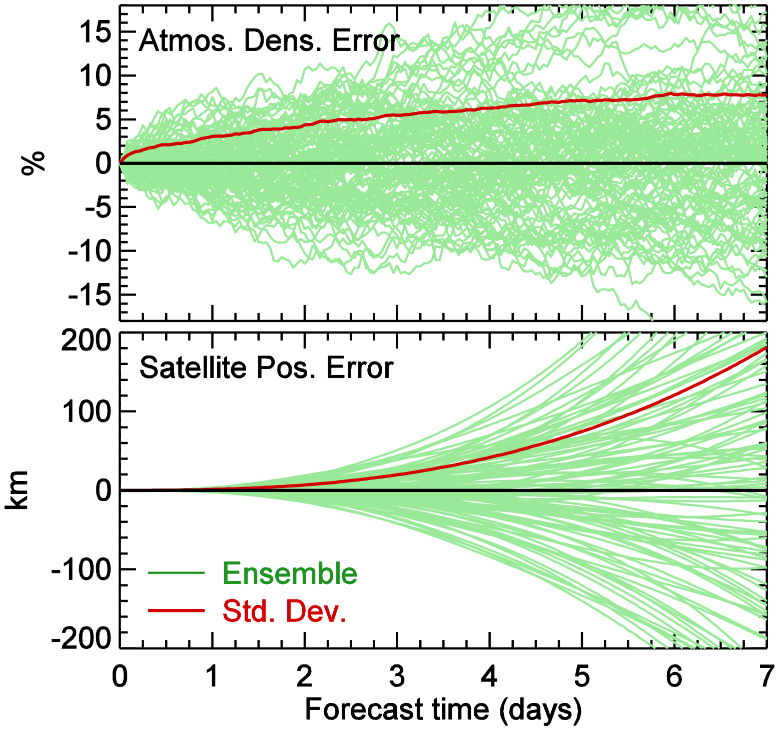

Figure 1.4: From Emmert et al. [2014]: The consequent relative density error (top) and in-track position error (bottom) of a simulated 100-member, random-walk ensemble (green) and their standard deviation (red).

1.5 Indirect and Dynamically Induced Energy Mechanism in the Earth's Upper Atmosphere

Thermospheric neutral properties, such as wind, temperature, and composition, are determined by both momentum and energy. Plenty of work (see Prölss [1980] and citing literature) has focused on the response of the thermosphere when driven by energy input from the Sun and the magnetosphere (i.e. direct circulation), but there has been less attention paid to the significance of internal processes, such as a wind-driven mechanism (i.e. indirect circulation) on the thermosphere system. An indirect circulation is where hydrodynamics prompt thermodynamic changes to the system. A seminal study done by Mayr and Harris [1978] was one of the first to compare the effects of momentum versus energy processes on the neutral circulation patterns in the Earth's I/T region. Figure 1.6 is taken from Mayr and Harris [1978] and demonstrates the different thermospheric sig-

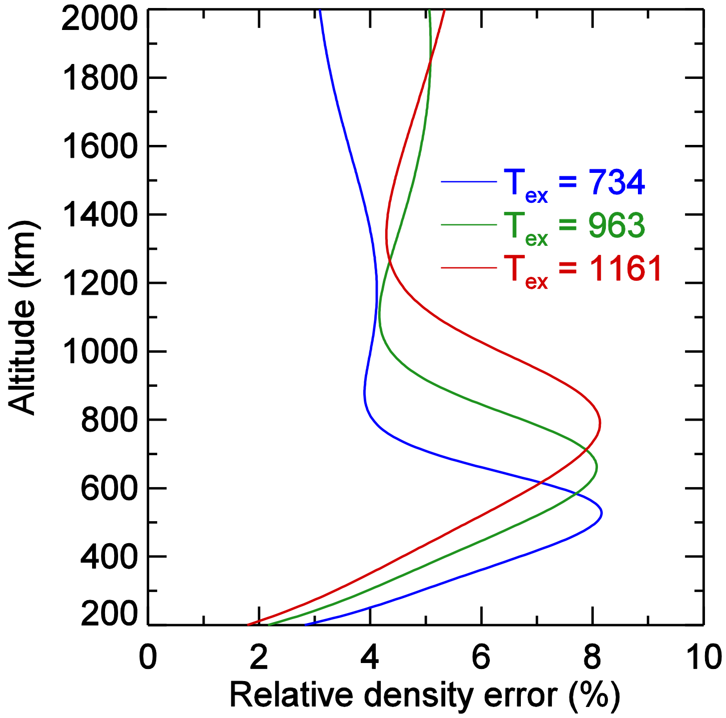

Figure 1.5: From Emmert et al. [2014]: Relative density error caused by a 1% error in exospheric temperature, under low (blue), moderate (green), and high (red) solar activity conditions.

natures from an energy source (e.g., Joule heating) and a momentum source (e.g., $E \times B$ ion drifts). According to Mayr and Harris [1978], an external heat source Q (or Joule heating) increases the neutral temperature of the major gas and produces a pressure field that leads to divergent motion in the winds. In contrast, a momentum source can also drive a divergent wind flow, but the neutral temperature decreases. Both cases create significant temperature and composition changes in the thermosphere.

Using measurements from the mass spectrometers aboard the S3-1 and ESRO 4 satellites, Trinks et al. [1978] investigated the effects of a momentum source on thermospheric neutral composition. They presented two examples of anomalous composition observations near 200 km and slightly poleward of the dayside polar cusp that could not be explained by the most important energy sources within the auroral oval (Joule heating and particle precipitation). They postulated

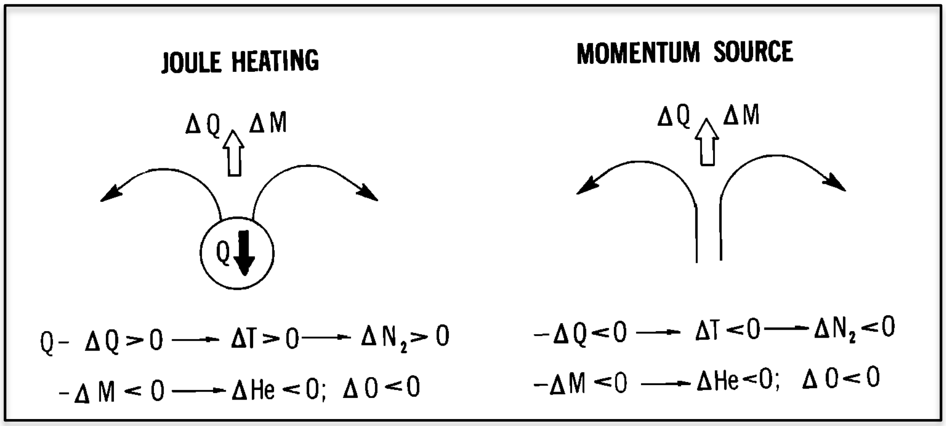

Figure 1.6: From Mayr and Harris [1978]: Heuristic illustration of the differences between Joule heating and momentum source signatures in densities and temperature, where Q is the external heat source, M is mass, T is temperature, and N_2, He and O are the concentrations of N_2, He and O, respectively.

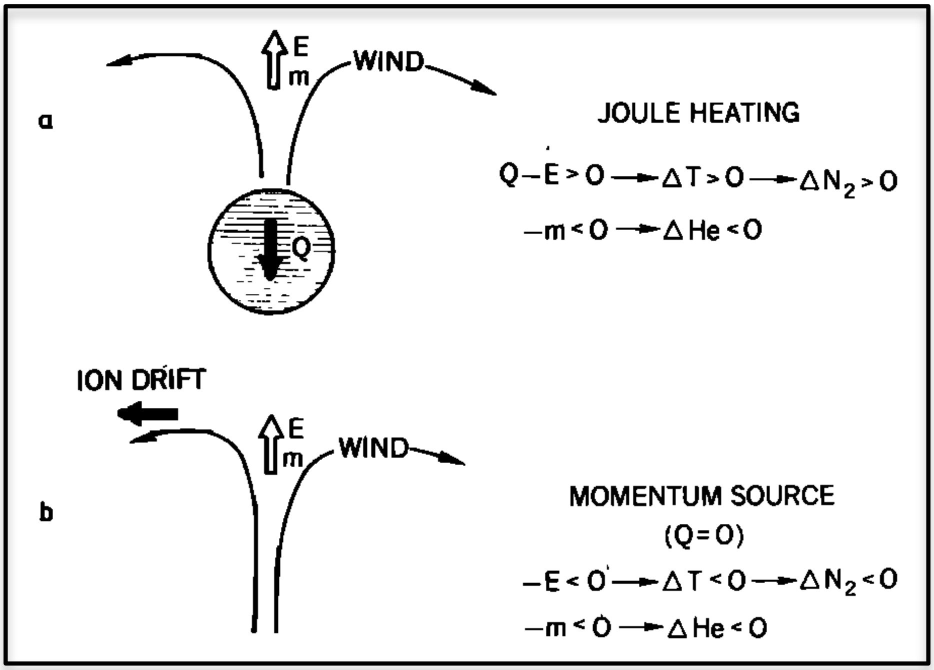

Figure 1.7: From Trinks et al. [1978]: Diagram illustrating the energy (E) and mass (m) budgets for (a) Joule heating and (b) momentum source. The symbols T, N_2, and He refer to disturbances of temperature, N_2 concentration, and He concentration.

that thermospheric winds driven by momentum sources associated with ion convection were the predominant cause for the composition disturbances. Similar to Figure 1.6, the illustration in Figure 1.7 describes the different effects between an energy source (Joule heating) and a momentum source. They arrive at the same conclusions as Mayr and Harris [1978], in that a divergent wind field generated by an energy source enhances the neutral temperature, while a momentum source creating divergent motion will reduce the temperature, and induce composition perturbations that cannot be resolved by Joule heating or particle precipitation.

Momentum and energy are entirely distinct physical quantities. However, changing terms in the momentum equation can alter internal energy through dynamics. This wind-driven process (or indirect energy mechanism) may turn out to be pertinent in resolving the origins of various space weather features. For example, a recent study by Lühr et al. [2004] presented CHAMP observations at 400 km of a thermospheric neutral density enhancement in the Earth's cusp region. They reported neutral density enhancements of almost a factor of two whenever the satellite passed over the cusp. While Lühr et al. [2004] suggested that this cusp enhancement was due to local Joule heating from small-scale field-aligned current filaments, the exact mechanism for this thermospheric feature is still unknown, and much work continues to be pursued in explaining its occurrence, specifically through utilizing intricate, fully-coupled I/T models. Demars and Schunk [2007] simulated a large cusp density enhancement using a global thermospheric model developed by Ma and Schunk [1995], Crowley et al. [2010] reproduced a neutral density enhancement in the cusp region in the TIMEGCM, and Deng et al. [2013] manifested the feature with GITM. However, all of these modeling studies required a large amount of energy input that is not necessarily validated by satellite Poynting flux observations. As mentioned previously, a wind-driven mechanism can cause neutral density disturbances with an indirect circulation pattern. Thus, the thermospheric cusp neutral density enhancement could be a phenomenon that is not only driven by an energy source, but also by internal momentum processes, specifically changes in drag forces (e.g., Zhang et al. [2016]).

1.5.1 I/T Plasma and Neutral Structures

Space weather features can be global-scale or regionally confined. Analogous to weather in the troposphere, more localized weather events in the I/T system pose a greater, tangible threat to human lives and technologies. Localized features include tongues of ionization and plasma patches at high-latitudes, subauroral polarization streams and electron density troughs at mid-latitudes, and equatorial plasma bubbles and the equatorial ionization anomaly at low-latitudes. These structures are classified as mesoscale in that their spatial scales range from 50 to 1000 km.

An essential corollary to recognize about I/T structures is that if one observes a plasma structure, then there is an associated neutral structure, and vice versa [Schunk and Nagy, 2009]. An example of this exchange is shown with an I/T simulation performed by Ma and Schunk [2001]. Figure 1.8 encapsulates their study on the thermospheric effects from a series of propagating plasma patches, where cigar-shaped plasma patches determined from measurements were introduced in the southern polar region of their model and allowed to propagate across the polar cap. They found that, in general, propagating plasma patches act as a snowplow that leaves behind a neutral density hole in its wake, while dragging the neutral perturbation along with its motion, instituting considerable wind, temperature, and composition changes. The Ma and Schunk [2001] study is an excellent paradigm of the intimate bond between the plasma and the neutrals in that their behaviors cannot be detached, indicating that a disturbance in one signals a disturbance in the other.

Chapter 4 of this dissertation will address how the equatorial ionization anomaly, an I/T plasma structure, generates the equatorial thermosphere anomaly trough, an I/T neutral structure, and how variations in the plasma translate to variations in the neutrals.

1.5.2 Interplay of Drag Forces in the I/T System

The notion that ion drag and pressure gradients are the principal forces that control neutral wind dynamics in the upper thermosphere has been entrenched in the aeronomy community for decades. This hypothesis has been promulgated largely by Rishbeth [1971a], Rishbeth [1971b],

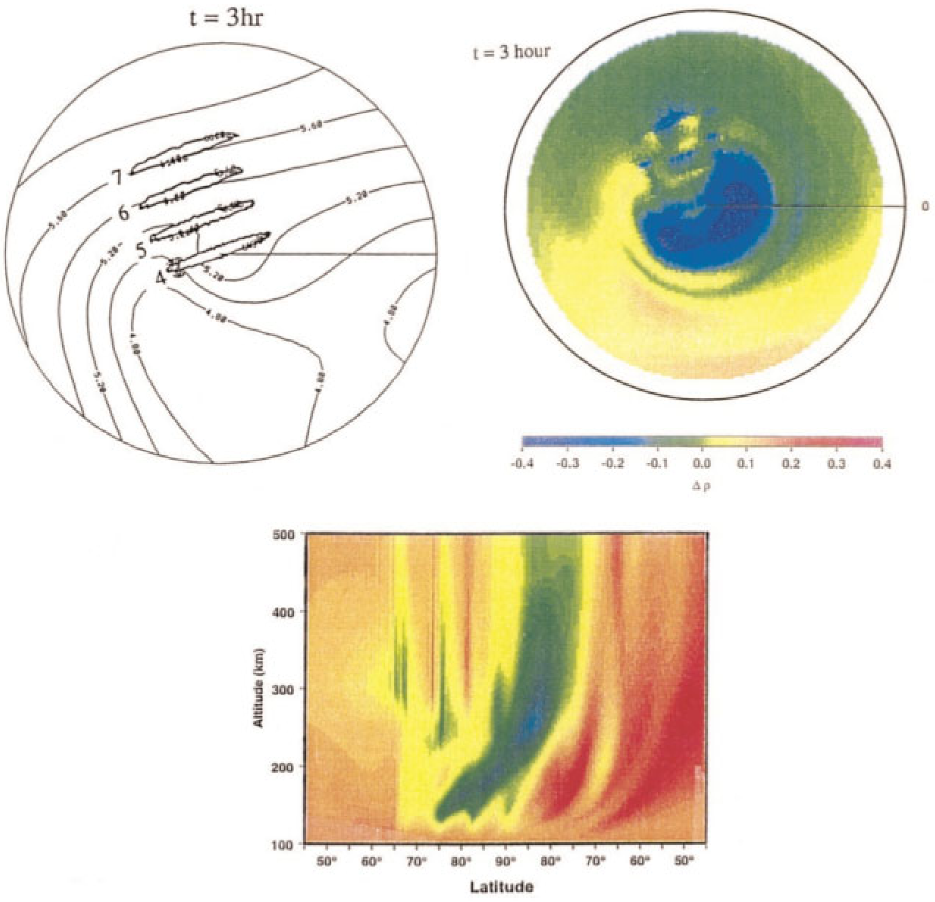

Figure 1.8: From Ma and Schunk [2001]: Effect of multiple propagating plasma patches at t =3 hr on electron densities at 300 km (top left), on neutral densities at 300 km (top right), and the neutral density perturbation as a function of altitude and latitude across the polar cap.

Rishbeth [1979a], Rishbeth [1971b], Rishbeth [1981], and Rishbeth [1998], where viscosity (and hence viscous drag) is omitted from the analyses due to its supposed minor effects on the wind field at F-region altitudes (approximately above 200 km). However, Rishbeth [1971b] and Rishbeth [1971a] acknowledge that the viscous drag force could become important at night.

Recent studies have unearthed the possibility of viscous drag playing an integral role in thermospheric dynamics, wherein some instances, viscous drag eclipses ion drag in the upper I/T system. Kondo et al. [2011] used model simulations to explain the formation of the fast thermospheric zonal wind at the magnetic dip equator. They concluded that the zonal winds in the low-latitude region are dictated by both ion drag and viscous drag, where the strong zonal wind at the dip equator in the vicinity of the equatorial ionization anomaly (∼250-450 km) is controlled by the plasma via ion drag, while the zonal equatorial jet in the topside ionosphere (above 450 km) is mainly affected by viscous drag. Studies by Miyoshi et al. [2011], Clemmons et al. [2013], and Evonosky et al. [2016] arrive at a similar conclusion, where the dominance of the viscous drag force is invoked in order to interpret the motions of the neutral gas.

Chapter 5 of this dissertation will detail the complex interplay between the ion drag and viscous drag forces in the upper thermosphere by establishing its effects on neutral wind and thermal structure.

1.5.3 Indirect, Dynamically Induced Energy Mechanism Tracer

The ratio of O/N_2 has been used extensively to study the effects of geomagnetic storms on the I/T system. In particular, O/N_2 is a helpful tool to assess positive and negative storm-time effects. Taking advantage of helium for its convenient properties, specifically its sensitivity to dynamical changes and insensitivity to thermal changes, helium can be utilized as a tracer for a wind-driven, indirect energy mechanism. Helium, due to its non-reactive and relatively light nature, is an effective measuring tool for the effects of transport processes in the thermosphere and exosphere [Reber, 1976], and it traces the dynamical systems that redistribute energy and mass [Cageao and Kerr, 1984]. Interestingly, studies on other planets, such as Mars and Saturn, have also exploited the chemical inertness of helium to track the homopauses (the transition between turbulent eddy diffusion to molecular diffusion) of the planetary atmospheres [Bell et al., 2015; Parkinson, 2016]. Global circulation models are beginning to realize the benefits of exercising helium as a diagnostic tracer, foreseeing its potential relevance to operational space weather applications (e.g., Sutton et al. [2015]).

Chapter 6 of this dissertation will assess the feasibility of using helium to detect the signatures of a dynamically induced energy mechanism above the “thermopause” boundary.

1.5.4 Observational Challenges

Traditionally, observing ion-neutral coupling processes requires a suite of instruments that concurrently measures the properties of the plasma and the neutrals. An archetype for broad coverage of plasma-neutral interactions is the Dynamics Explorer program. This program comprised of two spacecraft that were launched into coplanar, elliptical, polar orbits in 1981 for the purpose of studying the coupling processes between the magnetosphere, ionosphere, and upper atmosphere [Hoffman, 1988]. Dynamics Explorer 2 (DE-2) was placed at ionospheric altitudes, while Dynamics Explorer 1 (DE-1) resided at much higher altitudes, with orbits passing through the magnetosphere. DE-2 provided a comprehensive global data base of thermospheric vector neutral winds and ion drifts, neutral and ionic concentrations and temperatures, precipitating particle fluxes and pitch angle distributions, electric and magnetic fields, and global-scale auroral luminosity distributions [Killeen and Roble, 1988]. However, there were challenges with the quality of measurements collected from the onboard Fabry-Perot interferometer (FPI) and the Wind and Temperature Spectrometer (WATS), which together assembled the neutral wind field. Historically, neutral winds are arduous measurements to acquire due to the fluctuating tendencies of the winds themselves, along with their extreme sensitivity to instrument stability. Thus, observing a wind-driven, indirect energy mechanism necessitates robust instruments with high temporal and spatial resolutions in order to capture the transient and localized essence of the neutral winds.

Despite the extensive set of observations from the DE satellites, it is incredibly difficult to parse out processes in an intrinsically, coupled system. It is at this juncture where self-consistent, physics-based models are advantageous to dissect the multitude of processes occurring within the I/T region. Conducting controlled numerical experiments with these mature models allows for fundamental ideas to be tested in order for clarity to emerge, thereby supplying a framework to effectively mine thermospheric data for discovery science.

1.6 Objectives and Science Questions

Section 1.5 highlights three matters where a wind-induced energy mechanism due to plasma-neutral interactions is at the crux of the studies. Much effort is targeted towards explaining variations in the neutral gas by direct magnetospheric input during intense geomagnetic storms, but the neutral variations that arise during quiet periods from momentum changes within the I/T system have not been fully probed and are not well understood. **The primary objective of this thesis work is to quantify and fundamentally understand how changes in drag forces *indirectly* affect the hydrodynamic and thermodynamic response of the Earth's upper thermosphere.** Using a sophisticated general circulation model, the science questions we seek to answer are as follows:

(1) **How can a drag force contribute to the formation of a thermospheric neutral mass density and temperature anomaly?**

This question is addressed with the following sub-questions:

  (a) What is the effect of field-aligned ion drag on the equatorial thermosphere anomaly (ETA)?
  (b) What is the underlying physical mechanism for the formation of the ETA trough?
  (c) How and why does the ETA trough vary with local time and solar activity?

(2) **What are the thermospheric consequences of the complex interplay between drag forces?**

This question is addressed with the following sub-questions:

  (a) How does a drag force indirectly change the energy budget of the I/T system?
  (b) How does the the resultant wind and thermal structure of the upper thermosphere change depending on the type of drag force environment?

   (c) How do the drag forces vary with solar activity and how does this impact the global neutral temperature distributions?

(3) **What are the signatures of an indirect, dynamically induced energy mechanism in the thermosphere?**

This question is addressed with the following sub-questions:

   (a) What is the altitude range of penetration for the indirect energy mechanism due to drag forces?
   (b) What are the compositional effects due to this mechanism, specifically with regards to helium?
   (c) What signatures of this mechanism might be observed by past, current, and future thermospheric missions?

This dissertation is organized into seven chapters. Chapter 2 reviews the equations that govern the physics applied to this work, including kinetic theory and fluid mechanics approaches to the hypothesis. Chapter 3 provides a thorough description of the model used for the numerical experiments, as well as a summary of the methodology. Chapters 4, 5, and 6 concentrate on answering science questions 1, 2, and 3, respectively. Finally, Chapter 7 recapitulates the major findings and new science achieved from this thesis work. A glossary of commonly used variables is listed in Appendix A, and supplemental figures and analysis for Chapters 4, 5, and 6 are separated into Appendices B, C. and D, respectively.

Chapter 2

Governing Equations

Whether studying the atmospheres of Earth, Mars, or any other plasma-neutral environment, the same fundamental kinetic equations apply to all of these domains. The equations become system dependent when considering the collisional and ionization aspects of the environment (the intrinsic magnetic field of the system is also a very important aspect to consider). Figure 2.1 summarizes the governing equations for a plasma-neutral atmosphere, and denotes where the universal kinetic equations branch off and become system dependent.

2.1 Universal Equations

From Fig. 2.1, the root of the governing equations begins with the Liouville equation. The Liouville equation is the basic statistical mechanics equation for a gas that expresses the conservation of N particle distribution functions in $6N$ dimensional phase space [Bird, 1994]. In other words, this equation tracks every single particle in the ionized gas (note that an ionized gas is composed of ions, electrons, and neutrals, and here plasma is defined to refer to the ions and electrons). However, using the Liouville equation is not practical or a tractable method in studying the physics of a plasma-neutral atmosphere. Instead, the equation must be simplified to represent a single particle distribution function in phase space. This approximation is known as the Boltzmann equation. It should be noted that the Boltzmann equation assumes molecular chaos, which means that the velocities of the interacting particles, before collision, are assumed to be uncorrelated [Bittencourt, 2010]. If this criteria is not satisfied by the plasma-neutral gas under consideration, then a hierarchy

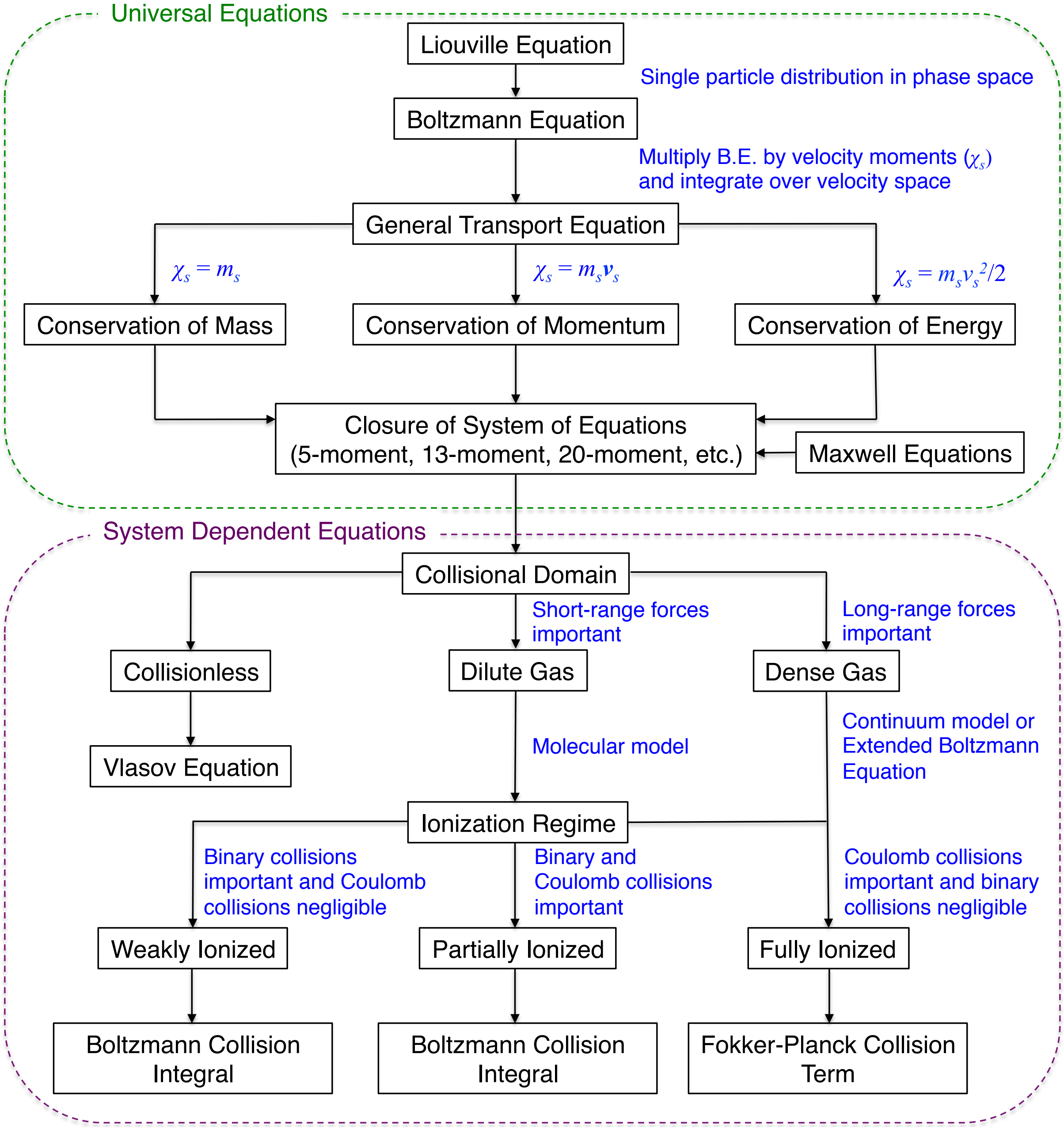

Figure 2.1: Summary of the governing equations for a plasma-neutral atmosphere. The section highlighted in green is the universal kinetic equations that apply to plasma-neutral gases, and the section partitioned in purple is the equations that depend on the properties of the system under study. See text for details on the stages of the diagram.

of equations known as the BBGKY equations must be used. The BBGKY equations result from the repeated integration of the Liouville equation, and the final equation in the hierarchy with the assumption of molecular chaos is the Boltzmann equation.

The Boltzmann equation is written as

$$\frac{\partial f_s}{\partial t} + \mathbf{v}_s \cdot \nabla f_s + \mathbf{a}_s \cdot \nabla_v f_s = \left(\frac{\delta f_s}{\delta t} \right)_{coll}, \tag{2.1}$$

where f_s is the species distribution function, $\mathbf{v}_s$ is the particle velocity of species type s, $\mathbf{a}_s$ is the particle acceleration of species type s, and $\left(\frac{\delta f_s}{\delta t} \right)_{coll}$ represents the effects of collisions. The species distribution function f_s is a function of the particle position $\mathbf{r}$, $\mathbf{v}_s$, and time t, i.e. $f_s\left(\mathbf{r}, \mathbf{v}_s, t\right)$. Equation 2.1 is a differential kinetic equation that accounts for the statistical distribution of a gas. With this approach, one is not interested in the motion of individual particles in the gas, but instead with the distribution of particles [Schunk and Nagy, 2009], and the dependence of the distribution function on $\mathbf{r}$, $\mathbf{v}_s$, and t is governed by the Boltzmann equation.

A general transport equation may be derived from the Boltzmann equation, and it will be used to obtain the conservation equations for a plasma-neutral system. The general transport equation for some physical property of the particles in the plasma-neutral mixture, $\chi\left(\mathbf{v}_s\right)$, is

$$\frac{\partial}{\partial t}\left(n_s \langle \chi \rangle_s\right) + \nabla \cdot \left(n_s \langle \chi \mathbf{v} \rangle_s\right) - n_s \langle \mathbf{a} \cdot \nabla_v \chi \rangle_s = \left[\frac{\delta}{\delta t}\left(n_s \langle \chi \rangle_s\right) \right]_{coll}, \tag{2.2}$$

where n_s is the species number density and the average value of a property is defined as

$$\langle \chi\left(\mathbf{v}\right) \rangle_s = \frac{1}{n_s\left(\mathbf{r}, t\right)} \int_v \chi\left(\mathbf{v}\right) f_s\left(\mathbf{r}, \mathbf{v}, t\right) d^3 v. \tag{2.3}$$

The conservation equations are attained by multiplying Eq. 2.1 by $\chi\left(\mathbf{v}_s\right)$ and integrating over all velocity space. The following equations present the conservation equations that may be applied to a plasma-neutral environment:

Conservation of Mass:

$$\chi\left(\mathbf{v}_s\right) = m_s, \tag{2.4a}$$

$$\frac{\partial \rho_s}{\partial t} + \nabla \cdot \left(\rho_s \mathbf{u}_s\right) = S_s, \tag{2.4b}$$

where m_s is the species mass, ρ_s is the species mass density ($\rho_s = n_s m_s$), $\mathbf{u}_s$ is species average velocity, and S_s is the collision term that represents the rate per unit volume at which particles of type s and mass m_s are produced or lost as a result of collisions;

Conservation of Momentum:

$$\chi\left(\mathbf{v}_s\right) = m_s \mathbf{v}_s, \tag{2.5a}$$

$$\rho_s \frac{D\mathbf{u}_s}{Dt} = n_s \langle \mathbf{F} \rangle_s - \nabla \cdot \overleftrightarrow{P_s} + \mathbf{A}_s - \mathbf{u}_s S_s, \tag{2.5b}$$

where D/Dt is the total derivative that is equivalent to $\partial/\partial t + \mathbf{u}_s \cdot \nabla$, $\mathbf{F}_s$ are the external forces applied on particles of type s, $\overleftrightarrow{P_s}$ is the kinetic pressure dyad, and $\mathbf{A}_s$ denotes the rate of change of the mean momentum per unit volume due to collisions;

Conservation of Energy:

$$\chi\left(\mathbf{v}_s\right) = \frac{m_s {v_s}^2}{2}, \tag{2.6a}$$

$$\frac{D}{Dt}\frac{3p_s}{2} + \frac{3p_s}{2} \nabla \cdot \mathbf{u}_s + \left(\overleftrightarrow{P_s} \cdot \nabla\right) \cdot \mathbf{u}_s + \nabla \cdot \mathbf{q}_s = M_s - \mathbf{u}_s \cdot \mathbf{A}_s + \frac{1}{2} {u_s}^2 S_s, \tag{2.6b}$$

where p_s is the scalar pressure, $\mathbf{q}_s$ is the heat flow vector, and M_s is the change in the thermal energy density due to collisions.

It is seen from the conservation equations that in order to specify $\mathbf{F}_s$ for the plasma, the electric and magnetic fields must be known. Electromagnetic fields in free space obey the Maxwell equations, which are shown below.

$$\nabla \times \mathbf{E} = -\frac{\partial \mathbf{B}}{\partial t}, \tag{2.7}$$

$$\nabla \times \mathbf{B} = \mu_0 \epsilon_0 \frac{\partial \mathbf{E}}{\partial t} + \mu_0 \mathbf{J}, \tag{2.8}$$

$$\nabla \cdot \mathbf{B} = 0, \tag{2.9}$$

$$\nabla \cdot \mathbf{E} = \rho_c/\epsilon_0, \tag{2.10}$$

where ρ_c is the charge density, $\mathbf{E}$ is the electric field, $\mathbf{B}$ is the magnetic field, $\mathbf{J}$ is the current density, and ϵ_0 and μ_0 are the electric permittivity and the magnetic permeability of free space.

It should be noted that in Eq. 2.6b, $\overleftrightarrow{P_s}$ and $\mathbf{q}_s$ are dependent on higher-order velocity moments. Thus, in order to close the system of transport equations, the higher-order velocity moments must be expressed in terms of the lower-order moments. This is achieved by truncating the system at some approximation. For example, the 13-moment approximation assumes that the plasma-neutral gas can be characterized by 13 parameters. The more severe the approximation, the more limitations the set of transport equations will have in describing the behavior of the gas mixture.

The conservation of mass (Eq. 2.4b), the conservation of momentum (Eq. 2.5b), the conservation of energy (Eq. 2.6b), the Maxwell equations (Eqs. 2.7-2.10), and the closure of the system of transport equations form a complete set of governing equations for a plasma-neutral atmosphere. However, the collision terms in these universal equations are not of any practical use, and they must be evaluated on a system-dependent basis.

2.2 System Dependent Equations

The universal equations for a plasma-neutral environment begin to diverge when considering the collisional domain and the ionization regime of the system. In a collisionless system, the collision term in Eq. 2.1 disappears, resulting in the Vlasov equation. Without having to account for collisions, it is possible to describe the kinetics of the ionized gas through a self-consistent solution for the single particle distribution function, f_s, using the Vlasov equation and the Maxwell equations. However, if collisions cannot be ignored, then it must be determined if the neutral gas is dilute (short-range forces are important and a molecular model must be used) or dense (long-range forces are important and a continuum model or an extended form of the Boltzmann equation, e.g. the BBGKY equations, must be used). The degree of rarefaction of a neutral gas is generally defined by the local Knudsen number (Kn), which is the ratio of the mean free path to the characteristic dimension of the flow [Bird, 1994]. As Kn approaches zero, the gas is in a continuum state, and in the limit of infinite Kn, the gas reaches a collisionless or free-molecule flow regime. Once the collisional domain of the system is determined, the plasma-neutral atmosphere must be classified into an ionization regime. The degree of ionization is used as a criterion on the magnitude of ionization of a plasma-neutral gas, and it is defined as the ratio of the number of charged particles to the total number of particles (charged and neutral). The ionization regime dictates what types of collisions need to be considered and what form the collision term should be in the Boltzmann equation.

2.2.1 Governing Equations for Earth's Ionosphere-Thermosphere System

The region under study for this work is the Earth's ionosphere-thermosphere (I/T) system, specifically the F-region (approximately 200-500 km). The I/T system is a dilute gas that transitions from a weakly ionized atmosphere (the E-region) to a partially ionized atmosphere (the F-region). In the E-region, binary collisions (collisions between two particles) are dominant over Coulomb collisions (collisions between charged particles), while in the F-region, binary and Coulomb collisions are both significant. For the Earth's F-region I/T system, the 13-moment approximation is used to close the set of transport equations. This approximation assumes the following:

(1) The stress tensor $\overleftrightarrow{\tau_s}$, where $\overleftrightarrow{P_s} = \overleftrightarrow{\tau_s} + p_s \overleftrightarrow{I}$ and p_s is the scalar pressure and $\overleftrightarrow{I}$ represents the identity matrix, is symmetric and traceless.

(2) The species velocity distribution functions are not too far from Maxwellian velocity distribution functions.

(3) Temperature and heat flow anisotropies are small.

The Earth's I/T region is composed of three fluids: neutrals, ions, and electrons. Therefore, it is typical to describe this system with a multi-fluid approach. With the closure of the transport equations using the 13-moment approximation, and from the universal conservation equations defined in Eqs. 2.4b, 2.5b, and 2.6b, the conservation equations for the Earth's F-region I/T system in a rotating reference frame may be formulated as detailed in the subsequent sections.

2.2.1.1 Conservation of Mass

Using Eq. 2.4b, the continuity equation for the 13-moment approximation is:

$$\frac{\partial\left(m_s n_s\right)}{\partial t}+\nabla\cdot\left(m_s n_s \mathbf{u}_s\right)=S_s, \tag{2.11}$$

where $\rho_s = m_s n_s$. Equation 2.11 states that the rate of change of $m_s n_s$ and the divergence of the species mass particle flux is equal to the production and loss of particles of type s.

With the multi-fluid approach, the conservation of mass equations in the Earth's I/T system for the neutrals, ions, and electrons are:

$$\frac{\partial\left(m_n n_n\right)}{\partial t}+\nabla\cdot\left(m_n n_n \mathbf{u}_n\right)=\Gamma^{rec}-\Gamma^{ion}, \tag{2.12}$$

$$\frac{\partial\left(m_i n_i\right)}{\partial t}+\nabla\cdot\left(m_i n_i \mathbf{u}_i\right)=\Gamma^{ion}-\Gamma^{rec}, \tag{2.13}$$

$$\frac{\partial\left(m_e n_e\right)}{\partial t}+\nabla\cdot\left(m_e n_e \mathbf{u}_e\right)=\Gamma^{ion}-\Gamma^{rec}, \tag{2.14}$$

where Γ^{rec} is the rate of loss of ions or electrons due to recombination and Γ^{ion} is the rate of gain of ions or electrons due to ionization.

2.2.1.2 Conservation of Momentum

The equation of motion for the 13-moment approximation is:

$$\begin{aligned}\rho_s \frac{D_s \mathbf{u}_s}{Dt} &+ \nabla p_s + \nabla \cdot \overleftrightarrow{\tau_s} - n_s e_s \left(\mathbf{E} + \mathbf{u}_s \times \mathbf{B}\right) \\ &+ \rho_s \left[-\mathbf{G} + 2\mathbf{\Omega}_r \times \mathbf{u}_s + \mathbf{\Omega}_r \times \left(\mathbf{\Omega}_r \times \mathbf{r}\right)\right] \\ &= \sum_t n_s m_s \nu_{st} \left(\mathbf{u}_t - \mathbf{u}_s\right) + \sum_t \nu_{st} \frac{z_{st}\mu_{st}}{kT_{st}} \left(\mathbf{q}_s - \frac{\rho_s}{\rho_t}\mathbf{q}_t\right),\end{aligned} \tag{2.15}$$

where the property $\overleftrightarrow{P_s} = \overleftrightarrow{\tau_s} + p_s \overleftrightarrow{I}$ has been used, e_s is the species charge, $\mathbf{G}$ is the acceleration due to gravity, $\mathbf{\Omega}_r$ is the Earth's angular velocity, and $\mathbf{r}$ is the radius vector from the center of the Earth. The right hand side of Eq. 2.15 represents the linear collision terms that are derived from the Boltzmann collision integral, where ν_{st} is the collision frequency for momentum transfer from particles of type t to particles of type s, the parameter z_{st} is dependent on the Chapman-Cowling collision integrals, μ_{st} is the reduced mass ($\mu_{st} = \frac{m_s m_t}{m_s + m_t}$), and T_{st} is the reduced temperature ($T_{st} = \frac{m_s T_t + m_t T_s}{m_s + m_t}$) [Schunk and Nagy, 2009]. The first linear collision term in Eq. 2.15 is a drag force imparted onto species s from species t, while the linear collision term accounts for thermal diffusion effects. The linear collision terms were derived with the assumptions that (1) the drift velocities between the interacting species are small, and (2) the species temperature differences are small compared to the individual species temperatures.

If the heat flow terms in Eq. 2.15 are small (which is generally true for a partially ionized plasma-neutral domain), then the neutral and ion momentum equations for the Earth's I/T system may be written as:

$$\rho_n \frac{D\mathbf{u}_n}{Dt} = -\nabla p_n - \nabla \cdot \overleftrightarrow{\tau_n} + \rho_n \left[\mathbf{G} - 2\mathbf{\Omega}_r \times \mathbf{u}_n - \mathbf{\Omega}_r \times \left(\mathbf{\Omega}_r \times \mathbf{r}\right)\right] - n_n m_n \nu_{ni} \left(\mathbf{u}_n - \mathbf{u}_i\right), \tag{2.16}$$

$$\begin{aligned}\rho_i \frac{D\mathbf{u}_i}{Dt} =& -\nabla p_i - \nabla \cdot \overleftrightarrow{\tau_i} + n_i e \left(\mathbf{E} + \mathbf{u}_i \times \mathbf{B}\right) \\ &+ \rho_i \left[\mathbf{G} - 2\mathbf{\Omega}_r \times \mathbf{u}_i - \mathbf{\Omega}_r \times \left(\mathbf{\Omega}_r \times \mathbf{r}\right)\right] - n_i m_i \nu_{in} \left(\mathbf{u}_i - \mathbf{u}_n\right),\end{aligned} \tag{2.17}$$

where e is the electron charge and collisions with electrons have been neglected due to its small mass, i.e. $m_n \gg m_e$ and $m_i \gg m_e$.

In order to fully capture the dynamics of the Earth's I/T system, the motion of the electrons must be specified. This may be achieved by using the electron momentum equation (substitute electrons for species s in Eq. 2.15), or by using the generalized Ohm's law. The latter will be expounded upon here. Generalized Ohm's law can be represented as an equation for $\partial \mathbf{J}/\partial t$, or equivalently, it is an expression that relates the electric field and the current density, $\mathbf{J}$, in some particle rest frame. It may be obtained by multiplying Eq. 2.15 by e_s/m_s, and then summing the resultant equation over all species (neutrals, ions, and electrons), or it can be derived by starting from the electron momentum equation and relating it to a linear combination of the neutral and ion momentum equations. Details on the derivation of generalized Ohm's law may be found in Leake et al. [2014] or Song et al. [2001]. The steady-state Ohm's law that is applicable to the Earth's I/T system uses the neutral wind frame of reference, and it can be expressed as [Richmond and Maute, 2014]:

$$\mathbf{J} = \sigma_P \left(\mathbf{E}_\perp + \mathbf{u}_n \times \mathbf{B}\right) - \sigma_H \frac{\left(\mathbf{E}_\perp + \mathbf{u}_n \times \mathbf{B}\right) \times \mathbf{B}}{B} + \sigma_\parallel \mathbf{E}_\parallel + \mathbf{J}^P, \tag{2.18}$$

where σ_P is the Pedersen conductivity, σ_H is the Hall conductivity, $\sigma_\parallel$ is the parallel conductivity, $\mathbf{u}_n$ is the neutral wind vector, $\mathbf{J}^P$ is the current driven by plasma gravitational and pressure gradient forces, and $\mathbf{E}_\perp$ and $\mathbf{E}_\parallel$ are the components of $\mathbf{E}$ perpendicular and parallel to $\mathbf{B}$, respectively. Eq. 2.18 is the low-frequency limit of the generalized Ohm's law, where the following assumptions were employed:

(1) The system is in steady-state and inertial forces (centrifugal and Coriolis) have been neglected.

(2) Ionization and recombination rates are much faster than the Earth's I/T system frequency.

(3) The ions consist of singly ionized species.

(4) Charge neutrality prevails ($n_e = n_i = n$).

(5) The linear collision terms given by Eq. 2.15 are appropriate and the heat flow contribution to these terms can be ignored.

(6) Terms of order m_e/m_i can be neglected compared with terms of order one.

(7) Frequencies of interest in the I/T region are smaller than the collision frequencies and gyrofrequencies, i.e. changes in the system are greater than the order of minutes (low-frequency limit).

The coupling (i.e. collision frequencies) between the electrons, ions, and neutrals are encapsulated in the conductivities. Typically, studies of the Earth's I/T system ignore the electron-ion collisions. This is a valid assumption for the Earth's E-region, where the gas is weakly ionized, but this assumption is harder to justify in the partially ionized regime of the F-region [Song et al., 2001].

2.2.1.3 Conservation of Energy

Using the relation $\overleftrightarrow{P_s} = \overleftrightarrow{\tau_s} + p_s \overleftrightarrow{I}$ and rewriting the collision terms that are relevant for the Earth's I/T system, Eq. 2.6b becomes:

$$\frac{D_s}{Dt}\left(\frac{3}{2}p_s\right) + \frac{5}{2}p_s\left(\nabla\cdot\mathbf{u}_s\right) + \nabla\cdot\mathbf{q}_s + \left(\overleftrightarrow{\tau_s}\cdot\nabla\right)\cdot\mathbf{u}_s = \sum_s Q_s + \sum_s L_s, \tag{2.19}$$

where $\sum_s Q_s$ represents the total rate of change of thermal energy density for species s due to heating, and $\sum_s L_s$ is the sum of all cooling rates for species s. The first term in Eq. 2.19 is the total rate of change of the thermal energy density, the second term is adiabatic compression and expansion work, the third term is heat flux divergence, the fourth term is viscous heating, and the terms on the right hand side are the heating and cooling rates for the system. It should be noted that the 13-moment approximation is introduced into Eq. 2.19 through the stress tensor, the heat flow vector, and the heating and cooling terms. These terms account for various processes, such as diabatic heating due to solar radiation and thermal and frictional heat exchanges between the neutrals, ions, and electrons. In Eq. 2.19, the species s is replaced with n, i, and e to get the conservation of energy equations for the neutrals, ions, and electrons, respectively. The exact formulations of Q_s and L_s depend on the two interacting molecules and the type of collision they undergo. Furthermore, Eq. 2.19 is usually simplified by applying certain assumptions, and the ion temperature is commonly calculated from an equation involving the electron and neutral temperatures and the differential velocity between the ions and neutrals.

The conservation of mass (Eqs. 2.12-2.14), the conservation of momentum (Eqs. 2.16, 2.17), Ohm's law (Eq. 2.18), the conservation of energy (Eq. 2.19), and the Maxwell equations (Eqs. 2.7-2.10) form a complete set of equations that governs the neutral dynamics and electrodynamics of the Earth's I/T region, and captures many of the complex coupling processes between the plasma and the neutrals in the system. The types of plasma-neutral interactions are chemical heating (associated with the continuity equation), ion drag (associated with the momentum equation), frictional heating (associated with the energy equation), and conductivity (associated with the electrodynamics of the system).

2.3 Momentum-Energy Coupling through Dynamics

Forces that cause a change in the neutral gas momentum, i.e., altering wind systems, can lead to processes, i.e., adiabatic heating and cooling, that convert the change in mechanical energy to a change in the internal energy of the gas. This exchange progresses until the system reaches a new steady state form. Terms in the neutral momentum equation can change terms in the neutral energy equation through dynamics and work due to adiabatic heating and cooling. This concept is central to an indirect energy mechanism. This mechanism is analogous to a refrigeration cycle that converts work into heat (the converse is a heat engine cycle that converts heat into work, which is the parallel to a direct energy mechanism). The conservation law displayed in Eq. 2.19 was derived from a kinetic theory perspective, however, a form of the internal energy equation can also be developed from a fluid mechanics approach. This method is useful because it provides valuable insight into the expansion and compression process pertinent to the neutral gas adiabatic heating and cooling, illustrating the access point for changes in momentum to beget changes in energy through variations in neutral wind circulation patterns.

The internal energy equation for the neutral species ($s = n$) accounting for only adiabatic expansion and compression work processes is derived from the first law of thermodynamics and can be expressed in various forms. The first law of thermodynamics for any system states that the total time rate of change in internal energy is equal to the net heat rate added to the system minus the net work rate done by the system:

$$\frac{DU}{Dt} = \dot{Q} - \dot{W}, \tag{2.20}$$

where U is internal energy, $\dot{Q}$ is heat transfer rate, and $\dot{W}$ is the work rate. It should be noted that D/Dt refers to the total derivative ($D/Dt = \partial/\partial t + \mathbf{u} \cdot \nabla$, where $\mathbf{u}$ is the flow velocity).

Enthalpy (H), a thermodynamic property describing the total heat content of a system, and its associated time rate of change are defined as:

$$H = U + pV, \tag{2.21}$$

$$\frac{DH}{Dt} = \frac{DU}{Dt} + p\frac{DV}{Dt} + V\frac{Dp}{Dt}, \tag{2.22}$$

where p is pressure and V is volume. Work associated with the expansion and compression of the gas, also known as boundary work, is expressed as pDV, while the work rate is $p\frac{DV}{Dt}$. Equations 2.20 and 2.22 can be rewritten in terms of specific values u, $\dot{q}$, $\dot{w}$, h, and v by dividing through by mass:

$$\frac{Du}{Dt} = \dot{q} - \dot{w}, \tag{2.23}$$

$$\frac{Dh}{Dt} = \frac{Du}{Dt} + p\frac{Dv}{Dt} + v\frac{Dp}{Dt}. \tag{2.24}$$

If the work term in Eq. 2.23 is defined as only due to expansion and compression ($\dot{w} \equiv p\frac{Dv}{Dt}$), then Eq. 2.23 becomes:

$$\frac{Du}{Dt} = \dot{q} - p\frac{Dv}{Dt}. \tag{2.25}$$

Since $u = c_v T$, where c_v is the constant volume specific heat and T is temperature, one form of the neutral internal energy equation is derived as:

$$c_v\frac{DT}{Dt} = \dot{q} - p\frac{Dv}{Dt}. \tag{2.26}$$

Eq. 2.26 illustrates the proportional relationship between the internal energy of the system and expansion / compression work.

The $v\frac{Dp}{Dt}$ term can be teased out by solving for the expansion / compression work from Eq. 2.24, and substituting the result into Eq. 2.23 for $\dot{w}$. Using the relation $h = c_p T$, where c_p is the constant pressure specific heat, an alternate form of the internal energy equation is:

$$c_p\frac{DT}{Dt} = \dot{q} + v\frac{Dp}{Dt}, \tag{2.27}$$

where the change in enthalpy with time is directly related to $v\frac{Dp}{Dt}$.

The $v\frac{Dp}{Dt}$ term in Eq. 2.27 can be expanded by replacing p with the ideal gas law ($p = \rho RT$, where ρ is neutral mass density and R is the specific gas constant) and multiplying the result by the specific volume:

$$v\frac{Dp}{Dt} = R\left(\frac{DT}{Dt} + \frac{T}{\rho}\frac{D\rho}{Dt}\right). \tag{2.28}$$

The material derivative of the continuity equation for the neutral gas is:

$$\frac{1}{\rho}\frac{D\rho}{Dt} = -\nabla \cdot \mathbf{u}. \tag{2.29}$$

Equation 2.28 can be expanded when Eq. 2.29 is substituted into Eq. 2.28:

$$v\frac{Dp}{Dt} = R\frac{DT}{Dt} - \frac{p}{\rho}\left(\nabla \cdot \mathbf{u}\right), \tag{2.30}$$

and Eq. 2.30 is placed into Eq. 2.27 to arrive at a third form of the internal energy equation:

$$c_p\frac{DT}{Dt} = \dot{q} + R\frac{DT}{Dt} - \frac{p}{\rho}\left(\nabla \cdot \mathbf{u}\right). \tag{2.31}$$

Equations 2.26, 2.27, and 2.31 are equivalent in that they all represent the first law of thermodynamics, but they vary in form where different terms are explicitly related. In essence, this form of the energy equation includes heat transfer rates, internal energy changes with time, and the work rate associated with gas expansion and compression. The form of Eq. 2.31 is useful because it expresses this behavior in terms of gas properties that are measurable. Furthermore, Eq. 2.31 is particularly relevant to this study because it demonstrates that neutral temperature can be altered through a divergence in the neutral wind.

Equation 2.30 highlights that the $v\frac{Dp}{Dt}$ term is dependent on the divergence in the flow field. This translates into a direct connection to vertical motion. To confirm this relationship, the total derivative in $v\frac{Dp}{Dt}$ is expanded as:

$$\frac{1}{\rho}\frac{Dp}{Dt} = \frac{1}{\rho}\frac{\partial p}{\partial t} + \frac{w}{\rho}\frac{\partial p}{\partial z}, \tag{2.32}$$

where w is a physical vertical wind and z is the spatial vertical coordinate. Note that the advection operator is only in the vertical because pressure gradients are typically steepest in this direction. The hydrostatic law ($\partial p/\partial z = -\rho g$, where g is gravity) is inserted into Eq. 2.32, and the excellent assumption of a zero local time derivative in pressure ($\partial p/\partial t = 0$) is used to simplify Eq. 2.32:

$$\frac{1}{\rho}\frac{Dp}{Dt} = -gw. \tag{2.33}$$

Therefore, vertical movement in the neutral gas is directly proportional to adiabatic heating and cooling with gravity as the proportionality constant. In summary, the various forms of the energy equation demonstrate that the energy required to expand or compress the gas can be given in several but equal forms:

$$p\frac{Dv}{Dt} = \frac{p}{\rho}\left(\nabla \cdot \mathbf{u}\right) = R\frac{DT}{Dt} + gw. \tag{2.34}$$

Equations 2.31 and 2.33 show how neutral gas motion can induce changes to the internal energy of the system, and they are fundamentally forms of energy conservation, where work to expand or compress the gas comes from or leads to a decrease or increase in the internal energy of the gas. This indirect path for energy conversion is essentially a conversion of mechanical energy into internal energy. The mechanical energy equation is derived by taking the dot product of the momentum equation with the velocity vector, where a general form is (from Kundu [2004]):

$$\frac{D}{Dt}\left(\frac{1}{2}\mathbf{u}^2 + gz\right) = \mathbf{u}\cdot\mathbf{F}, \tag{2.35}$$

where $\mathbf{F}$ is the net force acting on the fluid element. The net force accelerates / decelerates the local fluid and increases / decreases the bulk kinetic energy of the gas through work done by the force, where $\mathbf{u}$ is the bulk velocity (not to be confused with u in Eq. 2.23, which is the specific internal energy). Equation 2.35 is a variant of the conservation of energy law that accounts for only the mechanical energy. It states that the change in the sum of kinetic and potential energies of the system must be equal to the bulk "kinetic energy work", $W_{KE} = \mathbf{u}\cdot\mathbf{F}$, or mechanical energy. The W_{KE} term only affects kinetic energy since potential energy can be incorporated into W_{KE} as work due to a body force. The sum of the mechanical energy and internal energy leads to the total energy of the system.

A useful form of Eq. 2.35 evaluates how kinetic energy can be transformed into internal energy through the deformation of fluid elements. The total work rate is defined as:

$$W_{tot} = W_{KE} + W_{def}, \tag{2.36}$$

where W_{def} accounts for deformation work [Kundu, 2004], which encompasses boundary work and viscous dissipation ($W_{def} \equiv -\frac{p}{\rho}(\nabla \cdot \mathbf{u}) + \phi$, where ϕ is the viscous term). By rewriting the mechanical energy equation in terms of W_{tot}, Eq. 2.35 becomes:

$$\frac{D}{Dt}\left(\frac{1}{2}\mathbf{u}^2 + gz\right) = W_{tot} + \frac{p}{\rho}(\nabla \cdot \mathbf{u}) - \phi. \tag{2.37}$$

The deformation work term also appears in the internal energy equation but with a reversed sign, see Eq. 2.31. It should be noted that the ϕ term is not in Eq. 2.31 because work was assumed to be solely due to expansion and contraction. If viscous effects were included into the definition of work, then ϕ would be present in Eq. 2.31 with the opposite sign of ϕ in Eq. 2.37. The term $\frac{p}{\rho}(\nabla \cdot \mathbf{u})$ is a two-way link between the mechanical and internal energy equations, while ϕ represents a loss of mechanical energy and a gain of internal energy due to the deformation of the fluid element. Thus, $\frac{p}{\rho}(\nabla \cdot \mathbf{u})$ is a reversible conversion between mechanical and internal energy, whereas ϕ is an irreversible conversion of mechanical energy to internal energy due to viscous effects. Equations 2.31 and 2.37 establish the concept that neutral wind dynamics can reshape energy through the transfer of mechanical energy to internal energy via adiabatic means.

Chapter 3

Model Description and Methodology

This chapter supplies a thorough description of the National Center for Atmospheric Research (NCAR) Thermosphere-Ionosphere-Electrodynamics General Circulation Model (TIEGCM), the principal tool used in this thesis work. Specifically, it reviews and discusses the conservation equations implemented in the model, along with detailed explanations of terms relevant to this dissertation, and it provides a general summary of the numerical experiments performed.

3.1 NCAR TIEGCM

3.1.1 General Overview

The TIEGCM is a global 3-D numerical model that simulates the coupled I/T system from ∼97 km to ∼600 km altitude [Qian et al., 2014]. It self-consistently solves the nonlinear, hydrodynamic, thermodynamic, and continuity equations for the neutrals, ions, and electrons, and includes the electrodynamic interactions between the thermosphere and ionosphere [Roble et al., 1988; Richmond et al., 1992].

The TIEGCM employs a geomagnetic field model specified by the International Geomagnetic Reference Field using magnetic apex coordinates [Richmond, 1995b], and the amplitudes and phases of migrating tides (diurnal and semidiurnal) at the lower boundary of the model are specified by the Global Scale Wave Model [Hagan and Forbes, 2002]. The model adopts a spherical coordinate system fixed with respect to the rotating Earth, with latitude and longitude as the horizontal coordinates and pressure surface as the vertical coordinate (ranges from -7 to 7) [Qian et al., 2014].

Typical resolutions for the TIEGCM are 5°× 5° (longitude × latitude), a vertical resolution of half a scale height, and a time step of 2 min. It outputs various neutral and plasma parameters, such as neutral temperature and winds, ion temperature and drift, and electron temperature and density.

The high-latitude convection pattern may be specified by either the Heelis et al. [1982] or the Weimer [2005] empirical model, along with the hemispheric power and cross-polar cap potential which serve as geomagnetic proxies for high-latitude forcings. Alternatively, the TIEGCM possesses the capability to apply a potential pattern derived from the assimilative mapping of ionospheric electrodynamics (AMIE) procedure [Richmond and Kamide, 1988], which merges various electrodynamic data sets together to construct a high-latitude convection pattern for a specific event.

A comprehensive description of the TIEGCM that includes details on its boundary conditions and numerical techniques may be found in Qian et al. [2014], HAO [2011], Wang [1998], and references therein. The formulation of terms and processes important to this thesis work will be expounded upon in the rest of the chapter.

3.1.2 Conservation Equations

The TIEGCM includes the neutral continuity, horizontal momentum, and energy equations to simulate the composition, wind, and temperature of the upper atmosphere, and the equations are executed within the model using discretization schemes.

3.1.2.1 Continuity Equation

The conservation of mass in the TIEGCM is denoted in spherical and log-pressure coordinates as [Wang, 1998]:

$$\frac{1}{R_E \cos\phi}\frac{\partial U_n}{\partial \lambda} + \frac{1}{R_E \cos\phi}\frac{\partial}{\partial \phi}\left(V_n \cos\phi\right) + e^{Z}\frac{\partial}{\partial Z}\left(e^{-Z}\omega\right) = 0, \tag{3.1}$$

where ϕ is latitude, λ is longitude, Z is the vertical coordinate ($Z = \ln p_0/p$, where p_0 is a reference pressure at $Z = 0$), R_E is the radius of the Earth, U_n and V_n are the zonal and meridional components of the neutral wind, respectively, and ω is the TIEGCM "vertical velocity" ($\omega = dZ/dt$). In the strictest sense, the curvature terms in Eq. 3.1 are a function of the radial distance from the center of the Earth, a, where $a = R_E + h$ and h is the height above the Earth's surface. However, since $R_E \gg h$, then $a \simeq R_E$. Equation 3.1 assumes that the neutral gas is incompressible, i.e., the change in neutral mass density with time is small, such that, any horizontal divergence is balanced by a gradient in the vertical wind. Thus, it states that the net spherical divergence of the wind must equal zero and vertical motions cannot be large. The exponent term in Eq. 3.1 arises from the transformation of the spatial vertical coordinate z into the log-pressure coordinate system, where $z = H \cdot Z$ (H is the pressure scale height) and the barometric law is exercised for the conversion [Sutton et al., 2015]:

$$p = p_0 e^{-z/H}, \tag{3.2a}$$

$$\rho H = \frac{p_0}{g} e^{-Z}. \tag{3.2b}$$

The definition in Eq. 3.2b is substituted into the z-coordinate continuity equation, forming the TIEGCM continuity equation in log-pressure coordinates (Eq. 3.1).

A model vertical velocity is computed through the kinematic method, where Eq. 3.1 is integrated in the vertical direction that results in ω. A physical vertical wind, W_n, is extracted by multiplying ω by the pressure scale height H, i.e. $W_n = \omega \cdot H$. It should be noted that the kinematic method is highly sensitive to errors in the horizontal wind field, where a 10% error in evaluating one of the wind components can easily cause the estimated divergence (and subsequent vertical wind calculation) to be in error by 100% [Holton, 1992]. Therefore, if spurious fluctuations exist in the horizontal winds, particularly in observations, then the kinematic method is not recommended for estimating vertical motion. However, given the deterministic nature of the model, the kinematic method is suitable.

3.1.2.2 Momentum Equation

The conservation of horizontal momentum in the TIEGCM is separated into directional components and given as [Wang, 1998]:

$$\begin{aligned}\frac{\partial U_n}{\partial t} =& \frac{g e^Z}{p_0}\frac{\partial}{\partial Z}\left(\frac{\mu}{H}\frac{\partial U_n}{\partial Z}\right) + fV_n + \lambda_{XX}\left(U_i - U_n\right) + \lambda_{XY}\left(V_i - V_n\right) - \mathbf{u}_{n,h}\cdot\nabla U_n \\ &+ \frac{U_n V_n}{R_E}\tan\phi - \frac{1}{R_E\cos\phi}\frac{\partial\Phi}{\partial\lambda} - \omega\frac{\partial U_n}{\partial Z},\end{aligned} \tag{3.3a}$$

$$\begin{aligned}\frac{\partial V_n}{\partial t} =& \frac{g e^Z}{p_0}\frac{\partial}{\partial Z}\left(\frac{\mu}{H}\frac{\partial V_n}{\partial Z}\right) - fU_n + \lambda_{YY}\left(V_i - V_n\right) - \lambda_{YX}\left(U_i - U_n\right) - \mathbf{u}_{n,h}\cdot\nabla V_n \\ &- \frac{U_n^2}{R_E}\tan\phi - \frac{1}{R_E}\frac{\partial\Phi}{\partial\phi} - \omega\frac{\partial V_n}{\partial Z},\end{aligned} \tag{3.3b}$$

where g is the acceleration due to gravity, μ is the viscosity coefficient, f is the Coriolis parameter ($f = 2\Omega\sin\phi$), Φ is the geopotential, $\mathbf{u}_{n,h}$ is the horizontal wind velocity, U_i and V_i are the zonal and meridional components of the ion drift, respectively, and λ_{XX}, λ_{YY}, λ_{XY}, λ_{YX} are the ion drag coefficients.

Equations 3.3a and 3.3b state that the time rate of change in the zonal (Eq. 3.3a) and meridional (Eq. 3.3b) directions of the neutral wind is determined by the forcing terms on the right hand sides of the equations: vertical viscosity (first term), Coriolis force (second term), ion drag force (third and fourth terms), nonlinear horizontal momentum advection (fifth term), curvature apparent force (sixth term), pressure gradient force (seventh term), and vertical momentum advection (last term).

The TIEGCM does not utilize a momentum equation in the vertical direction, but instead employs the hydrostatic assumption. Hydrostatic equilibrium asserts that the gravity force must be exactly balanced by the vertical component of the pressure gradient force [Holton, 1992]:

$$\frac{\partial\Phi}{\partial Z} = RT_n, \tag{3.4}$$

where R is the specific gas constant and T_n is neutral temperature. Equation 3.4 is the log-pressure version of the hydrostatic relation, and it only applies when gravitational acceleration is assumed to be constant. Although the model assumes hydrostatic balance, this does not preclude the existence of vertical winds. Applying this relation only signifies that the vertical velocity cannot be determined from the vertical momentum equation, and that vertical motion must be deduced indirectly via an alternate route, such as the kinematic method. The hydrostatic condition is an excellent approximation for the vertical dependence of the pressure field in the real atmosphere, and only for intense small-scale features is it necessary to consider departures from hydrostatic balance [Holton, 1992]. Specifically in the thermosphere, this assumption can accommodate vertical winds on the order of 100 m s^{-1}, and it is an appropriate condition to apply to studies that are not concerned with acoustic waves [Fuller-Rowell, 2014].

The viscosity coefficient, μ, is comprised of the eddy and molecular viscosity coefficients. In the TIEGCM, the effect of gravity wave breaking in the mesosphere-lower-thermosphere (MLT) region is included by specifying a constant eddy diffusivity at the lower boundary that declines with altitude [Qian et al., 2009]. However, Qian et al. [2009] recently added the option in the model to set the eddy viscosity coefficient to vary with season. All of the numerical experiments in this thesis work use a constant eddy diffusivity parameterization at the lower boundary.

The molecular viscosity coefficient, k_m, is prescribed by an empirical relationship that relies on the composition of the dominant neutral constituents in the atmosphere, as shown below [Sutton et al., 2015]:

$$k_m = \frac{10^{-6} T_n^{0.69}}{n_n} \left(4.03 n_{O_2} + 3.90 n_O + 3.43 n_{N_2} + 3.84 n_{He}\right), \tag{3.5}$$

where n_n is the total neutral number density, n_j refers to the number density of the subscripted species, and k_m has units of g$\cdot$cm^{-1}s^{-1}. The term with helium in Eq. 3.5 is included or excluded from the model depending on its version number. Sutton et al. [2015] recently implemented helium as a major species into the newest release of the TIEGCM. The studies completed for this dissertation will use model versions with and without helium.

The ion drag force perpendicular to the magnetic field, **B**, in the TIEGCM is calculated from a tensor that contains ion drag coefficients. These coefficients describe the Ampère force, which represents the momentum transferred to the neutrals through collisions with ions and electrons, and it is often synonymous with the perpendicular ion drag force under certain assumptions [Richmond and Thayer, 2000]. Ohm's law in Eq. 2.18 is expressed in the frame of reference moving with the medium, i.e., the neutral gas reference frame moving at velocity $\mathbf{u}_n$, where the electric field, $\mathbf{E}'$, is related to the electric field in the frame of reference of the Earth, $\mathbf{E}$, through a nonrelativistic Lorentz transformation:

$$\mathbf{E}' = \mathbf{E} + \mathbf{u}_n \times \mathbf{B}. \tag{3.6}$$

The Ampère force, or $\mathbf{J} \times \mathbf{B}$ force, per unit mass is obtained by taking the cross product of Eq. 2.18 with the magnetic field $\mathbf{B}$ [Richmond and Thayer, 2000]:

$$\frac{\mathbf{J} \times \mathbf{B}}{\rho} = \frac{\sigma_P B^2}{\rho}\left(\frac{\mathbf{E} \times \mathbf{B}}{B^2} - \mathbf{u}_\perp\right) + \frac{\sigma_H B^2}{\rho}\mathbf{b} \times \left(\frac{\mathbf{E} \times \mathbf{B}}{B^2} - \mathbf{u}_\perp\right), \tag{3.7}$$

where $\mathbf{u}_{n,\perp}$ is neutral wind perpendicular to $\mathbf{B}$, B is the magnitude of the magnetic field, ρ is the total neutral mass density, and the following assumptions have been applied:

(1) $\mathbf{J}^P$ is assumed to be zero in Eq. 2.18 (gravitational and pressure gradient forces have been neglected in the equations of motion for the ions and electrons).

(2) The effects of collisions between ions and electrons are neglected (the force balance is between the Lorentz force and the collisional force with neutrals).

Thus, the Ampère force is equal to the perpendicular ion drag force when the above two assumptions are satisfied, and the resultant conductivities, σ_P and σ_H, are constructed based on this equality. Between the two assumptions, the first one is more restrictive, but it mainly affects motion along the magnetic field lines. For example, ions are assumed to move at the neutral velocity in the direction along $\mathbf{B}$, but plasma pressure gradients and gravity can set up an ambipolar electric field parallel to the field lines and compel ion motion [Richmond, 1995a]. The consequences of neglecting these forces from the ion and electron momentum equations are investigated in Richmond [2016], with a complete re-derivation of Ohm's law with the ramifications of gravitational and pressure gradients forces incorporated. The second assumption is particularly valid for plasma motion perpendicular to **B** in the upper ionosphere, where although electron-ion collisions are important (the electron-ion collision frequency ν_{ei} is significant), the ions and electrons move with almost the same velocity in the direction perpendicular to **B**, rendering the differential velocity between the ions and the electrons to be approximately zero.

The conductivities in Eq. 3.7 are defined as [Richmond, 1995b]:

$$\sigma_P = \frac{n_e e}{B}\left(\frac{\nu_{in}\Omega_i}{\nu_{in}^2 + \Omega_i^2} + \frac{\nu_{en\perp}\Omega_e}{\nu_{en\perp}^2 + \Omega_e^2}\right), \tag{3.8a}$$

$$\sigma_H = \frac{n_e e}{B}\left(\frac{\Omega_e^2}{\nu_{en\perp}^2 + \Omega_e^2} - \frac{\Omega_i^2}{\nu_{in}^2 + \Omega_i^2}\right), \tag{3.8b}$$

where n_e is the number density of the ions and electrons (assuming charge neutrality where n_i=n_e), e is the magnitude of the electron charge, ν_{in} is the ion-neutral collision frequency, $\nu_{en\perp}$ is the perpendicular component of the electron-neutral collision frequency, Ω_i is the ion gyrofrequency ($\Omega_i = eB/m_i$, where m_i is the ion mass), and Ω_e is the electron gyrofrequency ($\Omega_e = eB/m_e$, where m_e is the electron mass). Above 90 km, it is adequate to consider all ion species together, where the mass, velocity, and collision frequencies are representative of the mass-density-weighted averages over all ion species, due to the fact that these values are normally similar among the different ion species [Richmond, 1995b]. In reality, the collision frequencies in Eqs. 3.8a and 3.8b are tensors rather than scalars, and above 80 km, the electron-neutral collision frequency is about 1.4 times stronger for motions perpendicular to the magnetic field than for motions parallel to **B** [Gagnepain et al., 1977]. However, for ions, the anisotropy of the collision frequency is trivial [Richmond, 1995b]. Hence, it is important to distinguish between components across and along **B** for the electron-neutral collision frequency, but these directional markers are not necessary for the ion-neutral collision frequency. It should be noted that there exists an implicit assumption in the formulation of the collision frequencies derived from the Boltzmann collision integral, in which the collision frequencies are independent of the fluid velocities. This is a reasonable assumption as long as the relative velocities are small compared to the thermal velocities, a criteria that is generally fulfilled at low to mid-latitudes, but in auroral regions, strong electric fields driven by the magnetosphere can propel ion and neutral velocities to be on the same order of magnitude with the thermal velocities, which can lead to inaccuracies in Ohm's law (Eq. 2.18) and Eqs. 3.8a - 3.8b [Richmond, 1995b].

The perpendicular ion drag tensor in geomagnetic coordinates, $\overleftrightarrow{\lambda}_{mag}$, is [HAO, 2011]:

$$\overleftrightarrow{\lambda}_{mag} = \begin{bmatrix} \lambda_{xx}^{mag} & \lambda_{xy}^{mag} \\ \lambda_{yx}^{mag} & \lambda_{yy}^{mag} \end{bmatrix} = \begin{bmatrix} \lambda_1 & \lambda_2 \sin I \\ -\lambda_2 \sin I & \lambda_1 \sin^2 I \end{bmatrix}, \tag{3.9}$$

where I is the inclination angle of the Earth's magnetic field, λ_1 is the Pedersen ion drag coefficient (equal to $\frac{\sigma_P B^2}{\rho}$), and λ_2 is the Hall ion drag coefficient (equal to $\frac{\sigma_H B^2}{\rho}$). Notice that λ_1 and λ_2 match the values in front of the vector terms in Eq. 3.7, confirming the correlation between the ion drag force perpendicular to $\mathbf{B}$ and the Ampère force in the TIEGCM. The ion drag tensor is rotated into geographic coordinates using the declination angle D of the magnetic field and the following relation:

$$\overleftrightarrow{\lambda}_{geo} = \underline{R}\,\overleftrightarrow{\lambda}_{mag}\underline{R}^T, \tag{3.10}$$

where $\underline{R}$ represents the rotation matrix from geomagnetic to geographic coordinates and is defined as:

$$\underline{R} = \begin{bmatrix} \cos D & \sin D \\ -\sin D & \cos D \end{bmatrix}. \tag{3.11}$$

Performing the rotation in Eq. 3.10 and simplifying terms leads to the ion drag tensor in geographic coordinates, $\overleftrightarrow{\lambda}_{geo}$:

$$
\begin{aligned}
\overleftrightarrow{\lambda}_{geo} = \begin{bmatrix} \lambda_{xx} & \lambda_{xy} \\ \lambda_{yx} & \lambda_{yy} \end{bmatrix} = \\
\begin{bmatrix} \lambda_{xx}^{mag} \cos^2 D + \lambda_{yy}^{mag} \sin^2 D & \lambda_{xy}^{mag} + (\lambda_{yy}^{mag} - \lambda_{xx}^{mag}) \sin D \cos D \\ -\lambda_{xy}^{mag} + (\lambda_{yy}^{mag} - \lambda_{xx}^{mag}) \sin D \cos D & \lambda_{xx}^{mag} \sin^2 D + \lambda_{yy}^{mag} \cos^2 D \end{bmatrix}.
\end{aligned}
\tag{3.12}
$$

The tensor in Eq. 3.12 is utilized in the TIEGCM to compute the ion drag force perpendicular to the magnetic field in geographic coordinates.

The reason for exercising the Ampère force as a surrogate for the ion drag force perpendicular to **B** is computational efficiency. The Pedersen and Hall ion drag coefficients, λ_1 and λ_2, are used in numerous instances in the model source code to calculate a variety of terms, including the perpendicular ion drag force and the frictional heating rate between ions and neutrals.

The ion drag force parallel to **B** is not included in the default TIEGCM because it is presumed that its effects on the I/T system are minor. However, it will be demonstrated in Ch. 4 that field-aligned ion drag effects can have a notable impact on the neutrals and contribute to localized thermospheric variations. Chapter 4 will cover the formulation of the parallel ion drag force, along with the procedure for its implementation into the model.

3.1.2.3 Energy Equation

The conservation of energy in the TIEGCM is given as [Roble et al., 1988]:

$$
\begin{aligned}
\frac{\partial T_n}{\partial t} =& \frac{g e^Z}{p_0 c_p} \frac{\partial}{\partial Z} \left\{ \frac{K_T}{H} \frac{\partial T_n}{\partial Z} + K_E H^2 c_p \rho \left(\frac{g}{c_p} + \frac{1}{H} \frac{\partial T_n}{\partial Z} \right) \right\} \\
&- \mathbf{u}_{n,h} \cdot \nabla T_n - \omega \left(\frac{\partial T_n}{\partial Z} + \frac{\bar{R} T_n}{c_p \bar{m}} \right) + \frac{(Q - L)}{c_p},
\end{aligned}
\tag{3.13}
$$

where c_p is the specific heat per unit mass at constant pressure, K_T is molecular thermal conductivity, K_E is the eddy diffusion coefficient (assumed to be equal to the eddy thermal conductivity), $\bar{R}$ is the universal gas constant, $\bar{m}$ is the mean molar mass, and Q and L are heating and cooling rates due to other processes, respectively. From Eq. 3.13, the local time variation of neutral temperature is determined by vertical molecular heat conduction and adiabatic heating and cooling due to eddy diffusion (first term), horizontal heat advection (second term), vertical heat advection and adiabatic heating and cooling caused by vertical motion (third term), and all other heating and cooling processes (last term).

The last term in Eq. 3.13 can be expanded as follows [Lei et al., 2012a]:

$$\frac{(Q-L)}{c_p} = \frac{Q_{ph}}{c_p} + \frac{Q_{ic}}{c_p} + \frac{Q_{coll}}{c_p} + \frac{Q_{jh}}{c_p} - \frac{L}{c_p}, \tag{3.14}$$

where Q_{ph} is solar radiation heating including non-Maxwellian electron heating and absorption on the solar UV Schumann-Rünge continuum, Q_{ic} is the excess heat produced by ion chemical reactions, Q_{coll} is the heat transferred from thermal electrons and ions to the neutrals through collisions due to temperature differences, Q_{jh} is the Joule heating term that accounts for frictional heating between the plasma and neutrals due to velocity differences, and L is radiational cooling caused by CO_2, NO, and the fine structure of $O(^3P)$.

Combining Eq. 3.14 with a condensed version of Eq. 3.13 results in:

$$c_p \frac{\partial T_n}{\partial t} = Q_{con} + Q_{advh} + Q_{adb} + Q_{advv} + Q_{ph} + Q_{ic} + Q_{coll} + Q_{jh} - L, \tag{3.15}$$

where Q_{con} is vertical heat conduction and eddy heat transport, Q_{advh} is horizontal wind heat advection, Q_{adb} is adiabatic heating and cooling due to vertical motion, and Q_{advv} is vertical wind heat advection (note that the sum of Q_{advh} and Q_{advv} is the total heat advection term, Q_{adv}, due to the neutral wind field). All terms in Eq. 3.15 are heating rates per unit mass.

The frictional heating term in the TIEGCM is assumed to be equivalent to Joule heating, denoted as Q_{jh} and designated with the following expression [Thayer and Semeter, 2004]:

$$Q_{jh} = \frac{\mathbf{J}\cdot\mathbf{E}'}{\rho} = \frac{\sigma_P \mathbf{E}'^2}{\rho}. \tag{3.16}$$

In the TIEGCM, only the perpendicular electric field contribution to the Joule heating rate is considered. Heating due to the parallel component of $\mathbf{E}'$, or $\sigma_{\parallel}\mathbf{E}'^2$, does affect Q_{jh}, but its role is presumed to be minimal. Projecting the electric field onto the perpendicular direction, $\mathbf{E}'_{\perp} = \mathbf{E}'\times\hat{\mathbf{b}}$, and using Eqs. 3.6 and 3.16, the Joule heating rate per unit mass can be rewritten as a function of the Pedersen ion drag coefficient:

$$Q_{jh} = \lambda_1 \left(\mathbf{u}_{i,E\times B} - \mathbf{u}_n\right)^2, \tag{3.17}$$

where $\mathbf{u}_{i,E\times B}$ is the drift velocity ($\frac{\mathbf{E}\times\mathbf{B}}{B^2}$) and $\mathbf{u}_n$ is the total neutral wind velocity. The term is multiplied by a tuning factor that usually ranges from 1.0 to 1.5 in order to account for heating due to small-scale electric fields [HAO, 2011]. A factor of 1.5 is applied to all of the model simulations in this thesis work.

It is worth mentioning that the neutral frictional heating rate is not always equivalent to the Joule heating rate, differing primarily in their origins. The Joule heating rate is a term in the magnetohydrodynamic (MHD) internal energy equation that characterizes the conversion of electromagnetic energy into thermal energy of the neutral gas, while the frictional heating rate is a term in the individual species description of the energy equation and it depicts the interaction between the relative drift velocities of the ions and neutrals [Thayer and Semeter, 2004]. Joule heating will equal neutral frictional heating when the following assumptions are valid:

(1) Ion and electron equations of motion perpendicular to the magnetic field line are in steady-state.

(2) Ion and electron momentum equations include only the Lorentz and ion drag forces.

(3) Electron mobility coefficient, $k_e = \Omega_e/\nu_{en}$, where Ω_e is the electron gyrofrequency and ν_{en} is the electron-neutral collision frequency, is large (generally true above 90 km).

Therefore, the Joule heating rate and the neutral frictional heating rate are two separate entities, but after some reasonable assumptions, the terms can represent the same quantity.

3.2 Analysis Methodology

The main methodology conducted for this dissertation is to turn on and off the ion drag force and neutral frictional heating terms in the TIEGCM in order to comprehensively assess the effects of an indirect, dynamically induced energy mechanism on the Earth's I/T system. Turning on / off simply means including / excluding a term from the neutral momentum (e.g., ion drag) or neutral energy (e.g., frictional heating) equations. When the frictional heating term is neglected, the impact of terms in the momentum equation on neutral structure can be observed. The interplay between the ion drag force and the viscous drag force can be examined by excluding the ion drag force from the model (viscous drag environment), and by including ion drag into the simulations (ion drag-viscous drag environment). The frictional heating is added back into the model to broaden the implications of the conclusions from the more controlled experiments.

This thesis work is focused on geomagnetically-quiet conditions in order to fully understand how the complex, internal coupling between the plasma and the neutrals can indirectly mold distributions and fields of the neutral gas. To effectively isolate momentum forcing effects, high-latitude forcing is essentially eliminated by setting the fractional presence of the high-latitude convection electric field in the global electric field solver at each grid point to one. This setting instructs the model to determine the electric field solely based on the dynamo equation instead of merging the computation with the specified high-latitude convection pattern.

Various plasma and neutral parameters are explicitly calculated in the model, including all momentum forces and energy terms. These outputs are analyzed as time evolutions or diurnally-reproducible states, depending on the intent of the study.

Attempting to untangle a severely intertwined and complicated mechanism, such as the indirect and dynamically induced energy mechanism, requires strictly controlled numerical experiments, and there is still fundamental science to be learned from these types of simulations. A cogent way to test and truly understand the cornerstone physics is to pare down the model and understand how each added component and layer of complexity affects the system. Even though the basic physics and chemistry are already in the model, this does not mean that it is wholly understood how these processes interact, and this lack of understanding can lead to erroneous conclusions on why the atmosphere is behaving as it is, leading to incorrect corrections to the model when it does not agree with the data. Through carefully designed model runs, the myriad of processes occurring simultaneously in the upper atmosphere can begin to be extricated, thereby understanding, improving, and advancing I/T models.

Chapter 4

Plasma-Neutral Coupling of the EIA and ETA

An ionization anomaly prompts a neutral thermosphere anomaly, as was discussed in Section 1.5.1. This chapter investigates this matter by exhibiting the distinct plasma-neutral coupling between the equatorial ionization anomaly (EIA) and the equatorial thermosphere anomaly (ETA) as a case study of an indirect, dynamically induced energy mechanism that translates disturbances in the plasma to localized variations in the neutral gas thermal and mass density structure. This chapter aims to address science questions 1a-1c, where the TIEGCM is used to simulate the formation of the ETA and its local time and solar cycle variations to illustrate in detail how a change in momentum forcing can create a thermospheric feature in neutral temperature and mass density through dynamics. The new science achieved through this study is as follows:

(1) The formation process of the ETA trough due to field-aligned ion drag is extensively dissected to a level that has not been done in previous studies.

(2) The local time and solar cycle variations of the ETA trough is addressed and solidifies the enduring connection between an ionization anomaly, the EIA, with a thermospheric anomaly, the ETA.

The driving mechanism for the generation of the ETA trough in the model is field-aligned ion drag. In our simulations, during the daytime, field-aligned ion drag on the north-south flanks of the magnetic equator causes a divergence in meridional winds, leading to an upwards change in vertical winds, adiabatic cooling, and a reduction in neutral temperature of about 30 K over the magnetic equator near 400 km. This response closely links ETA behavior to variations in the equatorial ionosphere anomaly (EIA) associated with local time and solar cycle. As the EIA begins to disappear in the evening, the processes in the ETA mechanism recede, causing the ETA trough to subside. In our simulations, the trough becomes more prominent as the solar cycle progresses from low (F10.7 = 80) to high (F10.7 = 180), in agreement with observations. The neutral-ion collision frequency (proportional to variations in electron density) controls ETA day-to-night and solar cycle variations, while plasma scale height and gradients in electron number density and plasma temperature produce a secondary structure in ETA local time behavior that varies with solar cycle levels. This chapter expands on the results in the JGR: Space Physics journal article by Hsu et al. [2014]. Note that the runs and run numbers are unique to the chapter, and that all notation will be explained in the text. Supplemental figures and analysis are located in Appendix B.

4.1 Introduction

There has been much effort to observe and understand the formation mechanism of the equatorial thermosphere anomaly (ETA), which is a feature in the upper thermosphere, characterized in properties such as temperature, density, and zonal winds. Thermosphere density and temperature exhibit two crests around $\pm 20-30°$ magnetic latitude and a trough at the magnetic equator. Hedin and Mayr [1973] reported minima in daytime N_2 densities at the magnetic equator at 450 km and at all longitudes using the neutral mass spectrometer onboard the Orbiting Geophysical Observatory (OGO) 6 satellite. Raghavarao et al. [1991], Raghavarao et al. [1993], and Raghavarao et al. [1998] observed a trough at the dip equator and two maxima collocated with the equatorial ionosphere anomaly (EIA) crests in DE-2 neutral temperatures for multiple orbits. Recently, several studies have alluded to plasma-neutral interactions between the ETA and the EIA as the cause for the behavior in thermospheric neutral mass density satellite data at low latitudes [Liu et al., 2005, 2007; Lei et al., 2010]. Knowledge of how the ETA develops will help elucidate the plasma-neutral coupling between the EIA and the ETA, and understanding this coupling will help in comprehending the neutral gas processes that occur in the equatorial thermosphere.

Various studies have attempted to explain the mechanism for the formation of the ETA. Hedin and Mayr [1973] suggested that the ETA in the daytime is a result of latitudinal variations in zonal ion drag, meaning the energy flow from the dayside to the nightside is damped at latitudes of enhanced electron density leading to higher temperature and density at the EIA crests. However, Fuller-Rowell et al. [1997] and Lei et al. [2010] have revealed discrepancies with this mechanism, such as it requires a temperature bulge (or local warming) at the equator that is not seen in observations or models, which makes this zonal wind transport mechanism an unlikely source for the formation of the ETA. Fuller-Rowell et al. [1997] proposed that chemical heating from the exothermic recombination of O^+ was the likely explanation for the ETA, stating that their model simulations reproduced the correct direction of the observed vertical winds by DE-2. However, this mechanism is unable to explain the separation of the latitude locations in the crests between the ETA and the EIA, as well as the different longitudinal variations between the two anomalies [Lei et al., 2010]. Using DE-2 measurements and standard atmosphere models, Pant and Sridharan [2001] stated that chemical heating and ion drag were both important and necessary for the generation of the ETA (positing that ~30% of the neutral temperature enhancements in the ETA is due to exothermic reactions and the remaining is from zonal ion drag frictional heating). However, the estimates of chemical heating in this study were not based on realistic ion/O_2 densities [Raghavarao and Suhasini, 2002]. Miyoshi et al. [2011] suggested that the ETA in mass density during the daytime was caused by the in situ diurnal tide and the upward propagating terdiurnal tide. Although their model simulations were able to produce the ETA feature in mass density, they were not able to replicate the equatorial anomaly in neutral temperature, as observed by DE-2 [Raghavarao et al., 1991]. A recent study by Clemmons et al. [2013] used measurements from an ionization gauge on the Streak mission to investigate the ETA near 275 km altitude. They proposed that the heated gas under the EIA crests creates pressure gradients that drive meridional flow, leading to a four cell circulation pattern. This mechanism requires very rapid meridional winds ($\sim$400 m s^{-1}). Clemmons et al. [2013] attempted to validate these wind speeds by using a simplified model, but the dynamic and thermodynamic nature of the atmosphere requires a self-consistent and coupled model to accurately simulate the upper thermosphere response [Dickinson et al., 1971].

Recent studies using global circulation models have begun to shed light on the processes involved in the development of the ETA, and the importance of field-aligned ion drag on its formation. Using a three-dimensional coupled model of the global ionosphere and thermosphere, Maruyama et al. [2003] simulated the ETA temperature trough at the geomagnetic equator by including meridional ion drag into their model. However, the electric field in their model was not solved self-consistently. Lei et al. [2012b] expanded on this study by incorporating field-aligned ion drag into the fully-coupled self-consistent TIEGCM [Roble et al., 1988; Richmond et al., 1992]. They were able to simulate the ETA feature in both mass density and temperature, and their results agreed with observations from Raghavarao et al. [1991], Liu et al. [2007], and Lei et al. [2010].

The purpose of this study is to further develop and expand on the mechanism proposed in Lei et al. [2012b] by investigating local time and solar cycle ETA behavior. It should be noted that this study is focused only on the formation of the ETA trough. Lei et al. [2012a] is a companion study to Lei et al. [2012b] and gave evidence that the formation of the ETA trough and crests were due to separate mechanisms in the model. Additional studies on the ETA using the same modeling scheme address tidal influences and geomagnetic activity effects [Lei et al., 2014a,b]. We examine the local time and solar cycle variations of the ETA, which allows us to further analyze the intimate coupling between the EIA and the ETA. Our simulations can be compared with thermosphere temperature and mass density observations [Raghavarao et al., 1991; Liu et al., 2005, 2007; Lei et al., 2010] and ion velocity measurements [Burrell et al., 2011].

4.2 ETA Trough Formation

Ion drag is the force acting on neutral particles due to collisions with ions that may accelerate or decelerate the neutral gas. The horizontal momentum equation for the thermosphere can be written as:

$$\frac{D\mathbf{u}_n}{Dt} = \mathbf{g} - \frac{1}{\rho}\nabla p - 2\boldsymbol{\Omega} \times \mathbf{u}_n - \boldsymbol{\Omega} \times (\boldsymbol{\Omega} \times \mathbf{r}) \\ + \frac{1}{\rho}\nabla(\mu\nabla\mathbf{u}_n) - \nu_{ni}(\mathbf{u}_n - \mathbf{u}_i), \tag{4.1}$$

where $\mathbf{u}_n$ is the horizontal neutral wind, $\mathbf{u}_i$ is the ion velocity, ρ is the neutral mass density, p is the thermospheric pressure, $\mathbf{g}$ is the acceleration due to gravity, $\boldsymbol{\Omega}$ is the angular velocity of the Earth, $\mathbf{r}$ represents the outward-pointing radial distance from the center of the Earth, μ is the viscosity coefficient, and ν_{ni} is the collision frequency of momentum transfer for the neutral gas with the ions. $D\mathbf{u}_n/Dt$ is the total derivative of the neutral wind, and the forcing terms per unit mass are on the right hand side of Eq. (4.1): gravity (first term), pressure gradient force (second term), Coriolis force (third term), centrifugal force (fourth term), viscosity (fifth term), and ion drag force (last term).

The ion drag force per unit mass, $\mathbf{F_{ni}}$, may be decomposed into directions perpendicular and parallel to the magnetic field, as shown below (after Huba et al. [2000]):

$$\begin{aligned} \mathbf{F}_{ni} &= F_{ni,\perp}\hat{\mathbf{p}} + F_{ni,\parallel}\hat{\mathbf{s}} \\ &= -\nu_{ni}(\mathbf{u}_n - \mathbf{u}_i) \\ &= -\nu_{ni}(u_{n,\perp} - u_{i,\perp})\hat{\mathbf{p}} - \nu_{ni}\left(u_{n,\parallel} - u_{i,\parallel}\right)\hat{\mathbf{s}}, \end{aligned} \tag{4.2}$$

where $\hat{\mathbf{p}}$ and $\hat{\mathbf{s}}$ are the unit vectors pointing in the perpendicular and parallel directions, respectively. Although the TIEGCM includes ion drag forces perpendicular to the magnetic field, the parallel component has not been included in the neutral gas momentum equation. The parallel component of the ion drag force, or the field-aligned ion drag $F_{ni,||}$, can be written in terms of the parallel component of the ion diffusion velocity $\mathbf{W}_d$:

$$\mathbf{W}_d = \mathbf{u}_i - \mathbf{u}_n, \tag{4.3}$$

$$F_{ni,\parallel} = -\nu_{ni}\left(u_{n,\parallel} - u_{i,\parallel}\right) = \nu_{ni}W_{d,\parallel}. \tag{4.4}$$

The parallel component of the ion diffusion velocity is expressed as [Rishbeth and Garriott, 1969]:

$$W_{d,\parallel} = -D_a \left(\frac{1}{n_i} \nabla_\parallel n_i + \frac{1}{T_p} \nabla_\parallel T_p + \frac{m_i g_\parallel}{2kT_p} \right), \tag{4.5}$$

where $D_a = 2kT_p/m_i \nu_{in}$ (ambipolar diffusion coefficient), $T_p = (T_e + T_i)/2$ (plasma temperature), m_i is the mass of O^+ ions, n_i is the ion number density ($n_i = n_e$, where n_e is the electron number density), and k is the Boltzmann constant. With Eqs. 4.4 and 4.5, the ion drag force along the magnetic field line is computed and projected onto a geographic grid using the declination and inclination angles of the Earth's magnetic field.

The energy equation for the thermosphere expressed in the TIEGCM using log pressure coordinates is defined in Eq. 3.13. The adiabatic heating or cooling rate is of particular importance in this study because it couples the momentum equation with the energy equation. The mean atmospheric stability of the thermosphere is defined as [Holton, 1992]:

$$\Gamma = \frac{\partial T_n}{\partial z} + \frac{g}{c_p}, \tag{4.6}$$

where z is height. The first term in Eq. 4.6 is the atmospheric (environmental) lapse rate, while the second term is the dry adiabatic lapse rate. Since neutral temperature does not change significantly with the vertical coordinate in the upper thermosphere, the atmospheric lapse rate is close to zero. Thus, the adiabatic heating or cooling rate may be expressed as:

$$\left(\frac{\partial T_n}{\partial t} \right)_{adb} = -W_n \Gamma, \tag{4.7}$$

where W_n is the neutral vertical wind. Using the neutral pressure scale height $H = kT_n/mg$ (where m is the mean molecular mass), and rewriting equation (4.7) in terms of H, the adiabatic heating or cooling rate becomes:

$$\left(\frac{\partial T_n}{\partial t} \right)_{adb} = -\frac{W_n \bar{R} T_n}{c_p \bar{m} H} = \dot{Q}_{adb}. \tag{4.8}$$

The adiabatic heating or cooling rate is then directly proportional to the vertical wind.

Figure 4.1 is a summary diagram based on our simulations of the time evolution in our mechanism for the formation of the ETA neutral temperature trough over the magnetic equator during the daytime. A well formed EIA involves downward plasma diffusion and a field-aligned ion drag force with a component in the meridional plane, process 1, that causes a divergence in the meridional winds, process 2. This divergence produces an upwards change in the vertical winds resulting in a decrease in adiabatic heating and subsequent reduction in neutral temperature, process 3. The changes in the thermal structure in the equatorial region with time create a reactive pressure gradient force that acts to mostly balance the meridional component of the field-aligned ion drag force, process 4. Each process in the formation mechanism is labeled in Figure 4.1 and described in detail in section 4.4.1.

4.3 Numerical Experiments

In the default configuration of the TIEGCM, only the perpendicular component of the ion drag force is implemented, but the field-aligned component associated with the EIA is capable of imposing accelerations on the upper thermosphere gas that prove important. To elucidate the formation mechanism of the ETA trough, two simulations were performed using the TIEGCM: one without the field-aligned ion drag force (run 1) and one with the field-aligned ion drag force (run 2). The numerical experiments were conducted under high solar activity (F10.7 = 180) and March equinox conditions so that the ETA would be most evident [Liu et al., 2007]. The low-latitude electric field is self-consistently solved for in the TIEGCM through neutral wind dynamo effects. The model runs were initialized by a 20 day steady-state run, and we analyze all of the model outputs starting at day 20 into the simulations, or at day of year 80 (corresponding to March equinox). For the runs with field-aligned ion drag, the forcing was introduced at 00:00 UT on day of year 80.

Figure 4.2 demonstrates the impact of including field-aligned ion drag in the TIEGCM simulation. Run 2 clearly simulates the presence of a neutral temperature trough at the magnetic equator at the selected longitudes (the times for each chosen longitude are a few hours after the field-aligned ion drag was turned on in the model simulations to ensure that the trough had developed, but it should be noted that it takes less than a hour for the trough to form, as we will

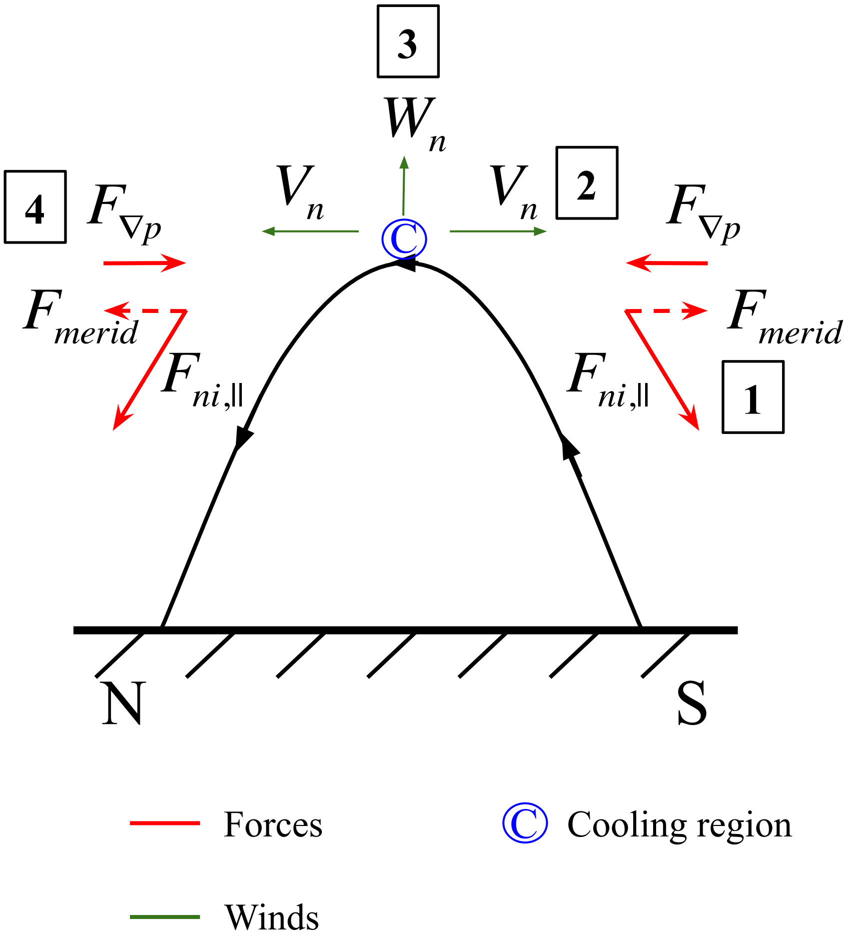

Figure 4.1: Summary diagram of the mechanism for the formation of the ETA neutral temperature trough, where the numbers represent the process in the sequence of the formation mechanism: (1) Field-aligned ion drag force; (2) Divergence of meridional winds; (3) Changes in vertical winds, adiabatic heating, and neutral temperature; (4) Reactive pressure gradient force. The black arrowed curve is a magnetic field line, and the north and south hemispheres are denoted as N and S, respectively.

demonstrate in the subsequent section). Specifically, the equatorial neutral temperatures decrease by 24 K, 23 K, and 29 K, or 1.9%, 1.8%, and 2.3%, from run 1 to run 2 for 60°W, 30°E, and 150°W, respectively. Similarly, the equatorial neutral mass densities decrease by 0.35 $\times 10^{-12}$ kg m^{-3}, 0.33 $\times 10^{-12}$ kg m^{-3}, and 0.38 $\times 10^{-12}$ kg m^{-3}, or 4.4%, 4.1%, and 4.9%, from run 1 to run 2 for 60°W, 30°E, and 150°W, respectively. By including field-aligned ion drag into our simulations, the equatorial depletions in neutral temperature and mass density become more pronounced.

In order to evaluate the effects of varying solar cycle on the ETA trough and mechanism, we

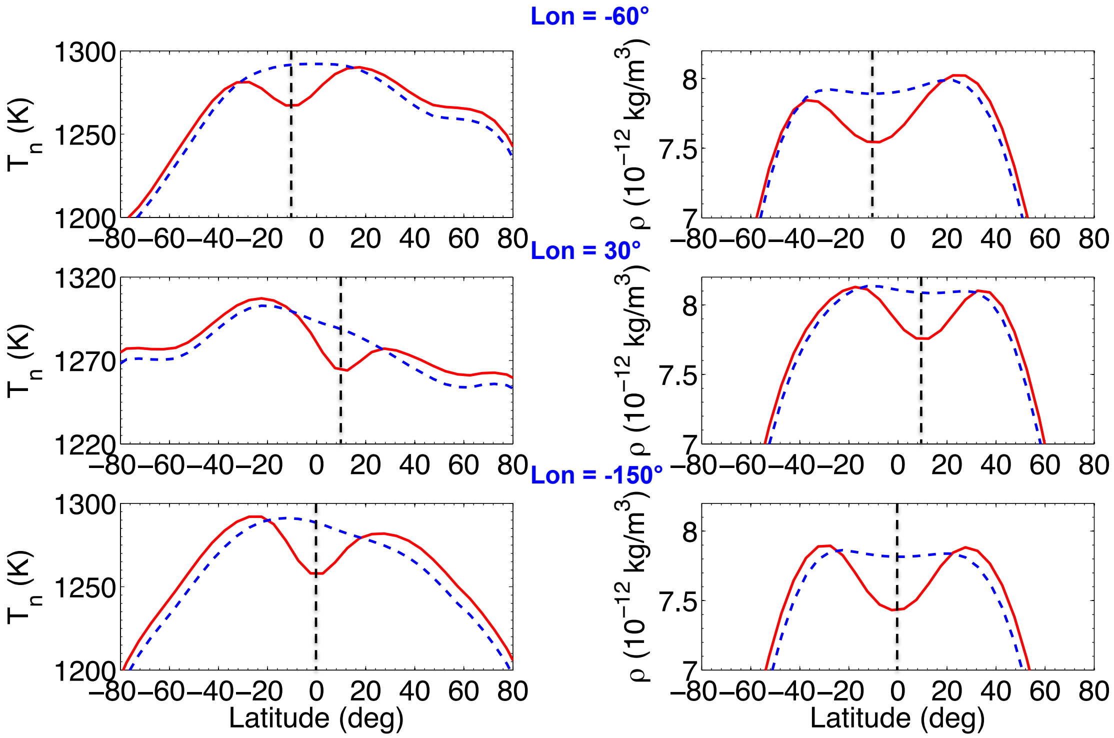

Figure 4.2: Neutral temperatures T_n (left column) and mass densities ρ (right column) as a function of geographic latitude at 400 km and 14:00 LT from run 1 (dashed blue line) and run 2 (solid red line). Shown are three different longitudes: 60°W (first row), 30°E (middle row), and 150°W (bottom row). The dashed black lines represent the dip equators at each of the selected longitudes.

conducted a control (without field-aligned ion drag) simulation and a modified (with field-aligned ion drag) simulation at a low solar activity level, F10.7 = 80, (runs 3 and 4) to compare with runs 1 and 2 at a high solar activity level, F10.7 = 180.

All of the model runs use a geomagnetic field model specified by the International Geomagnetic Reference Field using magnetic apex coordinates [Richmond, 1995b], and the amplitudes and phases of migrating tides (diurnal and semidiurnal) at the lower boundary of the model are specified by the Global Scale Wave Model [Hagan and Forbes, 2002]. The cross polar cap potential is 1 kV and the hemispheric power is 1 GW, representing quiet geomagnetic conditions. The horizontal resolution is set to 5°×5°, the vertical resolution is one-half scale height, and the time step of the simulations is 2 min. Details on the differences between the runs are shown in Table 4.1.

Runs 1 and 2 are used to illustrate the processes involved in forming the neutral temperature

Table 4.1: Description of Model Runs

Run	Type	F10.7
1	Control	180
2	Modified	180
3	Control	80
4	Modified	80

trough of the ETA and its local time variation (sections 4.4.1 and 4.4.2), and runs 1 through 4 are used to study the impact of varying solar cycle on the ETA trough and mechanism (section 4.4.3).

4.4 Results

4.4.1 Mechanism for ETA Trough Formation

Sections 4.4.1.1-4.4.1.4 detail our mechanism for the formation of the ETA neutral temperature trough based on our simulations, and describe the processes denoted in Figure 4.1.

4.4.1.1 Process 1: Field-aligned Ion Drag Force

Figure 4.3b shows the electron density and the meridional component of the field-aligned ion drag as a function of latitude and altitude at 14:00 LT and 150°W, where the magnetic equator lies at a geographic latitude of 0°. At this local time, the EIA is well formed, with downward and poleward diffusive plasma fluxes in the crest regions. These plasma fluxes produce a field-aligned ion drag force, $F_{ni,||}$, that flanks the magnetic equator. Figure 4.3a is a simple illustration of the Earth's geomagnetic field depicting $F_{ni,||}$, and its projection onto the meridional plane, resulting from diffusion of plasma along a magnetic field line. It should be noted that the zonal component of the field-aligned ion drag force is included in the simulation, but it is more than five times less than F_{merid} (the meridional projection of $F_{ni,||}$). Therefore, we will use field-aligned ion drag force and F_{merid} interchangeably hereafter.

It is the evolution of the field-aligned ion drag force - linked to the EIA - and the temporal response of the thermosphere gas that determines the behavior of the ETA trough. The next

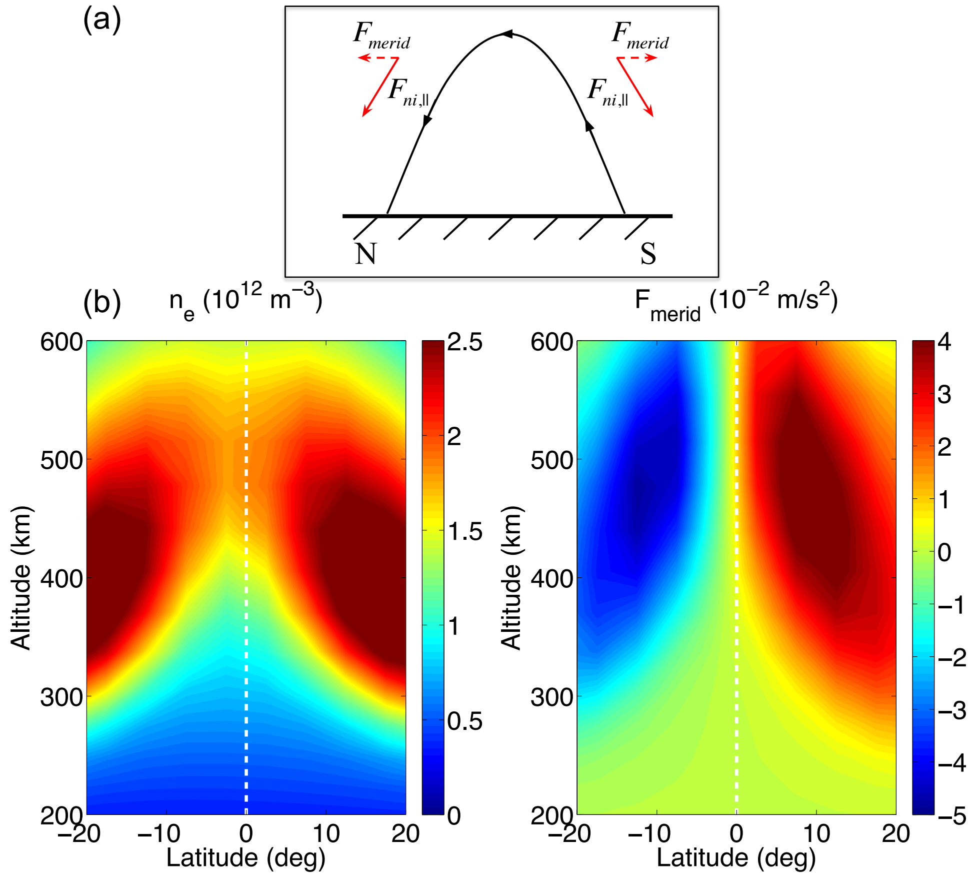

Figure 4.3: (a) Diagram of the first process of the mechanism, showing the meridional component of the field-aligned ion drag, F_{merid}, along with $F_{ni,||}$, and where the black arrowed line represents a magnetic field line and the north and south hemispheres are denoted as N and S, respectively, (b) electron density (left) and F_{merid} (right) from run 2 as a function of geographic latitude and altitude at the longitude 150°W and 14:00 LT, where the white dashed lines represent the magnetic equator at this longitude (around zero degrees geographic latitude). Note that positive values in (b) represent northward direction.

sections, and their associated figures, illustrate the duration of time it takes for processes to set up the ETA trough once the field-aligned ion drag force is initiated in run 2, i.e. on day 20 (day of year 80) at 0:00 UT. Determining this timeline is necessary so that, when evaluating the local time dependencies in section 4.4.2, the ETA processes, including field-aligned ion drag, are well established and the local time effects can be investigated.

4.4.1.2 Process 2: Divergence of Meridional Winds

The poleward meridional component of the field-aligned ion drag force leads to a divergence in meridional winds. Figure 4.4a illustrates the divergence of the meridional winds in response to the introduction of F_{merid}. The top panel of Figure 4.4b shows the temporal evolution of the meridional winds, V_n, from run 1, and the bottom panel of Figure 4.4b is the difference in meridional winds, δV_n, from run 1 to run 2. The magnitudes of V_n from run 1 to run 2 change by approximately 25 m s^{-1} or greater near the EIA crests. The bottom panel of Figure 4.4b demonstrates the difference in temporal evolution in the meridional winds when F_{merid} is introduced at time-zero minutes in run 2 and clearly shows the associated divergence in the meridional winds with peak differences occurring within 20 minutes. It should be noted that although the illustration in Figure 4.4a shows the meridional winds flowing in opposite directions, this configuration is not necessary for a divergence in the winds. A divergence in the meridional winds only requires a gradient in the meridional flow field that has a net flow that is poleward.

4.4.1.3 Process 3: Changes in Vertical Winds, Adiabatic Heating, and Neutral Temperature

The divergence in the meridional winds induces an upwards change in the vertical winds, W_n, from run 1 to run 2 by approximately 4 m s^{-1} around the magnetic equator (top row of Figure 4.5b). It should be noted that the perturbation values in the left column of Figure 4.5b are based on the values in the right column. The model latitudinal resolution is not fine enough to resolve the magnetic equator at 150°W (zero degrees geographic latitude), thus ±2.5° represents the lower and upper latitudinal boundaries of the magnetic equator at the selected longitude. As shown by equation 4.8, a positive change in W_n will produce an increase in adiabatic cooling $\dot{Q}_{adb}$ (middle row of Figure 4.5b). This increase in adiabatic cooling, with a peak value of about 35×10^4 ergs g^{-1} s^{-1} about 20 minutes following the introduction of F_{merid}, will result in a reduction of about 30 K in neutral temperature at the magnetic equator (last row of Figure 4.5b). This neutral temperature

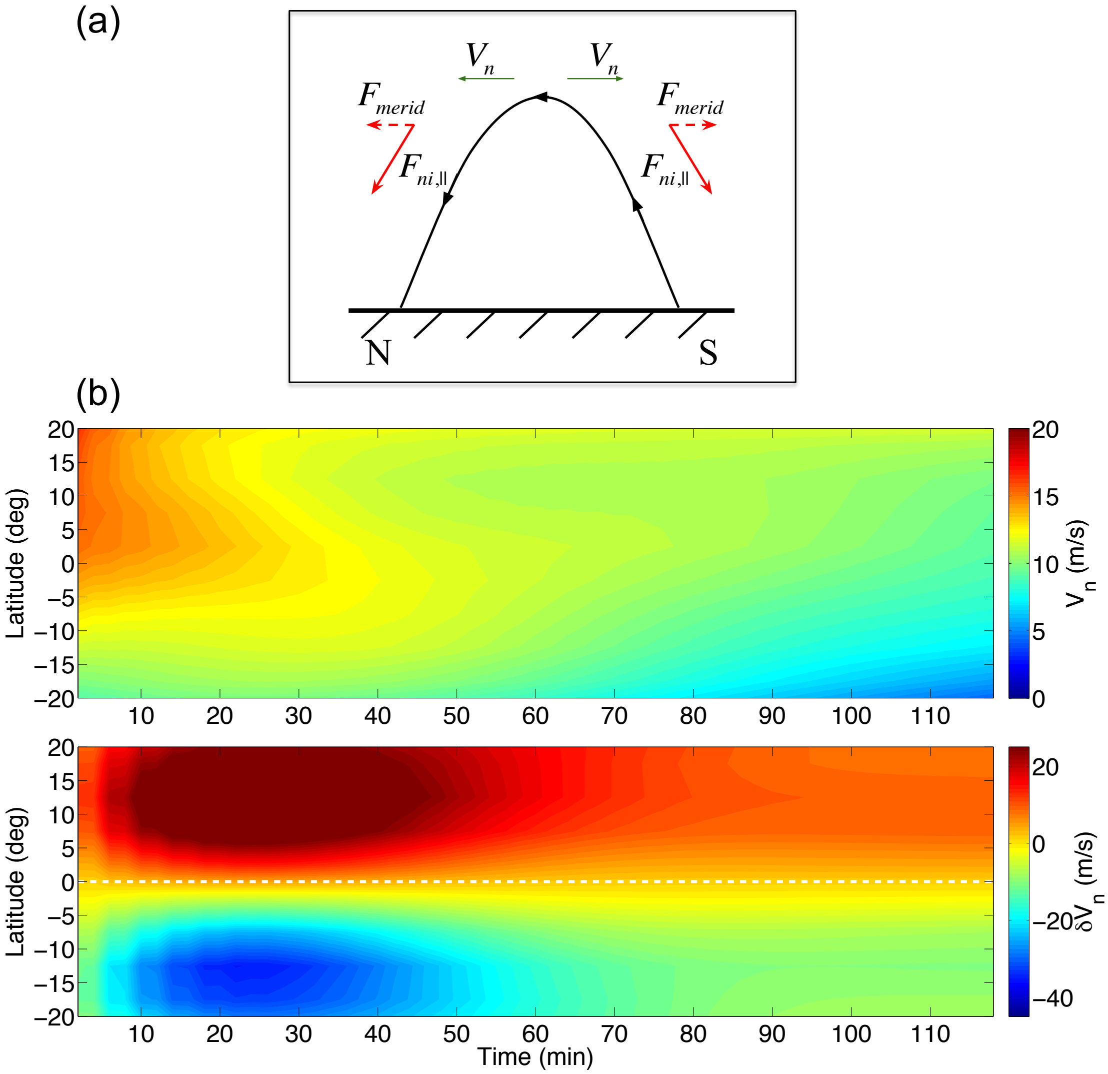

Figure 4.4: (a) Diagram of the second process of the mechanism that is a continuation of Figure 4.3a with the inclusion of the meridional winds V_n, (b) meridional winds from run 1 (top) and the changes in meridional winds δV_n between runs 2 and 1 (bottom) at the longitude 150°W and pressure surface 2.75 (around 400 km) during the first two hours of the model simulations (14:00-16:00 LT), where the white dashed line represents the magnetic equator at this longitude (around zero degrees geographic latitude). Note that positive values in (b) represent northward direction.

cooling will correspond to a trough in the total neutral mass density at a constant altitude per the hydrostatic law.

The individual terms in the energy equation for the neutral gas are heat conduction, heat advection, adiabatic heating/cooling, solar heating, collision heating between thermal electrons,

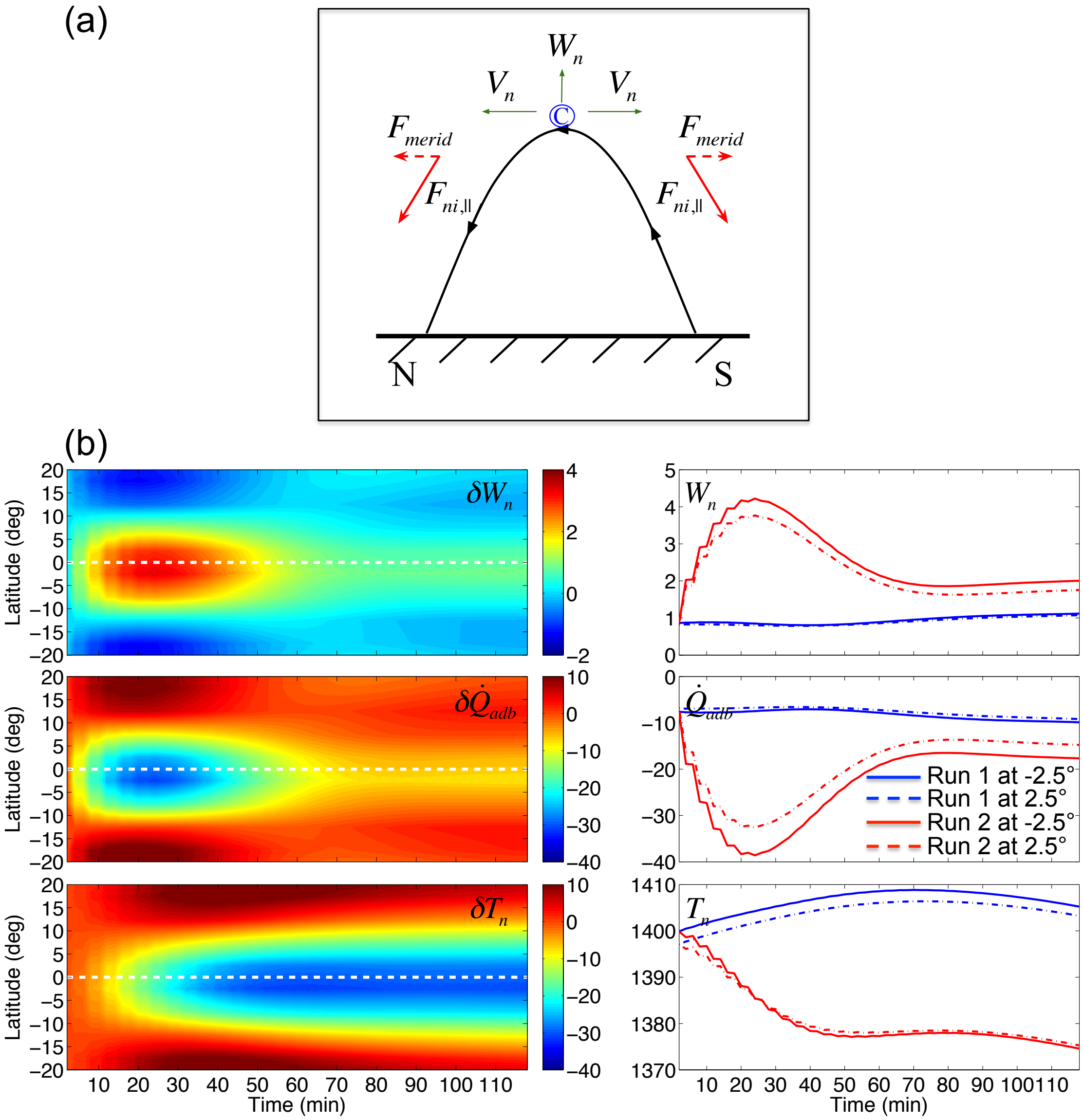

Figure 4.5: (a) Diagram of the third process of the mechanism that is a continuation of Figure 4.4a with the inclusion of the vertical winds W_n and the cooling region around the magnetic equator, (b) the changes in vertical winds (m s^{-1}), adiabatic cooling (10^4 ergs g^{-1} s^{-1}), and neutral temperature (K) between runs 2 and 1 as a function of latitude (left panel), and vertical winds, adiabatic cooling, and neutral temperature at ±2.5° geographic latitude from runs 1 and 2 (right panel), at the longitude 150°W and pressure surface 2.75 (around 400 km) during the first two hours of the model simulations (14:00-16:00 LT), where the white dashed line represents the magnetic equator at this longitude (around zero degrees geographic latitude). Positive vertical winds represent the upward direction.

ions and neutrals, Joule heating, and radiational cooling. Analysis of each term reveals that the most important terms contributing to our mechanism are adiabatic heating and heat conduction

[Lei et al., 2012a]. Because heat conduction acts to efficiently redistribute energy vertically in the upper thermosphere, it is a response to the changes in adiabatic cooling caused by the change in vertical wind. Thus, a 35 × 10^4 ergs g^{-1} s^{-1} change in adiabatic cooling triggers a 8 × 10^4 ergs g^{-1} s^{-1} enhancement in heat conduction in the region of the neutral temperature trough (shown in Appendix B as Fig. B.1).

The sustained neutral temperature trough can be attributed to the fact that the vertical winds do not return to their original state. The vertical winds at the end of the two hour simulation are about 1 m s^{-1} higher than the winds at the beginning of the simulation (represented in Figure 4.6a as δW_n). This 1 m s^{-1} vertical wind difference results in an approximately 10 × 10^4 ergs g^{-1} s^{-1} decrease between the initial and final stages of the simulation (i.e., less adiabatic heating or greater adiabatic cooling), inhibiting the neutral temperature from returning to its original state. During the temporal evolution, $\dot{Q}_{adb}$ is increasingly more negative for the first 20 minutes and then becomes less negative, reaching a roughly constant level in about 60 minutes time. This temporal behavior essentially follows the vertical wind behavior. The change results in a decrease in neutral temperature that by about 60 minutes into the simulation levels off at its new equilibrium but cooler state. The differences in W_n and $\dot{Q}_{adb}$ from the beginning to end of the two hour simulation form the persistent neutral temperature trough signature of the ETA.

4.4.1.4 Process 4: Reactive Pressure Gradient Force

The neutral temperature cooling causes changes in the circulation pattern around the equatorial region, producing an equatorward reactive pressure gradient force (in the meridional direction) that acts to nearly balance the poleward meridional component of the field-aligned ion drag force. Figure 4.6a depicts this approximate force balance along with other processes that are occurring at this time. The top panel of Figure 4.6b illustrates the temporal evolution of the meridional pressure gradient force, $F_{\nabla p}$, from run 1, and the bottom panel of Figure 4.6b is the difference in the meridional pressure gradient force, $\delta F_{\nabla p}$, from run 1 to run 2 over the first two hours after F_{merid} is introduced. The magnitudes of $F_{\nabla p}$ from run 1 to run 2 change by approximately 3 × 10^{-2} m

s^{-2} near the EIA crests, which is roughly equal to the magnitudes of $F_{ni,\parallel}$. However, $F_{\nabla p}$ cannot completely balance the meridional component of the field-aligned ion drag force. It is interesting to note the longer delay in time for the pressure gradient to respond to F_{merid} as the temperature change must occur to initiate the adjustment in the pressure gradient.

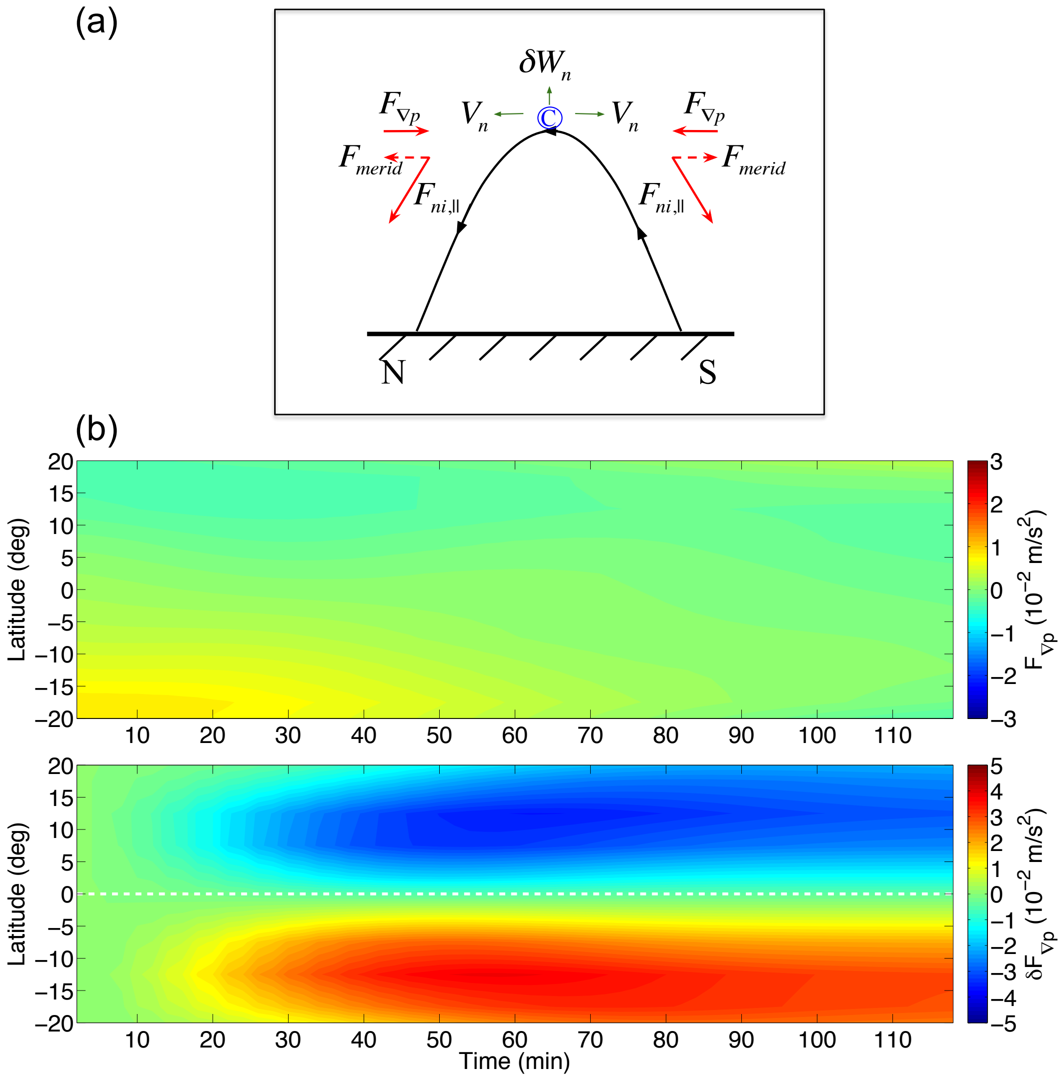

Figure 4.6: (a) Diagram of the fourth process of the mechanism that is a continuation of Figure 4.5a with the inclusion of the reactive pressure gradient force $F_{\nabla p}$, (b) meridional pressure gradient from run 1 (top) and the changes in the meridional pressure gradient $\delta F_{\nabla p}$ between runs 2 and 1 (bottom) at the longitude 150°W and pressure surface 2.75 (around 400 km) during the first two hours of the model simulations (14:00-16:00 LT), where the white dashed line represents the magnetic equator at this longitude (around zero degrees geographic latitude). Note that positive values in Figure 4.6b represent northward direction.

The combined processes produce a mechanism that leads to a new equilibrium state in the thermosphere: a neutral temperature trough at the magnetic equator, a meridional pressure gradient force acting to offset the original ion drag force, and weak upward vertical winds at this local time. Note from the bottom panel of Figure 4.4b, the meridional pressure gradient force does not fully balance the force by field-aligned ion drag, leading to a residual divergent meridional wind pattern that sustains a reduced vertical wind and decreased adiabatic cooling. Thus, the ETA attains a new equilibrium state with a T_n trough near the magnetic equator of about 30 K. We ran the TIEGCM for ten days to confirm that this new equilibrium state is diurnally reproducible. If no other forces disturb the conditions of the thermosphere, then the equilibrium will occur within about an hour or so.

4.4.2 Local Time Variation

The ETA is mainly a daytime phenomenon due to its tight coupling with the EIA, which dissipates rapidly after sunset. Figure 4.7 shows the essential parameters for our ETA trough formation mechanism at pressure surface 2.75 (approximately 400 km) and 150°W during the transition into nighttime (20:00-23:00 LT), when the EIA begins to disappear. In our simulations, when the EIA begins to subside (around 450 minutes after introducing F_{merid}), the processes in our mechanism recede: the meridional component of the field-aligned ion drag approaches zero, followed closely by a reduction in the reactive pressure gradient force, the vertical winds become more downward (approaching their control values from run 1) leading to adiabatic heating, the meridional winds become more convergent, and neutral temperatures in run 2 get warmer (δT_n becomes less negative). Without the field-aligned ion drag forcing on the thermosphere, $\dot{Q}_{adb}$, W_n, V_n, and T_n return to their control values. To further demonstrate this effect, Figure 4.8 shows the same parameters as Figure 4.7 from 1:00-4:00 LT when both the EIA and ETA are gone. As seen in the right panel of Figure 4.8, the deviations between the modified and control values (red and blue lines) are small, signifying the disappearance of the ETA trough at nighttime.

It is worth exploring the local time variations of the ETA trough to test the model's capability

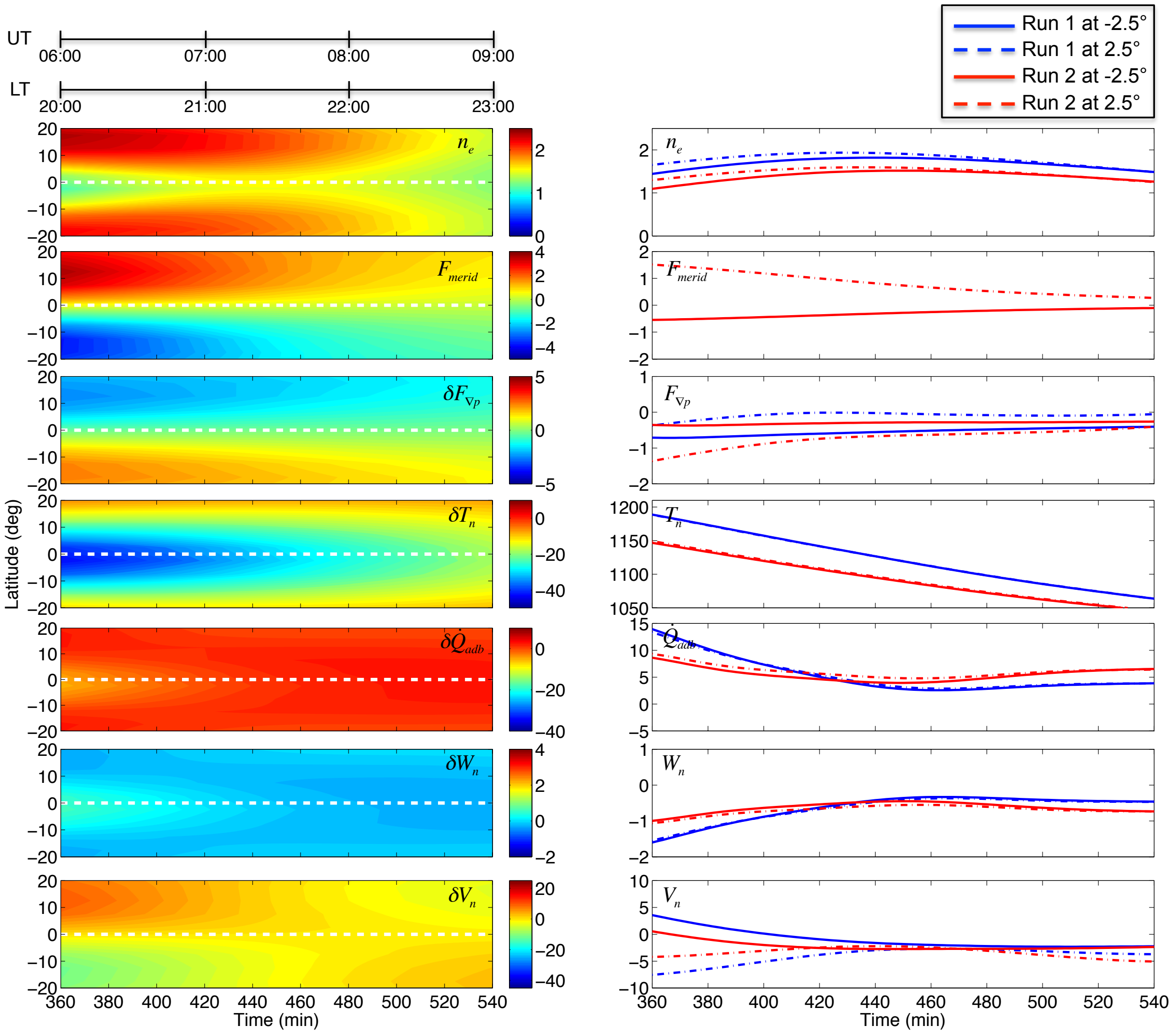

Figure 4.7: Electron density (10^{12} m^{-3}), meridional component of field-aligned ion drag (10^{-2} m s^{-2}), and the changes in pressure gradient force (10^{-2} m s^{-2}), neutral temperature (K), adiabatic cooling (10^4 ergs g^{-1} s^{-1}), vertical winds (m s^{-1}), and meridional winds (m s^{-1}) between runs 2 and 1 as a function of latitude (left panel), and n_e, F_{merid}, $F_{\nabla p}$, T_n, $\dot{Q}_{adb}$, W_n, and V_n at $-2.5°$ and 2.5° geographic latitude from runs 1 and 2 (right panel), at the longitude 150°W and pressure surface 2.75 (around 400 km) during hours 7-10 of the model simulations (20:00-23:00 LT), where the white dashed line represents the magnetic equator at this longitude (around zero degrees geographic latitude). Positive vertical winds represent the upward direction and positive meridional winds represent the northward direction.

to reproduce observed behavior. In the model, the meridional component of the field-aligned ion drag is dependent on the field-aligned ion diffusion velocity and the neutral-ion collision frequency (equation 4.4). From daytime (14:00-20:00 LT) to nighttime (1:00-7:00 LT), $W_{d,\|}$ decreases by about one-third and ν_{ni} reduces by more than an order of magnitude on the flanks of the magnetic

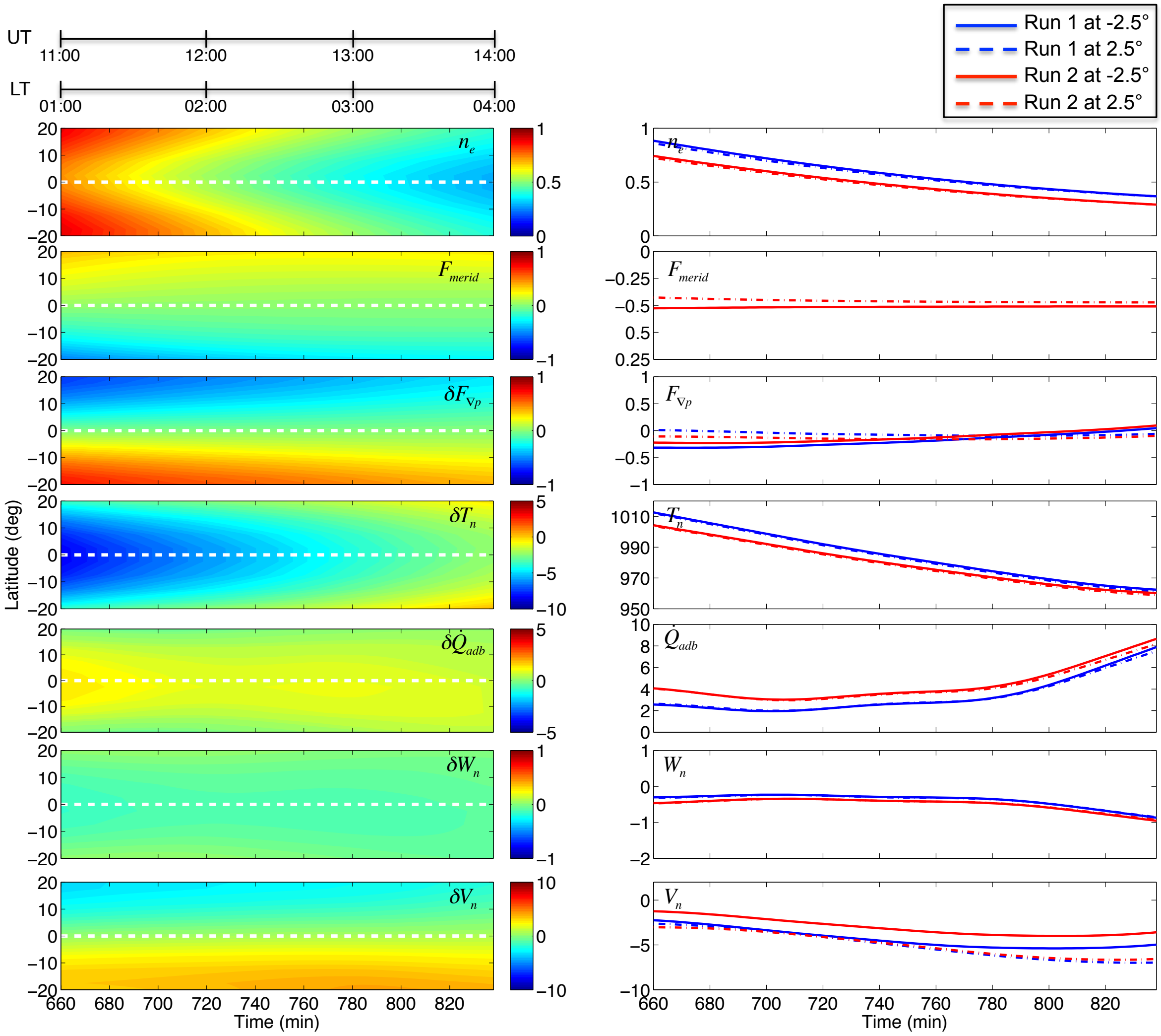

Figure 4.8: Same as Figure 4.7 but during hours 12-15 (1:00-4:00 LT).

equator, as seen in Figure 4.9. This result corresponds well with Figure 4.8, where F_{merid} is substantially reduced at these nighttime hours (it should also be noted that the configuration of F_{merid} cannot produce a divergence in the meridional winds at these hours), thus the neutral-ion collision frequency is the controlling factor for ETA trough behavior when transitioning from day to night. This result is consistent with the decrease in electron density, which causes a decrease in the neutral-ion collision frequency.

In order to assess ETA daytime behavior in our simulations, we dissected the field-aligned ion diffusion velocity with respect to plasma gradients, plasma scale height, and the ambipolar diffusion coefficient (see equation 4.5). It should be noted that the plasma gradients and plasma scale height encompass the items that are in parentheses in equation 4.5. For convenience, this term will be referred to as the plasma term hereafter. Figure 4.9 shows the terms that comprise the field-aligned ion drag and the ion diffusion velocity (neutral-ion collision frequency, ambipolar diffusion coefficient, and the plasma term). This figure also displays the differences in neutral temperature between runs 1 and 2 in order to clearly show the local time variation of the T_n trough. The electron density, plasma term, and ambipolar diffusion coefficient all change from 14:00 to 20:00 LT, but the most significant change is in the plasma term. From Figure 4.9, this term displays a two peak structure where the second peak corresponds with the secondary enhancement of the field-aligned ion drag that occurs around 18:00 LT. Thus the plasma scale height and the gradients in electron number density and plasma temperature are the dominant contributors to the variation of the ETA trough during the daytime.

4.4.3 Solar Cycle Variation

Figure 4.10 illustrates the solar cycle dependency of the ETA produced by the model (all of the runs shown in this figure include field-aligned ion drag). It quantitatively compares neutral temperatures, neutral mass densities, and electron densities for varying solar cycle levels at 400 km and 14:00 LT. From Figure 4.10, it is apparent that the ETA trough becomes more pronounced at higher solar activity levels. This is also observed in data [Liu et al., 2007]. The crest-to-trough differences and the percent changes from the crest values in neutral temperature are approximately 7.1 K and 0.9%, 19.7 K and 1.9%, and 34 K and 2.6% for F10.7 levels of 80, 125, and 180, respectively. The crest-to-trough differences and the percent changes from the crest values in neutral mass density increase from about 0.04 $\times 10^{-12}$ kg m^{-3} and 3.4% for F10.7 = 80 to approximately 0.5 $\times 10^{-12}$ kg m^{-3} and 5.9% for F10.7 = 180. Similar behavior is observed in the EIA structure as seen in the electron densities in Figure 4.10. The EIA becomes more evident at higher solar activity levels, with the crest-to-trough ratio increasing from ~1.06 at F10.7 = 80 to ~2.2 at F10.7 = 180.

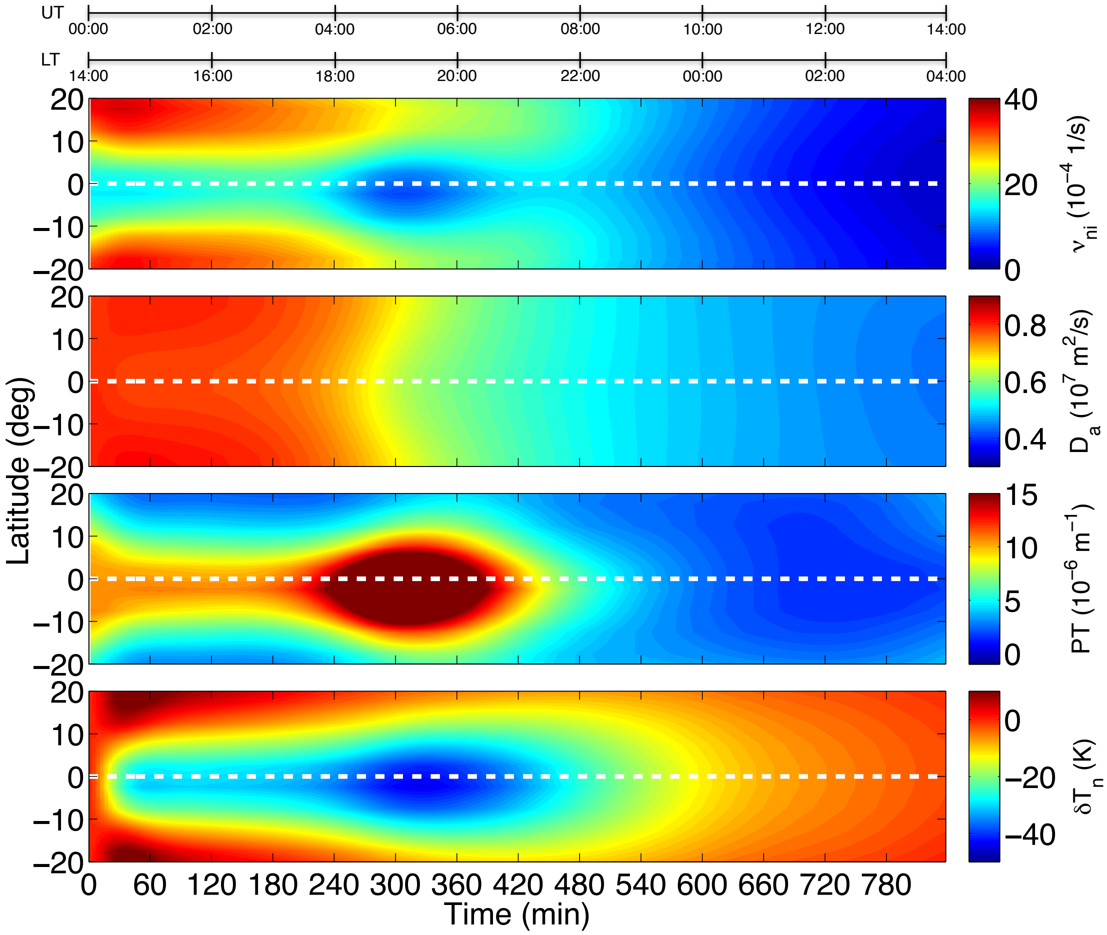

Figure 4.9: Neutral-ion collision frequency (top row), ambipolar diffusion coefficient (second row), and the plasma term, PT (third row) for run 2, and the differences in neutral temperature between runs 1 and 2 (last row) for F10.7 = 180 as a function of latitude at the longitude 150°W and at pressure surface 2.75 (around 400 km) during the first 14 hours of the model simulations (14:00-4:00 LT), where the white dashed line represents the magnetic equator at this longitude (around 0° geographic latitude).

In order to evaluate the effects of varying solar cycle levels on our mechanism, a map of the difference of residuals was constructed (Figure 4.11). The residuals refer to the difference between a modified run and a control run. The difference of residuals is the difference between two different

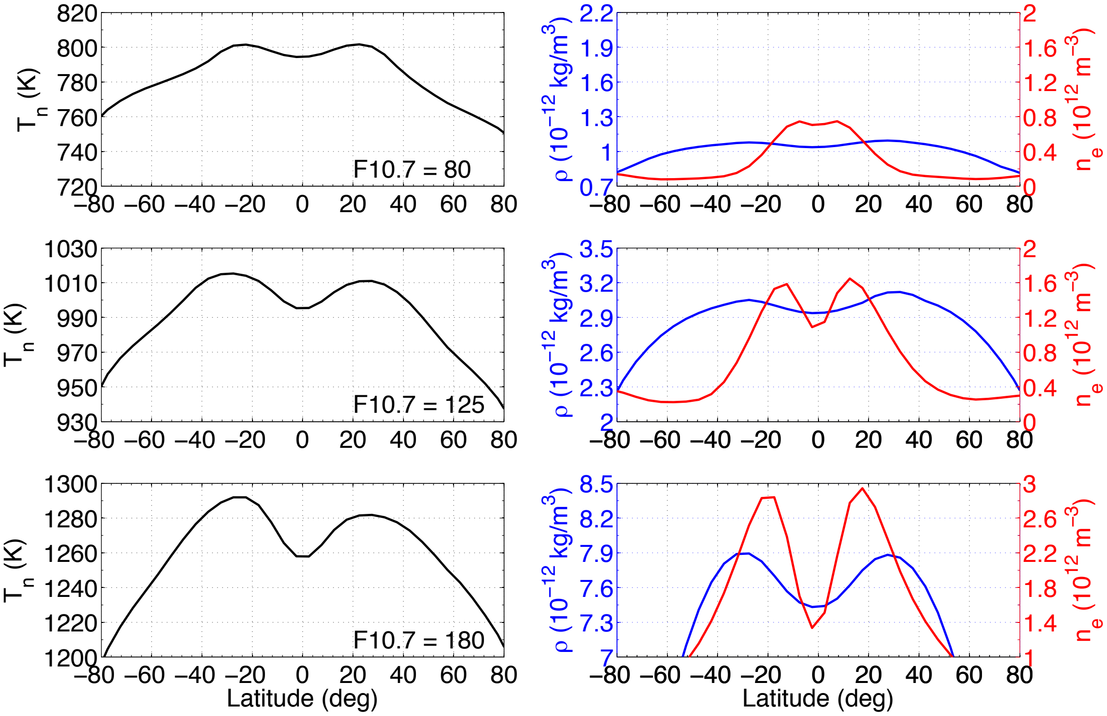

Figure 4.10: Neutral temperatures (left panel) and neutral mass densities and electron densities (right panel) as a function of geographic latitude at 400 km, a longitude of 150°W, and 14:00 LT from runs including field-aligned ion drag. Shown are three different solar cycle levels: F10.7 = 80 (first row), F10.7 = 125 (middle row), and F10.7 = 180 (bottom row).

model runs after the control run has been removed. An example of this is shown below:

$$\begin{aligned} r_1 &= y_{mod,F10.7=180} - y_{ctr,F10.7=180}, \\ r_2 &= y_{mod,F10.7=80} - y_{ctr,F10.7=80}, \\ \Delta\nabla y &= r_1 - r_2, \end{aligned} \tag{4.9}$$

where y represents a parameter in the mechanism. Residual one, r_1, is run 2 minus run 1 (high solar activity with and without field-aligned ion drag, respectively) and residual two, r_2, is run 4 minus run 3 (low solar activity with and without field-aligned ion drag, respectively). The difference of residuals, $\Delta\nabla y$, is residual two subtracted from residual one. Employing this differencing method ensures that the variations we observe in our simulations under the different solar activity levels are due solely to the field-aligned ion drag effect. Figure 4.11 shows that the difference of residuals in the mechanism parameters become distinct almost instantly from the beginning of the simulation and essentially illustrates that the magnitude of the mechanism is greater during high solar activity than at low solar activity. Specifically, the changes from F10.7 = 80 to F10.7 = 180 are (with percent changes from F10.7 = 80 reported): from the differences between runs 2 and 4, (1) the EIA crests are about 2.5 $\times 10^{12}$ m^{-3} larger ($\sim$400% increase), (2) the magnitude of the field-aligned ion drag increases by $\sim$5 $\times 10^{-2}$ m s^{-2} ($\sim$500% increase); and from the difference of residuals, (3) the divergence of the meridional winds is enhanced (the wind magnitudes increase by $\sim$25 m s^{-1}, or by $\sim$250%), (4) the vertical winds experience a more upwards change by $\sim$3 m s^{-1} ($\sim$300% increase), (5) there is more adiabatic cooling by $\sim$30 $\times$ 10^{4} ergs g^{-1} s^{-1} ($\sim$600% decrease), (6) the neutral temperature trough is colder by $\sim$25 K ($\sim$500% reduction), (7) and a $\sim$3 $\times 10^{-2}$ m s^{-2} ($\sim$300%) increase in the magnitude of the reactive pressure gradient force. There is another enhancement in the difference of residuals starting at $\sim$220 min into the simulation, albeit weaker in strength than the initial changes, that deepens the neutral temperature trough difference of residuals to about 50 K. Based on our simulations, our mechanism is augmented as solar cycle levels increase and produces a neutral temperature trough with lower temperatures.

In the case of different solar cycle levels, changes in ν_{ni} and $W_{d,\|}$ are what mainly control the time evolution of the mechanism between F10.7 = 180 and F10.7 = 80. The ν_{ni} on the flanks of the magnetic equator decrease by an order of magnitude from high to low solar activity (see Figures 4.9 and 4.12 and note the different color scales). However, the structure of the variability of the mechanism is also dictated by the plasma term in $W_{d,\|}$. Peaks in the differences in F_{merid} arise at the beginning of the simulation and at approximately 220 min (see Figure 4.11). The plasma term exhibits a two peak structure for F10.7 = 180 (Figure 4.9), while there is only one peak for the term when F10.7 = 80 (Figure 4.12). The first peak extends from the beginning of the simulation to about 120 min for both of the solar cycle levels (the magnitude of the peak for the low solar activity level is smaller than the peak magnitude for the high solar activity level). After 120 min, the plasma term begins to wane for the F10.7 = 80 case, while the term increases to another peak when F10.7 = 180. This second peak in the plasma term for F10.7 = 180 coincides well with the second peak of the difference of residuals in F_{merid}, V_n, W_n, $\dot{Q}_{adb}$, and T_n in Figure

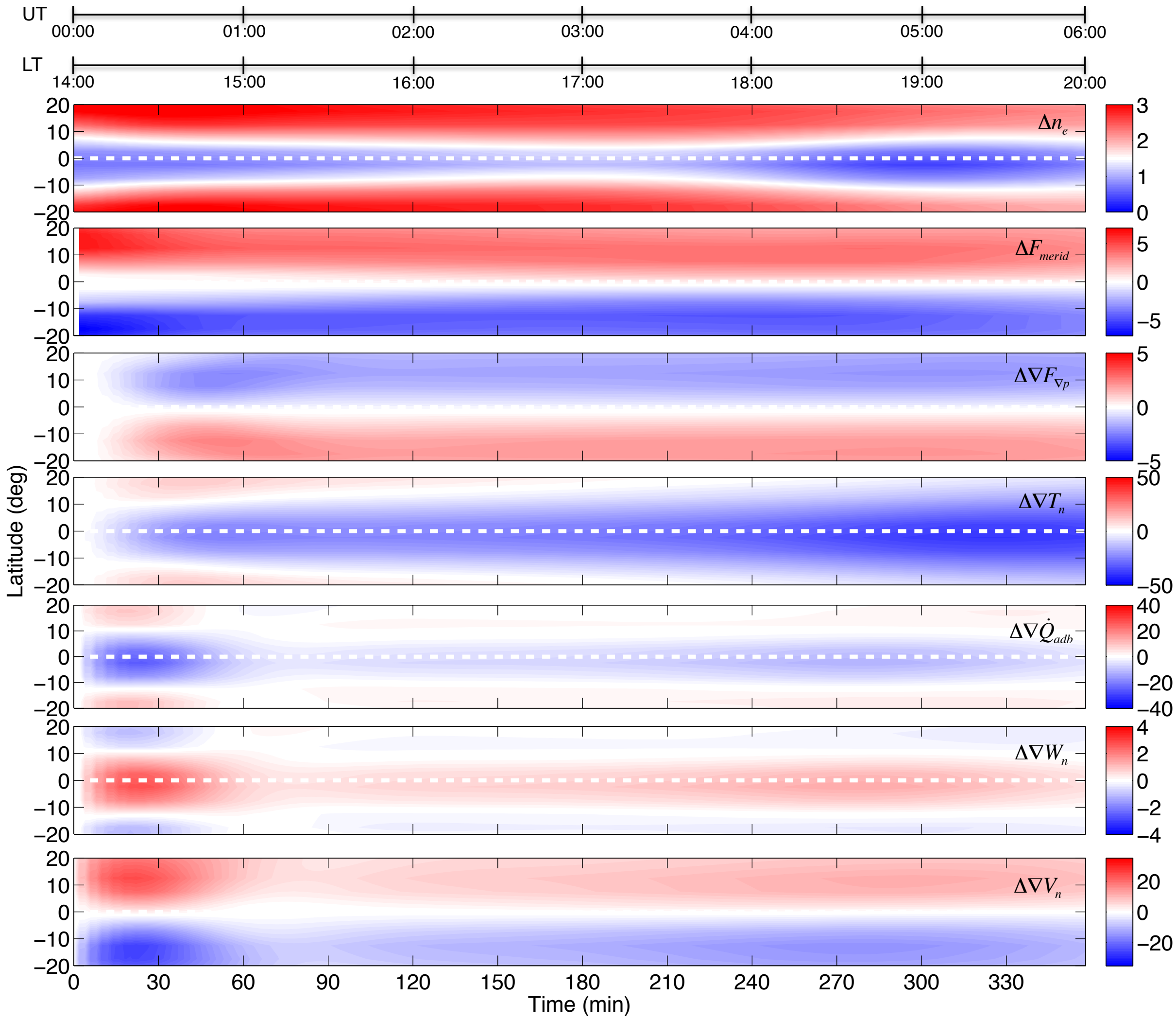

Figure 4.11: Changes in electron density (10^{12} m^{-3}) and the meridional component of field-aligned ion drag (10^{-2} m s^{-2}) between runs 2 and 4, and the difference of residuals (see text for definition) in meridional pressure gradient force (10^{-2} m s^{-2}), neutral temperature (K), adiabatic cooling (10^4 ergs g^{-1} s^{-1}), vertical winds (m s^{-1}), and meridional winds (m s^{-1}) as a function of latitude at the longitude 150°W and pressure surface 5.25 for F10.7 = 80 and pressure surface 2.75 for F10.7 = 180 (around 400 km for both solar activity levels) during the first six hours of the model simulations (14:00-20:00 LT), where the white dashed line represents the magnetic equator at this longitude (around 0° geographic latitude).

4.11. Therefore, the variation of the ETA trough with solar cycle exhibits a secondary structure in local time that depends on solar cycle. From our simulations, variations in the electron density are responsible for the large-scale solar cycle effects of the ETA trough, while plasma gradients and scale height produce a structure in the ETA that is not related to the absolute magnitude of the

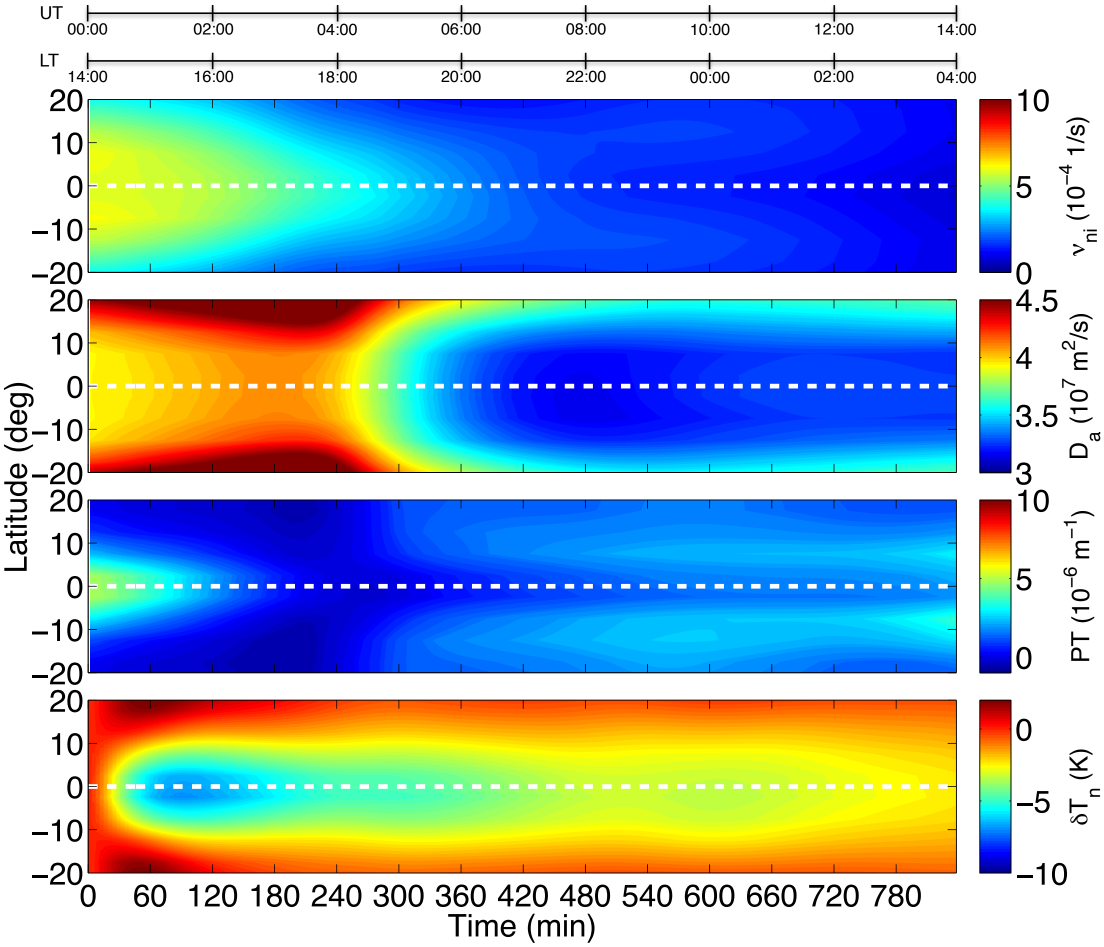

Figure 4.12: Same as Figure 4.9 but for F10.7 = 80 and pressure surface 5.25 (corresponding runs are 3 and 4).

electron density. It should be noted that during solar maximum (F10.7 = 180), the parameters under study are at the F_2 peak, while during solar minimum (F10.7 = 80), they are significantly above the F_2 peak. The potential impact of the altitude variation of the ETA on the solar cycle variation analysis is beyond the scope of this study and will be addressed in future work.

4.5 Discussion

The feasibility of this described mechanism for the formation of the ETA trough based on simulations may be supported through observations. Raghavarao et al. [1991] showed electron density, zonal wind, and neutral temperature from three DE-2 orbits over an altitude range of 280-

600 km. The crest-to-trough neutral temperature differences were approximately 60 K, 110 K, and 44 K for the three orbits. These differences are greater than the crest-to-trough differences from our simulations (see Figures 4.2 and 4.10). However, the conditions during these DE-2 orbits are not the same as the conditions in the model. All of the simulations were conducted at equinox, while the first two DE-2 orbits were at solstice. Furthermore, the electron densities in orbits one and two drop by an order of 2 from the crests to the trough, while the electron density behavior in orbit three aligns better with our simulations, which could be part of the reason why the crest-to-trough neutral temperature difference in DE-2 orbit three matches the closest with our model results.

As the vertical winds have time-varying behavior, it is important to clarify the relationship to observations. On a diurnal time scale, the simulations indicate upward vertical winds during the day and downward vertical winds during the night with a rather rapid transition occurring near the 19:00 LT for this equinoctial simulation. This general structure in the vertical winds is expected because of divergent horizontal motion on the dayside and convergent motion on the nightside under the equinoctial condition. Upon introduction of an additional drag force due to field-line plasma diffusion, the model simulations indicate a time response of the thermosphere on the order of an hour or so where vertical winds are being modified. From the daytime vertical wind plot in Figure 4.5, the inclusion of field-aligned ion drag causes the winds to become more upwards for a short duration (about 60 minutes) and then return to being slightly upwards once all forces have been balanced. The vertical winds serve to couple the momentum forcing with the thermodynamic response and so will vary as conditions change to reach a new equilibrium. The simulations indicate the process fades when transitioning to nighttime conditions where the vertical winds become more downwards. The behavior of downward vertical winds at night is consistent with observations. Raghavarao et al. [1993] reported downward vertical winds around the dip equator at 21:00 LT, and our TIEGCM vertical winds are also downward at this local time. There are substantial differences in the magnitude of the vertical winds estimated from DE-2 observations and the model. However, variability in the vertical winds, instantaneous observations, and the large uncertainty in the DE-2 vertical wind measurements [Raghavarao et al., 1993] make the magnitude differences difficult to compare. Furthermore, vertical winds undergo variations in response to changes in forcing and will also contribute to a thermodynamic feedback response which will further alter the vertical wind behavior. Vertical winds in the thermosphere are a very difficult measurement to make due to their transient nature, and the available data give limited temporal, spatial, and vertical coverage [Larsen and Meriwether, 2012]. Also, satellites are not optimal for monitoring the temporal evolution of a vertical wind field, and measuring small-magnitude winds requires high instrumental stability [Anderson et al., 2012]. In our case, the time evolutions of these small vertical winds are highly variable. Observing these types of winds would require an extremely sensitive instrument with high accuracy and precision that is at the correct locations when the vertical winds are changing.

We compare our local time and solar cycle variation results from our simulations with observations of thermospheric mass density from CHAMP data. Liu et al. [2005] presented the ETA feature in CHAMP data for the year 2002 for geomagnetically quiet and high solar activity conditions between 10:00-20:00 LT, with a substantial abatement in the feature after 20:00 LT. However, the ETA was still discernible from 20:00-23:00 LT. This is consistent with our model results (see Figures 4.7 and 4.8) where the ETA trough is still distinguishable until about 23:00 LT, albeit weaker than the trough in the daytime, but disappears after this time. Raghavarao et al. [1998] found that the ETA was evident during the period 9:30-15:00 LT and 18:00-22:00 LT at solar maximum using DE-2 neutral temperature measurements. Our results show a persistent ETA until about 23:00 LT. A possible reason Raghavarao et al. [1998] saw a weaker ETA from 15:00-18:00 LT could be due to the fact that their data between 14:00-20:00 LT corresponded to the solstice seasons, when the ETA is known to be less prominent [Liu et al., 2007]. They also stated that variations in solar and geomagnetic activity can significantly modulate the local time behavior of the ETA neutral temperature structure. An interesting study done by Liu et al. [2011] reported the appearance of the ETA in the postmidnight sector (1:00 - 6:00 LT) in CHAMP neutral mass densities. Through statistical analysis, they found that the postmidnight ETA was not always accompanied by a postmidnight EIA, and that the occurrence rates of the postmidnight ETA and

EIA exhibit contrasting behaviors with respect to local time, longitudinal, and solar cycle dependencies. The discrepancy between the clear EIA-ETA causal relationship that we describe in the pre-midnight sector that is not apparent in the postmidnight sector could be attributed to the notion that ion drag is not the dominant drag force in postmidnight. Viscous drag strengthens as ion drag weakens, leading to a different wind, temperature, and mass density field. Also, increased wave activity in the postmidnight sector can modify viscosity such that an ETA-like feature exists without the presence of the EIA (e.g., Ma et al. [2010]). This idea is expounded upon in Chapter 5 of this thesis, where it is demonstrated that the quiet-time thermosphere is strongly dependent on the interplay between the ion and viscous drag forces.

Liu et al. [2007] performed a climatological study of the ETA using CHAMP data from 2002-2005. They found that the ETA double-hump structure became more distinct at higher F10.7 levels, and the crest-to-trough neutral mass density difference increased from about 0.1 $\times 10^{-12}$ kg m^{-3} for F10.7 $<$ 100 to over 0.4 $\times 10^{-12}$ kg m^{-3} for 150 $\leq$ F10.7 $\leq$ 200. These crest-to-trough differences match well with our simulations (see section 4.4.3). Liu et al. [2007] also showed poleward movement of the ETA crests with increasing F10.7. We do not see so obvious a trend in our results, but this study is focused on simulating the variations in the ETA trough.

The CINDI instrument on the C/NOFS satellite provides an opportunity to compare our daytime simulations of field-aligned plasma diffusion with ion velocity observations. Burrell et al. [2011] used CINDI data from 2008 and 2009 to study the latitude and local time variations of the field-aligned ion motions near the equator. Only the geographic region between 140° and 250° longitude was considered in this study, thus it can only be compared to Figures 4.3 and 4.5, where the times are 14:00-16:00 LT and $F_{ni,\|}$ is prominent. Burrell et al. [2011] presented field-aligned ion drifts and the field-aligned component of the neutral wind from ±5° magnetic latitude as a function of local solar time and season. From these results, the field-aligned ion diffusion velocity may be extracted since $W_{d,\|}$ is the differential field-aligned velocity between the ions and the neutrals (equation 4.3). Their results indicate that during equinox, the field-aligned ion diffusion velocities are strong with poleward components in both the northern and southern hemispheres. This implies that the field-aligned ion drag will be substantial at these local times because, as equation 4.4 shows, a strong field-aligned ion diffusion velocity will lead to a significant field-aligned ion drag force. These findings agree well with Figure 4.3, where $F_{ni,\|}$ is prominent at 14:00 LT, as well as positive in the northern hemisphere and negative in the southern hemisphere. For the comparison to our simulations, the general nature of the field-aligned ion diffusion velocities is more relevant than the actual values, since the CINDI observations were collected during solar minimum, and our simulation in Figure 4.3 was performed under high solar activity conditions.

In general, the ETA formation and behavior in our simulations is a demonstration of how plasma-neutral interactions can alter the structure of the thermosphere gas. The response of the neutral thermosphere to an ion-drag momentum source has been examined before by Dickinson et al. [1971], where a two-dimensional, steady-state dynamic model was used to assess the interaction of a neutral wind with F-region anomalies of ionization. They found that for anomalies with a horizontal scale of a few hundred kilometers, the momentum source due to a perturbation in ion drag force was almost completely balanced by a perturbation pressure gradient force, and the temperature and circulation responses were negligibly small. For anomalies with a horizontal scale of a few thousand kilometers, the perturbation pressure gradient was not able to fully balance the momentum induced by ion drag, resulting in significant perturbations in horizontal velocity, vertical motion, and temperature field. Dickinson et al. [1971] stated that ion drag causes a perturbation in the horizontal flow, which leads to vertical winds. This generates a distribution of adiabatic warming and cooling that produces perturbation temperatures, resulting in pressures whose horizontal gradients partially balance the perturbation ion drag. This hypothesis from Dickinson et al. [1971] is tested using the TIEGCM and the results are presented in Appendix B. The EIA is a large-scale structure that has a horizontal scale that spans a few thousand kilometers. Our mechanism for the formation of the ETA matches the dynamic and thermal responses described by Dickinson et al. [1971], and it demonstrates that the equatorial thermosphere anomaly is the neutral response to the equatorial ionosphere anomaly.

It is worth mentioning that our modeling study on the formation of the ETA trough cannot refute other possible mechanism, such as the circulation cell theory purported by Raghavarao et al. [1993] and Clemmons et al. [2013]. The dearth of horizontal and vertical wind measurements during the daytime serves as the bottleneck for further verification of modeling studies. The diurnal variation of neutral winds must be established through observations before any mechanism can be thoroughly validated.

4.6 Conclusions

This study expands on the work of Lei et al. [2012b] to fully develop the formation and behavior of the ETA trough in thermosphere neutral temperature and mass density under geomagnetically quiet and March equinox conditions. It is found that the inclusion of field-aligned ion drag into TIEGCM simulations initiates plasma-neutral interactions around the magnetic equatorial region that leads to a series of hydrodynamic processes. Based on these simulations, the field-aligned ion drag creates a divergence in the meridional winds that causes an upwards change in the vertical winds, adiabatic cooling, and a neutral temperature (and mass density) trough over the geomagnetic equator. These changes in the circulation around the equatorial region generate a reactive pressure gradient force that serves to nearly balance the field-aligned ion drag force. The response time of the thermosphere for these simulations corresponding to solar maximum conditions is on the order of 60 minutes, although this will depend on the electron density concentration.

We also investigate the coupling between the EIA and the ETA through local time and solar cycle variations under March equinox conditions. It is found that when the EIA begins to disappear in the evening, the ETA formation process recedes. When the EIA is completely gone, the ETA trough is also absent, and the thermospheric parameters critical to this study (i.e. neutral winds, temperature, and adiabatic heating) return to their control values. In our simulations, the ETA trough becomes more evident at higher solar activity levels, where at 14:00 LT and 400 km, the crest-to-trough difference in neutral temperature increases from 7.1 K at F10.7 = 80 to 34 K for F10.7 = 180 (or 0.9% to 2.6% changes from crest values), and the crest-to-trough difference in thermosphere mass density changes from 0.04 $\times 10^{-12}$ kg m^{-3} to 0.5 $\times 10^{-12}$

kg m^{-3} (or 3.4% to 5.9% changes from crest values) for the same enhancement in solar activity. These results match fairly well with observations. It was found in our simulations that the day-to-night variations in local time and differences in solar cycle are mainly dependent on the neutral-ion collision frequency, which is proportional to electron density concentrations, with secondary structure of ETA behavior associated with plasma scale height and gradients in electron density and plasma temperature. Implementing field-aligned ion drag into the model enables the simulation of the ETA feature in neutral temperature and mass density, elucidates the dynamic and thermal processes that occur during its formation, reproduces the local time and solar cycle behavior, and indicates that the equatorial ionosphere anomaly produces a phenomenon in the neutral atmosphere that is the equatorial thermosphere anomaly.

As mentioned previously in this chapter, a disconnected link between the EIA and the ETA in the postmidnight sector has been published in the literature. The following chapter may yield clues as to why this non-correlation can occur by exploring the complex interplay between neutral drag forces, and its ensuing effects on the quiet-time thermosphere.

Chapter 5

The Complex Interplay between Drag Forces and its Thermospheric Consequences

Chapter 4 alluded to an inconsistency in the cause-and-effect relationship between the EIA and the ETA, indicating that in certain conditions, ion drag is not necessary for the formation of the ETA. This discrepancy could potentially originate from the complex interplay between neutral drag forces, ion and viscous, in the upper thermosphere. The prospect of viscous drag playing a central role in contributing to the development of upper atmospheric features has been acknowledged (as mentioned in Section 1.5.2), but the depth of insight on this topic is inadequate. The goal of this chapter is to answer science questions 2a-2c, where the TIEGCM is used to evaluate drag forces as modifiers of global wind and temperature structure in the upper thermosphere. The new science accomplished from this study is as follows:

(1) The effects of ion and viscous drag on the upper thermosphere system are isolated and shed new light on the relative roles of these forces in neutral dynamics and energetics, leading to results that are unexpected and that have not been reported in previous studies.

(2) Exploiting the coupling of the TIEGCM, it is discovered that ion and viscous drag forces lead to sustained divergent winds, adjustments in mass, modification of pressure gradients, and a redistribution of the radiatively-forced thermal energy.

The interplay between the relative magnitudes of the ion and viscous drag forces and its effect on the ionosphere-thermosphere system has not yet been addressed, and results in diverse behavior in the neutral wind and temperature structures of the upper atmosphere, dependent upon the type of drag acting on the gas. It is found that viscous drag is more efficient in causing cooling on the dayside thermosphere and heating on the nightside than the ion drag force in solar maximum and under quiet geomagnetic activity, resulting in a 150 K day-night temperature difference. The ion drag force inhibits the effective day-to-night energy circulation, culminating in a dynamically induced difference of about 400 K in the day-night temperature difference. It is demonstrated that the resultant wind and thermal structure greatly depends on the type of drag force environment, and a mechanism is introduced whereby ion and viscous drag forces can alter the energy budget of the upper thermosphere system. For example, in solar minimum, viscous drag is significant relative to other forces, leading to a circulation system that more effectively cools the dayside and warms the nightside, thereby reducing the day-night temperature gradient. This chapter expands on the results in the JGR: Space Physics journal article by Hsu et al. [2016]. Note that the runs and run numbers are unique to the chapter, and that all notation will be explained in the text. Supplemental figures and analysis are located in Appendix C.

5.1 Introduction

Neutral mass density is a critical parameter for satellite drag specification and prediction, and it is highly sensitive to exospheric temperatures due to the integrated effect of scale height with altitude. Emmert et al. [2014] showed that a relative exospheric temperature error of 1% could cause up to 8% relative error in neutral mass density near 400 km in altitude. Better understanding of the thermal structure in the upper thermosphere will lead to reduced errors in neutral mass density and proper assessment of atmospheric drag effects on the low-Earth orbit population.

Much work has been focused on explaining the thermal structure of the upper atmosphere by quantifying and specifying external energy sources that directly heat the neutral gas. However, the strong connection between thermosphere momentum and energy enables internal processes to influence its final thermal structure. This study addresses how prominent forces in the upper thermosphere, ion drag and viscous drag, can lead to significant neutral wind and temperature changes. A copious amount of work (for example, Prölss [1980], Knipp et al. [2004], Deng et al. [2008], Burke [2011], Weimer et al. [2011], Prölss [2011] and the literature therein, Clausen et al. [2014], and Chen et al. [2014]) has focused on the response of the thermosphere when driven by energy input from the magnetosphere, but less attention has been paid to the thermal structure produced by the thermosphere response to changes in momentum. A seminal study done by Mayr and Harris [1978] was one of the first to compare the effects of momentum versus energy processes on the neutral circulation patterns in the Earth's ionosphere-thermosphere (I/T) region. Although the heuristic descriptions given by Mayr and Harris [1978] to explain the neutral temperature changes due to wind circulation and direct energy inputs are limited, the key implication of their study is that the thermal signatures of a direct energy source versus a wind-driven mechanism are different. Here, it will be shown that drag forces, ion or viscous, can produce balanced motion with sustained divergent flow that can either heat or cool the thermosphere depending on the structure of the momentum forcing. It should be noted that momentum and energy are completely separate physical entities and they do not interact with each other. However, terms in the momentum equation can affect terms in the energy equation through dynamics.

Studies utilizing CHAllenging Mini Payload (CHAMP) accelerometer measurements have demonstrated a plethora of unexplained neutral mass density variations in the upper thermosphere [Liu et al., 2005; Schlegel et al., 2005; Kervalishvili and Lühr, 2013]. As intricate I/T models attempt to simulate the observed neutral mass density features, an accurate specification of localized drag forces may prove important in unraveling the formation mechanisms of these space weather phenomena. Evidence of momentum coupling influencing the thermal structure of the thermosphere can be found in recent modeling studies by Maruyama et al. [2003], Lei et al. [2012b], and Hsu et al. [2014]. These studies raised the importance of field-aligned ion drag, a momentum source, in contributing to the observed mass density equatorial thermosphere anomaly in I/T general circulation models. Although this work will focus on the global, large-scale impact of drag forces on the upper thermosphere, the outcomes may scale to help explain smaller-scale neutral density variations.

Previous studies have discussed the influence of the convective ion drag force in the high-latitude upper thermosphere as a driver of wind and temperature vortices [Roble et al., 1982], and as a generator of gyres that lead to thermal and density cell structure (Walterscheid and Crowley [2015], and references therein). The analysis in Walterscheid and Crowley [2015] addresses atmospheric adjustments to bring the largely rotational wind system into a new balanced state, which is presumed to be a gradient wind balance, where inertial forces (Coriolis and centrifugal) and pressure gradient forces are predominant. A secondary circulation is initiated when these forces are not balanced, leading to thermal and mass density cell structure. Although this may be appropriate for studying thermospheric gyres, a gradient wind balance, or the more approximate geostrophic wind balance and its associated adjustment is, in general, not appropriate for describing upper thermosphere motion due to the persistent influence of drag forces. Walterscheid and Crowley [2015] demonstrated that rotational motion can cause neutral temperature variation. This study will establish how divergent motion can influence upper thermospheric temperatures. In particular, it aims to analyze the role of drag forces, ion and viscous drag, in generating ageostrophic flow in the upper thermosphere, leading to a new balanced state with sustained, divergent motion that alters the thermal structure.

With increasing sophistication of numerical models, the underlying physics can become buried beneath the complexities. The purpose of this study is not to validate an I/T model. Instead, our goal is to exploit the flexibility and modularity of a comprehensive model in order to understand the physics in this region on a fundamental level. The ion drag force in I/T models is largely controlled by electron density, while viscous drag is highly dependent on the kinematic viscosity coefficient. The accuracy of these parameters varies widely in models, and their associated uncertainties can lead to significant error in neutral winds and temperatures. The notion that ion drag is important in the upper thermosphere is certain. However, the role of viscous drag and its interplay with ion drag in this region has not been fully described. This work will demonstrate that the relationship between these two drag forces contributes greatly to shape the upper atmosphere during geomagnetically-quiet periods, emphasizing the need for proper descriptions of these momentum forcings in I/T models.

5.2 Numerical Experiments

The model used in this study, the TIEGCM, is comprehensively described in Chapter 3 and by Qian et al. [2014] (reference also includes some validation examples and literature for TIEGCM model-data comparison studies). In order to assess the impact of drag forces, ion and viscous, on upper thermospheric properties, two runs were performed for this study: one without ion drag (run 1) and one with ion drag (run 2). The ion drag term in these model runs is complete in that it includes both of the components parallel and perpendicular to the magnetic field. The ion drag force per unit mass can be written as:

$$\mathbf{F}_{ni} = -\nu_{ni}\mathbf{u}_n + \nu_{ni}\mathbf{u}_i, \tag{5.1}$$

where ν_{ni} is the neutral-ion collision frequency, $\mathbf{u}_n$ is neutral wind velocity, and $\mathbf{u}_i$ is ion velocity. This term is isolated in the model and either turned off (run 1) or on (run 2). Turned off means the ion drag force (Eq. 5.1) was not included in the neutral momentum equation in the model, but all other forcing terms and energy processes are specified in the same manner as the default TIEGCM. Neglecting the ion drag force in the neutral momentum equation does not affect the horizontal ion momentum equation at these F-region altitudes due to the high mobility (ratio of gyrofrequency to collision frequency) of the ions, i.e. the ions are not influenced by the neutrals and mainly drift in the $E \times B$ direction. Plasma motion along field lines can be affected by meridional winds, causing variations in electron density. Although this process is included in the model, it seems to have a secondary effect on neutral behavior in the upper thermosphere. Vertical viscosity per unit mass is represented as:

$$\mathbf{F}_{vis} = \frac{1}{\rho}\frac{\partial}{\partial z}\left(\mu\frac{\partial \mathbf{u}_{n,h}}{\partial z}\right), \tag{5.2}$$

where ρ is the neutral mass density, μ is the viscosity coefficient (molecular and eddy), $\mathbf{u}_{n,h}$ is the horizontal neutral wind velocity, z is the vertical coordinate, and μ/ρ is the kinematic viscosity coefficient. Only the vertical flux of horizontal momentum is important in the thermosphere due to the dominance of vertical gradients over horizontal gradients [Richmond, 1983]. The numerical experiment setup allows for the separation of ion drag and viscous effects on the upper thermosphere, where run 1 delineates the influence of viscous drag and run 2, combined with the analysis of run 1, elucidates the consequences of ion drag.

The simulations ran for 20 days to allow them to reach their diurnally reproducible states. The numerical experiments were conducted under high solar activity (F10.7 = 180), very low geomagnetic activity levels (auroral hemispheric power of 1 GW and a cross polar cap potential of 1 kV - effectively eliminating auroral precipitation and ion convection), and March equinox conditions (day of year 80 in 2002). All of the model runs use a geomagnetic field specified by the International Geomagnetic Reference Field using magnetic apex coordinates [Richmond, 1995b], and the amplitudes and phases of migrating tides at the lower boundary of the model are specified by the Global Scale Wave Model [Hagan and Forbes, 2002]. The TIEGCM horizontal resolution is set to 5°×5°, the vertical resolution is one-half scale height, and the time step is 2 min.

It should be noted that all of the runs in this study have the frictional heating term (essentially Joule heating) in the energy equation turned off. This is necessary in order to observe the effects of drag on the thermal structure. In fact, in the manner by which these simulations are performed, the frictional heating term would be the overwhelming energy term in run 1. This is not a physical result but more an artifact of ignoring ion drag. Since this study is primarily concerned with evaluating the thermal effects due to ion and viscous drag forces, frictional heating is omitted from the simulations. A similar approach was taken by Walterscheid and Crowley [2015] in their simulations of thermosphere gyre behavior.

5.3 Analysis and Results

Any drag force, ion or viscous, can alter the thermal structure of the thermosphere system through its influence in producing divergent neutral winds. For ion drag, ions exchange momentum with the neutral winds through collisions, causing divergence in the wind field. As shown by Thayer and Killeen [1993], the momentum equation can be written in terms of vorticity and divergence equations, and the Pedersen component of the ion drag force can play an important role in the divergence equation of the upper thermosphere. For viscous drag, vertical shears in the horizontal wind transfer momentum vertically and, with an exponentially increasing kinematic viscosity coefficient, it becomes a significant force in the upper atmosphere. These drag forces cause divergent motion in the upper thermosphere. The modified divergent wind patterns redistribute mass leading to changes in the vertical winds to ensure mass continuity is maintained. The upward or downward vertical winds couple to the energy equation through adiabatic heating or cooling, resulting in adjustments to the internal energy of the system. This evolutionary process leads to a new thermospheric diurnally reproducible balanced state with secondary circulation and sustained divergent flow. It is important to note that ion drag can be a driving force under the influence of an electric field, while viscous drag is always a responsive force in the momentum equation.

The two different diurnally reproducible states, described in terms of neutral temperature and horizontal wind, resulting from excluding and including ion drag in the simulations are illustrated in Fig. 5.1 for solar maximum conditions. All figures are at UT = 0.0 hr and pressure level 3.25

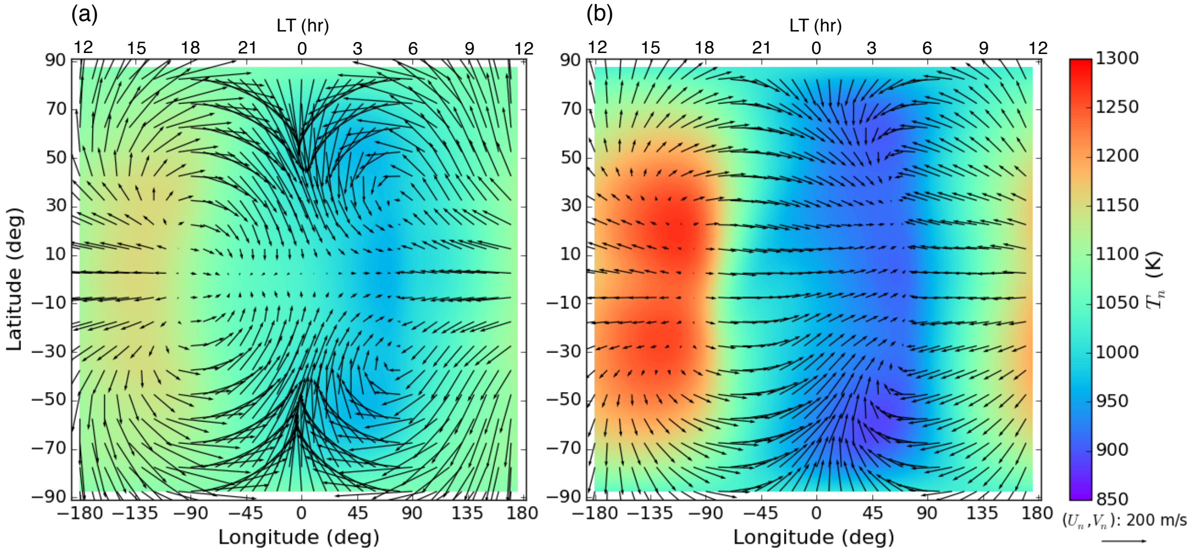

Figure 5.1: Neutral temperature T_n and horizontal wind vectors (U_n, V_n) as a function of latitude and local time (a) without ion drag (run 1), and (b) with ion drag (run 2) under solar maximum conditions at UT = 0.0 hr and pressure level 3.25 (∼400 km). Note local time as the top axis.

(∼400 km). A pressure level that corresponds to ∼400 km is chosen due to the abundance of thermospheric neutral mass density features that have been observed around this altitude with uncertain root causes. In order to assess the main drivers of horizontal wind variability in Fig. 5.1, the dominant forces in the upper thermosphere system are evaluated. A term analysis for each run was conducted on the TIEGCM neutral momentum equation once the runs reached their new balanced states. The major forces when excluding ion drag (run 1) are the pressure gradient force, Coriolis force, and the viscous drag force. With the inclusion of the ion drag force in the simulation (run 2), the Coriolis and viscous drag forces are markedly decreased in their relative magnitudes, and ion drag and pressure gradients become the predominant forces, a result that is consistent with the force balances displayed in Killeen and Roble [1984]. It should be noted that the relative forces could be different during the evolution to this diurnally reproducible state.

Key differences between Fig. 5.1a and Fig. 5.1b are in the magnitudes/structures of the wind and temperature fields. The magnitudes of the horizontal winds are about twice as strong for run 1 than run 2, with maximum winds of about 300 m s^{-1} in run 1 and 150 m s^{-1} in run 2. Because there is no ion drag in run 1, the neutral winds are primarily a balance between the pressure gradient, Coriolis, and viscous drag forces. Without the drag induced by the ions, neutral winds are greater in magnitude. The wind streamlines in Fig. 5.1a are also more curved than the winds in Fig. 5.1b. This effect is due to the Coriolis force, which becomes a dominant contributor when ion drag is neglected and the wind speed is relatively large. Thus, the neutrals in Fig. 5.1a experience more deflection from the Coriolis force when they do not feel the presence of the ions.

On a global scale, the day-night neutral temperature features are more accentuated in run 2 than in run 1, going from a 150 K day-night differential to as much as a 400 K differential. A term analysis was performed on the TIEGCM energy equation for both runs, and the relative importance of the energy terms in each run is shown in Figs. 5.2 and 5.3. Note that the labels in these figures correspond to the terms in Eq. 3.15. It was determined that solar radiation, adiabatic heating/cooling, and heat conduction are the main contributors to the thermal structure, with vertical heat conduction responding to vertical temperature gradients produced by the adiabatic heating/cooling term (collisional heating due to electron-neutral and electron-ion collisions can also be relevant in certain regions). It should be noted that the relative heat terms could be different during the evolutionary process, but this study is only concerned with the diurnally reproducible states of the neutral properties. The mean global temperature between runs 1 and 2 is the same, i.e. run 1 and run 2 have the same amount of energy, but the energy is distributed differently between the runs. The energy in run 1 is allocated relatively uniformly, while the energy in run 2 is more confined to localized regions, creating higher temperatures on the dayside, lower temperatures at night, and more significant neutral temperature anomalies. For example, the twin crest and trough structure of the equatorial thermosphere temperature anomaly is seen in the daytime thermosphere in Fig. 5.1b (run 2) but not in Fig. 5.1a (run 1). Also, nighttime low-temperature regions appear to form near the poles when ion drag is included in the simulation. Without ion drag, the thermosphere efficiently balances energy generated on the dayside solar heating region and the nightside IR cooling region via the adiabatic term enhanced by divergent winds caused by viscous drag, as will be shown below. When ion drag is included, the magnitude of divergence diminishes and the adiabatic term is less effective in offsetting solar radiation heating/cooling on the dayside/nightside, leading to large day-to-night temperature gradients. Thus, a more horizontally-structured upper thermosphere temperature distribution with greater day-to-night temperature differences is generated when ion drag is active in the model.

Figures 5.4 and 5.5 highlight the interdependence of viscous drag to the strength of the ion drag force. Without ion drag (run 1), viscous drag is high and wind and temperature effects are primarily governed by viscous drag and pressure gradients at mid-to-low latitudes (the Coriolis force becomes important at higher latitudes). However, when ion drag is dominant in a diurnally reproducible state (run 2), viscous drag is relatively low and neutral dynamics and thermal structure are largely regulated by the ion drag force and the pressure gradient force.

With the principal forces in the momentum equation known, the behavior of the horizontal winds can be dissected. The modeled winds can be separated into two parts: the geostrophic and ageostrophic components, or $\mathbf{V}_g$ and $\mathbf{V}_{ag}$, respectively. Geostrophic winds satisfy the horizontal

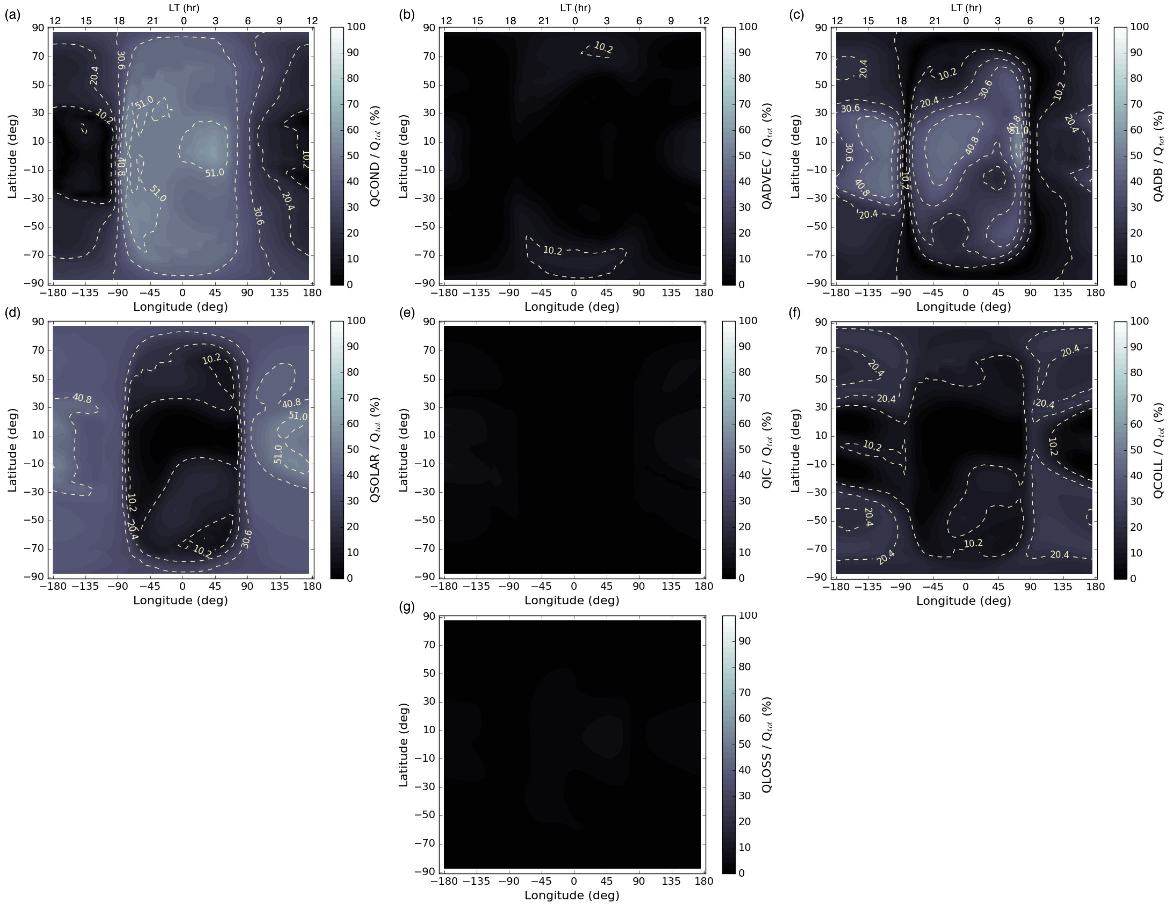

Figure 5.2: Relative percentage of heat terms to the total energy in run 1 for (a) conduction, (b) advection (horizontal and vertical), (c) adiabatic heating and cooling, (d) solar radiation, (e) ion chemical heating, (f) collisional heating, and (g) radiational cooling.

divergence-free condition on a constant pressure surface at a particular latitude, and are computed using geopotentials, Φ, and the Coriolis parameter, f, where $\mathbf{V}_g = \frac{\mathbf{k}}{f} \times \nabla_p \Phi$ ($\mathbf{k}$ is the unit vector of the vertical coordinate, ∇_p is the horizontal gradient operator on an isobaric surface, and $-\nabla_p \Phi$ is the pressure gradient force). By definition, the geostrophic wind represents the wind field resulting from the sole balance between pressure gradient and Coriolis forces. The ageostrophic wind represents the residual wind component necessary to produce the total wind field when combined with the geostrophic component. Clearly, a wind field dominated by pressure and Coriolis forces would have little ageostrophic flow.

Figure 5.6a shows the ageostrophic wind components for run 1, without ion drag. This

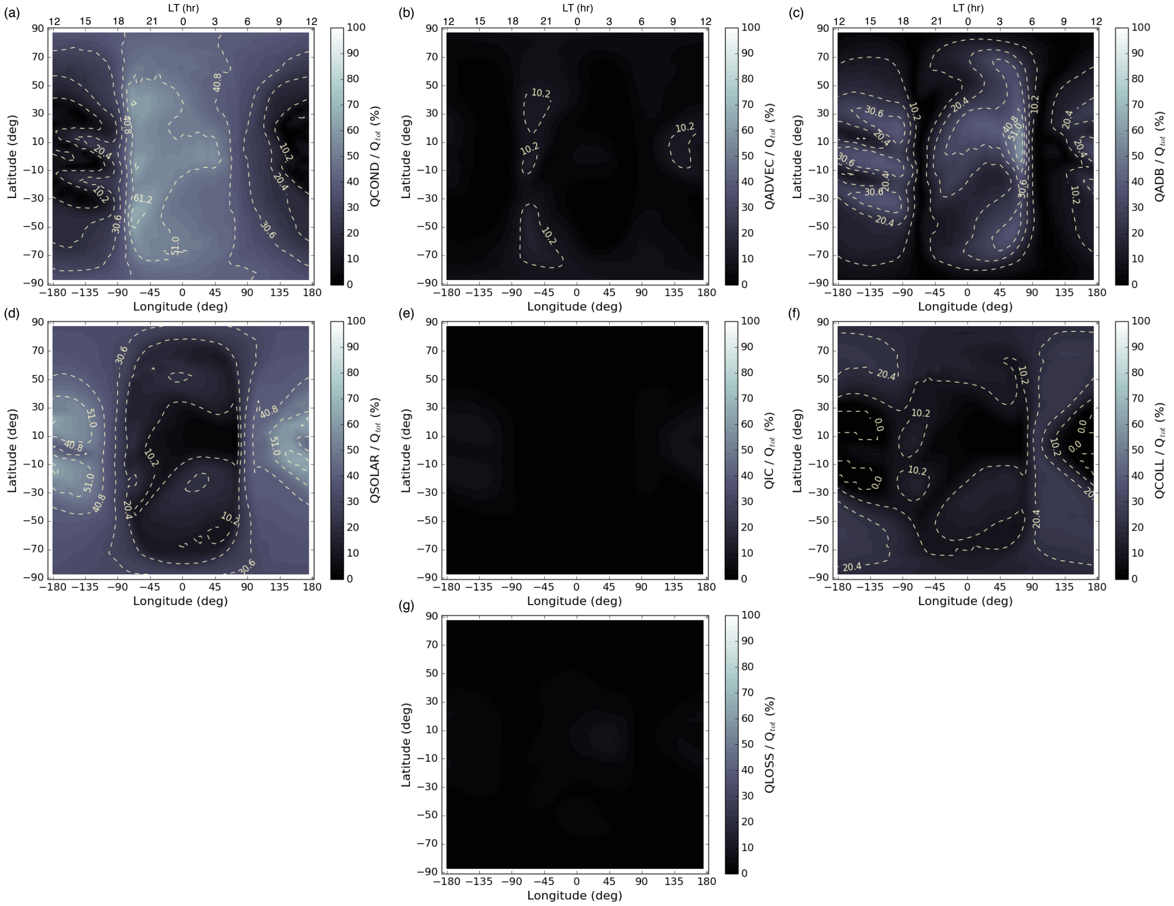

Figure 5.3: Same as Fig. 5.2 but for run 2.

vector field demonstrates the large deviations from geostrophy. Figure 5.6b is a vector illustration of geostrophic balance (the pressure gradient force and the Coriolis force are equal and opposite) in the northern hemisphere. This configuration does not exist in the upper thermosphere due to the importance of drag forces (viscous or ion drag) in this region. When pressure gradient and Coriolis are in control, vertical shears in the horizontal wind arise. This is a natural consequence of geostrophic flow, which is a common assumption in the lower atmosphere. However, geostrophy is never realized in the upper thermosphere because of the exponential increase with height of the kinematic viscosity coefficient and the presence of geostrophic vertical shears. Viscous drag then becomes an important term in the upper thermosphere momentum equation acting to reduce vertical shears in the neutral wind for run 1. Also, with little high-latitude convective forcing in

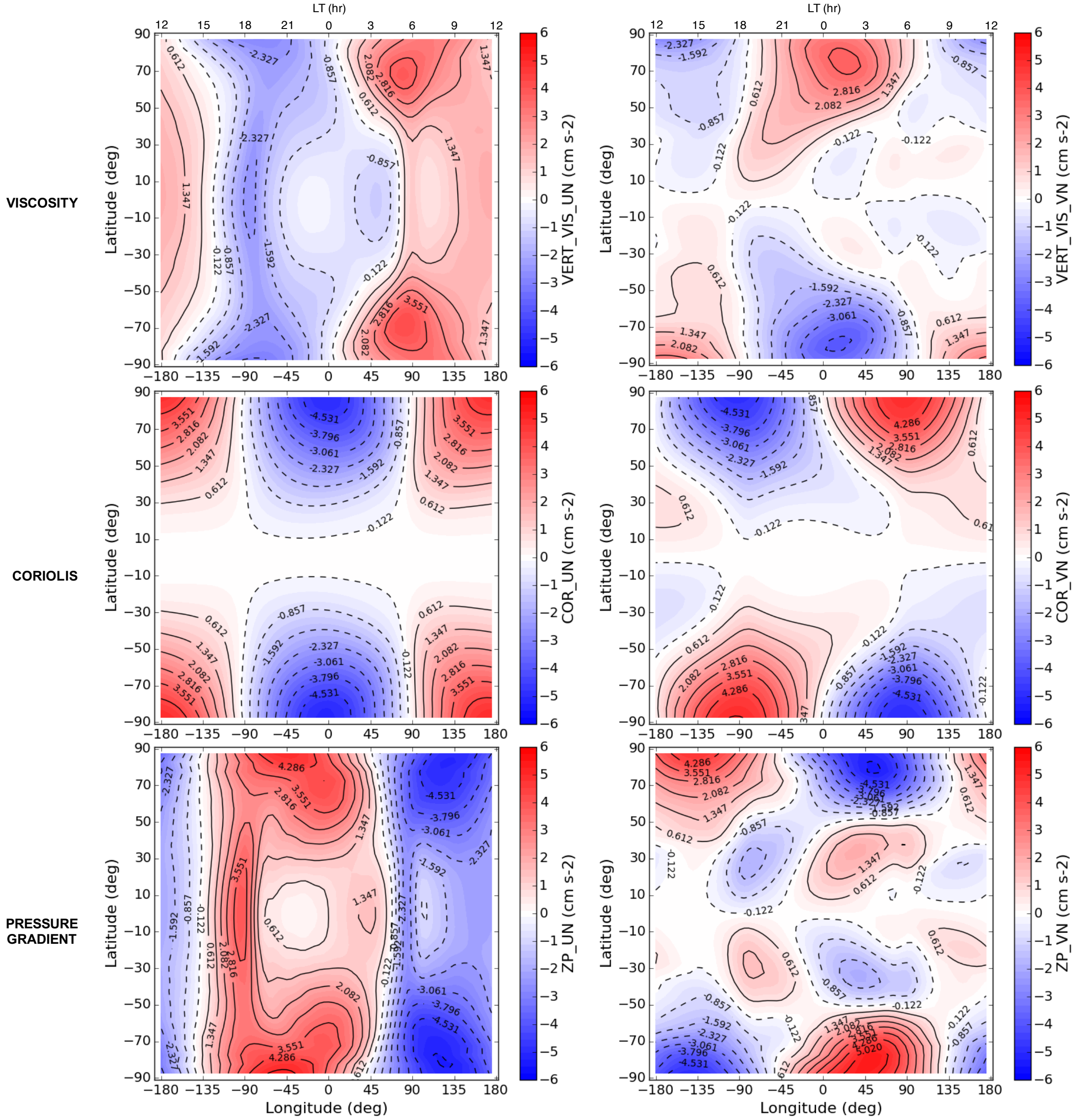

Figure 5.4: Viscous drag force (top), Coriolis force (middle), and pressure gradient force (bottom) in the zonal (left column) and meridional (right column) directions for run 1.

the simulations, centrifugal forces and momentum advection are small.

The ageostrophic winds are extracted by removing the geostrophic wind components depicted in Fig. 5.6b from the total neutral wind vectors shown in Fig. 5.1a. The diagram in Fig. 5.6c shows the force balance that would occur in a system devoid of ion drag that is approximately in steady-state (local accelerations are very small), i.e. a representative force balance from a point

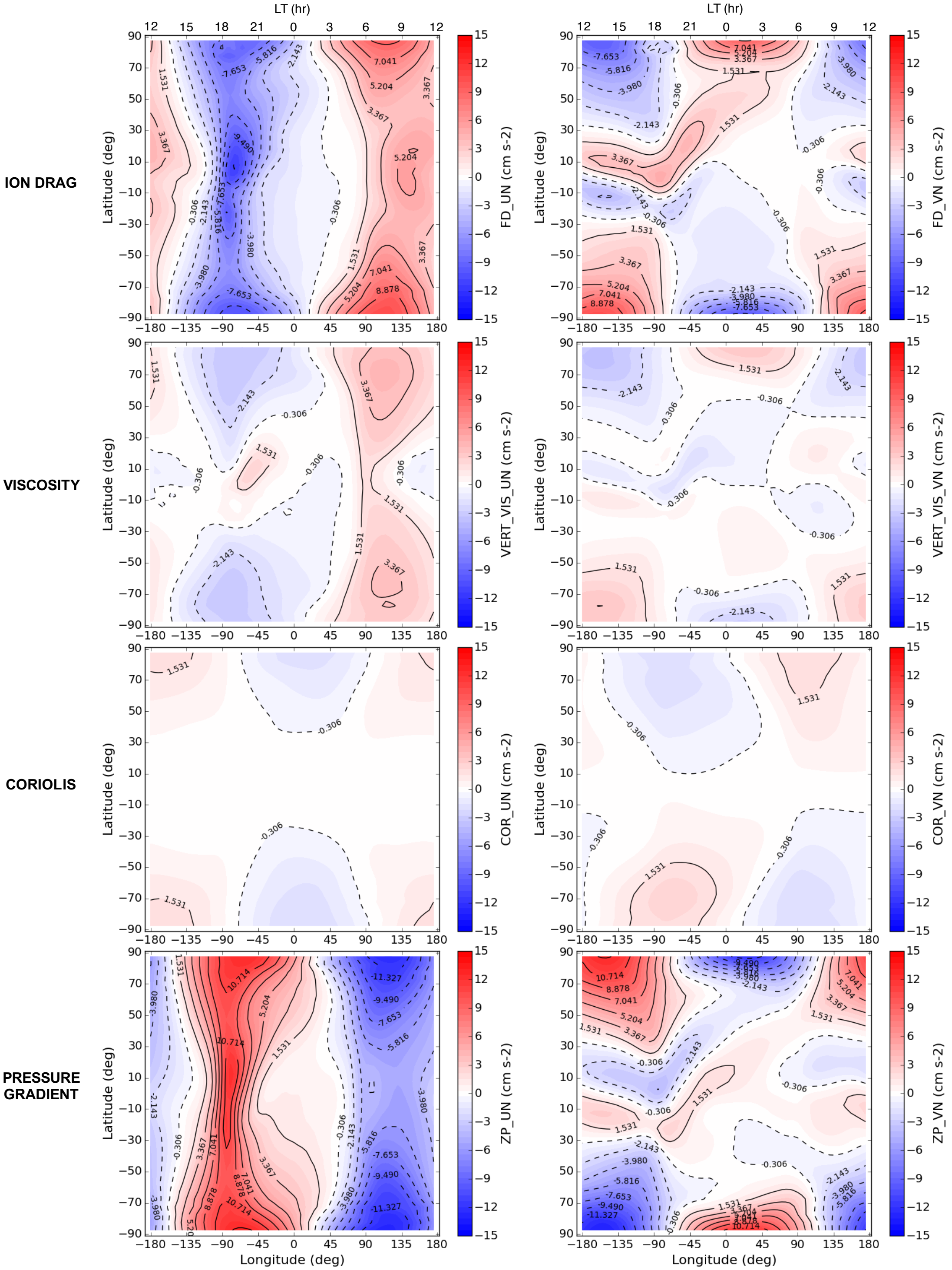

Figure 5.5: Ion drag force (first row), viscous drag force (second row), Coriolis force (third row), and pressure gradient force (fourth row) in the zonal (left column) and meridional (right column) directions for run 2.

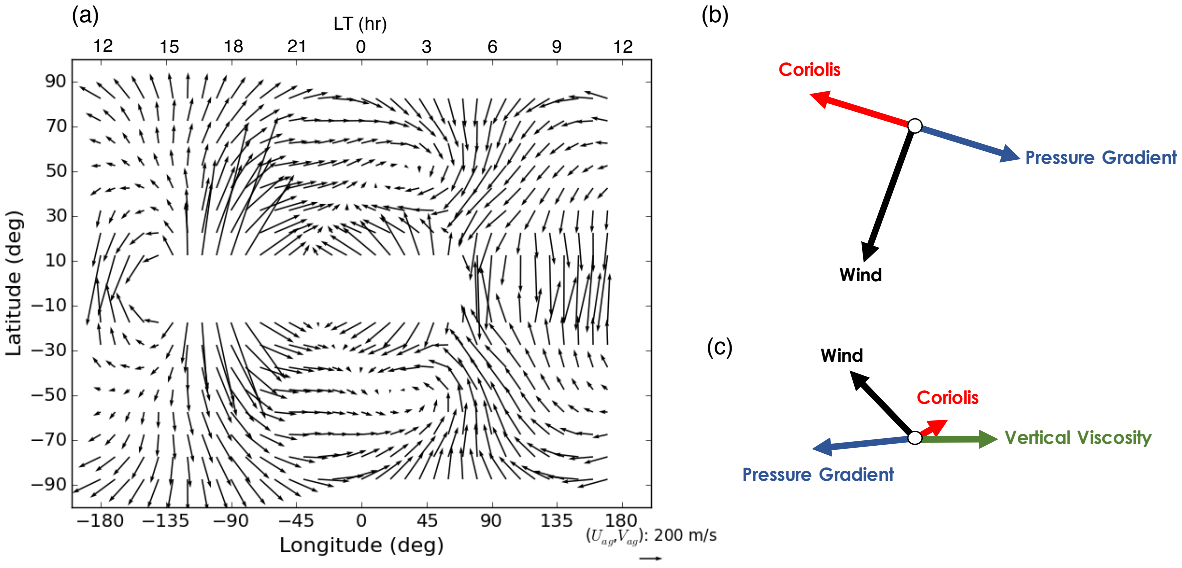

Figure 5.6: (a) Ageostrophic wind vectors (U_{ag}, V_{ag}) as a function of latitude and local time in the northern hemisphere for run 1, (b) Diagram of geostrophic balance, (c) Steady-state force balance diagram of dominant forces for run 1.

on the grid (mid-latitudes) from run 1. Viscous drag acts as a drag force that modifies the wind field structure and magnitude, requiring the Coriolis force to adjust, and causes the wind vectors to

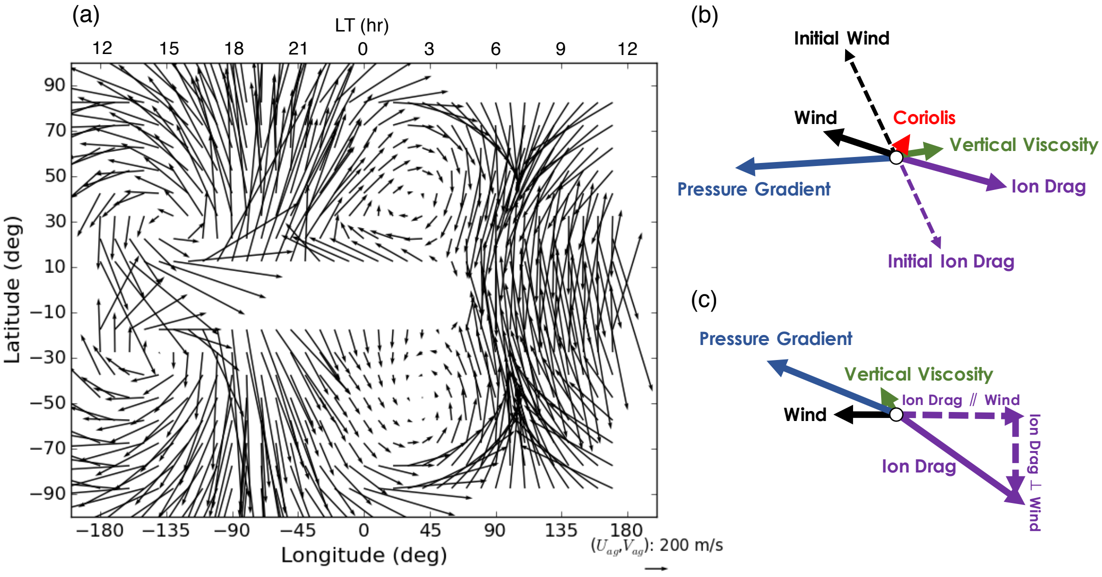

Figure 5.7: Same as Fig. 5.6 except for run 2.

rotate towards the pressure gradient force, which is inherently divergent. This behavior is exhibited in Fig. 5.6a, where the ageostrophic wind vectors tend to point in the direction of the pressure gradient force. In general, the inclusion of a drag force, whether viscous or ion drag, has this effect on geostrophic motion and leads to sustained divergent flow in the upper thermosphere.

When ion drag is incorporated into the simulations (run 2), the geostrophic wind is greater compared with run 1 due to its proportionality to the pressure gradient force (it will later be shown that ion drag increases pressure gradients, thus enhancing geostrophic winds). The ageostrophic wind is also stronger for run 2 than for run 1, as seen in Fig. 5.7a, indicating that the components of the ageostrophic wind in run 2 must partially offset the geostrophic components since the total wind vector equals the sum of the geostrophic and ageostrophic winds, and the total winds in run 2 are less than those in run 1 (see Fig. 5.1). Figure 5.7b illustrates a steady-state force balance situation when ions are stagnant ($\mathbf{u}_i \approx 0$). The ion drag force retards the neutral wind along its direct line of sight with a magnitude proportional to the wind speed and ion density (refer to Eq. 5.1), and reduces the role of viscous drag by decreasing vertical shears. If the ions are moving ($\mathbf{u}_i \neq 0$), then a component of the ion drag force may not be directly opposing the wind, and the analysis becomes more situationally dependent, as ion drag with ion motion can accelerate or decelerate winds and induce local shears which makes the behavior of viscous drag more complex. Figure 5.7c shows a situation where the Coriolis force is negligible, near the equator, and viscous drag acts against ion drag to balance the forces in the system.

Similar to viscous drag in run 1, the neutral wind rotates towards the pressure gradient force with ion drag included in the model, but with greater magnitudes in ageostrophic flow (as depicted when comparing Fig. 5.6a with Fig. 5.7a). Since the curl of a gradient is zero, the wind vector will be more divergent as it rotates into the pressure gradient force direction. Thus, viscous drag and stagnant ion drag produce wind fields with less curl and more divergence. Although divergent fields are expected to be transient occurrences in the lower thermosphere, particularly when applying geostrophic adjustment [Larsen and Mikkelsen, 1983], they are sustained fields in the upper thermosphere where geostrophy is not the final balanced state.

Divergence in the horizontal wind produces changes in the vertical winds, causing adiabatic heating or cooling. This relationship is depicted in Eq. 5.3 [Roble et al., 1988] and is evident in the model simulations:

$$\dot{Q}_{adb} = -\frac{W_n R T_n}{\bar{m} H}, \tag{5.3}$$

where W_n is the neutral vertical wind, R is the universal gas constant, T_n is the neutral temperature, $\bar{m}$ is the mean atmospheric mass, and H is the pressure scale height. In the TIEGCM, a model "vertical velocity" is calculated by integrating the continuity equation in log-pressure coordinates, and a physical vertical wind (W_n) is obtained by multiplying the result by the scale height. From Eq. 5.3, it is apparent that the adiabatic heating/cooling rate is directly proportional to the vertical wind. Figures 5.8a and 5.8b show W_n and the zonal pressure gradient force, respectively, from the simulations without (top) and with (bottom) ion drag. The meridional pressure gradient force is not shown because it exhibits similar behavior to the zonal direction from run 1 to run 2. Note that the pressure gradient maps in Fig. 5.8b are the same as the zonal pressure gradients shown in Figs. 5.4 and 5.5, except a different scale is used for run 1 in Fig. 5.8b.

Upward vertical winds cause adiabatic cooling, whereas downward vertical winds cause adiabatic heating, following Eq. 5.3. Similarly, a change in vertical wind causes a relative change in adiabatic heating and cooling. The magnitude of change in W_n and the pressure gradient force from run 1 to run 2 is dependent on location and the type of drag force that is active. The relative strength of each drag force, ion or viscous, determines the spatial structure of the vertical winds, where ion drag confines the winds to narrow regions while viscous drag causes the vertical winds to be more evenly distributed (see Fig. 5.8a). The variations in $\dot{Q}_{adb}$ oppositely mirror the vertical wind patterns in Fig. 5.8a (see Fig. 5.9), and they are echoed in the thermal structure of the upper thermosphere shown in Fig. 5.1. It is reminded that this study compares completely separate, diurnally reproducible states without and with ion drag, and runs should be evaluated in a static manner rather than with an evolutionary approach between states, i.e. run 1 does not develop into run 2, and the processes that transpire are exclusive to the individual state.

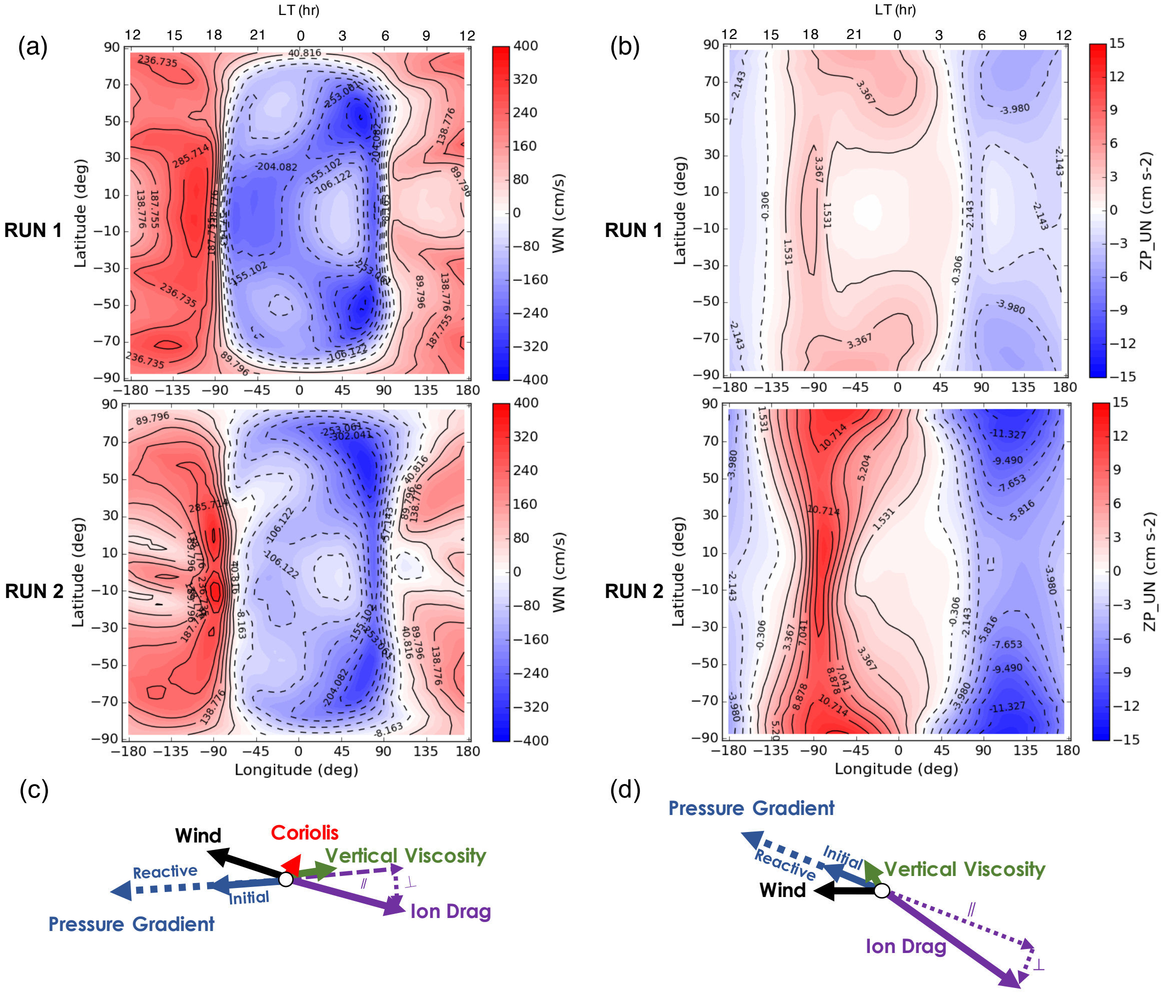

Figure 5.8: (a) and (b) Latitude versus local time maps of vertical wind and zonal pressure gradient without ion drag (top) and with ion drag (bottom), (c) and (d) Steady-state force balance diagrams similar to Figs. 5.7b and 5.7c (see text for details).

In the presence of drag forces, the final balanced state of the thermosphere prompts significant alterations to pressure gradients and temperature. This behavior is an inherent characteristic of the coupled ionosphere-thermosphere system, e.g. Dickinson et al. [1971]. The feedback of modifying adiabatic heating/cooling through vertical winds is to produce thermal changes that couple back to the momentum equation through the pressure gradient force. An additional pressure gradient is then imposed reacting to the thermodynamics induced by the drag forces in an attempt to balance these additional forces. This reactive pressure gradient force consequently enhances the divergent

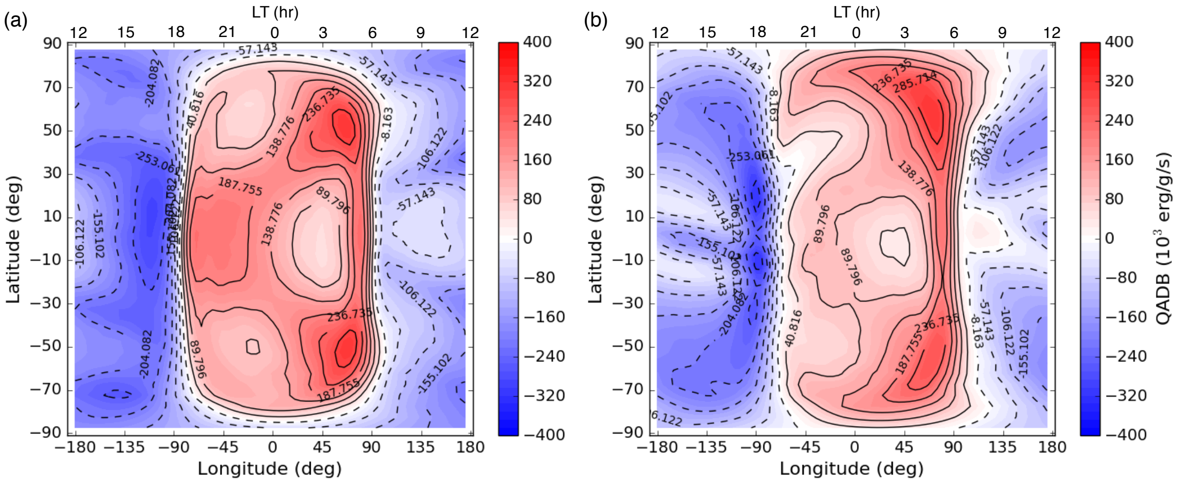

Figure 5.9: Latitude versus local time maps of adiabatic heating and cooling (a) without ion drag (run 1), and (b) with ion drag (run 2).

component of the wind, which leads to adjustments in the forces, causing the final force balance to occur primarily between the pressure gradient and the drag forces. If the momentum equation was not tied to the energy equation through the pressure gradient force, then the wind perturbations would be appreciably less with the original pressure gradient balancing the drag forces.

The final balanced state of the thermosphere when excluding ion drag represents the condition where the only drag force is viscous drag. As demonstrated in Fig. 5.1, this simulation produces a weaker gradient in temperature from day to night than when ion drag is included. Figure 5.8b reinforces this result with weaker pressure gradients in run 1 than in run 2. The reasoning for this behavior lies in the divergent / convergent wind system produced by the different drag types. Although the vertical winds in Figure 5.8a have similar magnitudes between run 1 and run 2, they differ in spatial configurations. Accounting only for viscous drag, vertical winds are upward on the dayside as the wind field is divergent and downward on the nightside where the wind field is convergent. This translates to adiabatic cooling on the dayside and adiabatic heating on the nightside, in opposition to the radiative forcing on the day and nightside. This results in a reduction of heating on the dayside and a reduction of cooling on the nightside making the day-night temperature difference only about 150 K.

The final balanced state of the thermosphere when including ion drag leads to much larger gradients in pressure and temperature (as seen in Figs. 5.8b and 5.1b). The divergent / convergent wind fields (upward / downward vertical winds) in run 2 are restricted to narrower areas on the dayside / nightside than in run 1 that cause adiabatic cooling / heating in localized regions, creating considerable temperature gradients that result in a day-night temperature difference of nearly 400 K. Thus, the steady-state thermospheric wind and temperature structure is highly dependent on the type of drag force environment.

A bridge between the energy and momentum equations occurs when the pressure gradient force reacts to the thermal changes induced by the drag forces. The pressure gradient attempts to restore a force balance, which happens progressively as the wind adjusts to accommodate changes in the Coriolis and drag forces. For the ion drag force case, Figs. 5.8c and 5.8d are replicas of Figs. 5.7b and 5.7c, respectively, except that the ion drag force is now decomposed into components parallel and perpendicular to the pressure gradient force and the reactive pressure gradient component is illustrated. The magnitude in the parallel component of the ion drag force largely depends on the amount of rotation of the wind towards the pressure gradient force. Fig. 5.8c demonstrates the final balanced state between basically the net pressure gradient force and a component of the ion drag force when ion motion is negligible, while Fig. 5.8d shows a balanced state when ion motion exists.

5.4 Discussion and Conclusions

We use the TIEGCM to analyze the impact of drag forces, ion and viscous, on the wind and thermal structures of the upper thermosphere under quiet geomagnetic conditions and during solar maximum. Drag forces shift the neutral wind system, leading to adiabatic heating or cooling and the creation of neutral temperature structures. The adjustments in the dynamics, and subsequently the thermodynamics, of the thermosphere that occur due to variations in drag forces stem from a balance of forces between pressure gradient, Coriolis force, viscous drag, and ion drag, but this balanced state is altitude dependent. In the literature, there are numerous studies of E-region wind dynamics (e.g. Larsen and Mikkelsen [1983], Walterscheid and Boucher Jr. [1984], Kwak and Richmond [2007], Walterscheid and Crowley [2015]). However, these studies often invoke geostrophic adjustment, or modified geostrophic adjustment due to Hall drag, to explain the wind behavior. Geostrophic adjustment assumes that the final balanced state will reach geostrophy through mass and wind adjustments. Consequently, divergent flow must be transient and accounts for the redistribution of energy by gravity waves. However, in the upper thermosphere, geostrophy is not the final balanced state, and persistent divergent flow and its associated sustained thermal structure can be, and is, a part of the final state at these altitudes.

In this study, we have shown a source of divergence in the horizontal wind field is captured in the ageostrophic wind. When ion drag is included into the model, the ageostrophic wind becomes larger and the pressure gradient force increases due to the addition of a pressure gradient force that works to counteract the ion drag force. The concept of a reactive pressure gradient force produced by a momentum source has been mentioned by earlier studies (e.g. Dickinson et al. [1971], Rishbeth [1979b], St.-Maurice and Schunk [1981]), where it was termed a perturbation pressure or back-pressure. Although these studies recognized the effects of temperature change on the momentum equation, the models used were not advanced enough to realize the full reactive effect of momentum due to thermal changes. We have demonstrated here that the global-scale temperature structure is explained by direct EUV heating / IR cooling and indirect internal heating / cooling produced by including the effects of drag forces. This result is supported by Rishbeth [1998], where a simple calculation determined that the power input to raise the whole neutral F-region atmosphere via vertical winds is a significant fraction of the daytime solar input. Composition, e.g. the O/N2 ratio, also changes significantly with the inclusion of the ion drag force. The composition changes due to drag forces will be addressed in detail in a future study. Here we emphasize the impact of drag forces on wind and temperature, but recognize that there are broader implications on composition and the ionosphere.

Although any drag force rotates the total wind vector towards the pressure gradient force thereby shifting the wind system into a more divergent flow field, the viscous drag force is a more efficient generator of divergence than the ion drag force. A hypothesis on the augmented efficacy of viscous drag over ion drag to drive divergent winds is the differing spatial variations of the drag forces. The spatial map of ion drag aligns with the pressure gradient force (Fig. 5.5), but the spatial configuration of viscous drag does not agree well with pressure gradient behavior (Fig. 5.4). This mismatch in spatial alignment between the dominant forces in run 1 could create wind structure that effectively induces more divergence.

To illustrate the ion-viscous drag relationship in a less controlled setting, the same methodology described in section 5.2 was applied to an TIEGCM simulation under solar minimum conditions (F10.7 = 80). Figure 5.10 illustrates the impact of drag forces on horizontal wind and temperature structure. By comparing Fig. 5.10 with Fig. 5.1, it is evident that the influence of the ion drag force on the upper thermosphere is significantly diminished in solar minimum, i.e. the wind and temperature fields are not altered as much from Fig. 5.10a to Fig. 5.10b compared to Figs. 5.1a and 5.1b. The more uniform thermal structure seen in Figs. 5.10a and 5.10b is strikingly similar to Fig. 5.1a, indicating that viscous drag is a dominant contributor to the force balance of the system under solar minimum conditions (with ion drag, pressure gradient, and the Coriolis force complet-

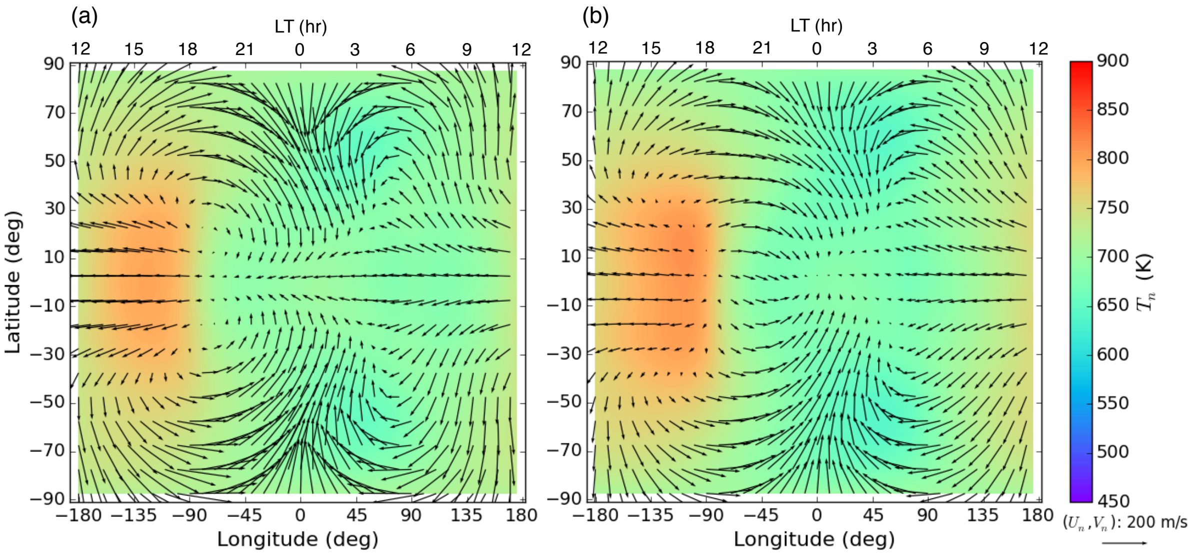

Figure 5.10: Same as Fig. 5.1 but for solar minimum conditions.

ing the balance). This is confirmed in Fig. 5.11, where ion and viscous drag are primary forces and they work together with the Coriolis force to offset the pressure gradient force (the meridional force components are shown in Appendix C). By inspecting the important energy processes in the

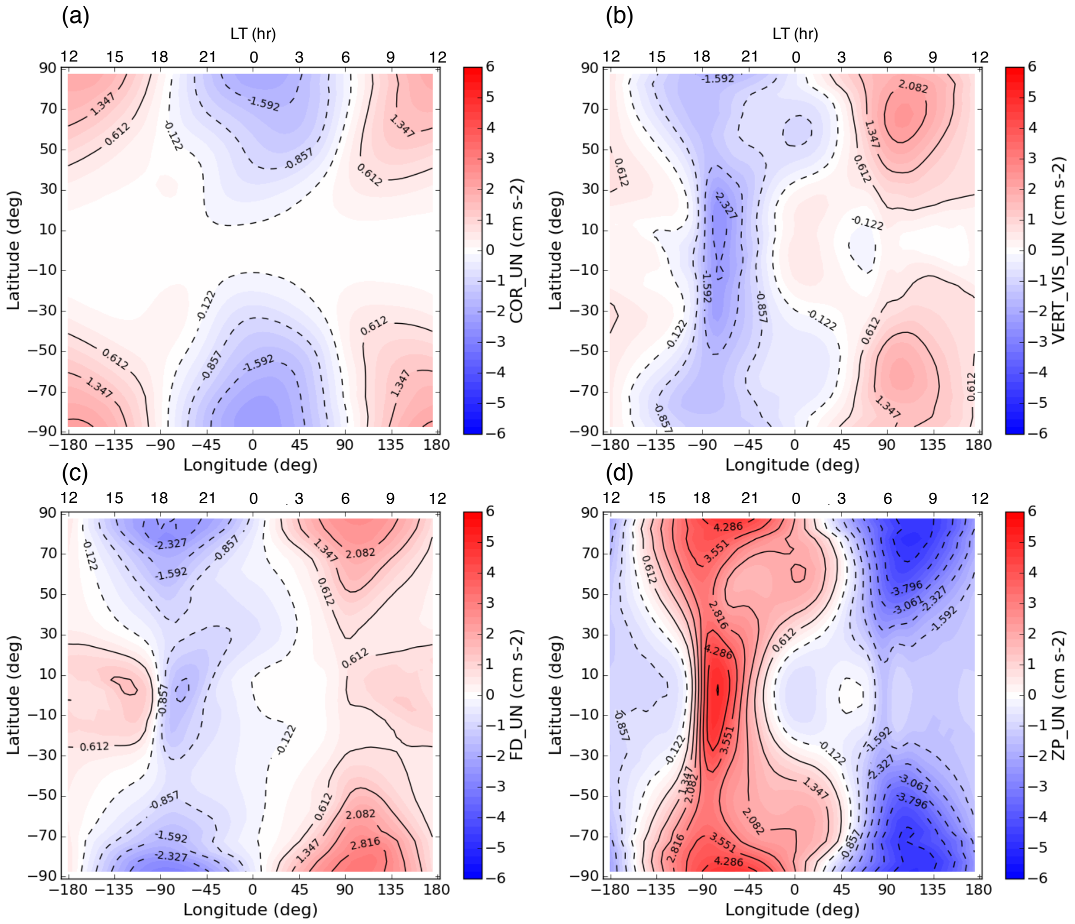

Figure 5.11: Zonal (a) Coriolis force, (b) viscous drag force, (c) ion drag force, and (d) pressure gradient force for solar minimum conditions.

solar minimum case, it is seen that the terms in the energy equation do not change much with the addition of ion drag into the model (see Figs. 5.12 and 5.13). The contribution from adiabatic heating and cooling is very similar to that in Fig. 5.2, implying that viscous drag has a meaningful role in influencing energy processes in solar minimum conditions.

The solar minimum case demonstrates that the conclusions gleaned from the ion drag on/off numerical experiments can apply to the physical world, and that the unrealistic, complete removal

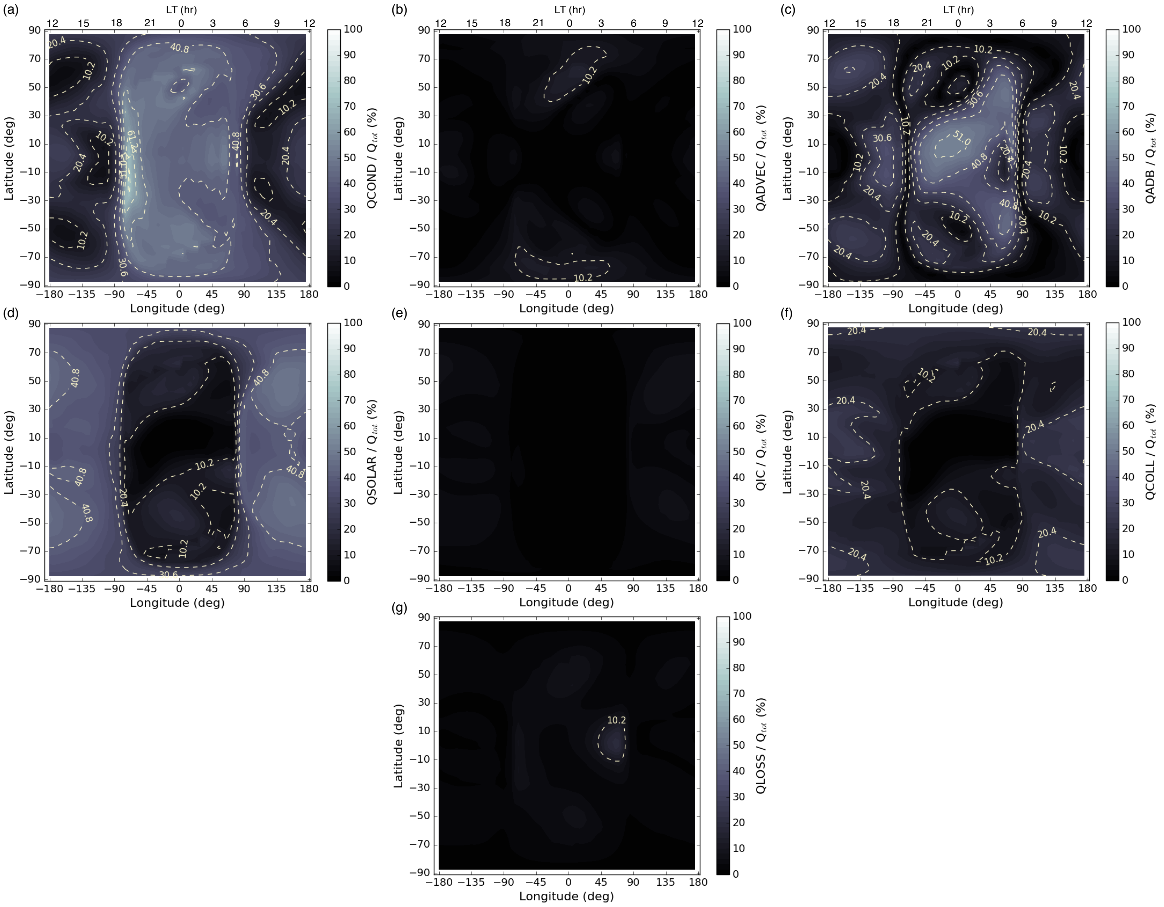

Figure 5.12: Same as Fig. 5.2 but for solar minimum conditions.

of the ion drag force from the I/T system is useful to explain the complex interplay between the ion and viscous drag forces and their effects on neutral winds and temperatures.

To further substantiate our results, complete TIEGCM runs were conducted (both the ion drag force and frictional heating are included into the model) for solar minimum and maximum conditions, shown in Fig. 5.14. The addition of frictional heating back into the model under extremely quiet conditions enhances the neutral temperatures globally by a few percent, essentially serving as a constant positive bias for each grid point. Also, the force balances for the complete runs are analogous to the ones displayed in Figs. 5.4, 5.5, and 5.11, and are located in Appendix C as Figs. C.2-C.5 (energy term analysis is also shown in Appendix C as Figs. C.6 and C.7). Therefore, the impact of frictional heating on the simulations does not alter the conclusions from

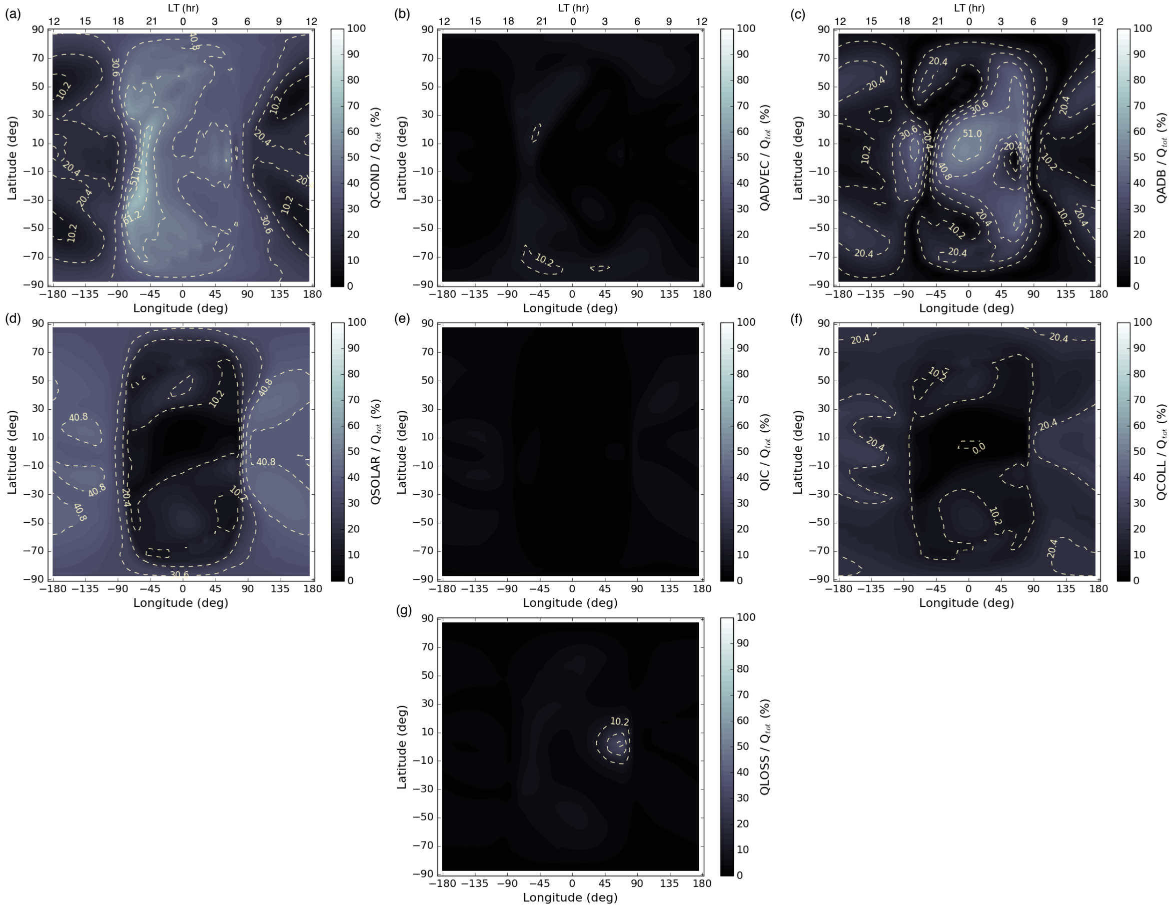

Figure 5.13: Same as Fig. 5.3 but for solar minimum conditions.

this study.

The numerical experiments performed for this work reduce the complexity of a global circulation model in an attempt to thoroughly understand the mechanisms that drive wind and temperature structure in the upper atmosphere during solar maximum and minimum conditions under quiet geomagnetic activity. The results reported in this study have practical applications, specifically ones that involve appreciable variations in ion drag or electron density, e.g. storm-time effects, large-scale day-night variations, solar maximum to solar minimum transitions, and the day-night terminator. For instance, geomagnetic storms cause positive and negative changes in electron density (e.g. Mannucci et al. [2005], Lei et al. [2014b], Liu et al. [2016], Zhong et al. [2016]), and the physical processes of these storm-time effects are strongly coupled such that it is very difficult to

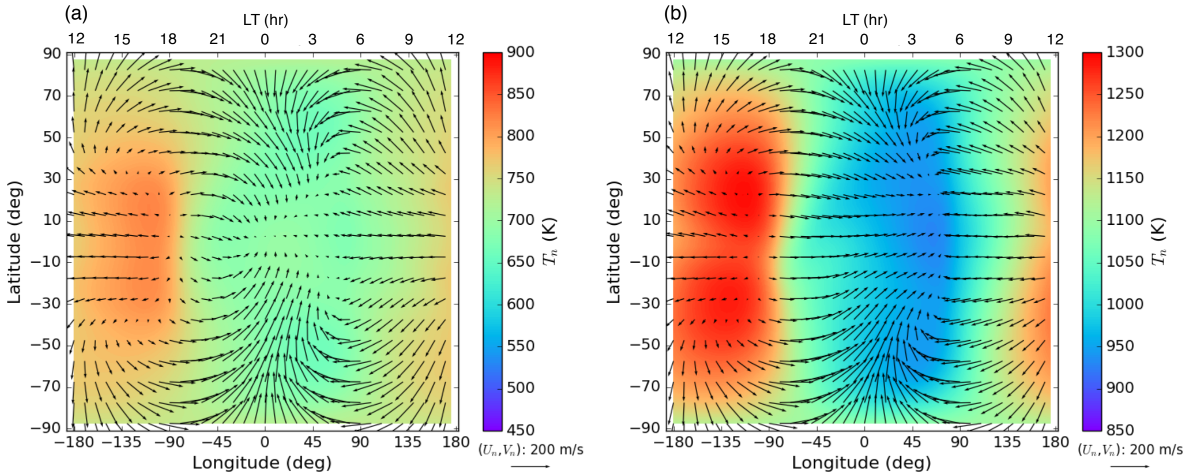

Figure 5.14: Neutral temperature T_n and horizontal wind vectors (U_n, V_n) as a function of latitude and local time in complete simulations for (a) solar minimum conditions, and (b) solar maximum conditions at UT = 0.0 hr and pressure level 3.25 (∼400 km).

separate the contribution of ion drag to the global I/T system in observations and models. The numerical experiments presented in this work provide a way to understand the fundamental physics that govern an important aspect of ion-neutral coupling (ion drag) in the upper atmosphere. Similar to positive and negative storm-time effects, the large-scale day-night variation of neutral mass density and temperature contains positive and negative diurnal variations in electron density that couple to viscous drag through changes in the kinematic viscosity coefficient. Empirically-based studies have shown disagreements in describing neutral day-night behavior [Müller et al., 2009; Qian and Solomon, 2012; Emmert, 2015], but a physics-based approach may resolve the mechanisms responsible for global diurnal variations in thermospheric density and temperature. The outcomes from this study, specifically the interplay between ion drag and viscous drag on neutral behavior, will serve as a baseline and reference for future work involving realistic model runs and observations that explore how the ion-viscous drag relationship regulates the response of the thermosphere by leaning on the core physical principles revealed in this study. In particular, the results from this chapter will be applied to Chapter 6, where signatures of drag effects will be examined.

We have demonstrated that the primary drag force vastly molds quiet-time, upper thermospheric dynamics and thermal structure. The factors that decide whether ion or viscous drag is dominant are their respective time constants and force magnitudes. The drag time constants are derived by solving the partial differential equation of the neutral momentum equation assuming each drag force is the only force acting on the gas. The time constants for ion drag and viscous drag are defined below, respectively:

$$\tau_{ion} = \frac{1}{\nu_{ni}}, \tag{5.4}$$

$$\tau_{vis} = \frac{\rho H^2}{\mu}. \tag{5.5}$$

Figure 5.15 depicts a time constant ratio (defined as $\frac{\tau_{vis}-\tau_{ion}}{\tau_{ion}}$) for solar minimum and solar maximum conditions for complete TIEGCM simulations, i.e., with ion drag and frictional heating. A negative τ ratio indicates $\tau_{vis} < \tau_{ion}$, zero τ ratio means $\tau_{vis} = \tau_{ion}$, and a positive τ ratio signifies $\tau_{vis} > \tau_{ion}$. From Fig. 5.15, it is evident that viscous drag almost always has a smaller time constant (on the order of minutes) than ion drag (ranges from minutes to hours), especially in solar minimum conditions. However, τ_{ion} begins to compete with τ_{vis} when electron densities are appreciable, e.g., in the equatorial region during solar maximum (see Fig. 5.15b). As mentioned previously, analyzing time constants alone is not sufficient to determine the primary drag force. The amplitudes of the forces must also be taken into account. For example, viscous drag may act on the neutral gas quicker than ion drag, but if its magnitude is significantly less than that of ion drag, then the ion drag force will prevail as the controlling drag force. The total ion and viscous drag forces are dictated by a coefficient (ν_{ni} and μ/ρ, respectively) and a physical process (differential motion between neutrals and ions, and vertical shear, respectively). The time constant calculations only consider the weight of the coefficients. Thus, evaluating drag time constants in conjunction with their relative force magnitudes sets the drag force environment, and subsequently designates the structure of the neutral gas in the upper thermosphere.

The simulations in this study bring to light the concept that specifying drag forces are possibly as important as specifying the direct energy sources in describing the wind and temperature

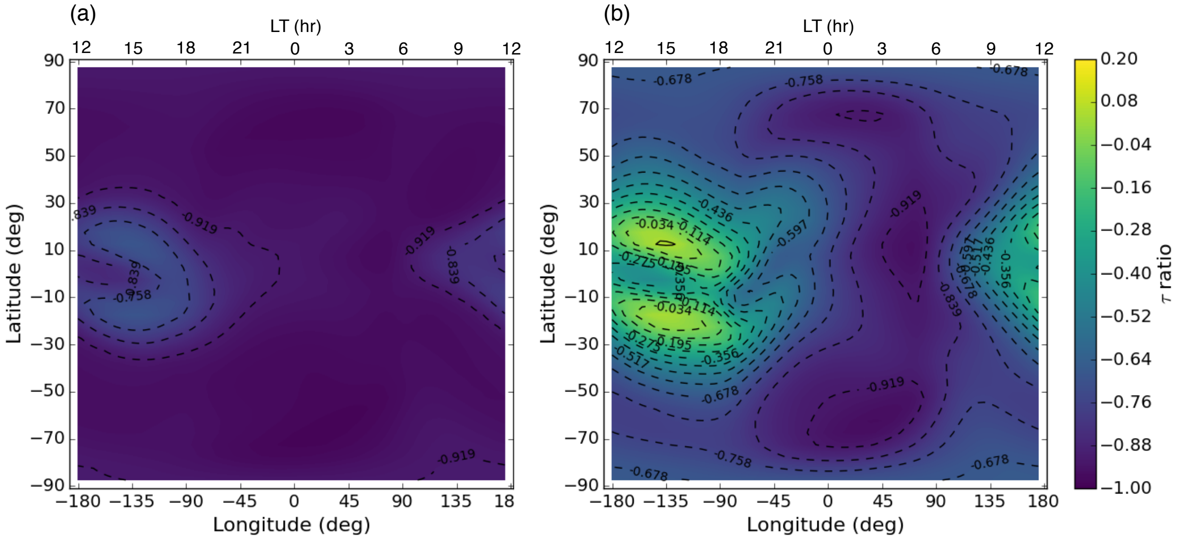

Figure 5.15: Time constant ratios as a function of latitude and local time in complete simulations for (a) solar minimum conditions, and (b) solar maximum conditions at UT = 0.0 hr and pressure level 3.25 (∼400 km).

structure of the upper atmosphere. Fuller-Rowell et al. [1999] alluded to this idea in their model simulations of neutral density holes at high latitudes during geomagnetic storms, concluding that the holes were dynamically-driven through ion drag in spite of the accompanying strong Joule heating. Variations in the ion drag force due to changes in ion motion driven by electric fields, or to changes in electron densities driven by chemistry or ionization, will induce the kind of hydrodynamic response in the upper thermosphere described in this study. The resultant thermal structure, as well as mass density structure, will depend on the scale size of the forcing and the condition of the thermosphere prior to the change. For example, Joshi et al. [2015] used the Super Dual Auroral Radar Network (SuperDARN) radars and the North American Thermosphere Ionosphere Observing Network FPIs to observe that ion drag is a dominant contributor to neutral winds during a geomagnetic storm depending on the storm's phase. Equally important is how the drag force modifies the spatial structure of the wind field, and whether this would lead to divergent-driven adiabatic heating and cooling. Walterscheid and Crowley [2015] demonstrated the importance of high-latitude, convective ion drag in producing large-scale neutral gyres whose enhanced radius of curvature produces significant centrifugal forces and cells of thermal and density structure. These studies, along with our results, are aptly poised for the plasma and neutral measurements that will come from the upcoming Ionospheric Connection Explorer (ICON) mission [Rider et al., 2015] that is slated to launch in 2017, as well as the Global-scale Observations of the Limb and Disk (GOLD) mission [Eastes et al., 2013], which will also launch that year and become operational in 2018. The main science objective of ICON and GOLD is to assess the impacts of energy and momentum drivers on our space environment. Combining measurements from ICON (e.g. horizontal winds and ion densities) with measurements from GOLD (e.g. exospheric temperatures), the mechanism that allows for changes in momentum to alter wind and temperature fields described in this study could potentially be observed in the equatorial region. It should be noted that this mechanism is ideally captured with smaller measurement spatial resolutions and time resolutions on the order of minutes. Furthermore, if electron density measurements are synthesized with neutral mass density observations, then ion and viscous drag time constants can be estimated to characterize the drag force conditions and infer the consequential upper thermospheric wind and temperature.

The intent of our study has been to draw attention to the commonly overlooked and unresolved complex interplay between ion and viscous drag, upper thermospheric forces, and their roles in establishing the wind and thermal structure of the I/T system. We stress the need in numerical models for a correct specification of not only direct energy inputs, but also parameters that affect ion-neutral coupling processes, such as electron density and the kinematic viscosity coefficient, in order to accurately describe and forecast exospheric temperature and mass density in the Earth's upper thermosphere.

A couple of recent studies have credited the vacillating force balance between pressure gradient, ion drag, and viscous drag to explain low-latitude wind phenomena in the thermosphere [Kondo et al., 2011; Evonosky et al., 2016]. The following chapter will help devise criteria for ground and space-based observing platforms to effectively search for cues of neutral drag-induced structures in the upper thermosphere, thereby supplying evidence of an indirect energy mechanism.

Chapter 6

Thermospheric Signatures of an Indirect and Dynamically Induced Energy Mechanism and its Altitudinal Extent

From Chapter 5, it has been demonstrated that the complex interplay between ion and viscous drag forces can clearly alter properties of the upper atmosphere and aid in the development of anomalies in the neutral gas. This chapter aims to answer science questions 3a-3c, where the the concepts broached in Chapter 5 are extended in order to identify signatures of indirect, dynamically induced thermospheric features, and to assess the vertical depth of the energy mechanism. In particular, helium is surveyed as a tracer for this mechanism due to its convenient attributes (as mentioned in Section 1.5.3). The new science accomplished from this study is as follows:

(1) A demarcation layer, the "thermopause," is distinguished by the vertical extent of this indirect mechanism, where the upper thermosphere response is isolated from the lower thermosphere.

(2) The horizontal gradient in neutral temperature above the "thermopause" follows the variation of the dominant neutral drag force, and changes in helium serve as a dynamical tracer that provides observational evidence of this indirect dynamical circulation.

(3) Criteria are forged to discern between direct versus indirect energy mechanisms, and to differentiate between ion and viscous drag effects in the upper thermosphere.

Note that the model runs and run numbers are unique to this chapter, and that all notation will be explained in the text. Supplemental figures are located in Appendix D.

6.1 Introduction

Certain layers of Earth's atmosphere are clearly demarcated by some property that changes with altitude. For example, as reviewed in Section 1.3, the atmosphere can be sectioned off by neutral temperature, plasma density, or other characteristics and processes within the domain. The troposphere, stratosphere, and mesosphere are divided by their respective vertical stabilities, a property that is related to the vertical profile of neutral temperature. However, while the lower atmosphere has vertical temperature gradients ($\partial T_n/\partial z$, where T_n is neutral temperature and z is altitude) that are unique to the associated layers, the thermosphere groups together two regions with dissimilar temperature gradients. The lower thermosphere has a positive $\partial T_n/\partial z$ and the upper thermosphere possesses a vertical temperature gradient that is approximately zero. This structure in temperature has a distinct connection to the dynamic stability of a layer. The reaction of the neutral gas to vertical displacements depends on its stability and its ability to restore the gas to an equilibrium. Using stability as a demarcation property, the lower and upper thermosphere can be identified as discrete atmospheric layers with a transition line that will be regarded as the "thermopause." This term does exist in the literature, but it is usually used in the context of the exosphere, e.g., the exospheric temperature is synonymous with thermopause temperature. The present study identifies the "thermopause" as a layer that can support certain sustained dynamical conditions, such as divergent motion and vertical winds.

Vertical stability specifies how an air parcel responds to vertical displacements from hydrostatic equilibrium. The restoring force for these vertical motions is the buoyancy force, which is determined by the stability environment. The dry adiabatic lapse rate, Γ_d, is defined as [Holton, 1992]:

$$\Gamma_d \equiv \frac{g}{c_p}, \tag{6.1}$$

where g is the acceleration due to gravity and c_p is the specific heat at constant pressure. The dry adiabatic lapse rate is used for unsaturated air parcels, an excellent assumption for the thermosphere. The environmental lapse rate, Γ, is defined as:

$$\Gamma \equiv -\frac{\partial T_n}{\partial z}, \tag{6.2}$$

where Γ_d and Γ are jointly used to form the following stability principles:

$$\Gamma < \Gamma_d\text{: Positive restoring force; Positive stability and hydrostatically stable,} \tag{6.3}$$

$$\Gamma = \Gamma_d\text{: Zero restoring force; Zero stability and hydrostatically neutral,} \tag{6.4}$$

$$\Gamma > \Gamma_d\text{: Negative restoring force; Negative stability and hydrostatically unstable.} \tag{6.5}$$

In the lower thermosphere, since the vertical temperature gradient is positive, then according to Eq. 6.2, the environmental lapse rate is negative ($\Gamma < 0$). From Eq. 6.1, Γ_d is always greater than zero. Therefore, the lower thermosphere satisfies criterion 6.3, where perturbations to the neutral gas are transient and damped away by a strong buoyancy force in order to return to equilibrium. This concept has been observed by many studies, a few which are discussed in Section 5.4.

In the upper thermosphere, the neutral temperature does not vary with altitude ($\partial T_n/\partial z = 0$). Applying this information into Eq. 6.2 leads to $\Gamma = 0$, which fulfills the requirements for a hydrostatically stable setting, similar to the lower thermosphere. However, the restoring force is weaker because of the zero environmental lapse rate, allowing for a higher probability of disturbances to the neutral gas to be sustained (as demonstrated in Chapter 5).

The variation of the restoring force of buoyancy in the thermosphere can be explained by recasting the vertical motion of the neutral gas as a simple harmonic oscillator. The vertical momentum balance for an unsaturated air parcel can be expressed as [Salby, 1996]:

$$\frac{\partial^2 z'}{\partial t^2} + N^2 z' = 0, \tag{6.6}$$

where z' is the virtual displacement of the air parcel and N^2 is the buoyancy, where N is the Brunt-Väisäillä frequency. By comparing Eq. 6.6 to a traditional harmonic oscillator differential equation, it is clear that N^2 represents the "stiffness" of the buoyancy spring. The buoyancy can be rewritten as [Salby, 1996]:

$$N^2 = \frac{g}{T_n}\left(\Gamma_d - \Gamma\right). \tag{6.7}$$

The buoyancy in the lower thermosphere is the addition of the environmental lapse rate with Γ_d, while buoyancy is solely dependent on the adiabatic lapse rate in the upper thermosphere. Therefore, the "stiffness", or strength, of the restoring force of buoyancy is greater in the lower thermosphere than in the upper thermosphere.

Several recent modeling studies have noticed the contrast in maintaining thermospheric structure between the lower and upper thermosphere [Kondo et al., 2011; Huang et al., 2012; Evonosky et al., 2016]. Kondo et al. [2011] and Evonosky et al. [2016] attempt to explain the persistence of low-latitude features in the neutral winds, where Kondo et al. [2011] observes in their simulations a fast, zonal wind in the altitude range of 280 to 600 km, and Evonosky et al. [2016] reports a steady evening, vertical shear in the zonal winds around 200 km. Huang et al. [2012] conducted simulations of the thermospheric response to Joule heating at different source altitudes. They found that Joule heating deposited at higher altitudes has a stronger impact on the atmosphere at 400 km. These studies augment the idea that there is a credible boundary that separates the lower thermosphere from the upper thermosphere, and that they should be treated as distinct, but vertically coupled, regions with regards to the development and progression of atmospheric structures. Huang et al. [2012] investigated the response of the upper thermosphere to an external energy input, while this study will elucidate the upper thermospheric response to an internal, dynamically induced mechanism, as well as explore observational signatures that can be used to disentangle the two energy drivers in a realistic, intertwined atmosphere.

6.2 Numerical Experiments

Table 6.1 outlines the various types of runs performed for this study, where it denotes whether ion drag or frictional heating was turned on or off (second and third columns), the solar flux level (fourth column), the latitude and longitude resolutions (fifth column), and the model version number (last column). The key difference between TIEGCM 1.94.2 and TIEGCM 2.0 is the implementation of helium as a major species module in version 2.0.

Table 6.1: Summary of TIEGCM Numerical Experiments

Run	Ion Drag	Frictional Heating	F10.7	Resolution	TIEGCM Version
1	X	X	180	5°×5°	1.94.2
2	✓	X	180	5°×5°	1.94.2
3	X	X	80	5°×5°	1.94.2
4	✓	X	80	5°×5°	1.94.2
5	X	X	180	2.5°×2.5°	2.0
6	✓	X	180	2.5°×2.5°	2.0
7	✓	✓	80	2.5°×2.5°	2.0
8	✓	✓	180	2.5°×2.5°	2.0

The simulations ran for 20 days to allow them to reach their diurnally reproducible states. The numerical experiments were conducted under very low geomagnetic activity levels (auroral hemispheric power of 1 GW and a cross polar cap potential of 1 kV - effectively eliminating auroral precipitation and ion convection), and March equinox conditions (day of year 80 in 2002). All of the model runs use a geomagnetic field specified by the International Geomagnetic Reference Field using magnetic apex coordinates [Richmond, 1995b], and the amplitudes and phases of migrating tides at the lower boundary of the model are specified by the Global Scale Wave Model [Hagan and Forbes, 2002]. All of the model runs use a time step of 2 min.

6.3 Analysis and Results

6.3.1 Altitudinal Extent

The altitude penetration of the wind-driven energy mechanism is probed by comparing the vertical wind differences between runs 1 / 3 and 2 / 4 for solar maximum / solar minimum conditions with the vertical gradient in neutral temperature, thereby gauging the location of the lower boundary where the induced circulations subside. Figures 6.1 and 6.2 illustrate the position of the "thermopause" and its spatial variations for solar maximum and solar minimum, respectively.

The circulation patterns permeate past the altitude where $\partial T_n/\partial z = 0$, but this is expected as the winds push as far down as possible into the lower thermosphere until the static stability, related to the temperature gradient, counters the vertical winds that are activated by internal plasma-neutral coupling processes to subsist. From Figs. 6.1 and 6.2, the "thermopause" is estimated to be situated in between 150-200 km for both of the solar maximum and solar minimum cases.

Figures 6.3 and 6.4 show the three-dimensional structure of central properties to the indirect, dynamically induced energy mechanism for runs 8 and 7, respectively. In Figs. 6.3a and 6.3b, the zonal temperature gradient and vertical wind structures are markedly different from 150 km to 200 km. Above 200 km, the structures remain relatively unchanged and sustained. The ion drag force is the dominant drag force from about 200-350 km (Fig. 6.3c), and above 350 km, viscous drag begins to compete with ion drag (Fig. 6.3d). Figure 6.3 complements the results from Chapter 5, where in solar maximum, the second-order structure of the quiet-time upper thermosphere is controlled predominately by ion drag, with minimal contribution from viscous drag at lower altitudes (below 450 km). Somewhere in the transition region between 150-200 km lies the "thermopause," where structures in the neutral gas above this line are persistent and considerably different from the ones in the lower thermosphere, agreeing with the height values from Fig. 6.1.

In Figs. 6.4a and 6.4b, the "thermopause" appears to be located in between 150-175 km for solar minimum conditions. Similar to what was found in Chapter 5, under low solar activity levels, viscous drag is consistently on par with ion drag throughout the *F*-region, resulting in

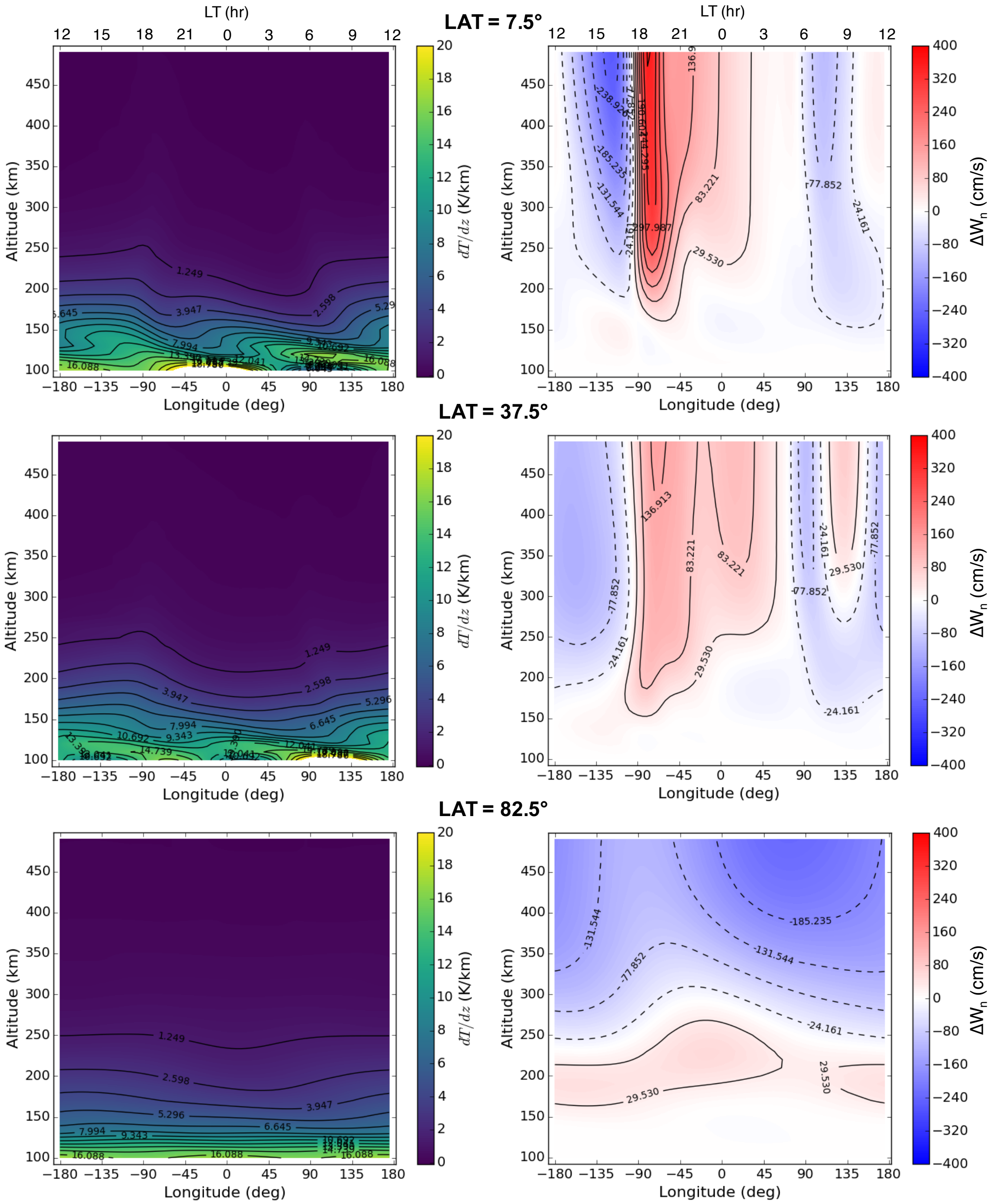

Figure 6.1: Vertical gradients of neutral temperature $\partial T_n/\partial z$ (left column) and the differences in vertical wind ΔW_n between runs 1 and 2 (right column) as a function of altitude and local time at (top) low-latitude, (middle) mid-latitude. and (bottom) high-latitude under solar maximum conditions at UT = 0.0 hr. Note that local time is the top axis.

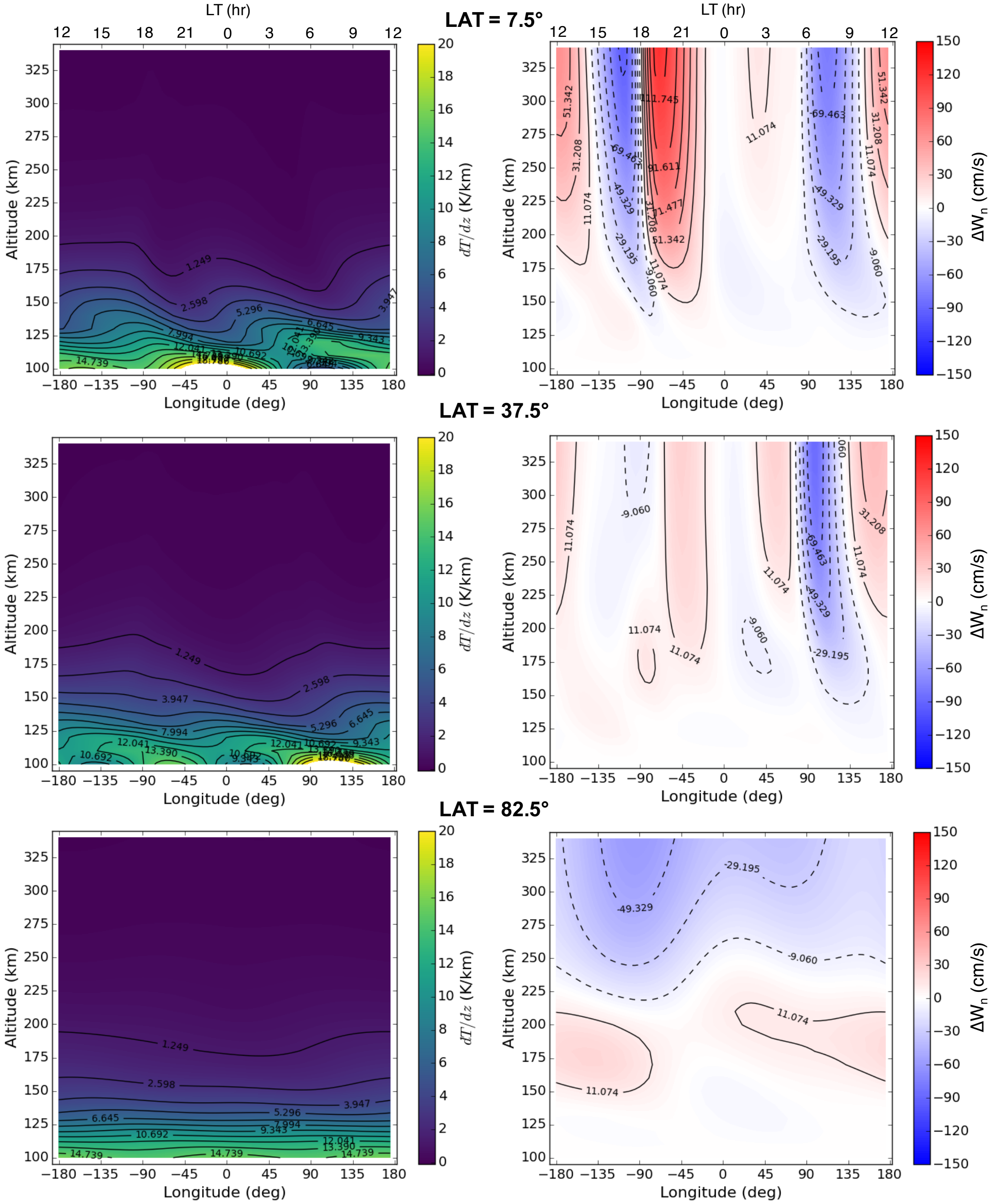

Figure 6.2: Vertical gradients of neutral temperature $\partial T_n/\partial z$ (left column) and the differences in vertical wind ΔW_n between runs 3 and 4 (right column) as a function of altitude and local time at (top) low-latitude, (middle) mid-latitude. and (bottom) high-latitude under solar minimum conditions at UT = 0.0 hr.

vertical wind structure that promotes reduced zonal temperature gradients (compare Fig. 6.4a

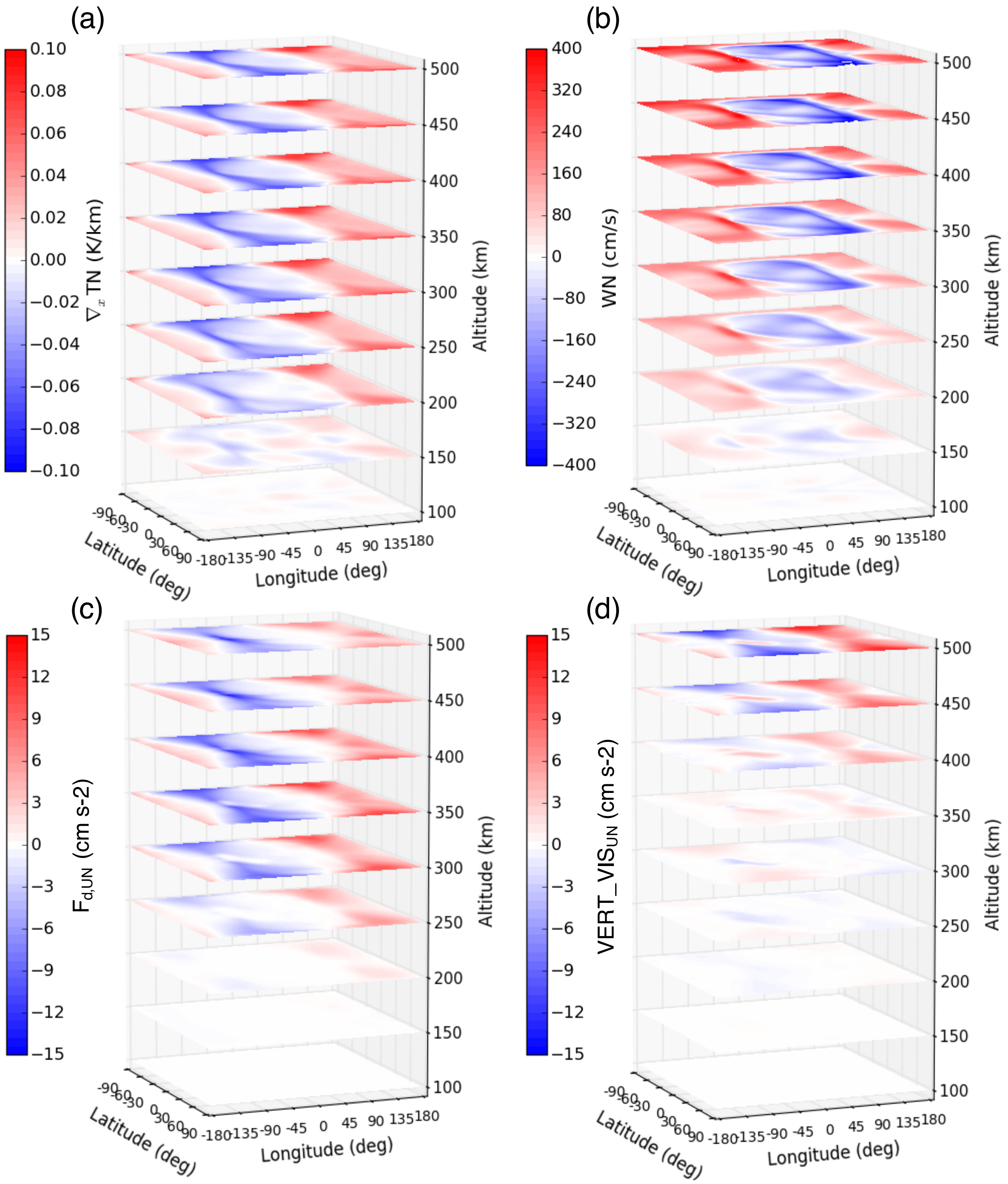

Figure 6.3: Zonal (a) neutral temperature gradient, (b) vertical wind, (c) ion drag force, and (d) viscous drag force as a function of latitude, longitude and altitude under solar maximum conditions at UT = 0.0 hr for run 8.

with Fig. 6.3a). The same arguments can be made for the meridional direction in solar maximum and minimum conditions, shown as Figs. D.1 and D.2 in Appendix D. Three-dimensional maps of

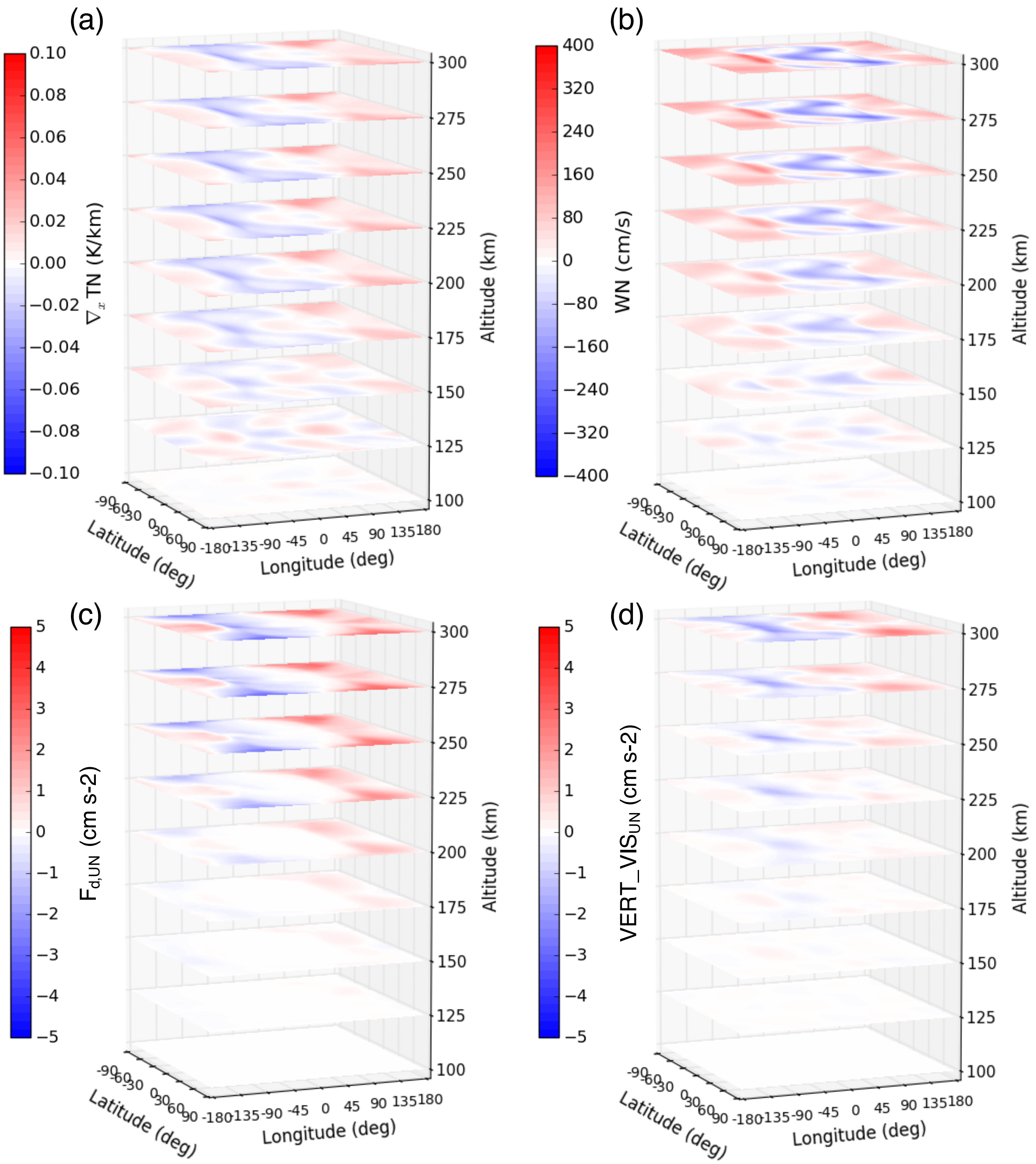

Figure 6.4: Same as Fig. 6.3 except for solar minimum conditions (run 7).

relevant properties are also constructed for run 5 (Fig. D.3 in Appendix D) in order to illustrate that the circulations generated by an indirect mechanism do not pierce below the “thermopause,” even when viscous drag is the sole neutral drag force in the system.

In solar minimum and maximum, neutral structures below the “thermopause” differ from the features above it. This boundary separates a region where perturbations to the neutral gas are quickly extinguished (the lower thermosphere) from a region where structures are sustained and consistent within an expansive altitude range (the upper thermosphere). The “thermopause” boundary may also explain why tidal activity originating from the lower atmosphere usually cannot propagate into the upper thermosphere, as the waves and tides are dissipated by drag forces [Richmond, 1971].

6.3.2 Thermospheric Signatures

As discussed in Chapter 5, the drag force environment largely regulates the radiatively forced wind and thermal structure in the upper thermosphere, and the horizontal, neutral temperature gradient reflects the balance of the primary drag force with the hydrodynamic forces of pressure gradient and Coriolis. Figures 6.5 and 6.6 present examples of this correlation with force balance maps and spatial temperature gradients for solar maximum (run 8) and solar minimum (run 7) conditions. In solar maximum (Fig. 6.5) and mid-latitudes, the temperature gradient (Fig. 6.5a) follows the ion drag force (Fig. 6.5b) in the daytime and pre-midnight sector (∼12:00-0:00 LT), but then it tracks viscous drag (Fig. 6.5c) in the post-midnight and morning hours (∼0:00-11:00 LT). Note that when one drag force is active, the other is close to zero at mid-latitudes, and that, globally, the pressure gradient force (Fig. 6.5e) nearly mimics the negative of the horizontal thermal gradient, as expected.

In solar minimum (Fig. 6.6), the influence of viscous drag is noticeably prominent, where particularly at mid-latitudes, the meridional temperature gradient (Fig. 6.6a) traces the structure of the viscous drag force (Fig. 6.6c) for the majority of the day. Again, the pressure gradient is opposite to the temperature gradient, confirming the elementary physics of the system. Similar conclusions are deduced from the zonal counterparts to Figs. 6.5 and 6.6, shown as Figs. D.4 and D.5 in Appendix D.

While the horizontal temperature gradient can be used to recognize the type of drag force

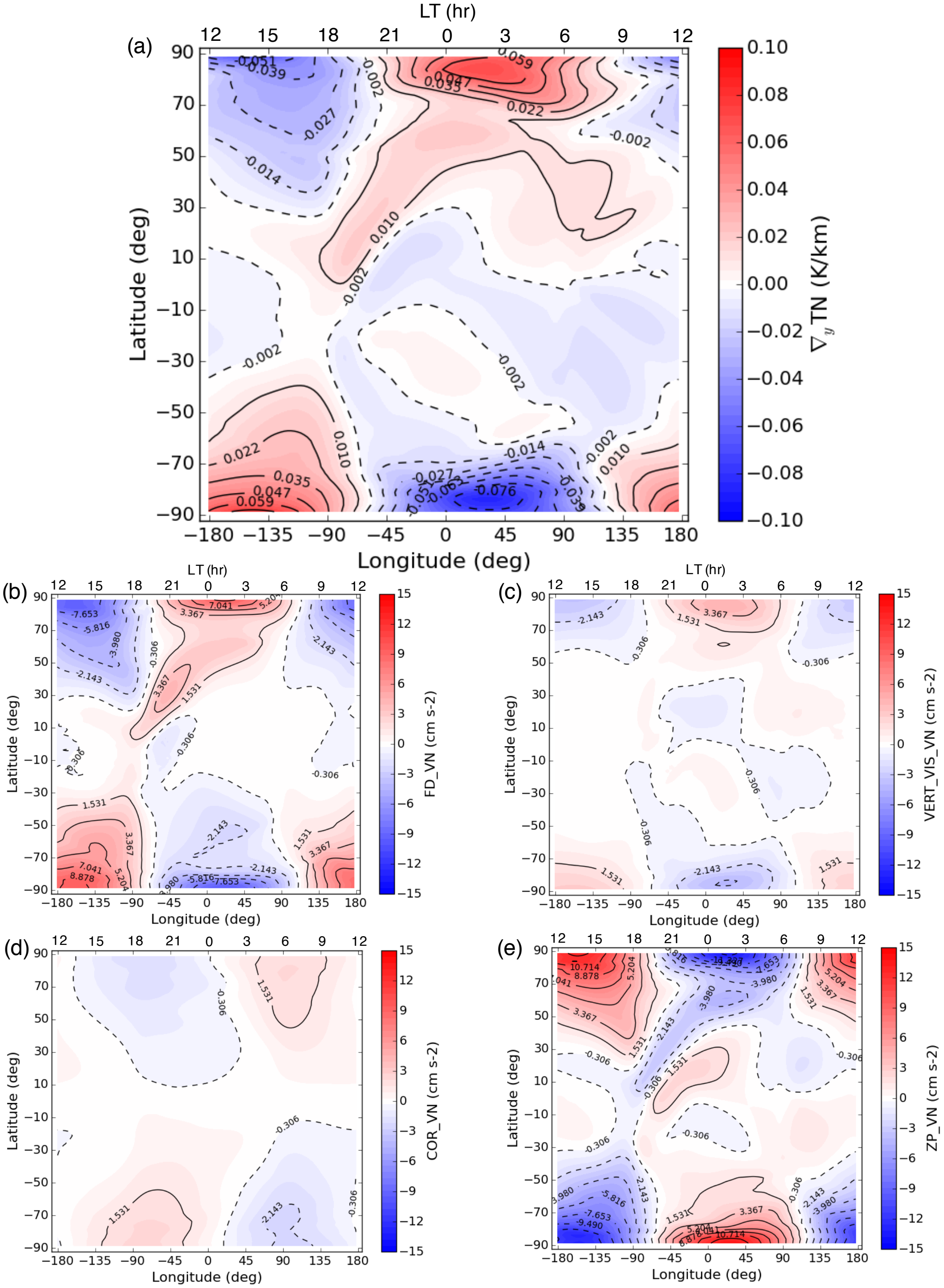

Figure 6.5: Meridional (a) neutral temperature gradient, (b) ion drag force, (c) viscous drag force, (d) Coriolis force, and (e) pressure gradient force as a function of latitude and local time under solar maximum conditions at 400 km and UT = 0.0 hr for run 8.

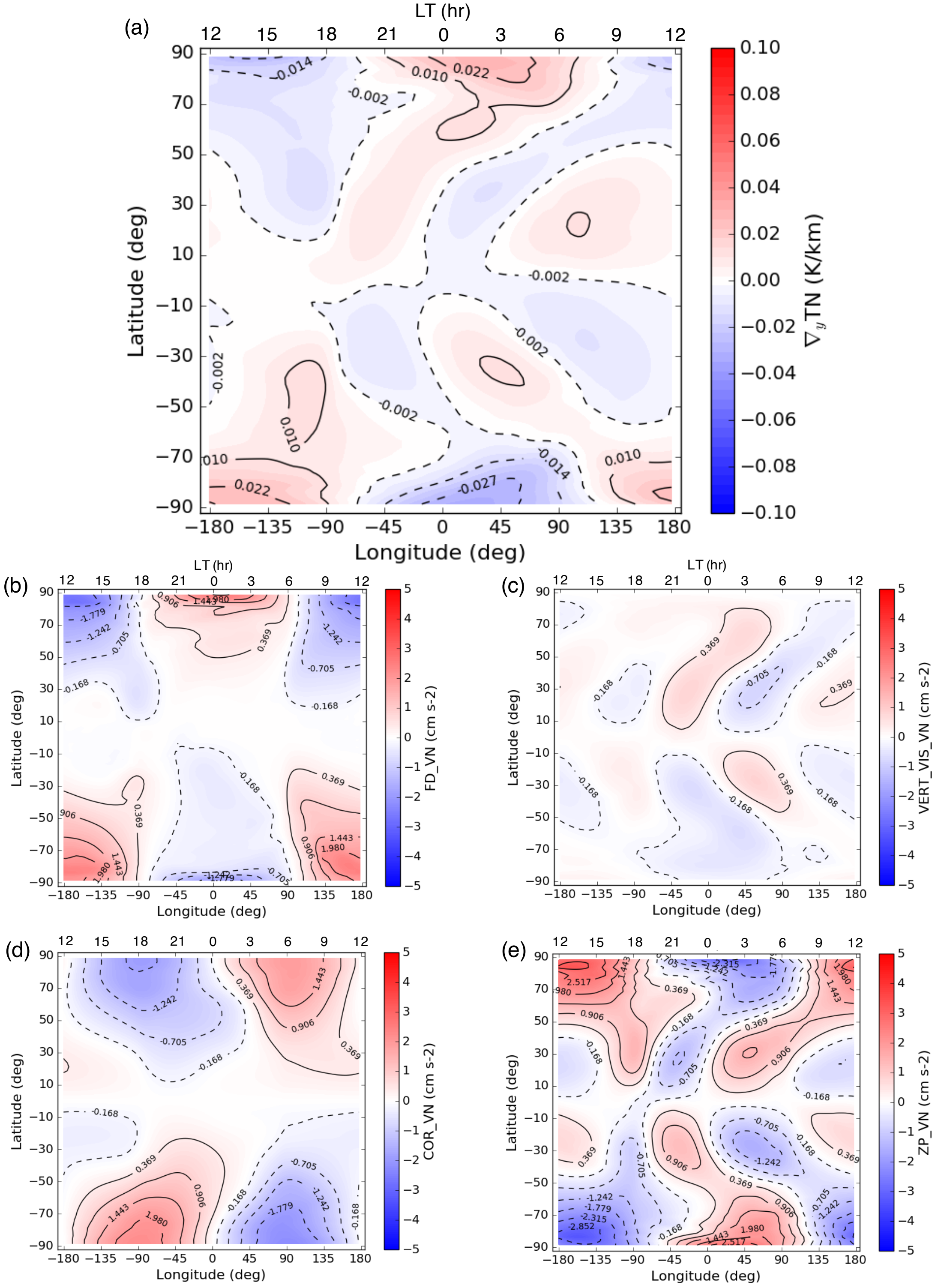

Figure 6.6: Same as Fig. 6.5 except for solar minimum conditions (run 7).

prevalent in the quiet-time upper thermosphere, helium can be a diagnostic for the dynamics operating within the system. Helium is an effective dynamic tracer because it is an extremely light, inert, and minor gas species in the thermosphere. These properties signify that helium is insensitive to temperature changes, chemical interactions are negligible, and it does not contribute to the mass balance of the thermosphere. Figure 6.7 confirms that helium follows circulation patterns by examining the behaviors of helium and neutral temperature in solar maximum. If helium responds to temperature changes, then from a scale height argument, an increase / decrease in T_n should increase / decrease helium concentrations. Thus, helium would closely mimic the neutral temperature pattern in Fig. 6.7b. However, as seen in Fig. 6.7a, helium is opposite with neutral temperature, verifying that helium is not a thermal tracer. This conclusion also holds in solar minimum, with evidence shown in Fig. D.6 in Appendix D. The structure of helium from the TIEGCM is bolstered by an empirical model, the Mass Spectrometer-Incoherent Scatter Radar (MSIS) model, where the output, Figs. 6.8 and D.7a, correspond well with Figs. 6.7a and D.6a, respectively.

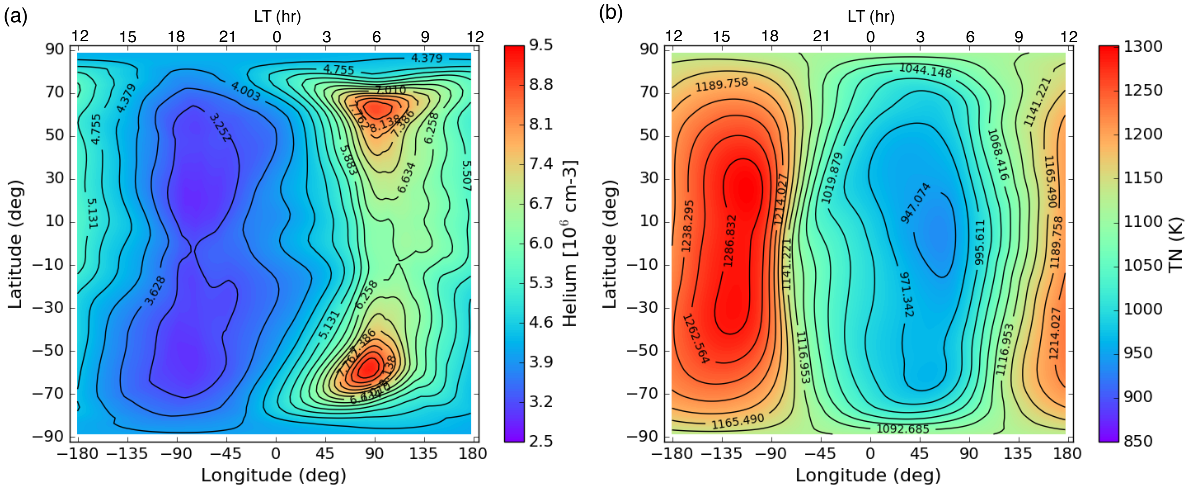

Figure 6.7: (a) Helium number density and (b) neutral temperature as a function of latitude and local time under solar maximum conditions at 400 km and UT = 0.0 hr for run 8.

Figure 6.9 presents differences between runs 5 and 6 in parameters that are vital to the momentum and energy processes occurring in the upper thermosphere. The changes from run 5

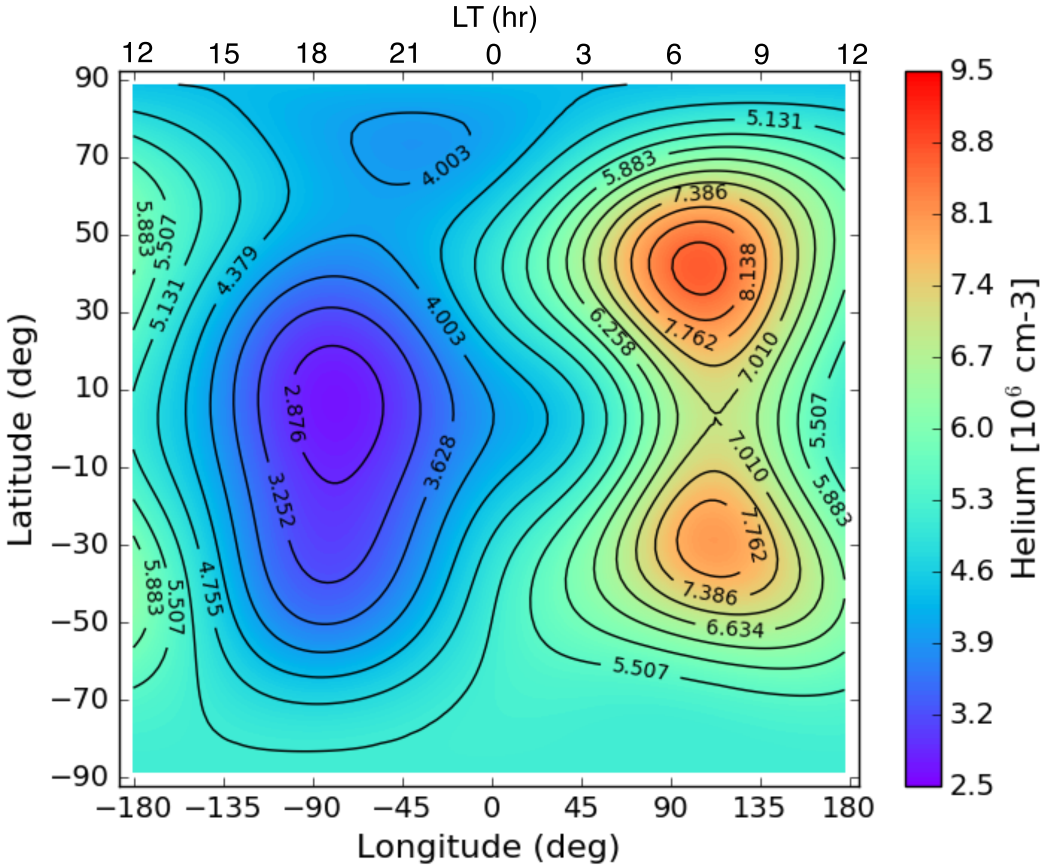

Figure 6.8: MSIS helium number density as a function of latitude and local time under solar maximum conditions at 400 km and UT = 0.0 hr for run 8.

to run 6 essentially represent how the system would respond to a strong momentum source, e.g., ion drag. The changes in vertical wind (Fig. 6.9b) are nearly anti-correlated with the changes in adiabatic heating and cooling (Fig. 6.9d), and the neutral temperature changes (Fig. 6.9a) directly reflect the neutral mass density changes (Fig. 6.9e). Overall, the positive / negative areas in 6.9b are aligned with the negative / positive parts in Fig. 6.9c, but there are pockets of vertical wind changes in Fig. 6.9b that are not accompanied by changes in helium. Nevertheless, Fig. 6.9 showcases the potential of utilizing helium as an adjudicator for an external, direct energy driver versus an internal, dynamically induced energy mechanism for neutral temperature and mass density structures in a region above the “thermopause.”

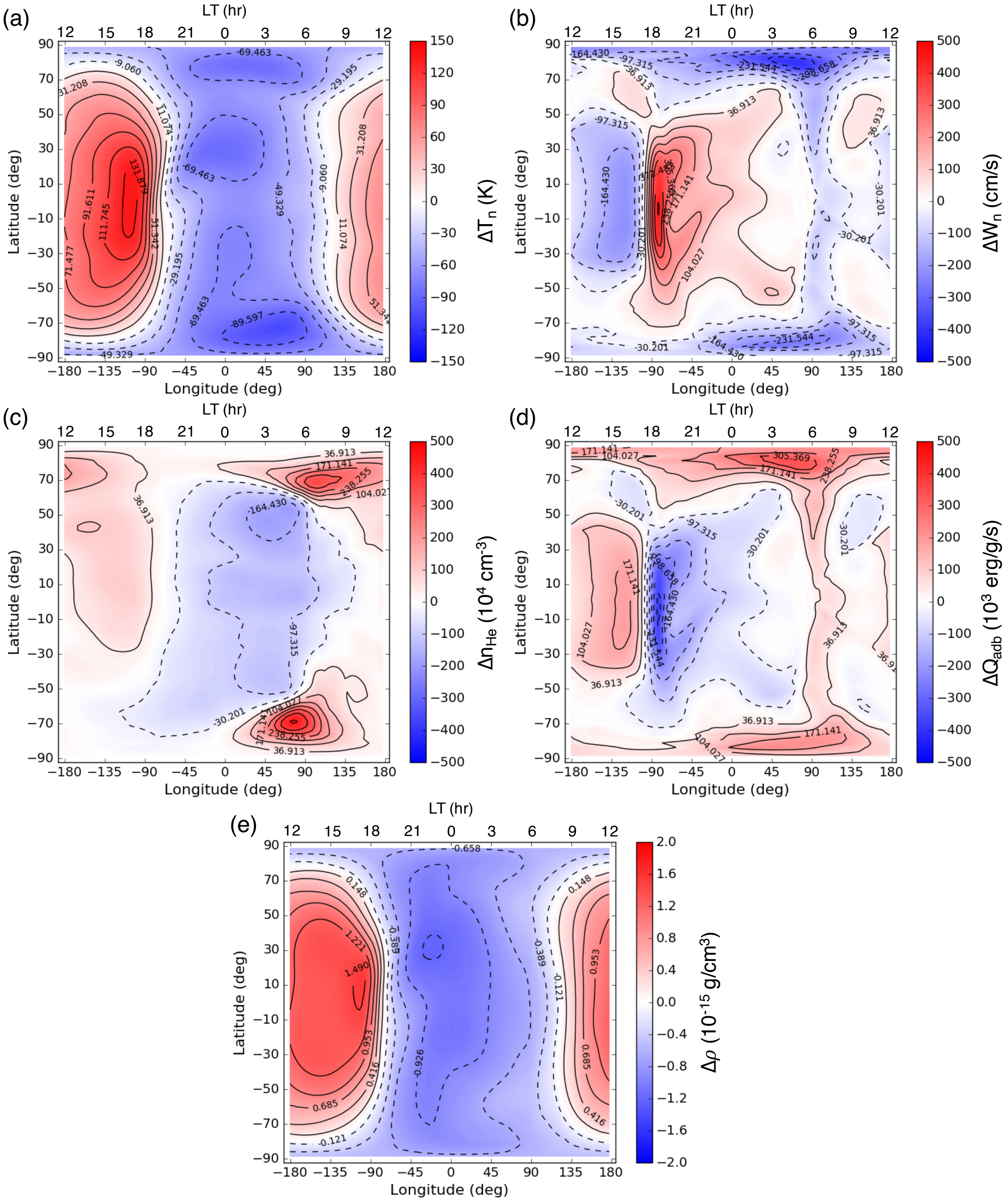

Figure 6.9: Differences between runs 5 and 6 in (a) neutral temperature, (b) vertical wind, (c) helium number density, (d) adiabatic heating and cooling, and (e) neutral mass density as a function of latitude and local time under solar maximum conditions at 400 km and UT = 0.0 hr.

6.4 Discussion and Conclusions

An external energy mechanism changes the internal energy of the system directly through the energy equation. An indirect, dynamically induced energy mechanism modifies the momentum equation, and through vertical winds and adiabatic heating and cooling, alters the internal energy of the system. Momentum and energy are interconnected via dynamics, thus the path for a direct energy process is to change the energy and then the momentum, while the route for an indirect energy process is to change the momentum and then the internal energy. Figure 6.10 shows various circulation patterns for direct and indirect energy mechanisms that can lead to heating and cooling of the neutral gas. It should be noted that a direct energy mechanism that causes heating and cooling corresponds to the right hand side of Eq. 3.13 (external heating and cooling rates), and an indirect energy mechanism for heating and cooling refers to the adiabatic heating and cooling term in Eq. 3.13. Figure 6.10 emphasizes the order that processes happen for a direct and indirect energy mechanism. For example, for a direct energy mechanism that produces heating, an external heat source Q is applied to the system, creating a temperature enhancement and pressure gradient forces, $\mathbf{F}_{\nabla p}$, that attempt to dispel the temperature gradient. This causes the horizontal winds, $\mathbf{u}_n$, to diverge, producing an upwards change in the vertical winds and drag forces, $\mathbf{F}_d$, that oppose the motion of the neutrals. This sequence of events is opposite for an indirect energy mechanism that produces heating, where changes in the neutral drag forces, ion or viscous, impel a convergence in the horizontal winds, resulting in downwelling, which causes adiabatic heating and an increase in temperature, generating reactive pressure gradient forces that aim to balance the drag forces. By monitoring how neutral properties vary throughout the evolution of a thermospheric feature, the dominant scenario (e.g. direct energy mechanisms or indirect energy mechanisms) can be surmised.

The behavior of helium with vertical motion is unique because it is lighter than the mean mass of the neutral gas. In a molecular diffusive atmosphere, a constituent that is heavier than the mean mass will be enhanced by an upward vertical wind and reduced by a downward wind. The opposite holds true for the lighter helium gas, where upwelling decreases helium densities and downwelling increases the densities [Reber, 1976]. This fact has been captured by space-based observing platforms. Figure 6.11 is an example of helium number density data from the OGO-6 satellite normalized to a model atmosphere during a geomagnetic storm. The time series depicted in Fig. 6.11 map out the energy processes occurring around 400 km, with N_2 tracking the temperature

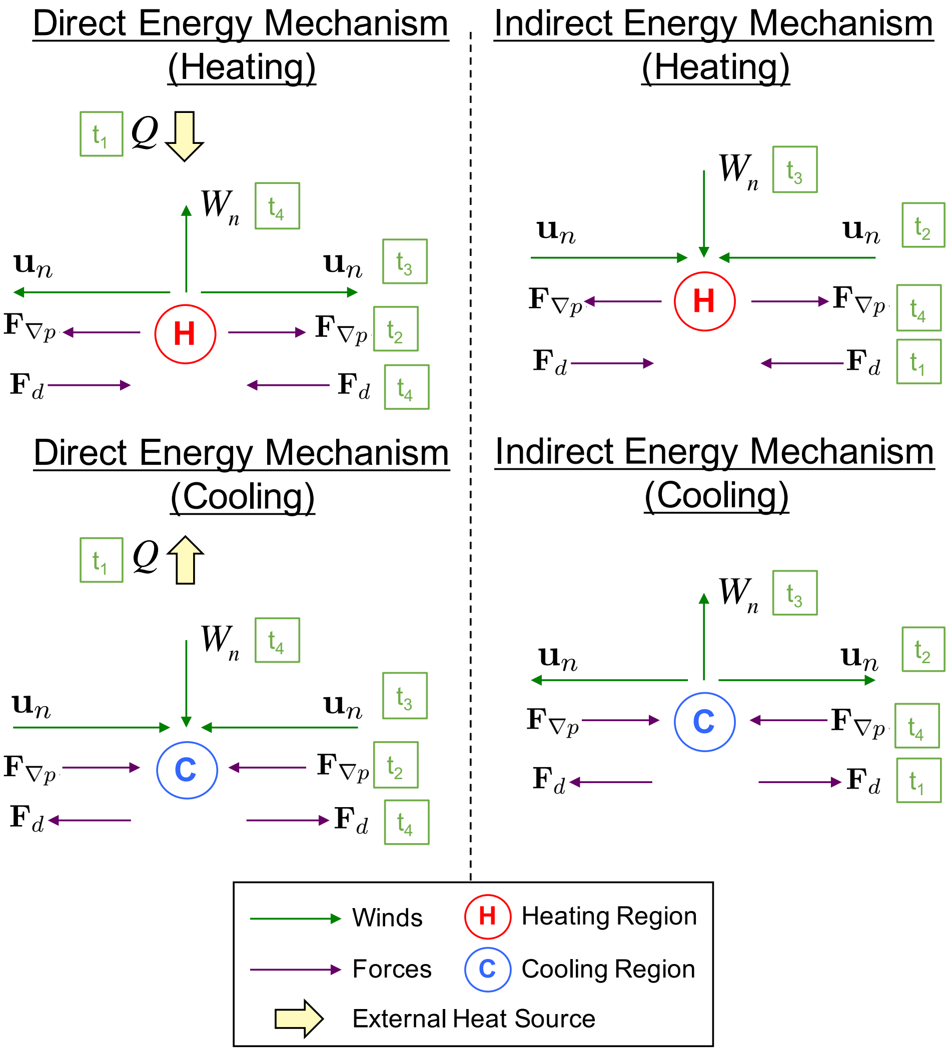

Figure 6.10: Heuristic depictions of circulation patterns and force vectors for direct and indirect energy mechanisms that lead to heating and cooling, where t represents the sequence of events in time.

variations and helium tagging along the vertical wind motions. The anti-correlation between helium concentration and vertical winds and the indifference of helium to thermal changes, makes it an ideal tracer for wind dynamics and an advantageous detector for a dynamically induced energy mechanism.

It is worth noting that the anti-correlated connection between helium and vertical motion is not one-to-one because vertical wind effects on helium are a column-integrated effect. In order to transport helium, vertical motion must distort the vertical profile of helium from diffusive equilibrium. Thus, vertical wind speeds need to be significant relative to the local diffusion velocity [Reber, 1976], and these velocities vary with altitude (i.e., diffusion environments depend on altitude). This caveat to the helium-wind relationship is the reason why in Fig. 6.9, there are upwelling and downwelling regions that are not reflected in the helium number densities. Figure 6.11 also reveals the rapid response of the neutral gas to magnetic activity [Reber, 1976]. This demonstrates that it does not take long for helium to react to neutral wind changes and for neutral structures to develop when spurred by a disturbance in the system.

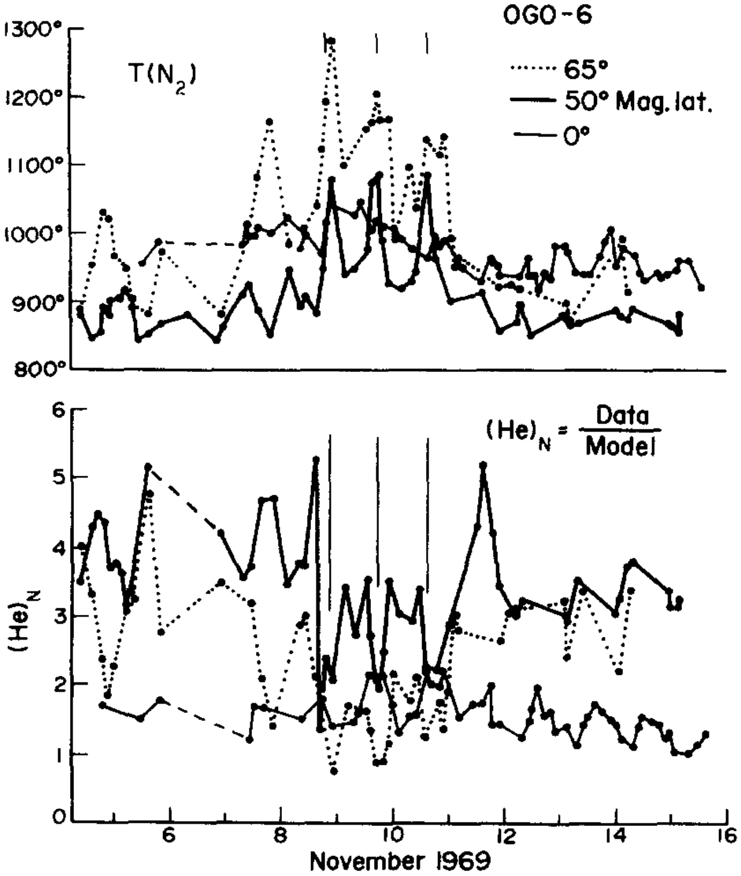

Figure 6.11: From Reber [1976]: Exospheric temperature (deduced from measured N_2 densities) and normalized helium densities at 0°, 50° and 65° magnetic latitude as a function of time. The three narrow vertical lines represent times of enhanced magnetic activity.

The observations in Fig. 6.11 highlight the promising utility of helium as a diagnostic for wind dynamics. If neutral temperature and helium number densities are measured, then the sources of upper thermospheric anomalies can potentially be uncovered. This procedure is demonstrated through the TIEGCM simulations in Fig. 6.9. Between -70° and 70° latitude, the patterns in the vertical wind, adiabatic heating, and helium indicate that an indirect, dynamically induced mechanism is responsible for the neutral temperature and mass density structures. For example, between 12:00 to 18:00 LT, there is a warming and enhanced neutral mass density region with a downwards change in the vertical wind, an increase in helium, and adiabatic warming. According to Fig. 6.10, this group of events corresponds to an indirect energy mechanism that results in heating. Evidence for an indirect energy mechanism that results in cooling is prominently shown in the postmidnight hours until about 5:00 LT. However, regions poleward of 70° latitude in the northern and southern hemispheres display behavior consistent with a direct energy mechanism that leads to cooling. The cooling and depletion in neutral mass density occurs in conjunction with a downwards change in the vertical wind and adiabatic heating, pointing to a direct energy mechanism as the culprit for the structures in the neutral gas.

Figure 6.12 is a decision tree for inferring the type of energy mechanism responsible for the neutral temperature and associated neutral mass density structure, along with the primary drag force that is operating on the neutral gas. For example, in Fig. 6.11, T_n increases as n_{He} decreases during times of intense geomagnetic activity. According to Fig. 6.12, a diverging relationship between neutral temperature and helium points to a net direct energy mechanism as the cause for the neutral disturbances. Energy from the magnetosphere is directly deposited into the I/T system, leaving a unique imprint on the neutral gas that is deciphered by the variations in T_n and n_{He}. If signatures of a net indirect energy mechanism are observed, and the spatial swath of the measurements are sufficient, then the drag force governing the wind motion can be deduced from the horizontal gradient in neutral temperature.

It is prudent to address the limitations of using Figs. 6.10 and 6.12 to pinpoint the sources of neutral temperature and mass density structure. The TIEGCM numerical experiments are performed in controlled settings that allow for the complete separation and isolation of direct and indirect energy processes. However, in reality, the I/T environment is deeply interweaved and

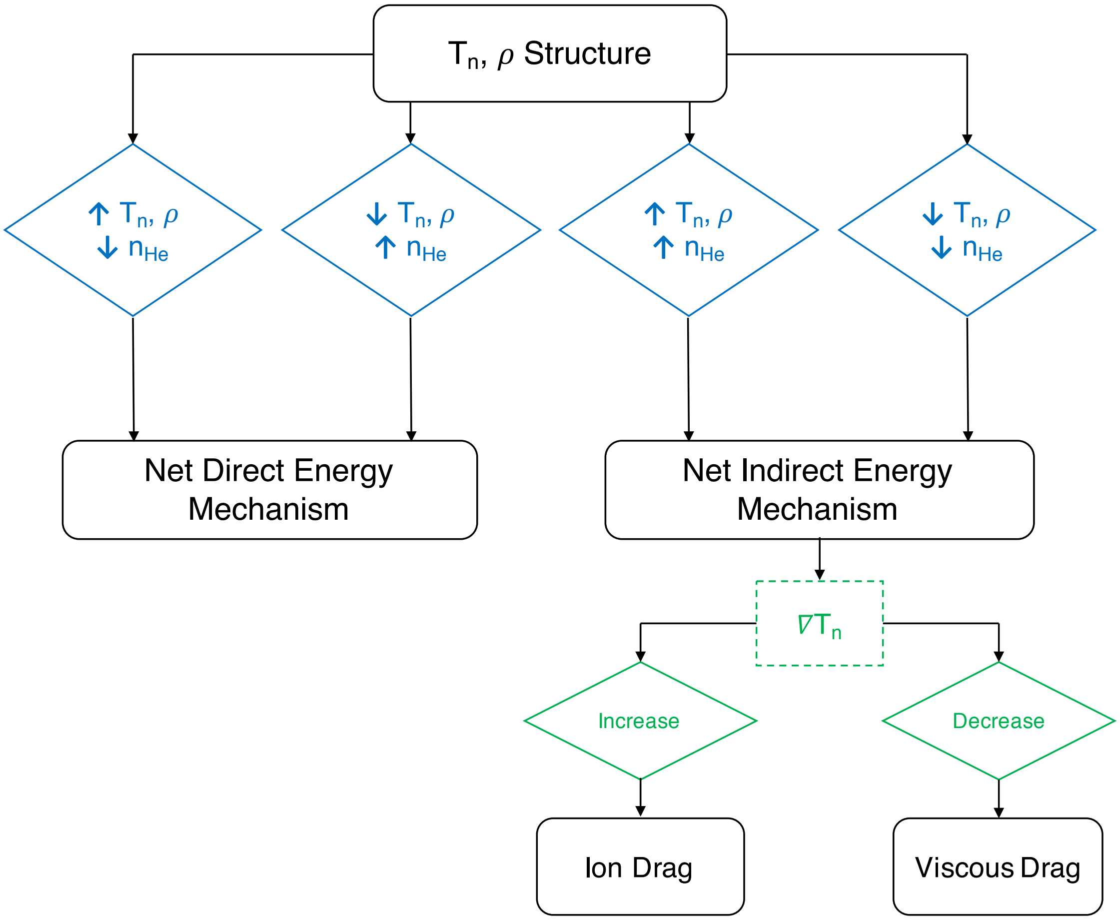

Figure 6.12: Flow diagram outlining roots of neutral temperature and mass density structures, where the triangles are used as guidelines to determine the kind of net energy mechanism (blue) and the primary neutral drag force (green).

only net mechanisms can be inferred. For example, if a satellite observes neutral temperature and helium signatures of a net direct energy mechanism, this does not preclude the possibility of an indirect energy process happening simultaneously. If a warming region is observed with a depletion in helium, an indirect energy mechanism could offset the strength of the direct energy mechanism, thereby weakening the neutral temperature and mass density effects. However, the direct energy heating is the net energy mechanism, and it is not possible to determine if a secondary, indirect energy mechanism is also influencing the neutral gas structure from the criteria in Fig. 6.12.

The processes that encompass an external, direct energy mechanism and an internal, indirect energy mechanism are different, and the impressions they etch onto the properties of the upper thermosphere can be distinguished. An indirect, dynamically induced energy mechanism can be further inspected by ascertaining the neutral drag force environment. Using helium as a dynamic tracer enables compelling conclusions to be discovered from analyzing two key properties: neutral temperature and helium number density. The findings from this chapter add to the knowledge base of assessing energy modifiers in the geospace system, facilitating the interpretation of data from past, current, and future thermospheric missions exploring the region above the Earth's "thermopause."

Chapter 7

Conclusions and Future Work

The energy budget of the Earth's I/T system is modulated by an energy mechanism that is initiated by momentum changes and powered through wind dynamics. The goal of this dissertation is to answer the overarching question of: **What is the impact of changes in neutral drag forces on properties of the upper thermosphere through an indirect, dynamically induced energy mechanism?** A series of TIEGCM simulations are used to address this question by evaluating how changes in the field-aligned ion drag force contributes to the formation of upper atmospheric phenomena (e.g., the ETA); weighing the importance of ion drag versus viscous drag and how this interplay can shape neutral structure; and assessing the altitudinal extent of the indirect, wind-driven energy mechanism and the prospect of utilizing helium as a component of an effective procedure to unravel and illuminate the concoction of energy processes occurring in the upper thermosphere.

Chapters 4, 5, and 6 of this thesis address the science questions asked in Section 1.6. The discussion below succinctly answers these questions by summarizing the major findings of this dissertation work.

(1) **How can a drag force contribute to the formation of a thermospheric neutral mass density and temperature anomaly?**

Changes to the ion drag force precipitate an indirect, dynamically induced energy mechanism that creates the trough of the equatorial thermosphere anomaly, and this process is tied to the local time and solar cycle variations in ion drag.

The addition of field-aligned ion drag into the TIEGCM causes a divergence in the meridional winds, an upwards change in the vertical winds, adiabatic cooling, and a trough in neutral temperature over the magnetic equator near 400 km. The local time and solar cycle dependence of the ETA strongly correlates with the variations in the EIA, with the ETA trough beginning to disappear in the late evening, and with the feature becoming more evident with increased solar activity. Electron density concentration is the main factor controlling ETA trough local and solar cycle variations, but secondary structure is produced by the plasma scale height and gradients in electron density and plasma temperature.

(2) **What are the thermospheric consequences of the complex interplay between drag forces?**

The neutral structure of the quiet-time upper thermosphere is greatly contingent upon the competition between ion and viscous drag forces, where each force produces different sustained structure in winds, mass, pressure gradients, and thermal energy.

Viscous drag generates a more divergent wind field than ion drag, thereby smearing the day-night temperature gradient through efficient adiabatic cooling on the dayside and adiabatic heating on the nightside. In solar maximum, the ion drag force is dominant and confines wind and temperature structure to narrow regions that creates substantial gradients in the energy distribution. In solar minimum, viscous drag becomes a primary drag force and it acts to neutralize thermal gradients through enhanced divergences in the horizontal wind, increased vertical motion, and stronger adiabatic heating and cooling.

(3) **What are the signatures of an indirect, dynamically induced energy mechanism in the thermosphere?**

The effects of a wind-induced energy mechanism on the neutral gas and maintained by ion and viscous drag extend to the "thermopause" boundary layer, and its characteristics in helium and neutral temperature are distinct and separable from a direct energy mechanism from a net perspective.

The “thermopause” signifies the edge of influence for a mechanism that alters energy via wind motion instituted by drag forces in the neutral momentum equation. It partitions a region where perturbations to the neutral gas can be persistent, the upper thermosphere, from an area where neutral displacements are quickly dampened, the lower thermosphere. The inverse relationship between vertical winds and helium number density allows for the parsing of direct versus indirect energy processes. Observing platforms that measure helium and neutral temperature can potentially supply evidence of a net indirect, dynamically induced energy mechanism, and also provide hints as to the primary drag force responsible for the structure of the upper atmosphere.

7.1 Future Work

The work of this dissertation establishes the impact of an indirect and dynamically induced energy mechanism on the properties of the Earth’s quiet-time upper thermosphere, emanating from the feedback loop between momentum and energy through neutral wind dynamics. It revisits elemental physical processes that were thought to be adequately understood, and reveals underlying concepts that have broad implications on basic science research of the upper atmosphere.

A straightforward follow-up to this work is to complement the numerical simulations with clear evidence of this indirect energy mechanism in observations. As mentioned in Section 1.5.4, the DE-2 dataset provides comprehensive measurements of plasma and neutral properties, and it is ripe for a re-analysis study that can use the groundwork achieved through the model studies in this thesis in order to effectively recognize differing energy mechanisms in the data, thereby bringing the aeronomy field a few steps closer to successfully excavating the root causes of various upper atmospheric phenomena. Although this work will certainly benefit from traditional thermospheric missions with large footprints in space, a suite of cubesats may be the ideal observing platform for these types of studies, as few measurements are needed (essentially only helium number densities and neutral temperature) and greater spatial coverage is desired.

Another logical avenue for future study is to investigate how the results from this dissertation vary with increased levels of geomagnetic activity and tidal effects. This thesis work is concerned with quiet-time conditions, as a baseline needs to be settled before moving on to more convoluted situations. Geomagnetic storms add in the influence of an external energy source and affect the behavior of the neutral drag forces. Also, tidal forcings from below could potentially have a significant effect on this energy process that is intimately connected to the drag forces, as tides and waves can change the electron densities and vertical shears in the wind, thus modifying ion and viscous drag. Therefore, it is imperative to extend the conclusions of this dissertation to examine how the indirect, dynamically induced energy mechanism detailed in this thesis interacts with the other two main energy drivers of the geospace system.

Finally, it would be worthwhile to widen the results presented in this thesis to other planetary atmospheres. It is essential to human curiosity and exploration to apply the science found on Earth to other bodies in the solar system. Comparative aeronomy is an active topic of research, and the same fundamental physical principles described in this work will apply to the atmospheres of other planets. For example, a recent study by Stallard et al. [2016] discovered a localized, quasi-stable cold spot in Jupiter's upper atmosphere, a Great Cold Spot, while observing emission lines from a ground-based telescope. They conclude that this feature cannot be driven by the atmosphere below the ionosphere or by direct interactions with magnetosphere, suggesting that the cold spot originates from processes that occur within the thermosphere. It is purported that heating in the auroral region and plasma convection generate vortex structures that spawns secondary circulations resulting in adiabatic cooling of the vortex core, forming a Great Cold Spot. This indirect, dynamically induced energy mechanism is astonishingly similar to the wind-driven energy processes that occur on Earth, solidifying the breadth of this subject matter and illuminating the exciting research paths that emerge from this dissertation work.

Bibliography

Anderson, C., Conde, M., and McHarg, M. G. (2012). Neutral thermospheric dynamics observed with two scanning Doppler imagers: 2. Vertical winds. Journal of Geophysical Research, 117(A3):A03305.

Bell, J. M., Bougher, S. W., Mahaffy, P., and Elrod, M. (2015). Simulating Helium abundances in the Martian upper atmosphere using 1-D and 3-D models. In AAS/Division for Planetary Sciences Meeting Abstracts, volume 47 of AAS/Division for Planetary Sciences Meeting Abstracts, page 419.21.

Bird, G. A. (1994). Molecular Gas Dynamics and the Direct Simulation of Gas Flows. Oxford University Press.

Bittencourt, J. A. (2010). Fundamentals of Plasma Physics. Springer-Verlag.

Bougher, S. W., Roble, R. G., and Fuller-Rowell, T. (2002). Simulations of the Upper Atmospheres of the Terrestrial Planets, pages 261–288. American Geophysical Union.

Burke, W. J. (2011). Solar cycle dependence of solar wind energy coupling to the thermosphere. Journal of Geophysical Research: Space Physics, 116(A6):n/a–n/a. A06302.

Burrell, a. G., Heelis, R. a., and Stoneback, R. a. (2011). Latitude and local time variations of topside magnetic field-aligned ion drifts at solar minimum. Journal of Geophysical Research, 116(A11):A11312.

Cageao, R. and Kerr, R. (1984). Global distribution of helium in the upper atmosphere during solar minimum. Planetary and Space Science, 32(12):1523 – 1529.

Chen, G.-m., Xu, J., Wang, W., and Burns, A. G. (2014). A comparison of the effects of cir- and cme-induced geomagnetic activity on thermospheric densities and spacecraft orbits: Statistical studies. Journal of Geophysical Research: Space Physics, 119(9):7928–7939. 2014JA019831.

Clausen, L. B. N., Milan, S. E., and Grocott, A. (2014). Thermospheric density perturbations in response to substorms. Journal of Geophysical Research: Space Physics, 119(6):4441–4455.

Clemmons, J. H., Walterscheid, R. L., Christensen, a. B., and Bishop, R. L. (2013). Rapid, highly structured meridional winds and their modulation by non migrating tides: Measurements from the Streak mission. Journal of Geophysical Research: Space Physics, 118(2):866–877.

Crowley, G., Knipp, D. J., Drake, K. A., Lei, J., Sutton, E., and Lhr, H. (2010). Thermospheric density enhancements in the dayside cusp region during strong by conditions. Geophysical Research Letters, 37(7):n/a–n/a. L07110.

Demars, H. and Schunk, R. (2007). Thermospheric response to ion heating in the dayside cusp. Journal of Atmospheric and Solar-Terrestrial Physics, 69(6):649 – 660.

Deng, Y., Fuller-Rowell, T. J., Ridley, A. J., Knipp, D., and Lopez, R. E. (2013). Theoretical study: Influence of different energy sources on the cusp neutral density enhancement. Journal of Geophysical Research: Space Physics, 118(5):2340–2349.

Deng, Y., Maute, A., Richmond, A. D., and Roble, R. G. (2008). Analysis of thermospheric response to magnetospheric inputs. Journal of Geophysical Research: Space Physics, 113(A4):n/a–n/a. A04301.

Dickinson, R. E., Roble, R. G., and Ridley, E. C. (1971). Response of the Neutral Thermosphere at F-Layer Heights to Interaction of a Global Wind with Anomalies of Ionization. Journal of the Atmospheric Sciences, 28(7):1280–1293.

Eastes, R. W., Mcclintock, W. E., Codrescu, M. V., Aksnes, A., Anderson, D. N., Andersson, L., Baker, D. N., Burns, A. G., Budzien, S. A., Daniell, R. E., Dymond, K. F., Eparvier, F. G., Harvey, J. E., Immel, T. J., Krywonos, A., Lankton, M. R., Lumpe, J. D., Prösss, G. W., Richmond, A. D., Rusch, D. W., Siegmund, O. H., Solomon, S. C., Strickland, D. J., and Woods, T. N. (2013). Global-Scale Observations of the Limb and Disk (Gold): New Observing Capabilities for the Ionosphere-Thermosphere, pages 319–326. American Geophysical Union.

Emmert, J. (2015). Thermospheric mass density: A review. Advances in Space Research, 56(5):773 – 824.

Emmert, J., Byers, J., Warren, H., and Segerman, A. (2014). Propagation of forecast errors from the sun to leo trajectories: How does drag uncertainty affect conjunction frequency? Open file rep., AMOS Conference, Maui, Hawaii.

Evonosky, W., Richmond, A. D., Fang, T.-W., and Maute, A. (2016). Ion-neutral coupling effects on low-latitude thermospheric evening winds. Journal of Geophysical Research: Space Physics, 121(5):4638–4646. 2016JA022382.

Fuller-Rowell, A. and Schrijver, C. (2009). On the ionosphere and chromosphere, pages 324–359. Cambridge University Press.

Fuller-Rowell, T. (2014). Physical Characteristics and Modeling of Earth's Thermosphere, pages 13–27. John Wiley & Sons, Ltd.

Fuller-Rowell, T., Codrescu, M., Fejer, B., Borer, W., Marcos, F., and Anderson, D. (1997). Dynamics of the low-latitude thermosphere: Quiet and disturbed conditions. Journal of Atmospheric and Solar-Terrestrial Physics, 59(13):1533–1540.

Fuller-Rowell, T., Matsuo, T., Codrescu, M., and Marcos, F. (1999). Modeling thermospheric neutral density waves and holes in response to high latitude forcing. Advances in Space Research, 24(11):1447 – 1458. Ionospheric/Thermospheric/Mesospheric Coupling.

Gagnepain, J., Crochet, M., and Richmond, A. (1977). Comparison of equatorial electrojet models. Journal of Atmospheric and Terrestrial Physics, 39(9):1119 – 1124.

Hagan, M. E. and Forbes, J. (2002). Migrating and nonmigrating diurnal tides in the middle and upper atmosphere excited by tropospheric latent heat release. Journal of Geophysical Research, 107(D24):4754.

HAO (2011). TIEGCM V1.94 Model Description. Technical report, Natl. Cent. Atmos. Res, Boulder, CO.

Hedin, A. E. and Mayr, H. G. (1973). Magnetic control of the near equatorial neutral thermosphere. Journal of Geophysical Research, 78(10):1688–1691.

Heelis, R. A., Lowell, J. K., and Spiro, R. W. (1982). A model of the high-latitude ionospheric convection pattern. Journal of Geophysical Research: Space Physics, 87(A8):6339–6345.

Hoffman, R. A. (1988). The magnetosphere, ionosphere, and atmosphere as a system: Dynamics explorer 5 years later. Reviews of Geophysics, 26(2):209–214.

Holton, J. R. (1992). An Introduction to Dynamic Meteorology. Academic Press.

Hsu, V. W., Thayer, J. P., Lei, J., and Wang, W. (2014). Formation of the equatorial thermosphere anomaly trough: Local time and solar cycle variations. Journal of Geophysical Research: Space Physics, 119(12):10,456–10,473.

Hsu, V. W., Thayer, J. P., Wang, W., and Burns, A. (2016). New insights into the complex interplay between drag forces and its thermospheric consequences. Journal of Geophysical Research: Space Physics, pages n/a–n/a. 2016JA023058.

Huang, Y., Richmond, A. D., Deng, Y., and Roble, R. (2012). Height distribution of joule heating and its influence on the thermosphere. Journal of Geophysical Research: Space Physics, 117(A8):n/a–n/a. A08334.

Huba, J. D., Joyce, G., and Fedder, J. A. (2000). Sami2 is Another Model of the Ionosphere (SAMI2): A new low-latitude ionosphere model. Journal of Geophysical Research, 105(A10):23035.

Joshi, P. P., H. Baker, J. B., Ruohoniemi, J. M., Makela, J. J., Fisher, D. J., Harding, B. J., Frissell, N. A., and Thomas, E. G. (2015). Observations of storm time midlatitude ion-neutral coupling using superdarn radars and nation fabry-perot interferometers. Journal of Geophysical Research: Space Physics, 120(10):8989–9003. 2015JA021475.

Kervalishvili, G. N. and Lühr, H. (2013). The relationship of thermospheric density anomaly with electron temperature, small-scale fac, and ion up-flow in the cusp region, as observed by champ and dmsp satellites. Annales Geophysicae, 31(3):541–554.

Killeen, T. L. and Roble, R. G. (1984). An analysis of the high-latitude thermospheric wind pattern calculated by a thermospheric general circulation model: 1. momentum forcing. Journal of Geophysical Research: Space Physics, 89(A9):7509–7522.

Killeen, T. L. and Roble, R. G. (1988). Thermosphere dynamics: Contributions from the first 5 years of the dynamics explorer program. Reviews of Geophysics, 26(2):329–367.

Knipp, D., Tobiska, W., and Emery, B. (2004). Direct and indirect thermospheric heating sources for solar cycles 2123. Solar Physics, 224(1-2):495–505.

Knipp, D. J. (2011). Understanding Space Weather and the Physics Behind It. McGraw Hill.

Kondo, T., Richmond, A. D., Liu, H., Lei, J., and Watanabe, S. (2011). On the formation of a fast thermospheric zonal wind at the magnetic dip equator. Geophysical Research Letters, 38(10):n/a–n/a. L10101.

Kundu, P. K. (2004). Fluid Mechanics. Elsevier Academic Press.

Kwak, Y.-S. and Richmond, A. D. (2007). An analysis of the momentum forcing in the high-latitude lower thermosphere. Journal of Geophysical Research: Space Physics, 112(A1):n/a–n/a. A01306.

Larsen, M. F. and Meriwether, J. W. (2012). Vertical winds in the thermosphere. Journal of Geophysical Research, 117(A9):A09319.

Larsen, M. F. and Mikkelsen, I. S. (1983). The dynamic response of the high-latitude thermosphere and geostrophic adjustment. Journal of Geophysical Research: Space Physics, 88(A4):3158–3168.

Leake, J., DeVore, C., Thayer, J., Burns, A., Crowley, G., Gilbert, H., Huba, J., Krall, J., Linton, M., Lukin, V., and Wang, W. (2014). Ionized plasma and neutral gas coupling in the suns chromosphere and earths ionosphere/thermosphere. Space Science Reviews, 184(1-4):107–172.

Lei, J., Thayer, J. P., and Forbes, J. M. (2010). Longitudinal and geomagnetic activity modulation of the equatorial thermosphere anomaly. Journal of Geophysical Research, 115(A8):A08311.

Lei, J., Thayer, J. P., Wang, W., Luan, X., Dou, X., and Roble, R. (2012a). Simulations of the equatorial thermosphere anomaly: Physical mechanisms for crest formation. Journal of Geophysical Research, 117(A6):A06318.

Lei, J., Thayer, J. P., Wang, W., Richmond, A. D., Roble, R., Luan, X., Dou, X., Xue, X., and Li, T. (2012b). Simulations of the equatorial thermosphere anomaly: Field-aligned ion drag effect. Journal of Geophysical Research, 117(A1):A01304.

Lei, J., Thayer, J. P., Wang, W., Yue, J., and Dou, X. (2014a). Nonmigrating tidal modulation of the equatorial thermosphere and ionosphere anomaly. Journal of Geophysical Research: Space Physics, 119(4):3036–3043.

Lei, J., Wang, W., Thayer, J. P., Luan, X., Dou, X., Burns, A. G., and Solomon, S. C. (2014b). Simulations of the equatorial thermosphere anomaly: Geomagnetic activity modulation. Journal of Geophysical Research: Space Physics, 119(8):6821–6832.

Liu, H., Lühr, H., Henize, V., and Köhler, W. (2005). Global distribution of the thermospheric total mass density derived from CHAMP. Journal of Geophysical Research, 110(A4):A04301.

Liu, H., Lühr, H., and Watanabe, S. (2007). Climatology of the equatorial thermospheric mass density anomaly. Journal of Geophysical Research, 112(A5):A05305.

Liu, J., Liu, L., Zhao, B., Lei, J., and Wan, W. (2011). On the relationship between the post-midnight thermospheric equatorial mass anomaly and equatorial ionization anomaly under geomagnetic quiet conditions. Journal of Geophysical Research: Space Physics, 116(A12):n/a–n/a. A12312.

Liu, J., Wang, W., Burns, A., Yue, X., Zhang, S., Zhang, Y., and Huang, C. (2016). Profiles of ionospheric storm-enhanced density during the 17 march 2015 great storm. Journal of Geophysical Research: Space Physics, 121(1):727–744. 2015JA021832.

Lühr, H., Rother, M., Khler, W., Ritter, P., and Grunwaldt, L. (2004). Thermospheric up-welling in the cusp region: Evidence from champ observations. Geophysical Research Letters, 31(6):n/a–n/a. L06805.

Ma, R., Xu, J., Wang, W., Lei, J., Liu, H.-L., Maute, A., and Hagan, M. E. (2010). Variations of the nighttime thermospheric mass density at low and middle latitudes. Journal of Geophysical Research: Space Physics, 115(A12):n/a–n/a. A12301.

Ma, T.-Z. and Schunk, R. W. (1995). Effect of polar cap patches on the polar thermosphere. Journal of Geophysical Research: Space Physics, 100(A10):19701–19713.

Ma, T.-Z. and Schunk, R. W. (2001). The effects of multiple propagating plasma patches on the polar thermosphere. Journal of Atmospheric and Solar-Terrestrial Physics, 63(4):355 – 366.

Mannucci, A. J., Tsurutani, B. T., Iijima, B. A., Komjathy, A., Saito, A., Gonzalez, W. D., Guarnieri, F. L., Kozyra, J. U., and Skoug, R. (2005). Dayside global ionospheric response to the major interplanetary events of october 29?30, 2003 ?halloween storms? Geophysical Research Letters, 32(12):n/a–n/a. L12S02.

Maruyama, N., Watanabe, S., and Fuller-Rowell, T. J. (2003). Dynamic and energetic coupling in the equatorial ionosphere and thermosphere. Journal of Geophysical Research, 108(A11):1396.

Mayr, H. G. and Harris, I. (1978). Some characteristics of electric field momentum coupling with the neutral atmosphere. Journal of Geophysical Research: Space Physics, 83(A7):3327–3336.

Miyoshi, Y., Fujiwara, H., Jin, H., Shinagawa, H., Liu, H., and Terada, K. (2011). Model study on the formation of the equatorial mass density anomaly in the thermosphere. Journal of Geophysical Research, 116(A5):A05322.

Müller, S., Lühr, H., and Rentz, S. (2009). Solar and magnetospheric forcing of the low latitude thermospheric mass density as observed by champ. Annales Geophysicae, 27(5):2087–2099.

Pant, T. K. and Sridharan, R. (2001). Plausible explanation for the equatorial temperature and wind anomaly (ETWA) based on chemical and dynamical processes. Journal of Atmospheric and Solar-Terrestrial Physics, 63(9):885–891.

Parkinson, C. (2016). Monitoring Saturn's Upper Atmosphere Density Variations Using Helium 584 Å Airglow. In AAS/Division for Planetary Sciences Meeting Abstracts, volume 48 of AAS/Division for Planetary Sciences Meeting Abstracts, page 514.10.

Prölss, G. (2004). Physics of the Earth's Space Environment. Springer-Verlag.

Prölss, G. W. (1980). Magnetic storm associated perturbations of the upper atmosphere: Recent results obtained by satellite-borne gas analyzers. Reviews of Geophysics, 18(1):183–202.

Prölss, G. W. (2011). Density perturbations in the upper atmosphere caused by the dissipation of solar wind energy. Surveys in Geophysics, 32(2):101–195.

Qian, L., Burns, A. G., Emery, B. A., Foster, B., Lu, G., Maute, A., Richmond, A. D., Roble, R. G., Solomon, S. C., and Wang, W. (2014). The NCAR TIE-GCM, pages 73–83. John Wiley & Sons, Ltd.

Qian, L. and Solomon, S. C. (2012). Thermospheric density: An overview of temporal and spatial variations. Space Science Reviews, 168(1):147–173.

Qian, L., Solomon, S. C., and Kane, T. J. (2009). Seasonal variation of thermospheric density and composition. Journal of Geophysical Research: Space Physics, 114(A1):n/a–n/a. A01312.

Raghavarao, R., Hoegy, W. R., Spencer, N. W., and Wharton, L. E. (1993). Neutral temperature anomaly in the equatorial thermosphere-A source of vertical winds. Geophysical Research Letters, 20(11):1023–1026.

Raghavarao, R. and Suhasini, R. (2002). Equatorial temperature and wind anomaly (ETWA)a review. Journal of Atmospheric and Solar-Terrestrial Physics, 64(12-14):1371–1381.

Raghavarao, R., Suhasini, R., Hoegy, W., Mayr, H., and Wharton, L. (1998). Local time variation of equatorial temperature and zonal wind anomaly (ETWA). Journal of Atmospheric and Solar-Terrestrial Physics, 60(6):631–642.

Raghavarao, R., Wharton, L. E., Spencer, N. W., Mayr, H. G., and Brace, L. H. (1991). An equatorial temperature and wind anomaly (ETWA). Geophysical Research Letters, 18(7):1193–1196.

Reber, C. A. (1976). Dynamical effects in the distribution of helium in the thermosphere. Journal of Atmospheric and Terrestrial Physics, 38(8):829 – 840.

Richmond, A. D. (1971). Tidal winds at ionospheric heights. Radio Science, 6(2):175–189.

Richmond, A. D. (1983). Thermospheric dynamics and electrodynamics. In Solar-Terrestrial Physics, pages 523–607. Springer.

Richmond, A. D. (1995a). Ionospheric Electrodynamics, pages 249–290. CRC Press, Inc.

Richmond, A. D. (1995b). Ionospheric Electrodynamics Using Magnetic Apex Coordinates. Journal of geomagnetism and geoelectricity, 47(2):191–212.

Richmond, A. D. (2016). Ionospheric Electrodynamics, pages 245–259. CRC Press, Inc.

Richmond, A. D. and Kamide, Y. (1988). Mapping electrodynamic features of the high-latitude ionosphere from localized observations: Technique. Journal of Geophysical Research: Space Physics, 93(A6):5741–5759.

Richmond, A. D. and Maute, A. (2014). Ionospheric Electrodynamics Modeling, pages 57–71. John Wiley & Sons, Ltd.

Richmond, A. D., Ridley, E. C., and Roble, R. G. (1992). A thermosphere/ionosphere general circulation model with coupled electrodynamics. Geophysical Research Letters, 19(6):601–604.

Richmond, A. D. and Thayer, J. P. (2000). Ionospheric Electrodynamics: A Tutorial, pages 131–146. American Geophysical Union.

Rider, K., Immel, T., Taylor, E., and Craig, W. (2015). Icon: Where earth's weather meets space weather. In 2015 IEEE Aerospace Conference, pages 1–10.

Rishbeth, H. (1971a). The f-layer dynamo. Planetary and Space Science, 19(2):263 – 267.

Rishbeth, H. (1971b). Polarization fields produced by winds in the equatorial f-region. Planetary and Space Science, 19(3):357 – 369.

Rishbeth, H. (1979a). Ion-drag effects in the thermosphere. Journal of Atmospheric and Terrestrial Physics, 41(7):885 – 894.

Rishbeth, H. (1979b). Ion-drag effects in the thermosphere. Journal of Atmospheric and Terrestrial Physics, 41(7):885 – 894.

Rishbeth, H. (1981). The f-region dynamo. Journal of Atmospheric and Terrestrial Physics, 43(5):387 – 392.

Rishbeth, H. (1998). How the thermospheric circulation affects the ionospheric f2-layer. Journal of Atmospheric and Solar-Terrestrial Physics, 60(14):1385 – 1402.

Rishbeth, H. and Garriott, O. K. (1969). Introduction to Ionospheric Physics. Academic Press, Inc.

Roble, R. G., Dickinson, R. E., and Ridley, E. C. (1982). Global circulation and temperature structure of thermosphere with high-latitude plasma convection. Journal of Geophysical Research: Space Physics, 87(A3):1599–1614.

Roble, R. G., Ridley, E. C., Richmond, A. D., and Dickinson, R. E. (1988). A coupled thermosphere/ionosphere general circulation model. Geophysical Research Letters, 15(12):1325–1328.

Salby, M. L. (1996). Fundamentals of Atmospheric Physics. Academic Press.

Schlegel, K., Lühr, H., St.-Maurice, J.-P., Crowley, G., and Hackert, C. (2005). Thermospheric density structures over the polar regions observed with CHAMP. Annales Geophysicae, 23(5):1659–1672.

Schunk, R. and Nagy, A. (2009). Ionospheres: Physics, Plasma Physics, and Chemistry. Cambridge University Press.

Song, P., Gombosi, T. I., and Ridley, A. J. (2001). Three-fluid ohm's law. Journal of Geophysical Research: Space Physics, 106(A5):8149–8156.

St.-Maurice, J.-P. and Schunk, R. W. (1981). Ion-neutral momentum coupling near discrete high-latitude ionospheric features. Journal of Geophysical Research: Space Physics, 86(A13):11299–11321.

Stallard, T. S., Melin, H., Miller, S., Moore, L., O'Donoghue, J., Connerney, J. E. P., Satoh, T., West, R. A., Thayer, J. P., Hsu, V. W., and Johnson, R. E. (2016). The great cold spot in jupiter's upper atmosphere. Unpublished manuscript.

Sutton, E. K., Thayer, J. P., Wang, W., Solomon, S. C., Liu, X., and Foster, B. T. (2015). A self-consistent model of helium in the thermosphere. Journal of Geophysical Research: Space Physics, 120(8):6884–6900. 2015JA021223.

Thayer, J. P. and Killeen, T. L. (1993). A kinematic analysis of the high-latitude thermospheric neutral circulation pattern. Journal of Geophysical Research: Space Physics, 98(A7):11549–11565.

Thayer, J. P. and Semeter, J. (2004). The convergence of magnetospheric energy flux in the polar atmosphere. Journal of Atmospheric and Solar-Terrestrial Physics, 66(10):807 – 824. Upper Atmosphere Tutorials from the 2001 Joint {CEDAR} {SCOSTEP} Meeting.

Trinks, H., Mayr, H. G., and Philbrick, C. R. (1978). Momentum source signatures in thermospheric neutral composition. Journal of Geophysical Research: Space Physics, 83(A4):1641–1643.

Walterscheid, R. L. and Boucher Jr., J. (1984). A simple model of the transient response of the thermosphere to impulsive forcing. Journal of the Atmospheric Sciences, 41(6):1062–1072.

Walterscheid, R. L. and Crowley, G. (2015). Thermal cell structures in the high-latitude thermosphere induced by ion drag. Journal of Geophysical Research: Space Physics, 120(8):6837–6850. 2015JA021122.

Wang, W. (1998). A thermosphere-ionosphere nested grid (TING) model. Ph.D. thesis, Univ. of Mich., Ann Arbor.

Weimer, D. R. (2005). Improved ionospheric electrodynamic models and application to calculating joule heating rates. Journal of Geophysical Research: Space Physics, 110(A5):n/a–n/a. A05306.

Weimer, D. R., Bowman, B. R., Sutton, E. K., and Tobiska, W. K. (2011). Predicting global average thermospheric temperature changes resulting from auroral heating. Journal of Geophysical Research: Space Physics, 116(A1):n/a–n/a. A01312.

Zhang, B., Wang, W., Wu, Q., Knipp, D., Kilcommons, L., Brambles, O. J., Liu, J., Wiltberger, M., Lyon, J. G., and Hggstrm, I. (2016). Effects of magnetospheric lobe cell convection on dayside upper thermospheric winds at high latitudes. Geophysical Research Letters, 43(16):8348–8355. 2016GL069834.

Zhong, J., Wang, W., Yue, X., Burns, A. G., Dou, X., and Lei, J. (2016). Long-duration depletion in the topside ionospheric total electron content during the recovery phase of the march 2015 strong storm. Journal of Geophysical Research: Space Physics, pages n/a–n/a. 2016JA022469.

Appendix A

Glossary

Frequently used acronyms and variables are defined below for convenience, but note that all variables and symbols in this dissertation are described in the text where they are used.

I/T: Ionosphere-Thermosphere

TIEGCM: Thermosphere-Ionosphere-Electrodynamics General Circulation Model

NCAR: National Center for Atmospheric Research

ETA: Equatorial Thermosphere Anomaly

EIA: Equatorial Ionosphere Anomaly

TIMEGCM: Thermosphere-Ionosphere-Mesosphere-Electrodynamics General Circulation Model

GITM: Global Ionosphere-Thermosphere Model

$\mathbf{u}_n$ or $\mathbf{u}$: neutral wind velocity vector

$\mathbf{u}_i$: ion velocity vector

$\mathbf{F}_{ni}$: ion drag force

$\mathbf{F}_{vis}$: viscous drag force

$\mathbf{F}_{\nabla p}$: pressure gradient force

ρ: neutral mass density

T_n: neutral temperature

$\nabla \cdot \mathbf{u}_{n,h}$: divergence in the horizontal wind field

U_n: Zonal component of neutral wind

V_n: Meridional component of neutral wind

W_n or w: vertical component of neutral wind

ν_{ni}: neutral-ion collision frequency

$\frac{\mu}{\rho}$: kinematic viscosity coefficient

n_e: electron number density

n_{He}: helium number density

σ_P: Pedersen conductivity

σ_H: Hall conductivity

$\mathbf{B}$: Earth's magnetic field

$\mathbf{E}$: Electric field in Earth's frame of reference

$\mathbf{E}'$: Electric field in neutral wind frame of reference

Φ: geopotential

H: pressure scale height

g: gravitational acceleration

f: Coriolis parameter

R_E: radius of Earth

$\bar{R}$: universal gas constant

R: specific gas constant

c_p: specific heat at constant pressure

ω: TIEGCM “vertical velocity”

λ_{XX}, λ_{XY}, λ_{YY}, λ_{YX}: ion drag coefficients in the TIEGCM

λ: longitude

ϕ: latitude

Z: TIEGCM vertical coordinate

z: spatial vertical coordinate (i.e., height)

Appendix B

Supplemental Figures and Analysis: Plasma-neutral Coupling of the EIA and ETA Study

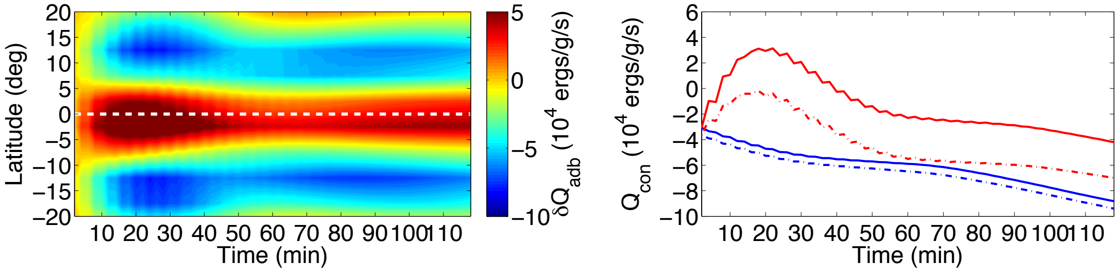

Figure B.1: Changes in heat conduction between runs 2 and 1 as a function of latitude (left panel), and heat conduction at ±2.5° geographic latitude from runs 1 and 2 (right panel), at the longitude 150°W and pressure surface 2.75 (around 400 km) during the first two hours of the model simulations (14:00-16:00 LT), where the white dashed line represents the magnetic equator at this longitude (around zero degrees geographic latitude).

B.1 Ionization Anomaly Scale Size Experiment

Dickinson et al. [1971] examined the response of the neutral thermosphere to an ion drag momentum source using a two-dimensional, steady-state model. They found that for a small-scale (∼100s km) ionization anomaly, the perturbations in winds and temperature were negligible and the perturbation ion drag force was almost completely balanced by the perturbation pressure gradient force (or the reactive pressure gradient force). For a large-scale (∼ 1000s km) ionization anomaly, there were significant perturbations in winds and temperature, and the perturbation pressure gradient force could not fully balance the perturbation ion drag force.

The TIEGCM was used to build upon the Dickinson et al. [1971] study by analyzing the neutral thermosphere response to anomalies of ionization with different scale sizes by creating an artificial ionization anomaly in the F-region. The artificial anomaly was constructed by linearly increasing electron density in a specified vertical range. Figure B.2 illustrates the linear function, B, used to describe the pressure level variation of the artificial ionization anomaly.

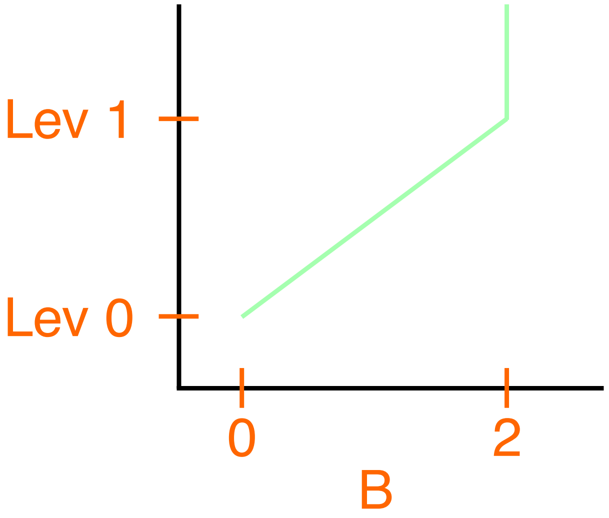

Figure B.2: Linear function (B) used for pressure level variation for artificial ionization anomaly in TIEGCM, where Lev1 and Lev2 are the lower and upper pressure levels of the anomaly, respectively.

Another function is created to express the latitude and longitude dependence of the ionization anomaly:

$$A_m = \cos\left[\pi\left(\frac{\phi - \phi_0}{\phi_m}\right)\right] \cdot \cos\left[\pi\left(\frac{\lambda - \lambda_0}{\lambda_m}\right)\right] \tag{B.1}$$

where λ_0 and ϕ_0 are the center longitude and latitude locations of the anomaly, respectively, and λ_m and ϕ_m are the longitude and latitude widths of the anomaly, respectively. The B function in Fig. B.2 is used with Eq. B.1 to represent the artificial ionization anomaly that is inputted into the TIEGCM:

$$n^*_{O+} = (1 + A_m \cdot B)\, n_{O+} \tag{B.2}$$

where n_{O+} is the number density of O^+ (assumed to be the dominant ion species in the F-region) and n^*_{O+} is the modified ion density, or the artificial ionization anomaly.

Figure B.3 shows an example of an artificial ionization anomaly in the TIEGCM placed at a specified location at around 300 km and solar maximum conditions.

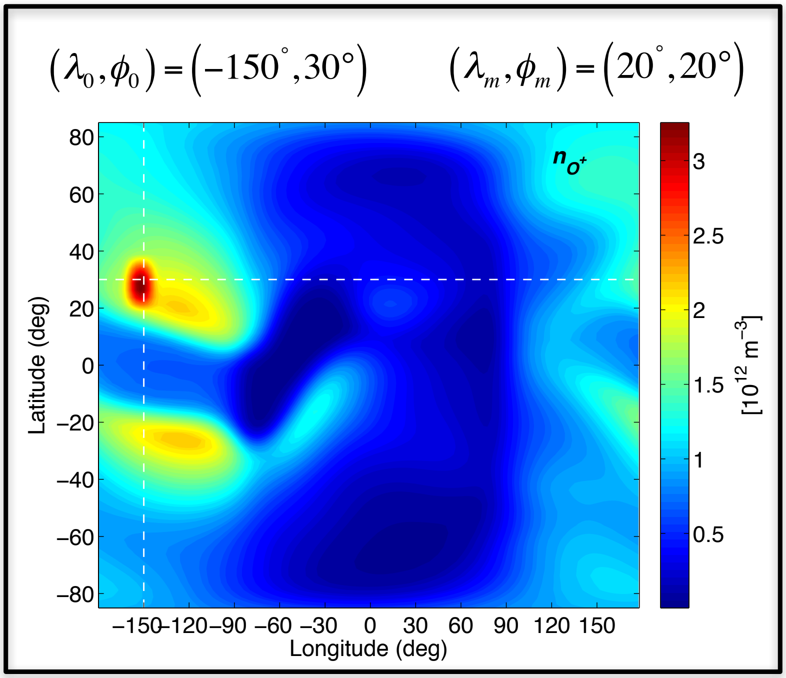

Figure B.3: O^+ number density as a function of latitude and longitude with artificial ionization anomaly placed at mid-latitudes and square width of 20° at ~300 km and F10.7 = 180.

Perturbations to the neutral thermosphere (differences between the runs with and without the artificial ionization anomaly) are analyzed for various ionization anomaly scale sizes, shown in Figs. B.4, B.5, and B.6.

From Figs. B.4, B.5, the artificial ionization anomaly causes downward plasma diffusion leading to a perturbation ion drag force. This force produces a convergence in the meridional winds, a downwards change in the vertical winds, and a pressure gradient force that acts to balance the meridional component of the perturbation ion drag force. As the horizontal scale of the ionization anomaly increases, the structure in the thermosphere response becomes stronger. For a small-scale ionization anomaly, the ion drag and pressure gradient forces are almost completely

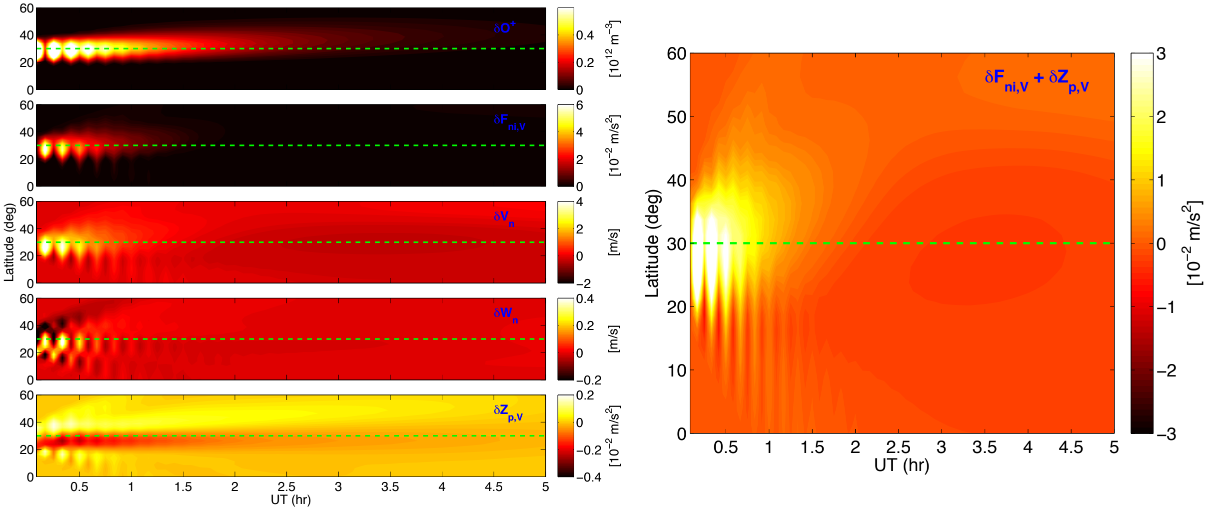

Figure B.4: (Left column) From top to bottom, changes in: O^+ number density, meridional ion drag force, meridional wind, vertical wind, and meridional pressure gradient force, and (Right column) Sum of meridional ion drag and pressure gradient forces as a function of latitude and universal time (representing 14:00-19:00 LT) for the 20°×20° artificial ionization anomaly shown in Fig. B.3

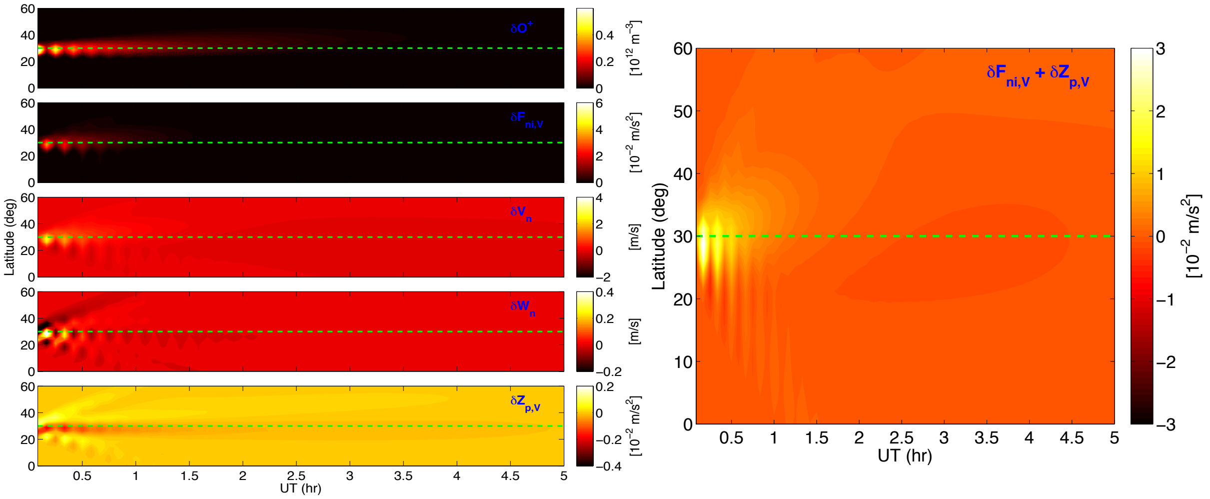

Figure B.5: Same as Fig. B.4 except for 10°×10° ionization anomaly.

balanced. The results from the ionization anomaly experiment are consistent with the conclusions from Dickinson et al. [1971], confirming the importance of scale-size of the ionospheric disturbance to the corresponding thermospheric response.

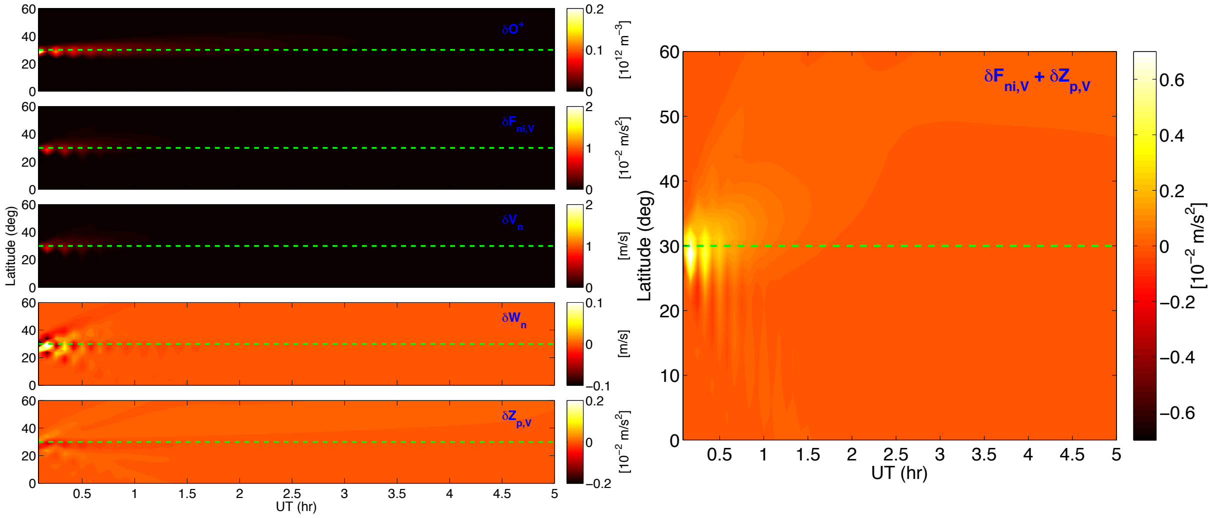

Figure B.6: Same as Fig. B.4 except for 5°×5° ionization anomaly.

Appendix C

Supplemental Figures and Analysis: Complex Interplay between Drag Forces Study

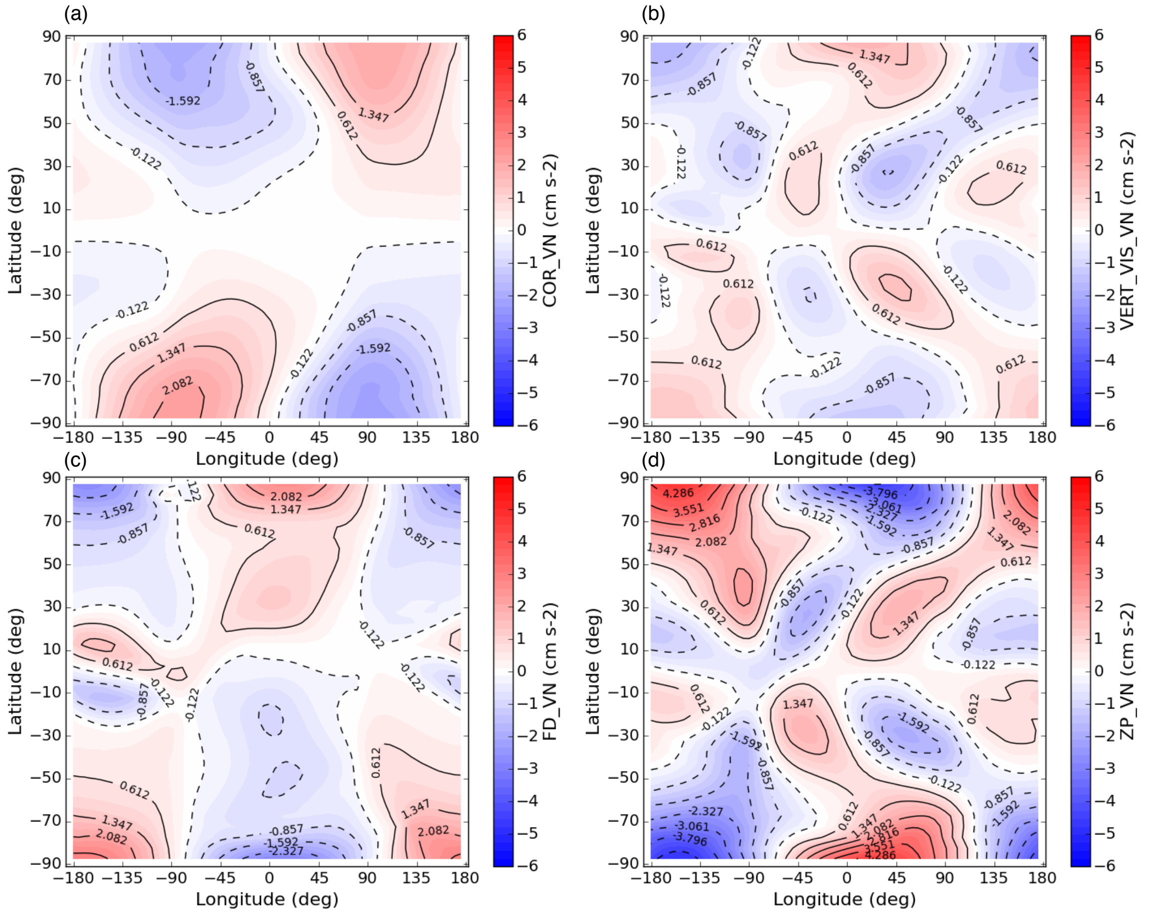

Figure C.1: Meridional (a) Coriolis force, (b) viscous drag force, (c) ion drag force, and (d) pressure gradient force for solar minimum conditions (paired with Fig. 5.11).

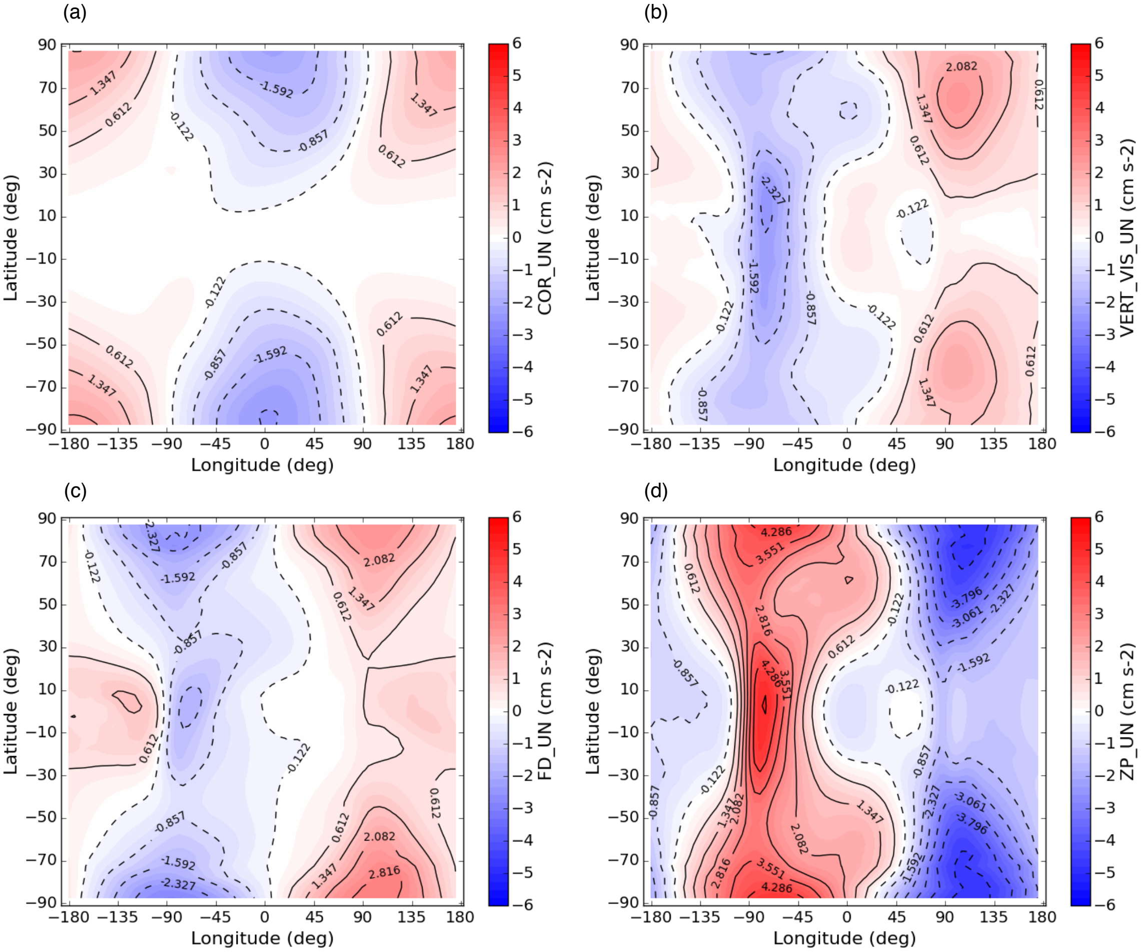

Figure C.2: Zonal (a) Coriolis force, (b) viscous drag force, (c) ion drag force, and (d) pressure gradient force for complete simulation and solar minimum conditions.

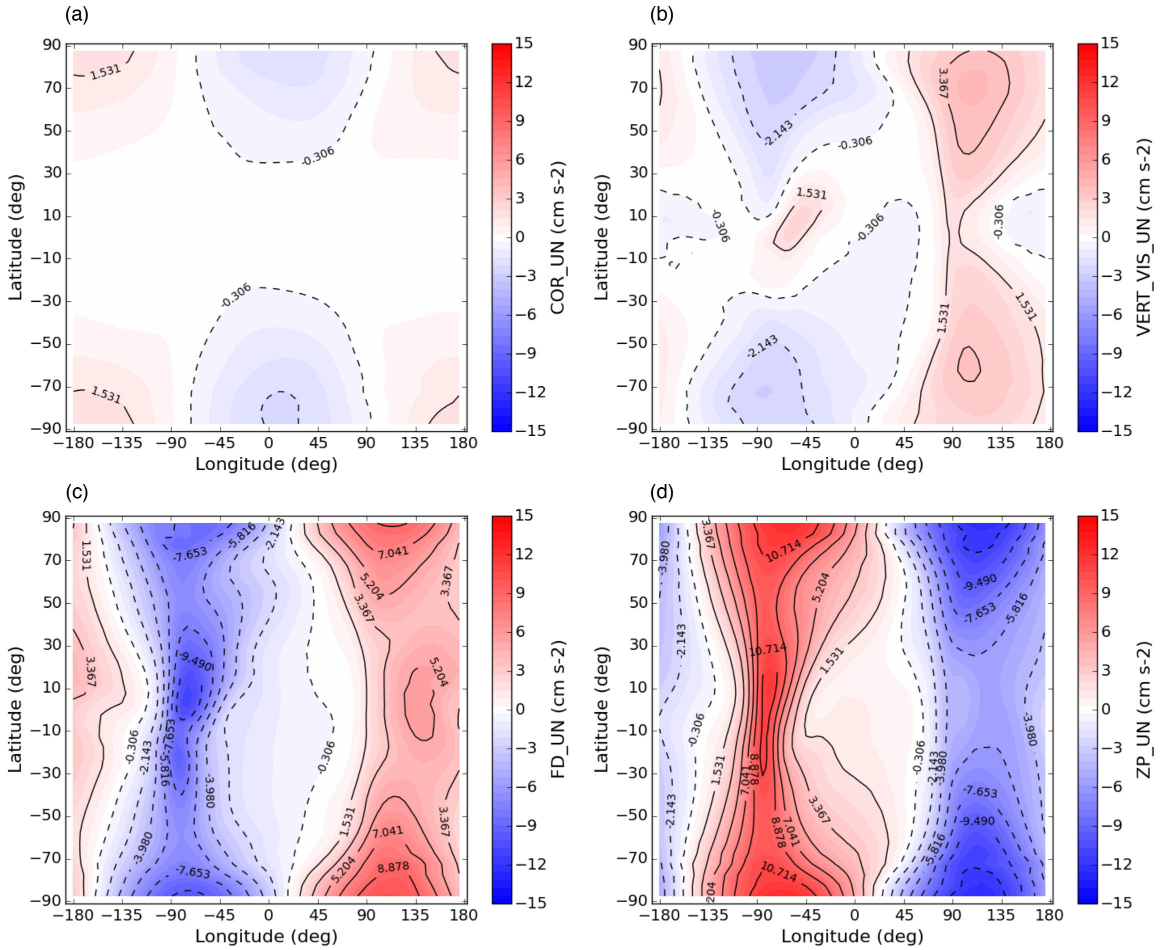

Figure C.3: Zonal (a) Coriolis force, (b) viscous drag force, (c) ion drag force, and (d) pressure gradient force for complete simulation and solar maximum conditions.

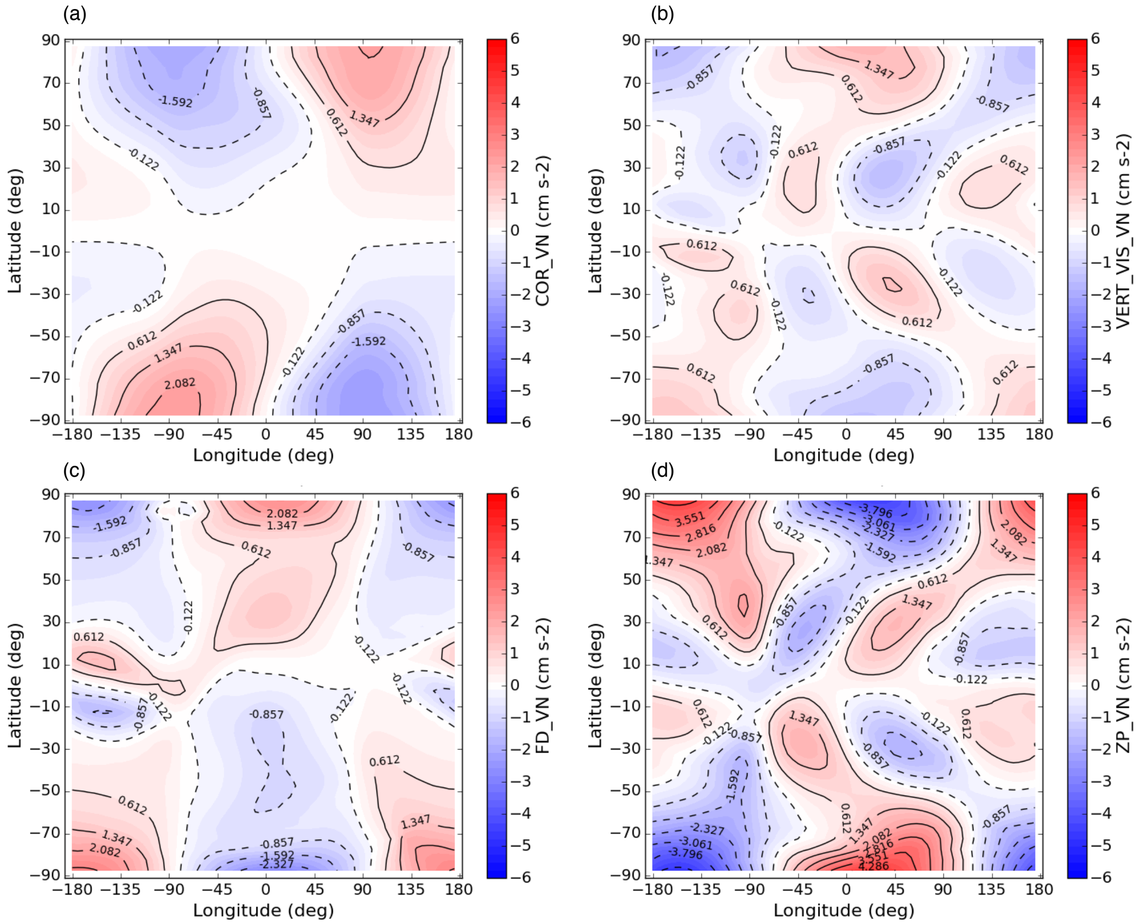

Figure C.4: Meridional (a) Coriolis force, (b) viscous drag force, (c) ion drag force, and (d) pressure gradient force for complete simulation and solar minimum conditions.

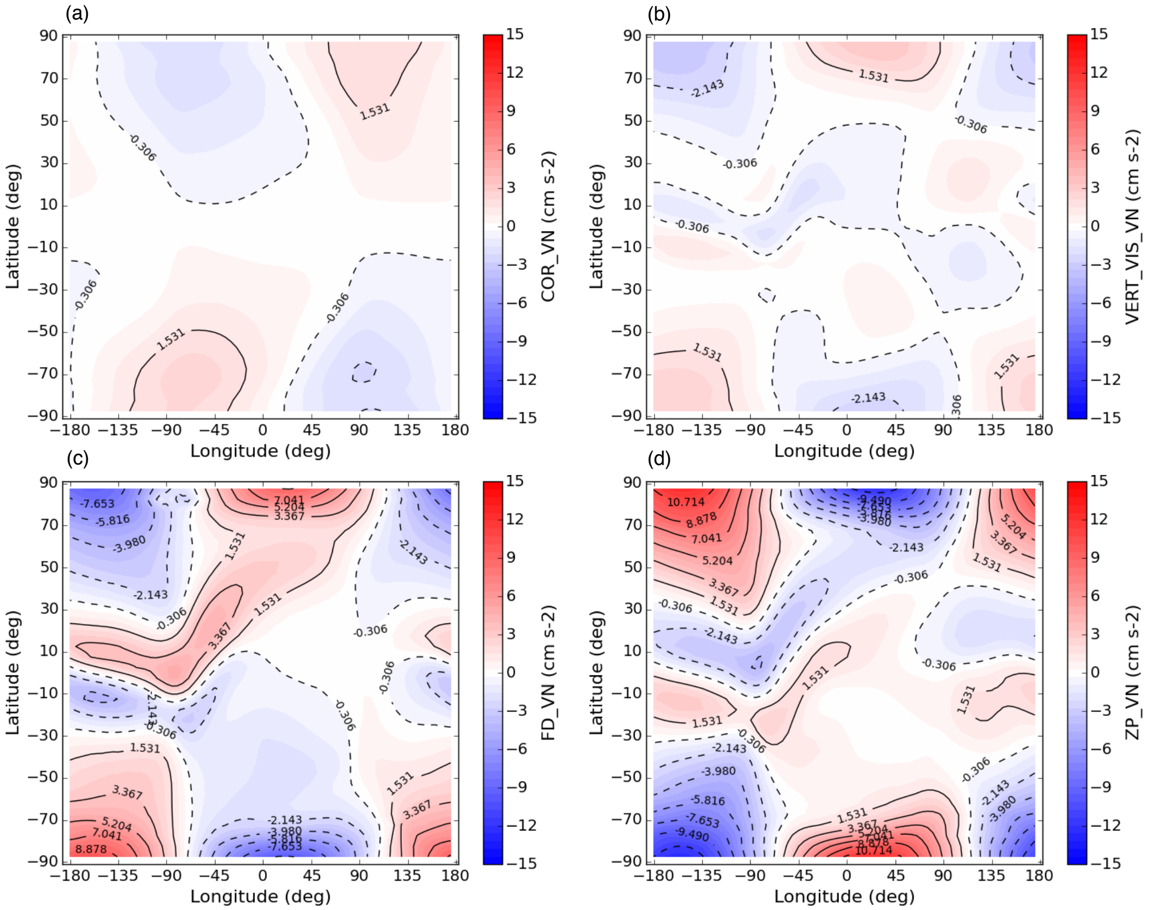

Figure C.5: Meridional (a) Coriolis force, (b) viscous drag force, (c) ion drag force, and (d) pressure gradient force for complete simulation and solar maximum conditions.

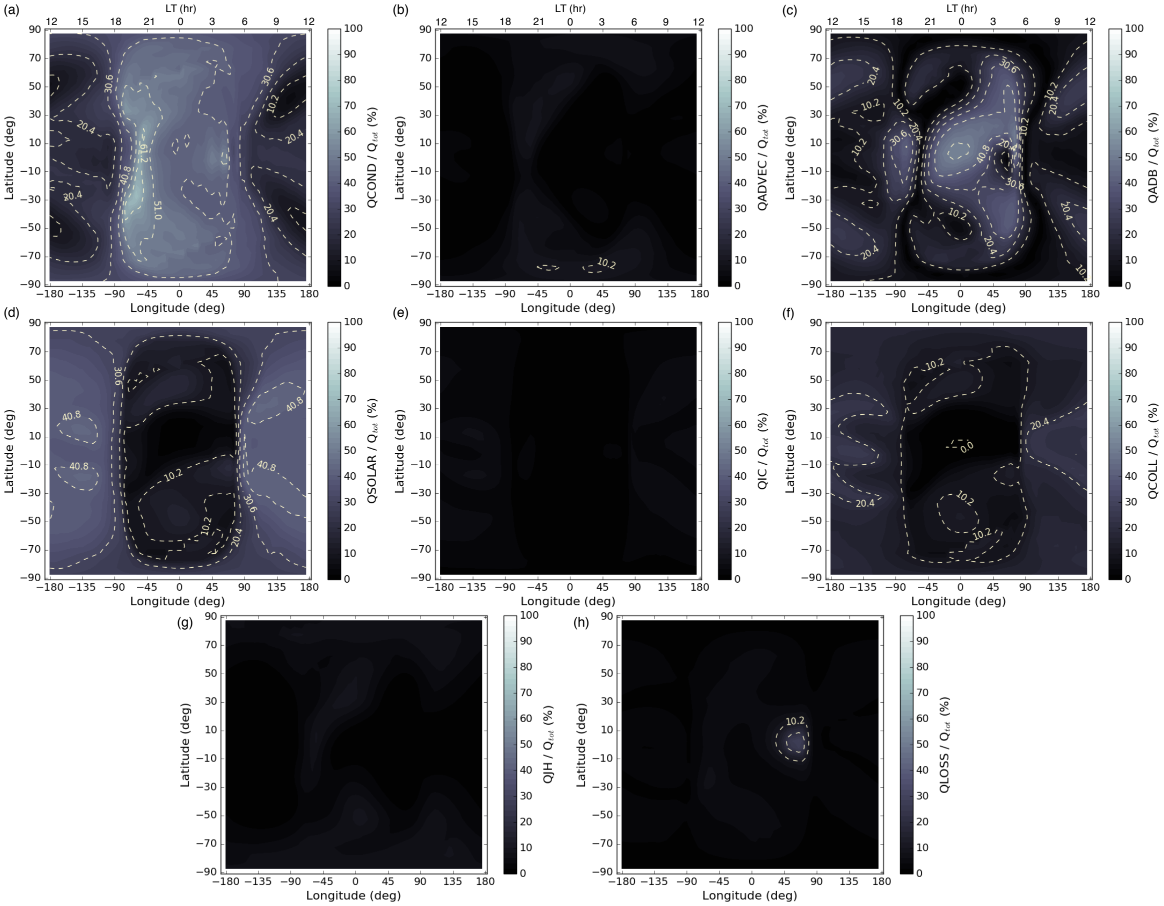

Figure C.6: Relative percentage of heat terms to the total energy in complete simulation under solar minimum conditions for (a) conduction, (b) advection (horizontal and vertical), (c) adiabatic heating and cooling, (d) solar radiation, (e) ion chemical heating, (f) collisional heating, (g) Joule heating, and (h) radiational cooling.

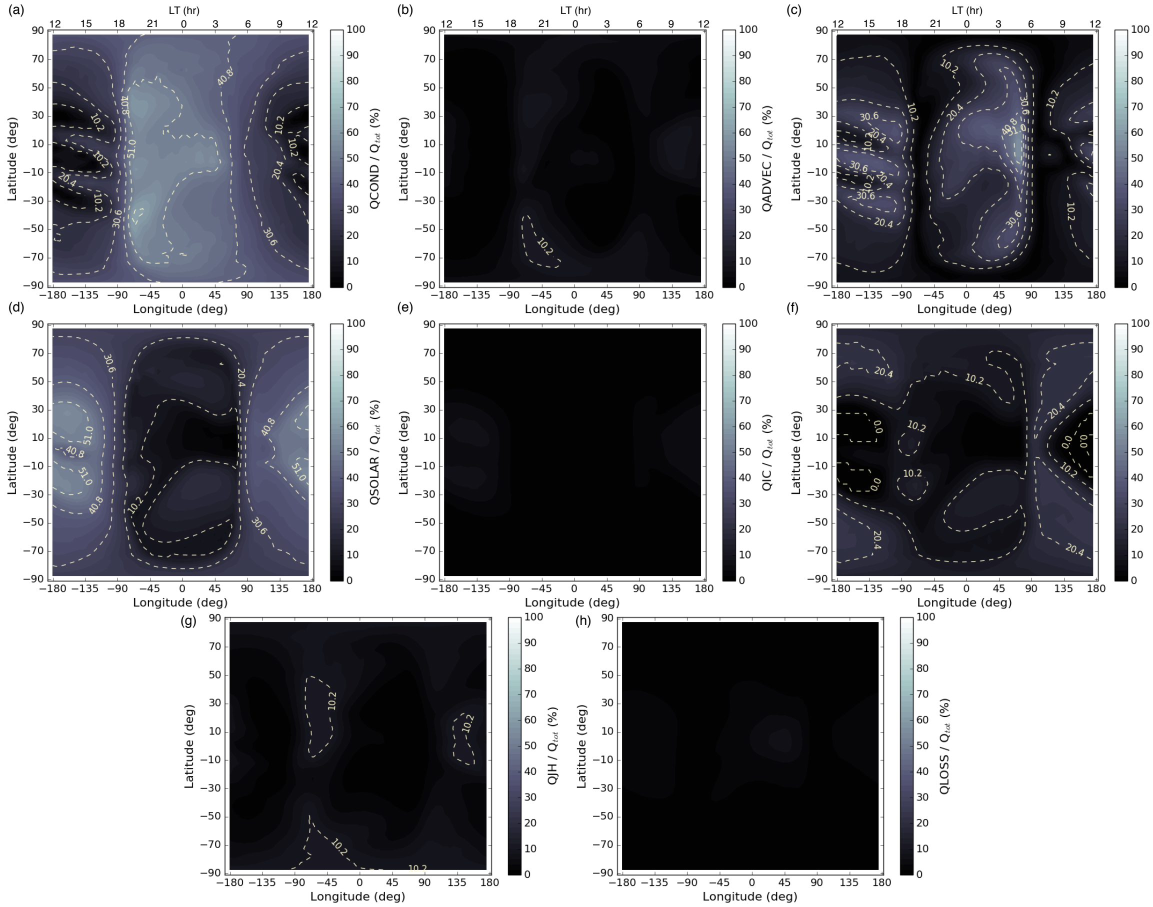

Figure C.7: Relative percentage of heat terms to the total energy in complete simulation under solar maximum conditions for (a) conduction, (b) advection (horizontal and vertical), (c) adiabatic heating and cooling, (d) solar radiation, (e) ion chemical heating, (f) collisional heating, (g) Joule heating, and (h) radiational cooling.

C.1 Day-night Ratio Analysis

In the quiet-time thermosphere, ion and viscous drag forces have a significant impact on the dayside and nightside energy distributions. The complete simulations (with ion drag and frictional heating) in Chapter 5 are compared with the MSIS empirical model for the same solar flux levels and geomagnetic activity , shown in Fig. C.8.

The sensitivity of the day-night ratio was tested by increasing or decreasing the ion drag force in the simulations. Modifying the ion drag force serves to enhance or reduce the dayside thermal energy. Day-night ratios are computed using the same local time bins as Müller et al.

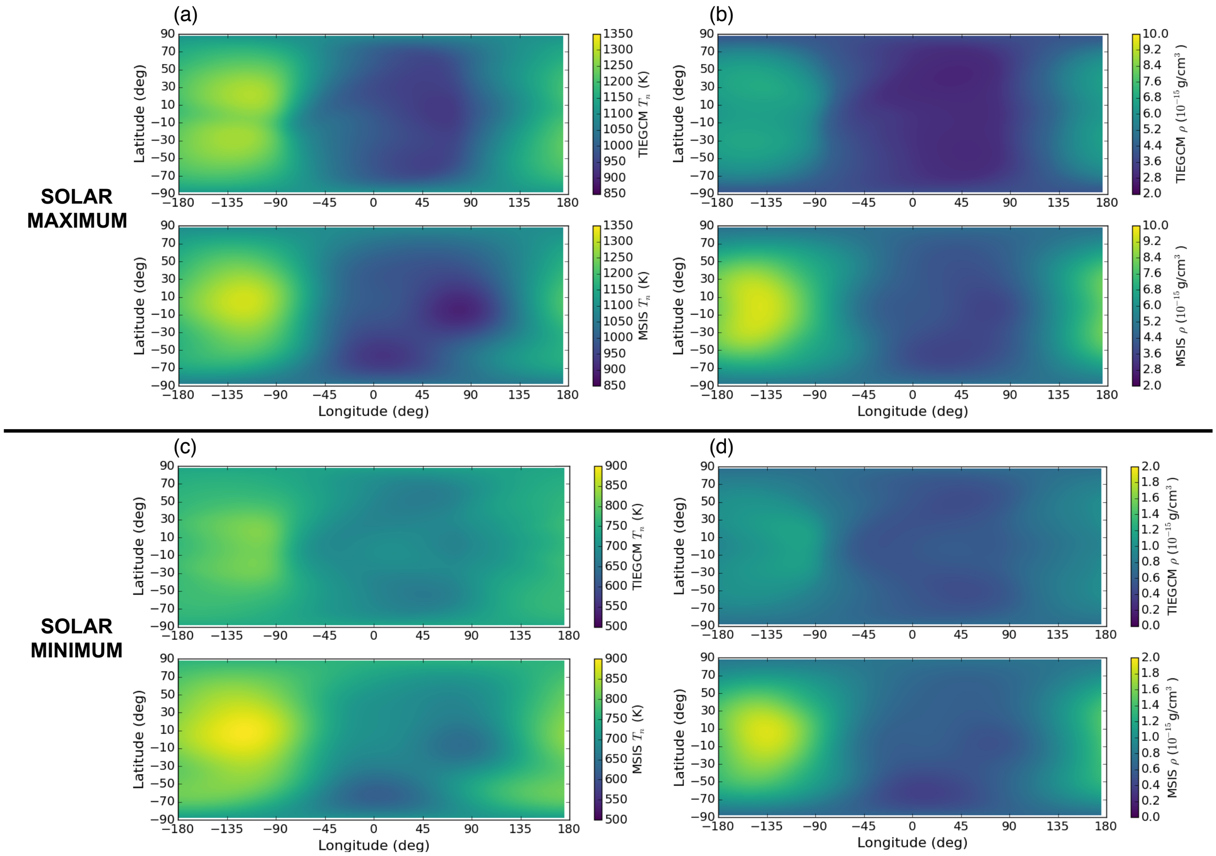

Figure C.8: Solar maximum (a) neutral temperature and (b) neutral mass density, and solar minimum (c) neutral temperature and (d) neutral mass density for TIEGCM (top) and MSIS (bottom) at UT = 0 hr and 400 km.

[2009], where dayside is considered the average of 11:00-17:00 LT and nightside spans 23:00-5:00 LT. The day-night T_n ratios for the normal TIEGCM simulations are 1.229 (or 1.867 ρ ratio) for solar maximum and 1.124 (or 1.738 ρ ratio) for solar minimum compared with MSIS day-night ratios of 1.208 (or 1.785 ρ ratio) and 1.189 (or 2.259 ρ ratio) for solar maximum and minimum, respectively. The TIEGCM ratio changes to 1.219 (or 1.814 ρ ratio) when ion drag is multiplied by 0.9 in solar maximum, and it changes to 1.156 (or 2.065 ρ ratio) when ion drag is multiplied by 2.0 in solar minimum. It is apparent that the ratio is proportional to the ion drag modifications, where an increase / decrease in the ion drag force results in an increase / decrease in the day-night ratio. These numerical experiments demonstrate the sensitivity of the temperature and mass density structure of the upper thermosphere to uncertainties of a term in the momentum equation (e.g., the ion drag force). They also further support one of the key findings in Chapter 5, where drag forces have great influence over the radiatively-forced neutral structure in the upper atmosphere.

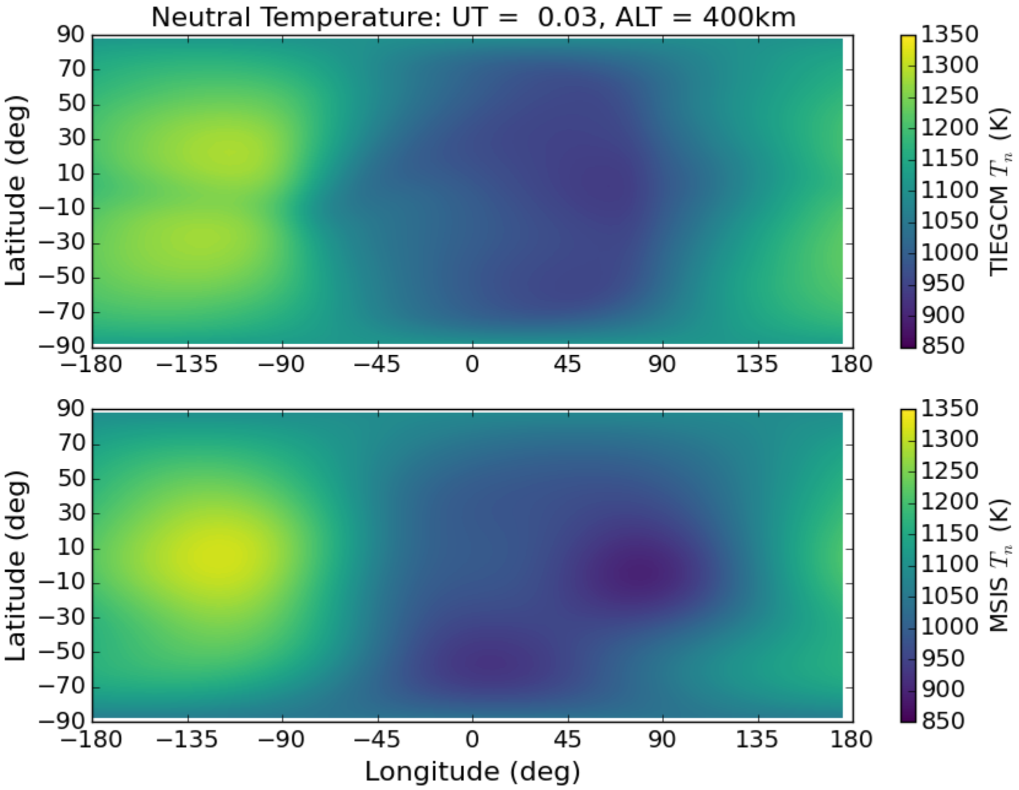

Figure C.9: Neutral temperature for TIEGCM (top) and MSIS (bottom) as a function of latitude and longitude with a ion drag multiplication factor of 0.9 for solar maximum conditions.

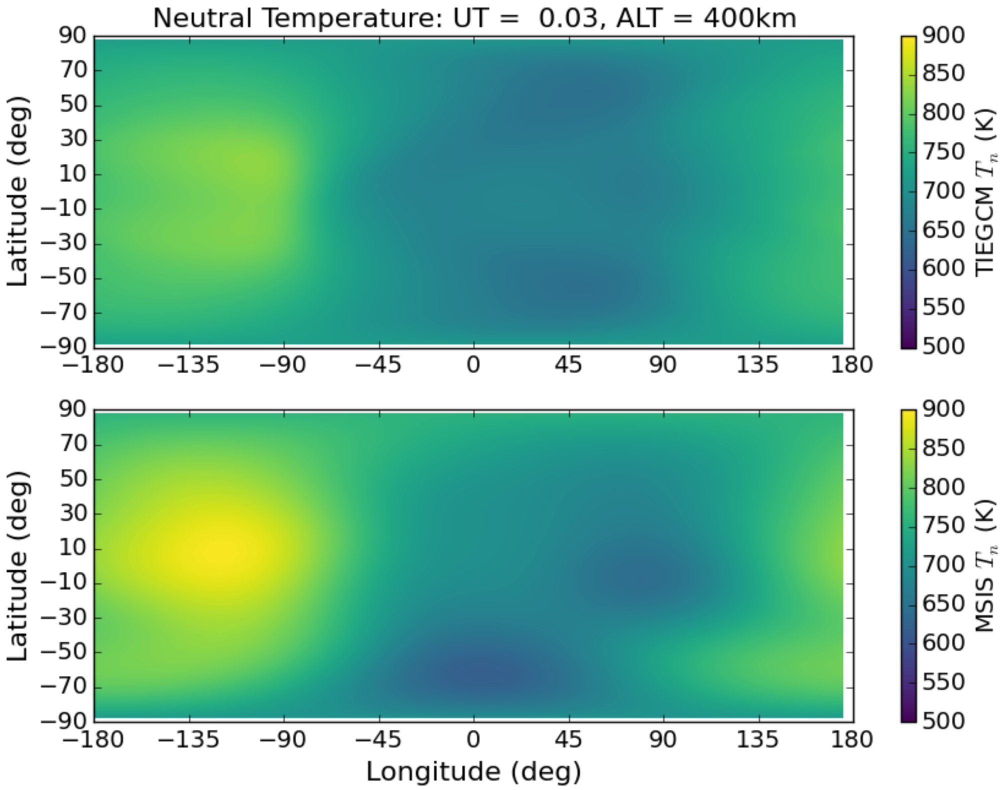

Figure C.10: Neutral temperature for TIEGCM (top) and MSIS (bottom) as a function of latitude and longitude with a ion drag multiplication factor of 2.0 for solar minimum conditions.

Appendix D

Supplemental Figures: Thermospheric Signatures of Energy Mechanism Study

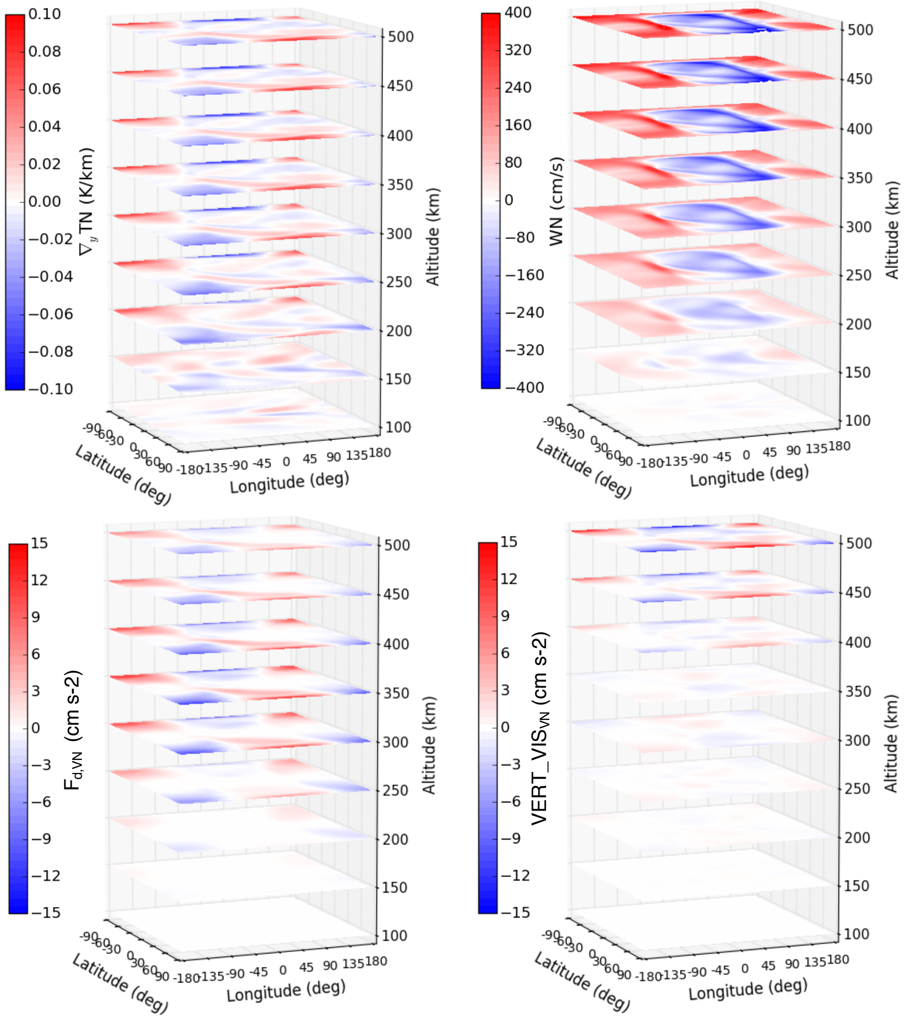

Figure D.1: Meridional neutral temperature gradient, vertical wind, ion drag force, and viscous drag force as a function of latitude, longitude and altitude under solar maximum conditions at UT = 0.0 hr.

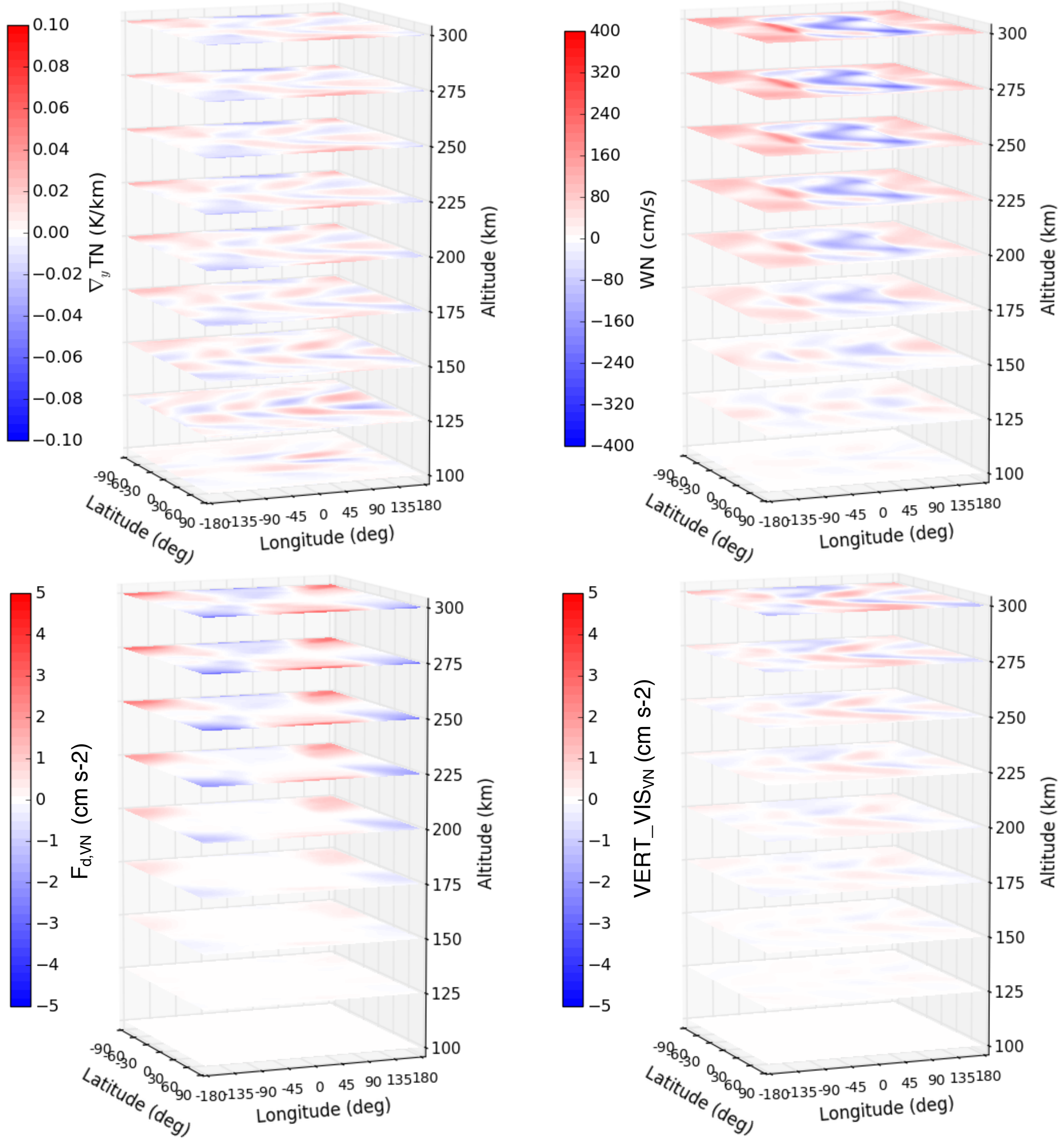

Figure D.2: Meridional neutral temperature gradient, vertical wind, ion drag force, and viscous drag force as a function of latitude, longitude and altitude under solar minimum conditions at UT = 0.0 hr.

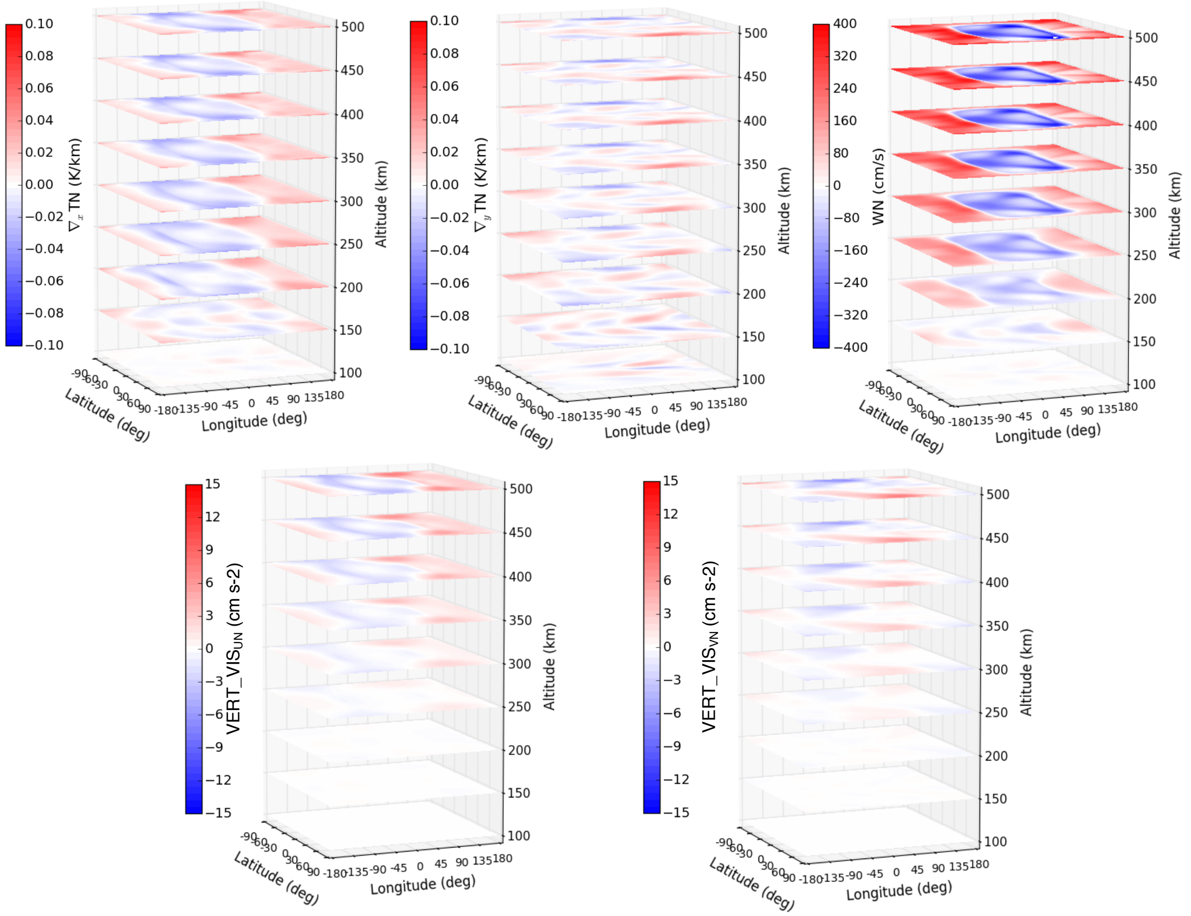

Figure D.3: Clockwise from left, Zonal neutral temperature gradient, meridional neutral temperature gradient, vertical wind, meridional viscous drag force, and zonal viscous drag force as a function of latitude, longitude and altitude under solar maximum conditions at UT = 0.0 hr for run 5.

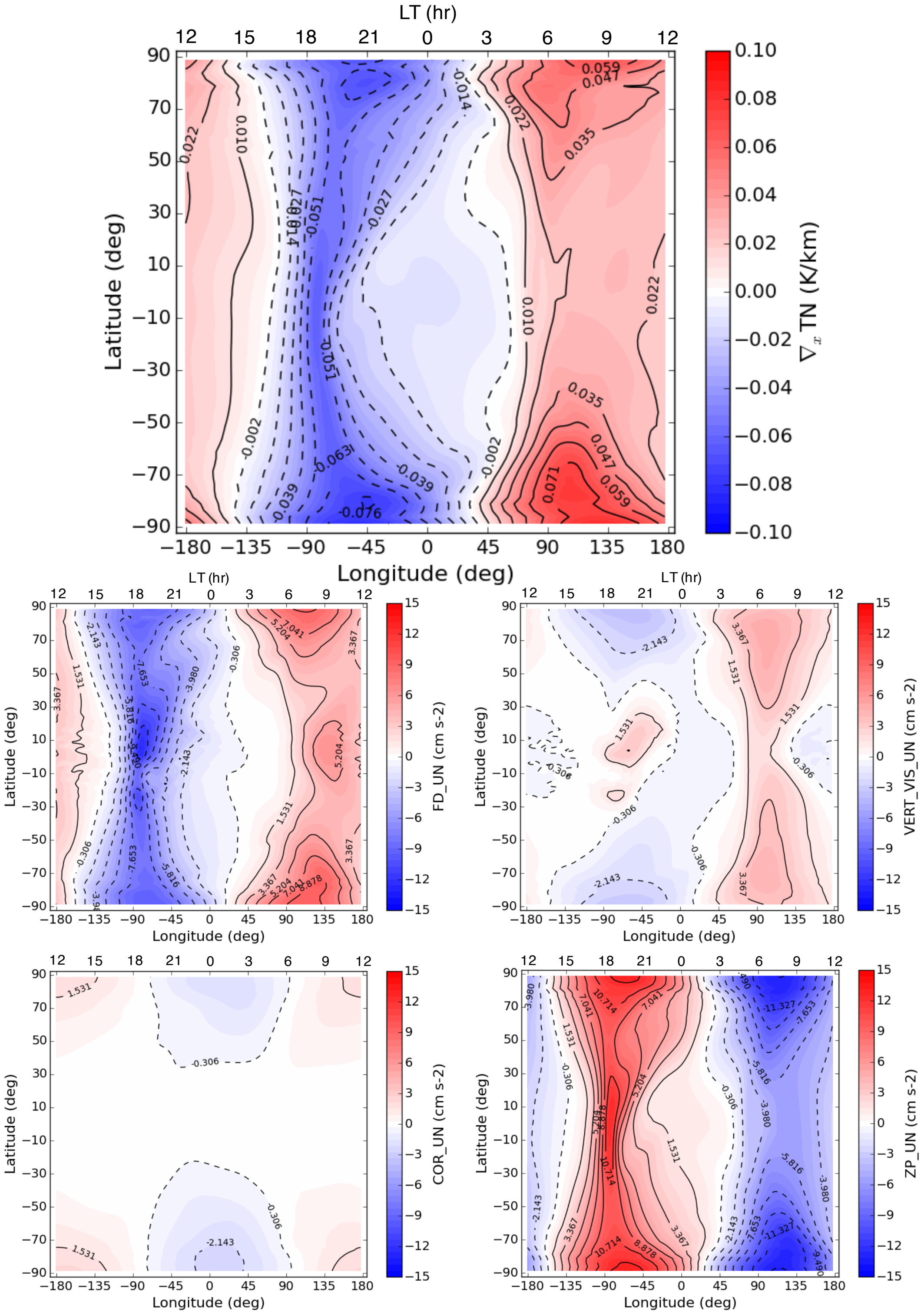

Figure D.4: Zonal neutral temperature gradient, ion drag force, viscous drag force, Coriolis force, and pressure gradient force as a function of latitude and longitude under solar maximum conditions at 400 km and UT = 0.0 hr for run 8.

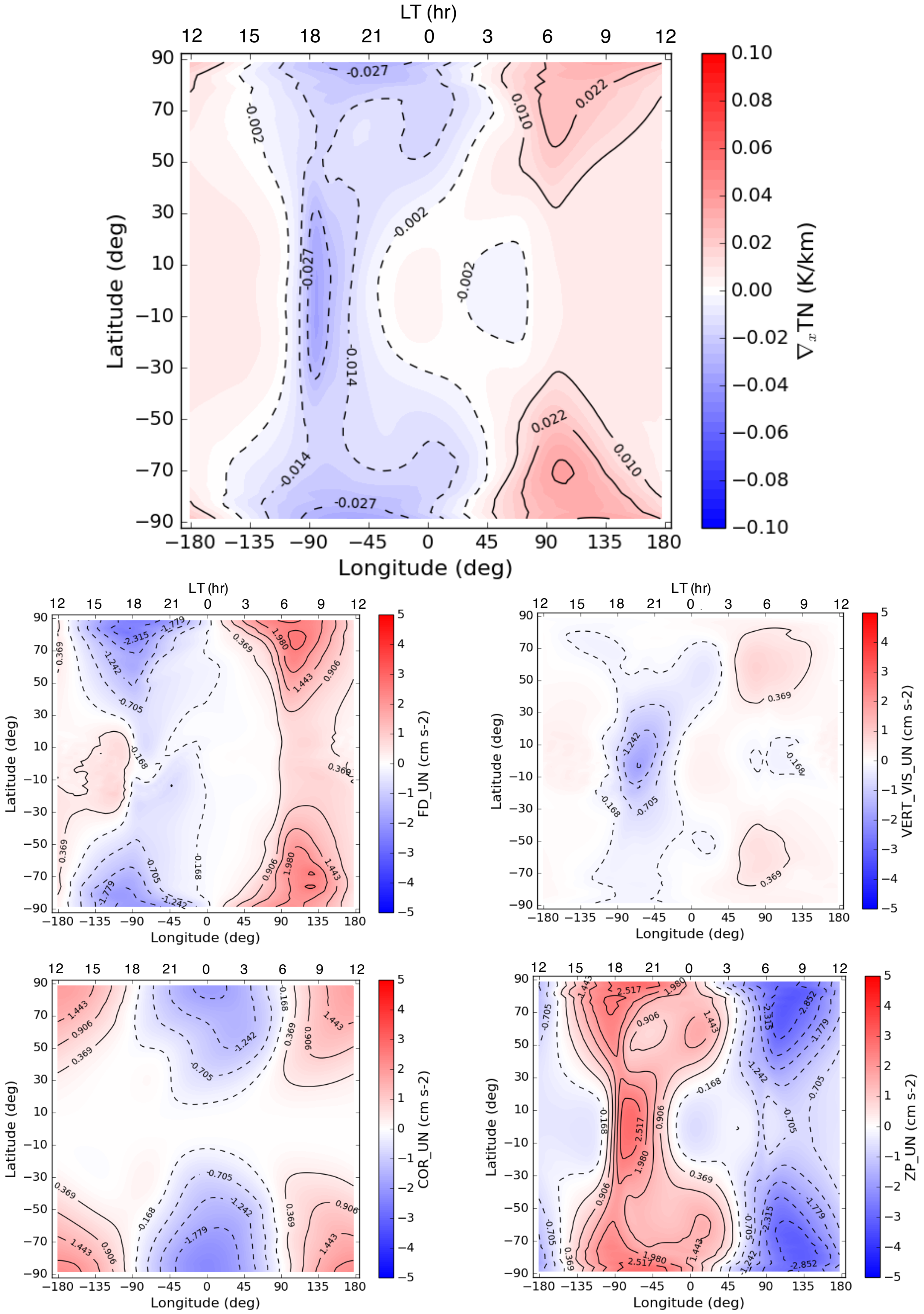

Figure D.5: Zonal neutral temperature gradient, ion drag force, viscous drag force, Coriolis force, and pressure gradient force as a function of latitude and longitude under solar minimum conditions at 400 km and UT = 0.0 hr for run 7.

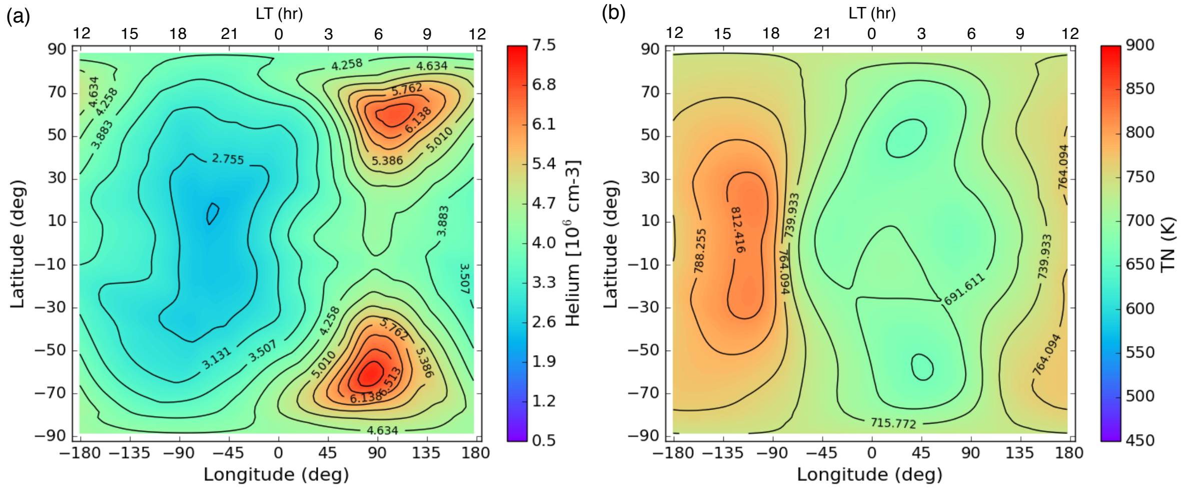

Figure D.6: (a) Helium number density and (b) neutral temperature as a function of latitude and local time under solar minimum conditions at 400 km and UT = 0.0 hr for run 7.

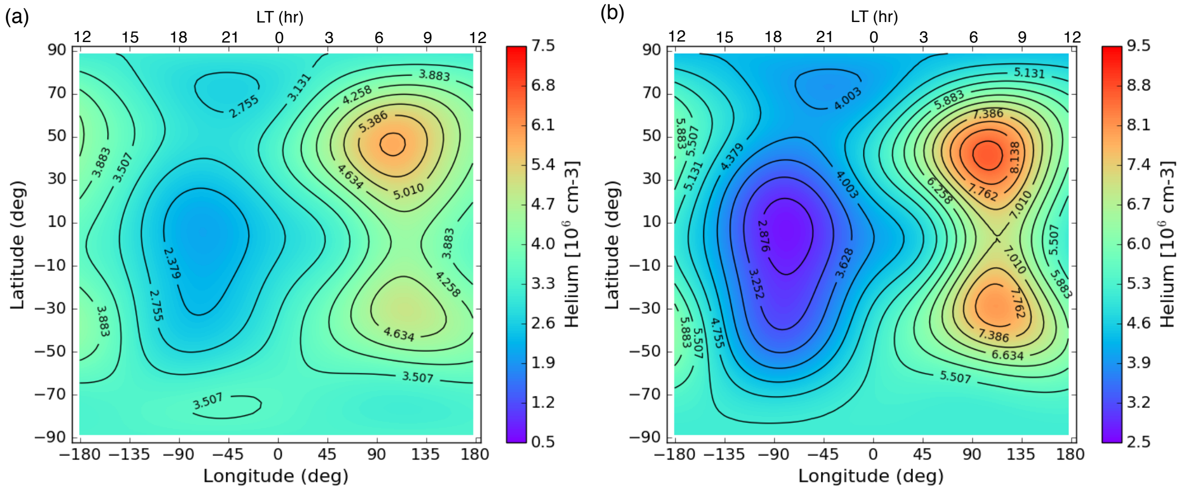

Figure D.7: MSIS helium number density for (a) solar minimum and (b) solar maximum as a function of latitude and local time at 400 km and UT = 0.0 hr.